Modellering van gekoppelde warmte- en vochtoverdracht
tussen lucht en poreuze materialen voor toepassingen in gebouwen

Modelling Coupled Heat and Moisture Transfer
Between Air and Porous Materials for Building Applications

Marnix Van Belleghem

Promotoren: prof. dr. ir. M. De Paepe, prof. dr. ir. -architect A. Janssens
Proefschrift ingediend tot het behalen van de graad van
Doctor in de Ingenieurswetenschappen: Werktuigkunde-Elektrotechniek

Vakgroep Mechanica van Stroming, Warmte en Verbranding
Voorzitter: prof. dr. ir. J. Vierendeels
Faculteit Ingenieurswetenschappen en Architectuur
Academiejaar 2012 - 2013

UNIVERSITEIT
GENT

ISBN 978-90-8578-580-4
NUR 961
Wettelijk depot: D/2013/10.500/13

Universiteit Gent
Faculteit Ingenieurswetenschappen en Architectuur
Vakgroep Mechanica van Stroming, Warmte en Verbranding

Promotoren: prof. dr. ir. Michel De Paepe
prof. dr. ir. arch. Arnold Janssens

Universiteit Gent
Faculteit Ingenieurswetenschappen en Architectuur

Vakgroep Mechanica van Stroming, Warmte en Verbranding
Sint-Pietersnieuwstraat 41, B-9000 Gent, België

Tel.: +32-9-264.32.88
Fax.: +32-9-264.35.75

Dit werk kwam tot stand in het kader van een specialisatiebeurs van het IWT-Vlaanderen IWT-SB/81322/VanBelleghem (Instituut voor de aanmoediging van Innovatie door Wetenschap en Technologie in Vlaanderen).

Department of Flow, Heat and Combustion Mechanics

Proefschrift tot het behalen van de graad van
Doctor in de Ingenieurswetenschappen:
Werktuigkunde - Elektrotechniek
Academiejaar 2012-2013

Dankwoord

Toen ik in 2007 vol goede moed en nog groen achter de oren het Technicum aan de Sint-Pietersnieuwstraat binnenstapte om mijn doctoraatstudies aan te vatten, had ik nog geen idee waar ik mij aan waagde. Nu, vijf jaar later, kan ik besluiten dat het een goede keuze was. Ik heb mij in de laatste vijf jaar enorm verrijkt, zowel wat kennis als wat vriendschappen betreft.

Natuurlijk liep niet alles altijd van een leien dakje. Ik startte mijn onderzoek aan de vakgroep met experimenteel werk. Maar wanneer je experimenteel onderzoek doet, komt daar vaak veel zweet, gezwoeg en gevloek bij kijken. Experimenten die mislukken of vreemde resultaten geven, sensoren die op de meest onmogelijke momenten falen, kortom wat fout kon gaan, ging meestal wel eens fout. Vaak keek ik vol bewondering en soms wel jaloezie naar mijn collega's die, schijnbaar eenvoudig, resultaten toverden met numeriek werk. Het duurde dan ook niet lang of numeriek onderzoek kreeg mijn aandacht. Eens ik mij verdiept had in de wondere wereld van numerieke stromingsmechanica, werd mij al snel duidelijk dat het produceren van deftige resultaten niet zo evident was. Blijkbaar zitten zowel experimenteel als numeriek werk vol valkuilen en obstakels...

Maar, als ik één ding geleerd heb tijdens mijn doctoraatsstudies, dan is het wel te volharden. Uit elke tegenslag of gefaalde proef leer je bij, elk obstakel zie je als een uitdaging. En nu, zie hier, na vijf jaar het resultaat! Een resultaat dat er niet zou geweest zijn zonder de bijdrage van een hele reeks personen. Ik had voor mezelf een lijstje gemaakt wie ik zeker allemaal moest bedanken en het is een behoorlijk uitgebreide lijst geworden.

Allereerst moet ik mijn promotoren Michel en Arnold bedanken. Michel, jij was degene die mij eerst wist te overtuigen om bij jou een thesis aan te vatten en nadien wist je me zelf te overhalen om 'te blijven'. Jouw enthousiasme voor onderzoek en wetenschap werkte aanstekelijk, en de gemoedelijke sfeer die heerste in de onderzoeksgroep heeft alleen maar bijgedragen aan mijn positieve keuze. Bedankt ook voor de vele interessante discussies, daarom niet altijd onderzoeksgerelateerd...
Arnold, als co-promotor van een andere vakgroep was ons contact misschien minder frequent, maar daarom niet minder belangrijk. Jouw heldere bouwfysische blik op mijn werk zorgde voor een niet onbelangrijke bijdrage.

Daarnaast moet ik ook de vele collega's bedanken met wie ik door de jaren heen

heb samengewerkt. Allereerst de collega's van het eerste uur. Hendrik-Jan, jouw werk was een belangrijke aanzet en inspiratiebron voor het mijne. Gedurende de eerste jaren stond je me steeds bij met raad en daad. Christoph, Hugo, Arnout, Ivan en Henk, jullie werkijver en inzet werkte aanstekelijk. De kwaliteit waarmee jullie onderzoek afleverden, tilde ook mijn werk naar een hoger niveau.
Vervolgens moet ik de 'nieuwe lichting' bedanken. Bernd, Kathleen, Sven, Tom en Steven, het is duidelijk dat Michel een neus heeft voor talent. Jullie raakten al snel ingewerkt in de groep en waren vaak een belangrijk aanspreekpunt bij allerhande vragen en problemen. Peter, als doctoraatstudent was jij een beetje een buitenbeentje. Jij werkte deels bij ons en deels bij een niet nader genoemde staaldraadproducent. Die combinatie was niet altijd evident. Ik heb zelden iemand ontmoet die met zoveel overgave, interesse en diepgang een doctoraatsonderzoek deed.
Ik mag zeker ook niet vergeten onze technische staf te bedanken! Robert en Patrick, de tijd die jullie gespendeerd hebben om mijn proefstanden draaiende te krijgen, was enorm. Vele oplossingen voor technische problemen waren enkel mogelijk dankzij jullie ervaring en vernuft. Patricia, Annie en Griet, dankzij jullie administratieve ondersteuning kon ik mij ten volle toeleggen op mijn onderzoek. Yves, dankzij jouw deskundig IT-beleid was gedurende de laatste vijf jaar mijn data steeds veiliggesteld.

Mijn onderzoek was sterk interdisciplinair en bevond zich ergens tussen werktuigkunde en bouwfysica. Gelukkig kon ik voor al mijn bouwfysische problemen terecht bij Arnold en zijn medewerkers. Het was ook vaak met hen dat ik menig conferentie afschuimde. Kim, Marc, Nathan, Jelle en Lien, bedankt voor de aangename tijd.
Ik moet ook mijn collega's uit andere universiteiten bedanken die bijdroegen aan dit werk. In het bijzonder prof. Hans Janssen, prof. Staf Roels en dr. ir. Thijs Defraeye. Zonder het misschien goed te beseffen hebben zij belangrijke input gegeven.

Wanneer er dan eens niet gewerkt werd, kon ik rekenen op een hele reeks vrienden, voetbal makkers en drinkebroeders om voor de nodige ontspanning te zorgen. Ook moet ik in het bijzonder mijn ouders en broers bedanken voor alle steun de afgelopen jaren. Zonder hen zou ik niet staan waar ik nu sta.

Tot slot moet ik nog mijn vriendin bedanken. Marijke, jij was van in het begin een grote hulp en steun. Onze vriendschap groeide intussen uit tot een hechte band en samen verwezenlijkten we ons eerste echte meesterstuk, onze zoon Nand. Ik kijk uit naar de komende boeiende jaren, wij als prille ouders, jij als mijn rots in de branding!

Aan iedereen en aan Marijke in het bijzonder,
Bedankt!

Gent, februari 2013
Marnix Van Belleghem

Table of Contents

Dankwoord **i**

Table of Contents **iii**

List of Figures **vii**

List of Tables **xiii**

Nomenclature **xv**

Nederlandse samenvatting **xxiii**

English summary **xxvii**

1 Moisture in buildings **1**
1.1 Introduction 1
1.2 Moisture damage phenomena 2
1.3 Heat and moisture modelling in buildings 5
1.4 Problem definition and research aim 8

2 Heat and moisture transport in air and porous materials **11**
2.1 Porous material model 11
2.1.1 Thermodynamic relations 11
2.1.2 Modelling a porous material 12
2.2 Heat and moisture transport in the air 19
2.2.1 General considerations 19
2.2.2 Moisture transport in air 25
2.2.3 Heat transport in air 26
2.3 Coupled heat and moisture transport in porous materials 29
2.3.1 Moisture transport in a porous material 29
2.3.2 Heat transport in a porous material 30

3 Numerical implementation **33**
3.1 Introduction: using Fluent® to solve transport equations 33
3.2 Coupled CFD-HAM model for vapour transport 38
3.2.1 Heat and moisture transport in air 38

3.2.2 Heat and moisture transport in the porous material 39
3.3 Coupled CFD-HAM model including liquid moisture transport . . 43
3.3.1 Mass fraction or capillary pressure? 44
3.3.2 Implementation of the heat and moisture transport equation 46
3.3.3 Coupling procedure and boundary conditions 48
3.4 Model verification 55
3.4.1 Verification of vapour transport 56
3.4.2 Adiabatic saturation 57
3.4.3 Comparison with commercial HAM-model 62

4 Vapour transport modelling: experimental validation 65
4.1 Introduction 65
4.2 State of the art in vapour transport experiments 66
4.2.1 Room-size moisture buffering and humidity distribution experiments 66
4.2.2 Performance of building envelope systems 70
4.2.3 Wind tunnel experiments - convection coefficient experiments 70
4.2.4 Discussion 72
4.3 Climate chamber design 72
4.3.1 Test chamber 72
4.3.2 Air handling unit 73
4.3.3 Instrumentation 75
4.4 Validating a coupled CFD-HAM model for vapour transport . . . 78
4.4.1 Experimental setup 78
4.4.2 Experimental validation 82
4.4.3 Discussion and conclusions 87
4.5 Sensitivity analysis of a coupled CFD-HAM model for vapour transport 87
4.5.1 Reference case 87
4.5.2 Material properties 90
4.5.3 Sensitivity analysis 94
4.5.4 Discussion en conclusions 106

5 Validating the coupled CFD-HAM model including liquid water transport 111
5.1 Introduction 111
5.2 Short introduction to drying phenomena 112
5.3 Modelling convective drying 116
5.3.1 Analytical modelling 117
5.3.2 Convective transfer coefficients as a boundary condition . 118
5.3.3 Conjugate modelling: a complete approach 122
5.3.4 Discussion 124
5.4 Validating the coupled CFD-HAM model including moisture transport 126

5.4.1 Experimental setup 126
5.4.2 Comparison of experiment and simulations 127
5.4.2.1 2D model of cross section 129
5.4.2.2 2D model of longitudinal section 132
5.4.2.3 3D model 139
5.4.3 Inter-model comparison for drying 141
5.4.4 Moisture distribution in the brick: comparison with neutron radiography measurements 147
5.4.5 Conclusion 151
5.5 New drying experiment 155
5.5.1 Introduction 155
5.5.2 Experimental setup 155
5.5.3 Limitations of the measurement setup 158
5.5.4 Simulation settings 160
5.5.5 Drying experiment - comparison with simulations 163
5.5.6 Conclusions 167

6 Case study: heat and moisture transport modelling in ventilated cavity walls 171
6.1 Introduction: modelling a ventilated cavity wall 171
6.1.1 Cavity wall modelling in WUFI® 174
6.1.2 Cavity wall modelling using the coupled CFD-HAM model 176
6.2 Radiation model 180
6.3 Air velocity in a cavity wall 182
6.4 Drying of a cavity wall under summer and winter conditions . . . 184
6.5 Constant inlet velocity versus constant inlet pressure 190
6.6 Discussion and conclusions 195

7 Conclusions and perspectives 201
7.1 General conclusions 201
7.2 Perspectives and future work 204

A Material properties 207
A.1 Air properties 207
A.2 Porous materials 208
A.2.1 Moisture transport properties ceramic brick 209
A.2.2 Moisture transport properties calcium silicate 211
A.2.3 Moisture transport properties gypsum board 211
A.2.4 Moisture transport properties wood fibre board (Celit®) . 212
A.3 Non-hygroscopic materials 213

B Publications 215

References 219

List of Figures

1.1 Examples of moisture problems and damage phenomena that often occur in buildings. 6

2.1 Microscopic detail of a porous material. 13
2.2 Moisture content in a hygroscopic porous material as a function of the relative humidity (sorption isotherm). 15
2.3 Detail of a pore with three possible adsorption mechanisms: monolayer adsorption, multilayer adsorption and capillary condensation. 15
2.4 Schematic representation of equilibrium in a pore filled with water. 16
2.5 Retention curve of a capillary porous material. 18
2.6 Schematic representation of the dimensionless velocity profile u^+ as a function of y^+. The law of the wall is compared with experiments (•) by for example [47] 24

3.1 Schematic representation of the diffusion flux between two adjacent cells. 36
3.2 Illustration of the difference between the mixed approach and the direct approach based on Janssen [62]. 40
3.3 Psychrometric chart, saturation mass fraction indicated in blue . . 45
3.4 Solution procedure for segregated transient solver 50
3.5 Schematic representation of the boundary conditions in the coupled CFD-HAM model 51
3.6 Detail of two neighbouring cells, one at the material side $C0_m$ and one at the air side $C0_a$. 52
3.7 Schematic representation of the verification case proposed by Milly [66] 56
3.8 Verification for transport equations in the porous material when only vapour transport is present. Comparison at different times between the numerical model $(-)$ and the analytical model $(\diamond : 500s, \square : 5000s, \bigcirc : 20000s, \times : 200000s, \triangle : 500000s)$ 58
3.9 Schematic representation of the adiabatic saturation process: water evaporates until the air at the oulet is saturated with water vapour. Fresh water is supplied at saturation temperature. $T_{sat} = T_{as}$. . . . 59
3.10 Details of 1D simulated case to illustrate adiabatic saturation. . . . 62

3.11 Temperature change in time in a sample of ceramic brick exposed to air at 23.8 °C and $44\%RH$. h_m^Y = $0.0258kg/m^2s$ (red line = simulation; Δ = analytic) corresponding with Le = 0.808. h_m^Y = $0.0224kg/m^2s$ (black line = simulation; o = analytic) corresponding with Le = 1. The moisture content of the material is kept constant. 63

3.12 Comparing temperature evolution in time and moisture content in ceramic brick during drying for the coupled CFD-HAM model (- -) and WUFI® with exponential liquid diffusivity (—). 64

4.1 Schematic representation of the climate chamber and the air handling unit (dimensions in cm): (1) recirculation fan, (2) cooling coil, (3) resistive heater, (4) steam humidifier, (5) buffer vessel and (6) flow straightener. 73

4.2 View on the outer and inner test chamber with test wall. 74

4.3 Algorithm used to control the supply air temperature and relative humidity. 75

4.4 Response of the relative humidity sensor to a change of temperature, at constant absolute humidity (b) and response of the relative humidity sensor to a change of absolute humidity, at a constant temperature (a). Temperature indicated in green, relative humidity indicated in black. 77

4.5 (a) Calibration setup. (b) Comparison between chilled mirror calibration (△) and two-pressure calibration (■) for a capacitive sensor. 79

4.6 Schematic representation of the calcium silicate test sample (a) and view on the test sample (b) 81

4.7 Influence of the cutting edge on the measured temperature and relative humidity in the sample: original sample (black line) and adapted sample (green line). Measurements in the sample at 25mm (a,b), measurements at the front surface of the sample (c,d) and measurements at the back of the sample (e,f) 83

4.8 Comparison of the measured velocity in the middle of the room (a) and the simulated velocity (b). Velocities are indicated in m/s. . . 86

4.9 Relative humidity (a) and temperature (b) at a depth of 10mm (—), 8.3mm (- -) and 11.5mm (- -) in the calcium silicate. Black line with error bars corresponds with the measurements. Similar graphs for relative humidity (c) and temperature (d) at 25mm depth (—), 23.2mm (- -) and 26.6mm (- -). Relative humidity (e) and temperature (f) at 50mm (—), 47.7mm (- -) and 52.5mm (- -) . . . 88

4.10 Test section of the wind tunnel setup [86] with three gypsum boards stacked on top of each other. 89

4.11 Sorption isotherms for gypsum board (data from [111]) (a) and measured differences between the curves (b). Full lines in (a) correspond with equation 4.1, ×, + and ∘ correspond with measurements. 91
4.12 Vapour resistance factors for gypsum board (data from [111]) (a) and measured differences between the curves (b). Full lines in (a) correspond with equation 4.3, ×, + and ∘ correspond with measurements. 92
4.13 Typical response of the relative humidity (a) and temperature (b) in gypsum board at a depth of $12.5mm$ for a step change induced in the relative humidity of the surrounding air (29.6 – $71.9\%RH$) 95
4.14 Effect of variation in sorption isotherm on the model outcome. Relative humidity at a depth of $12.5mm$ in the gypsum board(a). Temperature at a depth of $12.5mm$ (b). Relative humidity at $25mm$ (c). Temperature at $25mm$ (d). 96
4.15 Effect of variation in vapour resistance factor on the model outcome. Relative humidity at a depth of $12.5mm$ in the gypsum board (a). Temperature at a depth of $12.5mm$ (b). Relative humidity at $25mm$ (c). Temperature at $25mm$ (d). 99
4.16 Combined effect of sorption isotherm and vapour resistance factor. Relative humidity and temperature at a depth of $12.5mm$ in the gypsum board (a,b) and at $25mm$ (c,d). 101
4.17 Comparison of the model results for CaSi, brick and gypsum board. 103
4.18 Comparing the model with hysteresis and without at a depth of $12.5mm$ (a,b) and $25mm$ (c,d) for relative humidity and temperature. 105
4.19 Modelling gypsum board as a uniform material or layered. Temperature and relative humidity at a depth of $12.5mm$ (a,b) and $25mm$ (c,d). 107

5.1 Typical surface averaged drying rate curve 113
5.2 Typical moisture profiles with time for fired-clay brick. The time between subsequent profiles is 2 hours. (a) shows the measured profiles, (b) shows the simulations according to Landman et al. [118]. The x-axis represents the depth in the material [mm], the y-axis represents the moisture content [m^3/m^3]. 115
5.3 Moisture content profile evolution in time during the drying of (a) a capillary porous material and (b) a hygroscopic material. Figures based on [36]. 116
5.4 Schematic representation of wind tunnel used by Defraeye [43] to perform drying experiments. Above: side view. Under: top view . 128
5.5 Model of test section of experimental setup by [43] 128
5.6 1D model of drying experiment by [43] and electric analogue of the boundary conditions 130

5.7 (a) Temperature at 10mm in the brick. (b) Scaled mass loss. Comparison between different boundary conditions: heat flux through insulation (—), adiabatic side and bottom (. . .), adiabatic side and bottom with radiation at top (- -). Measurements by Defraeye [43] (■) 133

5.8 Moisture content along the depth of the ceramic brick sample every hour (total 12 hours) 134

5.9 (a) Longitudinal section of the test setup used in section 5.4.2.2 for simulations. (b) Velocity profile measured by Defraeye [43] (red line) compared with the 4_{th} order polynomial approximation (black line) 136

5.10 Simulation of the temperature at a depth of 10mm in ceramic brick using constant heat and mass transfer coefficients at the top (- -) and spatially varying transfer coefficients (—), comparison with measurements from [43] (■) 138

5.11 3D representation of the test sample embedded in insulation and plexiglass as it is used for the simulations. Only half of the setup is depicted and simulated since a symmetry plane is assumed along the sample centre. 139

5.12 Simulated temperature at various depths (—), compared with the measurements of Defraeye (□) [43]. Measurement error indicated on figure. The right bottom of the graphs show a cross section of the test section and the position of the temperature measurement . 142

5.13 Simulated temperature at 10mm in the ceramic brick, up stream of the centre (blue), in the centre (black) and downstream (red). Comparison with measurements upstream (○), centre (□) and downstream (△) 144

5.14 Scaled mass loss. Comparison between simulation with new CFD-HAM model (—), HAM model developed at KULeuven [43] (- -) and measurement performed by Defraeye [43] (■) 144

5.15 Drying rate. Comparison between simulation with new HAM model (—) and HAM model developed at KULeuven [43] (- -) . . 145

5.16 Comparison between new HAM model (—) and HAM model developed at KULeuven [43] (- -) for temperatures at various depths in the brick 146

5.17 Comparison of the measured (—) and simulated (—) moisture content distribution in the ceramic brick sample over time. Time difference between two lines is one hour. 148

5.18 Scaled mass loss. Comparison of experiment (■) and simulation with new CFD-HAM model (—), HAM model developed at KULeuven [43] (- -) and new CFD-HAM model with adjusted retention curve (—) and adjusted liquid permeability (—) 151

5.19 Comparison between HAM model with original material data (- -), HAM model with adjusted retention curve (—) and HAM model with adjusted liquid permeability (—) with measurements (■) for temperatures at various depths in the brick 152
5.20 Schematic representation of the climate chamber with the test sample of CaSi placed on top of a balance. For chamber dimension see Figure 4.1, for sample dimensions see Figure 5.22 156
5.21 Velocity profile at the inlet of the climate chamber 157
5.22 Schematic representation of the longitudinal (a) and cross section (b) of the test sample for the drying experiment with CaSi. PUR = polyurethane, Al = aluminum 159
5.23 Schematic representation of part of the climate chamber used to simulate the air flow over the top of the sample. Indicated in dark gray is the CaSi top surface, in light gray the PUR surface is highlighted. 160
5.24 Distribution of the convective transfer coefficients at the surface of CaSi. 162
5.25 Computational model for CaSi sample: boundary conditions on exterior surfaces. 163
5.26 Comparison of the simulated moisture content in CaSi (—) with the average of the measured moisture content (—) 164
5.27 Temperatures measured during the drying experiment of CaSi (—) compared to the simulations (—) 166
5.28 Temperature distribution in a longitudinal section of the CaSi sample 168

6.1 Illustration of possible heat fluxes occurring in and around a ventilated cavity wall. 173
6.2 Illustration of possible moisture fluxes occurring in and around a ventilated cavity wall. 173
6.3 Cavity wall configuration. 177
6.4 Climate conditions for a warm summer day in June and a cold day in December in Brussels. Temperature and relative humidity from climate data in TRNSYS [161], radiation from Hens [162]. 178
6.5 Case 1: the moisture content in the brick and wood fibre board for a summer day starting from saturated brick veneer and relatively dry wood fibre board. Comparison of the coupled CFD-HAM model ($0.1m/s$- -, $0.2m/s$—, $0.3m/s$—) and WUFI® ($0.1m/s$- -,$0.2m/s$—,$0.3m/s$—). 188
6.6 Case 2: the moisture content in the brick and wood fibre board for a winter day starting from saturated brick veneer and relatively dry wood fibre board. Comparison of the coupled CFD-HAM model (—) and WUFI® (- -). 189
6.7 The drying course of a wet wood fibre board in a cavity wall under summer (case 3) and winter (case 4) conditions. Comparison between the coupled CFD-HAM model (—) and WUFI® (- -). . . 191

6.8 Velocity profiles halfway the cavity when a constant inlet velocity of $0.2m/s$ is assumed. Profiles are shown for every four hours. The corresponding hours are indicated on each graph. 192
6.9 Figure (a) shows the average inlet velocity during 24 hours when a constant pressure of $0.06Pa$ is assumed at the cavity bottom. Positive average velocities indicate a flow from bottom to top, negative velocities indicate a reversed flow. Figure (b) shows the velocity profiles halfway the cavity for the same constant pressure at the bottom. Profiles are shown for every two hours. The corresponding hour is indicated on each graph. 194
6.10 Temperature profiles halfway the cavity for a constant pressure of $0.06Pa$ at the bottom. Temperature profiles every two hours are shown on the graph. 196
6.11 Moisture content profiles halfway the cavity for a constant pressure of $0.06Pa$ at the bottom. Moisture content profiles every two hours are shown on the graph. 197
6.12 Comparison of the moisture content in brick (a) and wood fibre board (b) for summer conditions, a constant inlet velocity of $0.2m/s$ (—) and a constant pressure of $0.06Pa$ at the bottom (- -). 198

A.1 Retention curve of brick. Original curve by Derluyn et al. [151] (—) and adjusted curve (- -) 209
A.2 Liquid permeability of ceramic brick. Original curve by Derluyn et al. [151] (—) and adjusted curve (- -) 210
A.3 Liquid permeability of calcium silicate 211

List of Tables

4.1 Overview of former and existing experimental test setups for moisture experiments 67
4.2 Material properties gypsum board. 93
4.3 Coefficients for sorption isotherms and vapour resistance factor of gypsum board needed in equation 4.1 and 4.3. 93
4.4 Relative humidity change in the adsorption phase ΔRH_a, relative humidity change in the desorption phase ΔRH_d and the maximum relative humidity RH_{max} at a depth of $12.5mm$ and $25mm$. . . . 97
4.5 Maximum temperature T_{max} and minimum temperature T_{min} during simulation at a depth of $12.5mm$ and $25mm$. 98
4.6 Material properties of calcium silicate and ceramic brick adopted from [108] 103
4.7 Coefficients for the sorption isotherm and vapour resistance factor of finishing paper and gypsum [117] 106

5.1 Comparison of average convective heat transfer coefficients (CHTC) and mass transfer coefficients (CMTC) 135
5.2 Comparison of the onset time of the falling rate period (FRP) and the equilibrium temperature during the constant drying rate period for different convective transfer coefficients. 137
5.3 Average heat and mass convective transfer coefficient for a course grid and a four times denser grid 161

6.1 Relative difference of predicted moisture content between WUFI® and CFD-HAM model. 186

A.1 Material properties of moist air (water vapour and dry air) 207
A.2 Other constants and parameters used in the CFD simulations . . . 208
A.3 Hygrothermal material properties 208
A.4 Parameters needed for Eq. A.5 210
A.5 Hygrothermal material properties 212
A.6 Material properties of XPS, PMMA and PUR 213

Nomenclature

a	Absorptivity	–
A	Surface Area	m^2
c_v	Specific heat at constant volume	J/kgK
c_p	Specific heat at constant pressure	J/kgK
C	Specific heat	J/kgK
dr	Distance from air-material interface to cell centre	m
D	Diffusion coefficient	m^2/s
D_{va}	Diffusion coefficient of water vapour in air	m^2/s
E	Total energy	J/m^3
E'	Specific total internal energy	J/kg
f	Friction factor	–
F	View factor	–
g	Gravitational acceleration	m/s^2
$\vec{g}$	Diffusion flux / Moisture flux	kg/m^2s
Gr	Grashof number	–
H'	Specific total enthalpy	J/kg
h	Specific enthalpy	J/kg
h	Convective heat transfer coefficient	W/m^2K
h_m	Convective mass transfer coefficient	s/m
J	Radiative energy flux	W/m^2
k	Turbulent kinetic energy	J
K_l	Liquid permeability	s

L	Latent heat of water evaporation	J/kg
Le	Lewis number	–
M	Molar weight	kg/mol
p	Pressure	Pa
P_{op}	Operating pressure	Pa
p_c	Capillary pressure	Pa
Ri	Richardson number	–
Pr	Prandl number	–
$\vec{q}$	Heat flux	W/m^2
$\vec{q_l}$	Sensible heat flux transported along with liquid water transport	W/m^2
$\vec{q_v}$	Sensible heat flux transported along with vapour transport	W/m^2
Q	Volumetric air flow rate	m^3/s
r	Pore radius	m
r	Distance	m
$\vec{r}$	Distance vector between upstream cell and centre of the face	m
R	Specific gas constant	J/kgK
$\mathcal{R}$	Universal gas constant	$J/molK$
Re	Reynolds number	–
RH	Relative humidity	–
s	Distance	m
S	Source/Sink	–
Sc	Schmidt number	–
t	Time	s
T	Temperature	K
T_0	Operating temperature	K
u	Internal energy	J
u	Velocity in the boundary layer	m/s

u^+	Dimensionless velocity in the boundary layer	–
u, v, w	x,y,z- component of velocity	m/s
u_τ	Friction velocity	m/s
$\vec{u}, \vec{v}$	Velocity vector	m/s
V	Volume	m^3
w	Moisture content	kg/m^3
$\frac{\partial \omega}{\partial p_c}$	Moisture capacity	$kg/m^3 Pa$
y^+	Dimensionless distance to the wall	–
y_P	Distance of first cell centre to the wall	m
Y	Mass fraction	kg/kg
Z	Mole fraction	mol/mol

Greek symbols

α	Thermal diffusivity	m^2/s
β	Thermal expansion coefficient	$1/K$
Γ	General diffusion coefficient	kg/ms
δ_{ij}	Kronecken delta	–
δ_v	Vapour diffusion coefficient	s
ϵ	Turbulence dissipation rate	m^2/s^3
ϵ	Emissivity	–
θ	Contact angle	–
θ	Volumetric moisture content	m^3/m^3
λ	Thermal conductivity	W/mK
μ	Water vapour resistance factor	–
μ	Dynamic viscosity	Pas
ν	Kinematic viscosity	m^2/s
ρ	Density	kg/m^3

ρ_{refl}	Reflectivity	–
ρ_0	Operating density	kg/m^3
σ	Surface tension	N/m
σ	Boltzmann's constant	W/m^2K^4
τ	Transmittance	–
τ	Shear stress	Pa
τ_w	Wall shear stress	Pa
ϕ	Arbitrary transported scalar variable	–
ψ_o	Open porosity	–
ψ	Metric head	m
ω	Humidity ratio	kg_{vapour}/kg_{db}
ω	Specific dissipation rate of turbulent kinetic energy	$1/s$

Subscripts

a	(Dry) air
atm	Atmospheric
avg	Averaged
db	Dry basis
c	Capillary
c	Centre
cap	Capillary
eff	Effective
en	Environment
ext	Exterior
f	Face
g	Gas
h	Heat

i	Inside
in	Inlet
$init$	Initial
int	Interior
l	Liquid
m	Material
m	Mass
mat	material, dry porous material
o	Outside
rad	Radiation
ref	Reference
$refl$	Reflectivity
s	Surface
sat	Saturation
t	Turbulent
v	Vapour

Superscripts

m	Current iteration
$m + 1$	Next iteration
t	Current time step
$t + \Delta t$	Next time step

Acronyms

1D	One-dimensional
2D	Two-dimensional
3D	Three-dimensional

ACH	Air Changes per Hour
AHU	Air Handling Unit
ASHRAE	American Society of Heating, Refrigeration and Air-Conditioning Engineers
BES	Building Energy Simulations
CaSi	Calcium Silicate
CFD	Computational Fluid Dynamics
CMTC	Convective Mass Transfer Coefficient
CRP	Constant Drying Rate Period
DNS	Direct Numerical Simulation
FRP	Falling Rate Period
HAM	Heat, Air and Moisture
HAMFEM	Heat, Air and Moisture Finite Element Model, HAM-model developed at the KULeuven
HRNM	High Reynolds Number Modelling
LES	Large Eddy Simulation
LRNM	Low Reynolds Number Modelling
MBC	Moisture Buffering Capacity
MIMO	Multiple Input Multiple Output
PE	Potential Energy
PIV	Particle Image Velocimetry
PMMA	Polymethyl Methacrylate
PUR	Polyurethane
RANS	Reynolds Averaged Navier-Stokes
SST	Shear Stress Transport
UDF	User Defined Function
UDS	User Defined Scalar
WUFI	Wärme und Feuchte instationär
XPS	Extruded Polystyrene

Nederlandse samenvatting
–Summary in Dutch–

De laatste jaren zijn de eisen die aan gebouwen en de gebouwschil gesteld worden met betrekking tot binnenluchtkwaliteit, energiegebruik en duurzaamheid steeds toegenomen. Dit leidde tot nieuwe en verbeterde materialen en constructietechnieken voor de gebouwschil. Toch gaat nog steeds een groot deel van de energievraag binnen Europa naar gebouwen. Verdere ontwikkelingen en verbeteringen zijn nog steeds aan de gang, maar zij vragen wel een grondig begrip van de warmte- en vochttransportmechanismen die optreden.
De eerste functie van een gebouw is mensen afschermen van buitencondities. Tegenwoordig volstaat het niet meer om enkel wind en regen buiten te houden, mensen verwachten een goede binnenluchtkwaliteit met comfortabele temperatuur- en vochtigheidniveaus. Om dit te verwezenlijken zonder te veel energiegebruik, is een goed ontwerp van de gebouwschil nodig. Dit houdt een laag energieverlies in door de gebouwschil en een goede vochthuishouding. Wanneer aan deze vereisten niet voldaan is, kan dit leiden tot het falen van de gebouwschil. Vochthuishouding heeft een belangrijke impact op de gebouwprestatie en de duurzaamheid. Talrijke problemen veroorzaakt door vocht en vochttransport kunnen voorkomen. Opstijgend vocht, inwendige condensatie en regendoorslag zijn maar een paar fenomenen die schade kunnen veroorzaken op en in de gebouwschil. Mogelijke vochtgerelateerde schadefenomenen zijn schimmelgroei, materiaaldegradatie door vries-dooi cycli, rotten van hout, corrosie enz....
Om deze problemen te vermijden en de gebouwschil verder te verbeteren, is een grondig begrip nodig van de heersende fenomenen. Tegelijk is er nood aan accurate modellen om de prestatie van de gebouwschil te voorspellen om zo vochtproblemen te vermijden. Het doel van dit werk is een verbeterd model te ontwikkelen dat in staat is het warmte- en vochttransport in de gebouwschil en in gebouwcomponenten te voorspellen. In dit werk ligt de nadruk vooral op problemen waar convectie een belangrijke rol speelt. Er wordt dan ook extra aandacht besteed aan de koppeling tussen warmte- en vochttransport in bouwdelen en de omgevende lucht.

In het **eerste hoofdstuk** van dit werk is een overzicht van vochtgerelateerde problemen gegeven. Om deze problemen op een juiste manier te voorspellen zijn accurate modellen nodig. Op dit moment zijn er slechts een beperkt aantal modellen beschikbaar die op een juiste manier het gecombineerde effect van

convectief warmte- en vochttransport in de lucht en transport in het materiaal omvatten. Op basis hiervan wordt besloten een nieuw model te ontwikkelen.
Vooraleer een nieuw model wordt geïmplementeerd, worden in **hoofdstuk 2** eerst de warmte- en vochttransportvergelijkingen afgeleid. De zogenaamde fenomenologische benadering wordt gebruikt om transport in poreuze materialen te beschrijven. Dit hoofdstuk duidt enkele beperkingen van deze aanpak aan. Tegelijk worden een aantal belangrijke materiaalkarakteristieken, van belang bij vochttransportmodellering, gedefinieerd en besproken.
In **hoofdstuk 3** wordt dan een numeriek model ontwikkeld gebaseerd op de vergelijkingen afgeleid in het vorige hoofdstuk. Een bestaande numerieke stromingsmechanicasolver gebaseerd op eindige volume methode wordt gebruikt om het transport in lucht op te lossen. Het commercieel beschikbare pakket Ansys Fluent® laat toe extra transportvergelijkingen toe te voegen naast de al beschikbare. Dit maakt het mogelijk een warmte- en vochtmodel (ook wel HAM-model genaamd) in Fluent® te implementeren om zo een gekoppeld CFD-HAM model te bekomen.
Een belangrijk onderdeel van het gekoppelde CFD-HAM model is de manier waarop de lucht en het poreuze materiaal gekoppeld zijn. Als enkel damptransport in de lucht en het poreuze materiaal moet gemodelleerd worden, is het mogelijk een directe koppeling toe te passen. Dit hoofdstuk toont aan hoe in dit geval de massafractie van waterdamp in lucht kan gebruikt worden als transportvariabele in zowel de lucht als het poreuze materiaal. Dit resulteert in een reeks gediscretiseerde vergelijkingen die in één keer kunnen opgelost worden door de solver.
Als ook vloeistoftransport in beschouwing wordt genomen, is het niet langer mogelijk de massafractie te gebruiken. Een nieuwe transportvariabele wordt daarom gekozen: de capillaire druk. Door twee verschillende transportvariabelen te gebruiken voor lucht en materiaal, is het niet langer mogelijk een directe koppeling toe te passen. Mogelijke alternatieve koppelingsmethodes worden besproken in dit hoofdstuk.
Vervolgens wordt het nieuw ontwikkelde model uitgebreid geverifieerd en gevalideerd. Dit gebeurt in twee fasen. In **hoofdstuk 4** wordt eerst het model voor damptransport gevalideerd. Dit model was eerder ontwikkeld door Steeman [1], maar de validatie was uitgevoerd met een onvolledige experimentele dataset. Hoewel het model goed overeenkwam met de beschikbare data, bleven toch een paar vragen rond modelnauwkeurigheid onbeantwoord. Daarom is een nieuw experiment uitgevoerd ter validatie van gekoppelde warmte- en vochttransportmodellen. Het experiment toont duidelijk de sterke koppeling tussen warmte- en vochttransport in poreuze materialen. Een volledigere validatie van het gekoppelde CFD-HAM model voor damptransport was mogelijk dankzij deze nieuwe data.
Hoewel de overeenkomst tussen experimenten en simulaties goed was, werd toch geen perfecte overeenstemming bekomen. Door de onzekerheid op de materiaaleigenschappen mee in rekening te brengen, kunnen echter de meeste afwijkingen verklaard worden. Om dit verder te onderzoeken is een

uitgebreide gevoeligheidsanalyse uitgevoerd in hoofdstuk 4. De gevoeligheid van de materiaaleigenschappen en de randvoorwaarden op de modeluitkomst werd onderzocht. Materiaaldata uit de literatuur toonde aan dat er een grote spreiding is op de gemeten hygrothermische eigenschappen. Tegelijk duidde de gevoeligheidsanalyse deze eigenschappen aan als meest invloedrijke. Er kan dus besloten worden dat een goede overeenkomst tussen simulaties en metingen enkel mogelijk is als de materiaaleigenschappen nauwkeuriger gemeten worden.

In **hoofdstuk 5** wordt het vloeistofmodel gevalideerd. Om vloeistoftransport in poreuze materialen te bestuderen, wordt één specifiek geval bekeken: convectieve droging. Convectieve droging kan beschreven worden als het verwijderen van water van een nat of verzadigd materiaal door een droog medium, in de meeste gevallen lucht, over het oppervlak van het materiaal te blazen. Tijdens convectieve droging transporteert water als vloeistof of damp doorheen het poreuze materiaal en dit transport is sterk gekoppeld aan warmteoverdracht.

In dit hoofdstuk wordt eerst een gedetailleerde beschrijving van drogingfenomenen gegeven. Nadien wordt een overzicht gegeven van de huidige stand van zaken in drogingsmodellen. Uit de literatuur werden drie types modellen geïdentificeerd: analytische modellen, modellen die convectieve transfercoëfficiënten gebruiken en volledig gekoppelde modellen. De literatuurstudie toonde aan dat het vaak volstaat om convectie te modelleren door middel van transfercoëfficiënten, zolang variaties over het oppervlak mee in rekening worden gebracht. Volledig gekoppelde modellen die iteratief of gelijktijdig het transport in de lucht en in het materiaal oplossen, zijn wel exacter, maar deze extra complexiteit is niet altijd noodzakelijk en gewild.

Het vloeistoftransportmodel is gevalideerd met een drogingsexperiment uit de literatuur. In dit experiment wordt een stuk met water verzadigde baksteen gedroogd in een wind tunnel. Om de impact van sommige vereenvoudigingen te onderzoeken wordt de complexiteit van het drogingsmodel stap voor stap opgedreven. Deze analyse toont aan dat 1D en 2D modellen niet volstaan om droging te modelleren. Het is nodig een 3D model te gebruiken waarbij de randvoorwaarden op een correcte manier geïmplementeerd zijn. Het was opnieuw niet evident om een perfecte overeenkomst te krijgen tussen metingen en simulaties. Opnieuw wordt geopperd dat de oorzaak bij de gemeten materiaaleigenschappen te zoeken is. Door de vloeistofpermeabiliteit aan te passen, is het mogelijk een goede overeenkomst van de massaverandering en de vochtdistributie te krijgen.

Een nieuw droogexperiment werd ontwikkeld om een beter zicht te krijgen op de impact van materiaaleigenschappen op het drogingsverloop. Een blok calciumsilicaat (een capillair, hygroscopisch en isolerend materiaal) werd gedroogd. Het drogingsverloop verschilt sterk van dat van baksteen. Toch was het drogingsmodel opnieuw in staat het verloop met voldoende nauwkeurigheid te bepalen.

In **hoofdstuk 6** wordt het nieuw ontwikkelde en gevalideerde model toegepast om de geventileerde spouwmuur te bestuderen. Een spouwmuur is typisch opgebouwd uit een buitenspouwblad, een luchtlaag en een binnenspouwblad. De

spouwbladen zijn daarbij vaak poreus van aard. De aanwezigheid van de luchtlaag leidt tot een gekoppeld warmte- en vochttransport in de lucht en in het poreus materiaal. Transportmechanismen zoals convectie, diffusie and straling treden hierbij samen op. Bij de hier uitgevoerde studie wordt de impact van convectie en de juistheid waarmee ze wordt gemodelleerd, nagegaan. Het gekoppelde CFD-HAM model wordt daarvoor vergeleken met een sterk vereenvoudigd spouwmuurmodel.
Tot slot worden in **hoofdstuk 7** de belangrijkste conclusies samengevat en wordt een blik geworpen op mogelijk verder onderzoek.

English summary

During the last decades requirements for buildings and building envelopes in terms of indoor air quality, energy use and durability have drastically increased. This resulted in new and improved materials and construction techniques for building envelopes. However, the building stock still accounts for a large part of the energy use in Europe. Further developments and innovations are still ongoing but they require a thorough understanding of the heat and moisture transport mechanisms that are involved.
The first function of a building is to shield people from outside weather conditions. Nowadays it no longer suffices to keep only wind and rain outside, people demand a good indoor air quality with comfortable temperature and humidity levels. To accomplish all this without excessive energy use, a good design of the building envelope is needed. A good envelope design includes low energy loss through the envelope and a good moisture management. If these prerequisites are not satisfied, the envelope or even the entire building may fail.
Moisture management has an important impact on building performance and durability. Problems caused by moisture and moisture transport in buildings are numerous. Rising damp, interstitial condensation or rain penetration are only a few phenomena that cause damage to occur in and on the building envelope. Possible moisture related damage phenomena are mould growth, material degradation by freeze-thaw cycles, wood rot or corrosion, etc....
In order to avoid these problems and further improve the envelope performance, a thorough understanding of the occurring phenomena is necessary. Simultaneously there is a strong need for accurate models to predict the envelope performance and to avoid moisture related problems. It is the objective of the present work to develop an improved model for the prediction of heat and moisture transport in building envelopes and building components. The emphasis of this work is on problems where convection has an important role. Therefore a lot of attention goes to the coupled solving of heat and moisture transport in building components and the surrounding air.

In the **first chapter** of this work, an overview of moisture related problems is given. Accurate models are needed to predict moisture related damage. At present there are only a few models available that are able to accurately predict the combined effect of convective heat and moisture transport in the air and transport in a porous material. Based on this analysis it is decided to develop an improved model.

Before implementing a new model, the governing equations for heat and moisture transport are derived and discussed in **chapter 2**. The so-called phenomenological modelling approach is used to describe transport in porous materials. The chapter indicates some of the constraints of this modelling approach. Some important material characteristics typical for moisture transport modelling in porous materials are defined and discussed.

Based on the transport equations derived in chapter 2 a numerical model is developed in **chapter 3**. An existing computational fluid dynamics (CFD) solver based on finite volume discretization is used to solve the transport in the air. The commercial available package Fluent® allows the implementation of additional transport equations next to the already implemented Navier-Stokes equations. This makes it possible to add a heat and moisture material (HAM) model to Fluent® which resulted in a coupled CFD-HAM model.

An important aspect of the coupled CFD-HAM model is the way the air and material domain are coupled. If only vapour transport in the air and the porous material is to be modelled, a direct coupling approach is possible. Chapter 3 shows how in this case the mass fraction of water vapour in air can be used as transported variable in the air as well as in the material. This results in a set of discretized equations which can be solved simultaneously by one solver.

However if liquid water transport is present, it is shown that using the mass fraction as transported variable no longer holds. A new transported variable is chosen namely capillary pressure. Two different transported variables for the air and the material implies that it is no longer possible to directly couple transport in air and porous material. Possible alternative coupling procedures are discussed in chapter 3.

Next the newly developed coupled CFD-HAM model is extensively verified and validated. This is done in two phases. In **chapter 4** first the model for vapour transport is validated. This model was first developed by Steeman [1] but the validation was performed with incomplete experimental data. Although the model agreed well with the available data, some questions on model accuracy remained. Therefore a new experiment is developed for coupled heat and vapour transport model validation. The experiment clearly showed the strong coupling between heat transport and vapour transport in a hygroscopic porous material. A more complete validation of the coupled CFD-HAM model for vapour transport was possible with the new experimental data set.

Although agreement with experiments was good, no perfect match between model and measurements was found. Simulations with altered material properties revealed that a better match could be found if the uncertainty on material properties is included in the model. To investigate this further, an extensive sensitivity study is performed in chapter 4. The sensitivity of material properties and boundary conditions on the model outcome was investigated. Material data provided in literature revealed that there is a large spread on measured hygrothermal properties. The sensitivity analysis at the same time showed that especially these material properties have the largest impact on the model. It was thus concluded that a good agreement between model and measurement will only be possible if the accuracy

of the hygrothermal properties improves.
In **chapter 5** the liquid transport model is validated. To study liquid moisture transport in porous materials one specific case is studied: convective drying. Convective drying can be defined as the removal of water from a wet or saturated material by a drying medium, in most cases air, which flows over the material. During convective drying of a porous material liquid water and water vapour is transported in the material in strong combination with heat transport.
In this chapter first a more detailed description of drying phenomena is given and an overview of the state of the art in convective drying models. Basically three model types were identified from literature: analytical drying models, drying models using transfer coefficients and fully conjugate models. The literature review revealed that convective transfer coefficients at the boundary often suffice as long as spatial variations of the transfer coefficients are allowed. Fully conjugate models that solve the transport in the air and in the material iteratively or simultaneously give more precise results but the extra model complexity is not always needed and justified.
The liquid transport model is validated with a drying experiment from literature. In this experiment a saturated sample of ceramic brick is dried in a wind tunnel. The complexity of the model is gradually increased to reveal the impact of certain model simplifications. The validation exercise shows that 1D and 2D modelling does not suffice to accurately capture the drying course. A 3D model with correct implementation of the boundary conditions is needed. Similar to the validation of the vapour transport it was difficult to get a perfect agreement between measurements and simulations. Again it was suggested that the discrepancies were due to uncertainty on material properties. Adjusting the liquid permeability showed it was possible to obtain a good match for the total weight change of the sample and for the moisture distribution in the sample.
For a better understanding of the impact of material properties on the drying phenomena, a new drying experiment is proposed and conducted. In this experiment a sample of calcium silicate (a capillary active, hygroscopic and insulating material) is dried. Calcium silicate has a different drying course than ceramic brick. Nevertheless, the drying model was able to capture temperature and moisture content evolution in time with sufficient accuracy.
Chapter 6 applies the newly developed model to a case study. As a case the ventilated cavity wall is studied. A cavity wall is typically built up out of an outside leaf, an air cavity and an inside leaf, where the cavity leafs often have a porous nature. The presence of the air layer results in a coupled heat and moisture transport in the air and the porous material. Transport mechanisms such as convection, diffusion and radiation co-occur. In this study the impact of convection and its accurate coupling to material models is investigated. The coupled CFD-HAM model is therefore compared with a simplified cavity wall model.
Finally **chapter 7** summarizes the main conclusions of this work and discusses future work.

1

Moisture in buildings

1.1 Introduction

During the last decades the requirements for buildings and building envelopes in terms of indoor air quality, energy use and durability have drastically increased. Where before the main function of a building was to shield people from outside weather conditions, nowadays people demand comfortable temperature and humidity levels without excessive energy use. This is only possible if a good performing building envelope is present.
Damage to the building envelope can to a great extent reduce the building envelope performance. This damage is often moisture related. The impact of moisture and moisture damage on the envelope is vast and affects thermal comfort, indoor air quality, human health, energy efficiency and building durability.
Building designers try to prevent moisture problems by applying an adequate building envelope design. This is however only possible if sufficient knowledge of the moisture transport mechanisms is at hand. The correct implementation of this knowledge in reliable predictive tools will help building designers to make correct decisions. Therefore this research will focus on the development of improved predictive tools.

1.2 Moisture damage phenomena

The resulting damage from moisture depends on the moisture source, the moisture quantity and the material type. A number of moisture sources can be identified in the building context. Some important examples are wind-driven rain and rising damp.

Wind-driven rain is rain that has a horizontal velocity component, given to it by the wind. It is a very important moisture source especially affecting the performance of building façades. A good overview of the state-of-the-art research on wind-driven rain is given by Blocken et al. [2].

When rain hits a building façade and this façade has a porous nature, part of the rain will be absorbed by the porous materials. The rain that is not absorbed, runs off. Water accumulating in the porous material may lead to various moisture related problems. When the envelope is poorly designed or constructed the rain can even penetrate to the inside.

Another important moisture source often found in constructions is **rising damp**. Rising damp in buildings occurs when water from the soil is absorbed in the porous wall by capillary action. This results in walls that are wet at the bottom. This can be avoided by installing a damp proof course. If however this damp proof course is poorly installed or in some way bridged, rising damp still occurs.

A third important moisture source in buildings is the **indoor environment**. Water vapour present in the indoor air comes from various sources. People or animals in a room breathe out moist air and transpire water vapour, but also the presence of plants can increase the moisture levels in a room. Human activity also introduces water vapour in the room air. For example during cooking or showering large amounts of water vapour are produced and released to the indoors. Also the burning of fossil fuels for example for heating purposes releases water vapour. Besides carbon dioxide, water vapour is the most important combustion product when burning for example natural gas. Sufficient ventilation is the key aspect to keep the humidity indoors at acceptable levels.

High humidity levels result in condensation phenomena on cold surfaces. If the temperature of a surface is below the dewpoint temperature, water vapour in the surrounding air will condense on that surface. For example in winter poorly insulated windows are often subjected to condensation. Also thermal bridges (local areas that are poorly insulated [3]) are very sensitive to condensation.

Interstitial condensation can occur when water vapour diffuses through the porous building envelope to the outside. If the temperature reaches the dewpoint temperature somewhere in the construction, the water vapour will condense inside the construction. This is a dangerous situation since the moisture and the associated damage stays hidden in the construction.

Besides the three aforementioned moisture sources, moisture in a building can

also be introduced during the construction phase (**construction moisture**) or by accident (**leaking pipes**). Some of the construction moisture can be avoided by keeping the construction materials dry during construction and reducing their exposure to outside (rainy) conditions to a minimum.

Moisture in buildings has a large impact on the building performance. Moisture in the building envelope can cause increased relative humidity in the indoor environment and the relative humidity is an important parameter for the thermal comfort in a building. If the air is too humid, it is perceived as uncomfortable [4,5]. On the other hand, a high relative humidity increases the risk of mould growth. If the surface relative humidity is above a certain threshold long enough, there is a risk of mould growth. Although there is still no general agreement on which criterion is most appropriate, in most cases an upper limit of 80%RH is prescribed. If the surface relative humidity does not exceed 80%, mould is most likely avoided. An overview of state-of-the-art mould prediction models and mould risk evaluation is found in [6]. Mould in buildings has an impact on the human health. Besides mould, other biological hazards such as insects and dust mites also thrive under high relative humidity (and temperature).
Another aspect that is influenced by moisture is the energy performance of the building envelope. Moist building envelopes, whether they are wetted by wind-driven rain, rising damp or condensation, will have a decreased heat conduction resistance. Damp walls, especially when the insulation is wetted, will act as a thermal bridge and increase heat losses through the envelope.
Moisture also causes aesthetic problems. Although these problems are not necessarily harmful for the building or the building occupant, they are still undesired. An example of aesthetic consequences of moisture is the possibility of soiling patterns on building façades. This is caused by wind-driven rain and the accompanying runoff.
Another example is salt efflorescence caused by water transport in moist concrete and masonry. These materials contain high salt concentration by nature and this salt can dissolve in the water present in the material. The salt can then transport through the porous material by diffusion and convection. If the salt solution becomes super-saturated, the salt will crystallize, resulting in salt efflorescence. The problems caused by the efflorescence of salt are not limited to aesthetics, but can also be structural. For example in concrete structural problems can arise. The continuous movement of moisture through the porous structure of the material will eventually wash out all the soluble salts and cause the breakdown of the cement matrix, leaving the concrete weak and sandy. Furthermore the alkalinity of the concrete will drop, and with it, the ability of the concrete to protect the embedded reinforced steel from corrosion. The naturally high alkalinity of good quality concrete is the main mechanism that prevents the corrosion of reinforced

steel by passivating the surface. Without protection, steel rapidly corrodes in the presence of moisture, ions and oxygen.
Salt crystallization also results in surface spalling of concrete. This is caused by the crystallization pressures [7]. A good description of salt transport in porous materials and the parameters that are involved, is found in Nicolai et al. [8].

Figure 1.1 shows some examples of moisture related damage. Besides the pure aesthetic consequences (e.g. Figure 1.1(a), salt efflorescence due to rising damp), moisture can also result in decay. For example Figure 1.1(b) shows the result of frost damage. Moisture for example coming from wind-driven rain or rising damp can wet a wall up to saturation. When the outside temperature drops below the freezing point, the water in the micropores freezes and expands, resulting in high pressures in the material. These pressures cause cracking. Alternating thaw and freeze cycle can eventually lead to significant structural damage.
Frost damage is however far from the only structural damage that can occur. Paint layers and wall paper can come lose or finishing layers such as plaster start to crack and crumble (Figure 1.1(c)). If the moisture content in wood is too high (max 20% by volume for safety according to ASHRAE [9]), wood can start to decay or rot. Finally metal elements corrode faster when moisture is present.
For a lot of moisture related problems, moisture transport in air (convection) plays a major role. On the one hand insufficient ventilation can lead to increased air humidity and consequently increased moisture loads. On the other hand, drying of wet materials is to a great extend determined by the air condition flowing over the material. For these cases there is a strong coupling between moisture transport in the air and moisture transport in the (porous) material. Figure 1.1(d) for example shows the consequences of a poorly ventilated cavity wall. Here moisture was infiltrated in a cavity of a wood frame wall. The outside surfaces of this wall were finished with a paint layer acting as a vapour barrier, trapping the moisture inside the cavity. As a consequence mould started to grow inside the cavity. Since the damage occurred inside the cavity wall, the problem could stay hidden for a long time. If ventilation of the cavity would have been allowed, moisture could have been evacuated from the cavity as water vapour and the wall would dry out slowly reducing the risk of mould growth.

This short overview clearly shows that problems caused by moisture affect the occupants health on the one hand and the building durability on the other hand. A good moisture management in the building envelope is a prerequisite to avoid these moisture related problems. For a building designer it is however not always easy to deliver an adequate design, since moisture related problems are complex and difficult to asses in advance. Therefore, hygrothermal models can be a very useful tool to asses the impact of moisture on buildings. These tools can be used

to predict and evaluate the moisture performance of buildings and their envelope. However, for a good evaluation of moisture related problems, hygrothermal models would have to be able to:

- capture heat and moisture transport in a variety of porous building material
- combine this with heat and moisture transport in the surrounding air
- and apply all this modelling on complex geometries and strongly fluctuating boundary conditions.

Most state-of-the-art (commercially) available hygrothermal models can handle some of these aspect, but only few combine all in a satisfactory manner. The next section will give a short overview of some of the currently available models.

1.3 Heat and moisture modelling in buildings

As stated in the previous section, modelling tools describing the moisture behaviour of buildings and building envelopes are very useful to predict moisture related problems. Nowadays a wide variety of modelling tools are available. A good overview of the state of the art in moisture modelling is found in ANNEX 41 subtask 1 [14]. Here a number of software tools are listed and compared, including commercially available software and open source software.
In this review two main groups of models are distinguished. The first group are the so-called *Building Energy Simulation* tools (BES). These models focus on the energy performance of buildings. In some of these models the impact of moisture on the energy performance is included, although often in a simplified way. Some widely used examples are EnergyPlus [15], ESP-r [16] and TRNSYS [17]. However for an accurate moisture response evaluation these models are not well suited.
The second group of models that focus more on the moisture transport in building components are referred to as *Heat, Air and Moisture transport* models or in short HAM models. These models are able to solve the combined transport of heat and moisture in building components. Again a wide variety of models exists of which WUFI® [18] and Delphin® [19] are the most widely used. Both models can solve 1D and 2D heat and moisture transport problems. Although these models are addressed as HAM, the air component is often modelled in a simplified way or is even not included. Recent attempts to improve the air transport modelling in these models are found in e.g. Langmans et al. [20].
To improve the performance of BES and HAM models, both models can be combined. This results in a Building Energy Simulation model with accurate heat and moisture transport modelling. These so-called coupled BES-HAM models focus on the interaction between the indoor environment and the building

(a) Rising damp with salt efflorescence [10]

(b) Frost damage [11]

(c) Crumbling plaster after rain penetration [12]

(d) Mould growth in a poorly ventilated cavity wall [13]

Figure 1.1: Examples of moisture problems and damage phenomena that often occur in buildings.

envelope and study the effect of hygroscopic materials on the energy use in buildings. Porous hygroscopic materials have the ability to store moisture in their pore structure. During periods of high relative humidity water vapour is stored while at low relative humidity water vapour is released. This results in reduced humidity fluctuations in the indoor environment also referred to as moisture buffering. A coupled BES-HAM model is able to better predict the energy use of HVAC systems including the effect of moisture buffering. For example Steeman et al. [21] coupled a 1D hygrothermal model with TRNSYS.

A large shortcoming of both BES and HAM models is that they model air flow and convection in a simplified way. The airflow is modelled with simple equations and at the boundaries constant transfer coefficients are used to model the interaction between the wall and the environment. Recently attempts are made to improve the air flow modelling in BES and HAM by coupling these models with sophisticated *Computational Fluid Dynamics* models (CFD). These CFD models can solve the air flow and the accompanying heat and moisture transport in more detail. Mirsadeghi [22] developed a coupled BES-CFD model. His study showed that this approach leads to a better prediction and evaluation of condensation risk, thermal comfort and mould growth risk indoor.

Steeman [23] developed a coupled CFD-HAM model for the assessment of moisture related damage in hygroscopic materials. His study concentrated on moisture related damage in historical artifact such as wooden panel paintings. For his study a detailed modelling of the interaction between the indoor environment and the hygroscopic material was needed. By implementing a detailed HAM model into an existing CFD package he was able to model the heat and moisture transport in the air and porous material simultaneously. However, Steeman only modelled vapour diffusion as transport mechanism in the porous material.

Other attempts of combining CFD with HAM models can be found in for example Mortensen et al. [24], Gnoth et al. [25] and Defraeye et al. [26]. Mortensen [24] investigated the interaction between so called microclimates and the heat and moisture transfer in porous building materials. These microclimates are zones in building spaces where the climate significantly differs from the overall space climate. For example in room corners or behind furniture such as closets, temperature and humidity conditions can differ from the overall temperature and humidity since ventilation conditions will differ. Ventilation or air movement in these cases will determine the air temperature and humidity and the heat and moisture transport to and from the present porous (building) materials.

Gnoth et al. [25] focused their study on convection in closed cavities. They combined a CFD model with Delphin. In their studies, heat and moisture transported through porous materials into a cavity where transport was dominated by (natural) convection. For these cases there is a strong interaction between transport in the air and transport in the porous material.

Defraeye et al. [26] finally combined CFD with an in house HAM model (HAMFEM) to study the drying behaviour of porous building materials. Especially for drying the ventilation condition are very important and they will determine the drying course and drying rate.

These resent attempts to combine existing HAM models with CFD show to be promising. They allow a more detailed and accurate modelling of the influence of convection on the heat and moisture transport in porous materials. However the development of this new class of hygrothermal models is still ongoing. Most of the aforementioned models are research tools. They require long computational time and are often only applicable for specific cases (e.g. only 2D, only vapour diffusion,...). A model able to cope with a broader range of problems in a computational efficient way would be a considerable asset for researchers and building designers.

1.4 Problem definition and research aim

It is clear from the previous analysis that a wide variety of moisture problems in buildings exists. The moisture sources and transport mechanisms are often numerous and complex. Current hygrothermal models can already handle a broad range of problems but lack the ability to accurately model the interaction of transport in a porous material and the surrounding air. It is the objective of this research to develop a model for heat and moisture transport in porous materials combined with convective transport in the surrounding air. This new model should be able to handle heat and moisture transport cases where transport in the surrounding air is important and where this transport should be solved simultaneously with the transport in the porous material.
This research starts from the work of Steeman [1], who developed a combined CFD-HAM model to model vapour transport in air and porous material simultaneously. A new approach for coupled heat and moisture modelling is investigated which includes liquid moisture transport. This results in a model able to capture combined heat and moisture transport in air and porous materials where the moisture transport includes transport by vapour diffusion and capillary moisture transport.

The development of the new coupled CFD-HAM model proceeds in two phases. First the existing vapour transport model of Steeman [1] is investigated in detail. Some advantages and shortcomings of this model are highlighted in the first part of chapter 3. In the second part of chapter 3 some of the shortcomings of the vapour transport model are overcome by adding a liquid transport model. This however alters the numerical implementation significantly.

The heat and moisture transport modelling is then extensively verified and validated in two phases. First the vapour transport model is studied. Steeman already conducted a first validation of that model, but could not explain all discrepancies he found between the model and experiments. He attributed most of them to inaccuracies in the measurements and model input data. To investigate this further, an extensive sensitivity analysis is performed in chapter 4 on the vapour transport model. Next a new experimental setup is developed and the produced data is used for further validation of the vapour model.
In chapter 5 the new coupled CFD-HAM model including liquid transport is validated using data from literature and data from experiments conducted in a new test setup. The model is used to study drying phenomena in porous (building) materials.
Finally a case study is performed and discussed in chapter 6. Heat and moisture transport in a cavity wall is investigated since here vapour transport, liquid transport and convection occur simultaneously, highlighting the strengths of the newly developed coupled CFD-HAM model. The new model is compared with a simplified cavity wall model to investigate the impact of accurate convection modelling in cavity walls.

However, before the numerical implementation of the model is discussed, chapter 2 first gives an overview of the heat and moisture transport modelling in a porous material. Here a more detailed description of the prevailing transport and storage mechanisms is given. This results in a set of transport equations describing heat and moisture transport in air and porous materials.

2

Heat and moisture transport in air and porous materials

2.1 Porous material model

A detailed description of the governing heat and mass transport equations in porous materials can be found in numerous handbooks, papers and reports [27–29]. This chapter only highlights some of the most important aspects and concepts in heat, air and moisture transport modelling in porous (building) materials.
In this first section some basic concepts concerning porous materials and the heat and mass transport inside porous materials are explained in more detail. The heat and moisture transport model itself for a porous material is discussed in detail in section 2.3. First some thermodynamic relations that are frequently encountered are listed and shortly discussed.

2.1.1 Thermodynamic relations

For the temperature and pressure ranges encountered in the building environment, moist air being mainly a mixture of N_2, O_2, H_2O and Ar, can be presumed to act as an ideal gas. For an ideal gas, the following relation, also called the ideal gas law, is valid:

$$p = \rho RT \tag{2.1}$$

Here p is the pressure $[Pa]$ of the gas, ρ the density $[kg/m^3]$, T the temperature $[K]$ and R the specific gas constant $[J/kgK]$.
The moisture content of air, also called the humidity of air can be described in numerous ways. A popular way to describe the absolute humidity is by using the partial vapour pressure of water vapour in air p_v $[Pa]$. Through the ideal gas law this vapour pressure can be related to the vapour density ρ_v $[kg/m^3]$. The ratio of the vapour pressure to the saturation vapour pressure p_{sat}, which is the maximum vapour pressure attainable at a certain temperature, is called the relative humidity RH. It is often represented as a percentage. Air at a given temperature T can only contain a certain amount of water vapour, the maximum being the saturation vapour content. This saturation vapour content is function of the temperature. Above this value water vapour will condense.

$$RH = \frac{p_v}{p_{sat}(T)} \tag{2.2}$$

The amount of water vapour that air can contain at a certain temperature is given by the Clausius-Clapeyron equation [30] (Eq. 2.3) which relates the saturation vapour pressure to the latent heat of evaporation. For this equation it is assumed that the specific volume of liquid water is much smaller than that of water vapour and that the vapour pressure is low enough so the ideal gas law applies.

$$\left.\frac{dp}{dT}\right|_{sat} = \frac{h_v - h_l}{RT^2} \tag{2.3}$$

The enthalpy difference between vapour and liquid, $h_v - h_l$, represents the latent heat of evaporation at temperature T $[K]$. Evaluating Eq. 2.3 results in e.g. :

$$p_{sat}(T) = 611 \exp\left(\frac{17.08\,(T - 273.15)}{T - 38.97}\right) Pa \tag{2.4}$$

2.1.2 Modelling a porous material

A porous material can be defined as a material built up out of a solid matrix laced with voids and cavities. These cavities are in turn filled with a gaseous and/or liquid phase. In the present study, the gas phase is a mixture of air and water vapour, the liquid phase is water. A microscopic view of a porous material is shown in Figure 2.1. The three phases present (solid, liquid, vapour) can be clearly distinguished. The objective of the present work is to study the heat and moisture transport in such a porous material. In order to develop an adequate model for the heat and moisture transport in such a porous material, it is important to know how water is stored and transported in the porous material. This section will shortly discuss some of the most important transport mechanisms in a porous material.

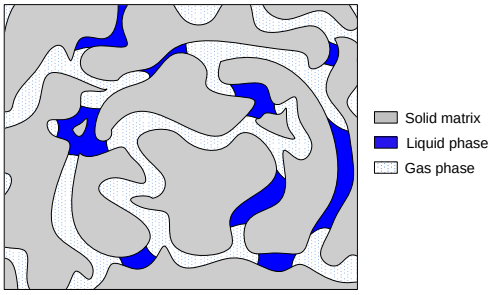

Figure 2.1: Microscopic detail of a porous material.

When modelling heat and moisture transport in a (multiphase) porous material, two approaches can be followed. The first is the *microscopic approach* [31, 32]. In this approach transport in each phase is modelled separately. These models are based on the actual physical phenomena occurring during transport in each phase. For the current study, the solid matrix is assumed invariable, so no shrinkage or deformation of the matrix is allowed. At the microscopic scale, moisture can be transport in the vapour phase by diffusion of water vapour in air or by convection or as liquid water. The governing continuity, conservation of momentum and conservation of energy equation can be written down for each phase separately. The difficulty lies in the implementation of the boundary condition for each phase. Three interfaces can be considered: liquid-solid interface, vapour-solid interface and liquid-vapour interface. The solid interface is fixed, while the liquid-vapour interface can move due to liquid movement, vapour movement and the phase change of water vapour to liquid (condensation) or liquid to water vapour (evaporation). This significantly complicates the modelling of transport phenomena at a microscopic scale and makes it impractical for numerical tools. Therefore in the present work the so called *phenomenological approach* is used. In this approach the porous material is considered at a macroscopic level. The idea is to develop a set of equations that are valid in every point in space and not just in the three separate phases.

Whitaker [33] was able to derive a set of transport equations for a phenomenological approach by applying a volume averaging technique on the governing point equations for each phase. To arrive to this set of equations a list of assumptions and restrictions where needed. These assumptions and restrictions also apply to the model implemented in this work. The following list is an adopted version from [33]:

- The solid phase is a rigid fixed matrix.
- Solid and liquid phase are modelled as incompressible and the enthalpy changes in the solid and liquid phase are assumed independent of pressure. The gas can be modelled as an ideal gas so the enthalpies for all phases are linear with temperature.
- The liquid phase contains only a single component (water in this case).
- Compressional work and viscous dissipation are negligible in the liquid and vapour phase.
- No chemical reactions occur.
- Interfacial energy is neglected in the thermal sense. This restriction can however easily be overcome for example by implementing latent heat of wetting [34].
- The density of the liquid is constant.
- The multi-phase system is assumed to be in local equilibrium.
- The porous material is homogeneous.

The objective of the volume averaging technique and the resulting phenomenological approach is to come to a set of transport equations where the remaining parameters are easy to measure material properties.

To understand the meaning of these material properties, a better understanding of the complex behaviour of porous materials is needed. According to Mujumdar [35] and Krischer [36] porous materials can be categorized according to their moisture transport and storage properties. This results in two main material groups: hygroscopic materials and capillary active materials. It is however possible that a material is hygroscopic and capillary active at the same time. Examples of capillary active materials are sand and some ceramics such as ceramic brick. Examples of hygroscopic materials are silica gel and alumina for strictly hygroscopic materials and wood, clay or textiles for hygroscopic-capillary active materials.

Hygroscopic materials

Hygroscopic materials are a class of porous materials that are able to store a significant amount of liquid moisture in their pore structure even at relative humidities below 100% (when normally no condensation would occur). Figure

2.2 shows the evolution of the moisture content as a function of the relative humidity for a typical hygroscopic material. At low relative humidities molecular adsorption occurs. First a mono-molecular layer develops on all the pore walls followed by multi-layer adsorption (Figure 2.3). The monolayer adsorption can be described by Langmuir's equation for monolayer adsorption, Multi-layer adsorption can be described by the Brunauer-Emmet-Teller theory [28]. These equations give the moisture content as a function of relative humidity and specific pore surface.

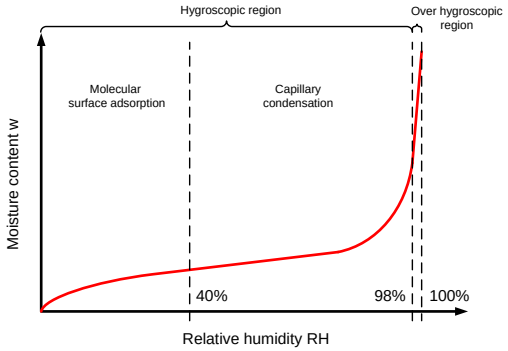

Figure 2.2: Moisture content in a hygroscopic porous material as a function of the relative humidity (sorption isotherm).

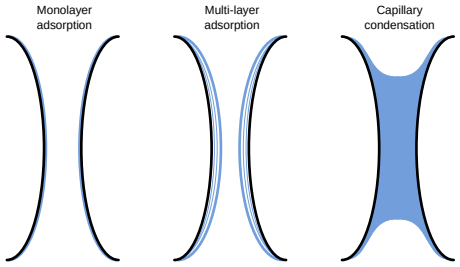

Figure 2.3: Detail of a pore with three possible adsorption mechanisms: monolayer adsorption, multilayer adsorption and capillary condensation.

At higher relative humidity (relative humidity approximately higher than 40%), pores can become completely filled with water. The smallest pores will be filled first. The surface tension forces the water molecules to change to a more stable arrangement forming a meniscus between the liquid and gaseous phase as shown

in Figure 2.3. Fore these water filled pores the so-called capillary pressure can be defined. The capillary pressure is defined as the pressure difference between the gas phase and liquid phase.

$$p_c = p_l - p_g \tag{2.5}$$

For cylindrical capillary tubes the capillary pressure can be determined with the Young-Laplace equation expressing the relation between the capillary pressure and the pore radius.

$$p_c = -\frac{2\sigma}{r}\cos\theta \tag{2.6}$$

In this equation σ is the surface tension, r is the radius of the capillary pore and θ is the contact angle of the liquid-gas interface. Figure 2.4 gives a schematic overview of the equilibrium in a small cylinder filled with water. When the contact angle of the liquid-gas interface is between 0 and 90° the capillary pressure will be negative and water is sucked into the pore.

The concave water-air interface has a consequence for the thermodynamic

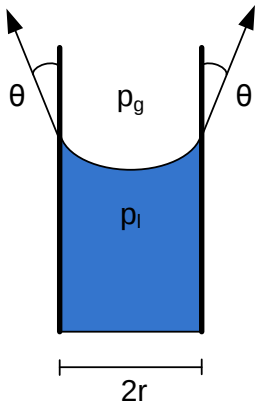

Figure 2.4: Schematic representation of equilibrium in a pore filled with water.

equilibrium near the this interface. Above a concave surface the relative humidity will be less than 1. This equilibrium can be described by Kelvin's law:

$$\ln(RH) = \frac{-2\sigma}{r}\frac{\cos\theta}{\rho_l R_v T} \tag{2.7}$$

Or in combination with Eq. 2.6 this results in:

$$p_c = \rho_l R_v T \ln(RH) \tag{2.8}$$

In these equations R_v is the specific gas constant for vapour and ρ_l the density of liquid water. Eq. 2.7 shows that the relative humidity will be lowest for capillary tubes with the smallest radius. In other words, capillary condensation will occur first in the smallest pores at low relative humidity. As relative humidity increases, the larger pores will be filled and capillary condensation will take place there. In this approach it is assumed that the pores distributed in the material are a bundle of small cylinders. In reality the pore structure will more likely consist out of a complex three-dimensional network of larger 'chambers' interconnected by narrow pores. This complex structure often results in a moisture content of the material which depends on the history of wetting and drying. This phenomenon is referred to as hysteresis.

The curve shown in Figure 2.2 is often referred to as the sorption isotherm. Two regions are distinguished on this curve: the hygroscopic and over-hygroscopic region. There is no strict boundary between the two regions and in literature values between 95% [29] and 98% RH [28] are found. These two regions are rather arbitrarily defined and in reality no actual physical difference exists. The distinction comes from the relevant moisture load. For the hygroscopic region this is contact with moist air, while for the overhygroscopic region this is contact with liquid water.

Capillary active materials

The over-hygroscopic region is poorly represented on a sorption isotherm curve such as Figure 2.2. It is however possible, by applying Kelvin's law (Eq. 2.8), to transform the relative humidity to capillary pressure. Since the relation between RH and p_c is logarithmic, a small variation in RH results in a large change of p_c. Figure 2.5 shows the transformation of the sorption isotherm. This type of curves is referred to as retention curves. Examples of retention curves for real materials are found in Appendix A.
The over-hygroscopic region can now be divided into two new regions: the capillary region and the supersaturation region. When a capillary active material is brought into contact with a free water surface, it absorbs water until the free water saturation or capillary moisture content w_{cap} is reached. In some pores however air can still be trapped. These remaining pores could be filled with water for example by placing the material in a vacuum. When all the pores are filled with water the saturation moisture content w_{sat} is reached.

The ability of a porous material to store moisture is often expressed by the moisture capacity. This moisture capacity is determined by taking the slope of the sorption isotherm or moisture retention curve, $\frac{\partial w}{\partial RH}$ or $\frac{\partial w}{\partial p_c}$ respectively. The moisture capacity is rather low in the hygroscopic region, but increases fast when

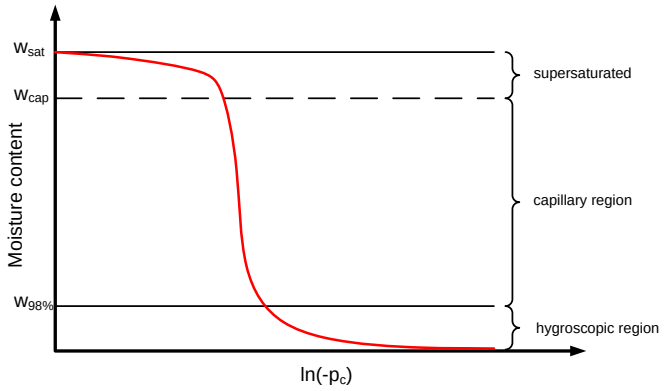

Figure 2.5: Retention curve of a capillary porous material.

going from the hygroscopic to the over-hygroscopic region.

Moisture transport mechanisms

As already mentioned earlier the moisture transport mechanisms studied here are limited to vapour diffusion and liquid water transport due to capillary forces. Effects of gravity, electrical field or ion concentration gradients are not important in a building physics context and are neglected here.
Different transport mechanisms in the capillary pores can be identified as for example listed by Künzel [29]. At low moisture content moisture is adsorbed on the pore walls. Because of high adhesive forces this water stays immobile. If a vapour pressure gradient is present across the pore then water vapour is transported from high vapour pressure to low vapour pressure by diffusion. In the current analysis it is assumed that the total pressure is constant so there is no air flow and thus no convection of water vapour through the pores.
At higher relative humidity the smallest pores become completely filled with water. From here on capillary condensation occurs. If the moisture content is so high that filled pores are connected, liquid water can be transported through the porous material by capillary forces.

It is clear from the previous analysis that moisture transport through a porous material is complex. In the phenomenological approach used in this work all possible transport mechanisms are attributed to vapour diffusion at low moisture content, resulting in a sort of generalised vapour diffusivity and liquid transport at

high moisture content resulting in some sort of generalised liquid permeability. However, a distinction between vapour diffusion at low moisture content and liquid transport at high moisture content is rather arbitrary since in reality both mechanisms occur simultaneously. In the hereafter presented model it is however assumed that both transport mechanisms can be modelled separately. In section 2.3 the governing transport equations for vapour diffusion and liquid transport are discussed in more detail.

2.2 Heat and moisture transport in the air

2.2.1 General considerations

Incompressible flow

Air flow in buildings can be modelled as incompressible [37]. Although air is a compressible fluid, at low velocities it behaves as an incompressible medium. The pressure differences are small enough to have no impact on the density. The density of the air is however affected by temperature and concentration variations. This is of importance when natural convection is considered. Therefore it is necessary to simultaneously solve the heat and moisture transport equations in air to account for a varying air density when modelling air flow in buildings.
Several approaches can be found in CFD to account for the temperature effect on air density. For an incompressible flow the temperature dependence of the density can be implemented by formulating for example a polynomial function representing the relation between both. An other approach which is often used, is the so-called Boussinesq approach [38]. For natural convection cases a faster convergence is achieved than when setting up the problem with temperature dependent density. This model treats density as a constant in all equations except for the buoyancy term in the momentum equation.

$$(\rho - \rho_0)\, g \approx -\rho_0 \beta\, (T - T_0)\, g \tag{2.9}$$

where ρ_0 is the constant density $[kg/m^3]$, g is gravitational acceleration $[m/s^2]$ T_0 is the operating temperature and β is the thermal expansion coefficient $[1/K]$. This approximation is only valid if changes in density are small or in other words if temperature changes are small $\beta\,(T - T_0) \ll 1$. However, this approach is not compatible with moisture transport (or species transport in general). Therefore a different approach is needed: the incompressible ideal gas model. In this approach the influence of temperature and concentration variations is incorporated in all transport equations. Still the effect of pressure variation on density is neglected.

Using the ideal gas law, the density is calculated as follows:

$$\rho = \frac{P_{op}}{\mathcal{R}T\sum_i \frac{Y_i}{M_i}} \tag{2.10}$$

with P_{op} the average operating pressure $[Pa]$, $\mathcal{R}$ the universal gas constant $[J/molK]$, Y_i the mass fraction of species i $[-]$ and M_i the molar weight of species i $[kg/mol]$.

Turbulence modelling

Air flow in a building context has often a turbulent nature. Turbulent flow is characterized by three-dimensional chaotic unsteady behaviour. In Direct Numerical Simulations (DNS) turbulent motion is directly solved. However, capturing all this turbulence would require a very small time scale and a very fine grid resolution and results in extreme computational resources. For this reason turbulent simulations are performed in practice by modelling the effects of turbulence.
One popular class of turbulence models are the Reynolds Averages Navier-Stokes (RANS) models. In literature a lot of reference works can be found were an overview of the state of the art in RANS turbulence modelling is given (e.g. [39]). In this section only a short introduction to this turbulence modelling is given, for more detail the reader is referred to the cited reference work.

Consider a velocity vector in Cartesian coordinates $\vec{u} = (u, v, w)$, where u is the x-component of the velocity, v is the y-component and w is the z-component. The continuity and Navier-Stokes equations for an incompressible flow with constant viscosity are then given by:

$$\nabla \cdot \vec{u} = 0 \tag{2.11a}$$

$$\frac{\partial u}{\partial t} + \nabla \cdot (u\vec{u}) = -\frac{1}{\rho}\frac{\partial p}{\partial x} + \nu\nabla \cdot (\nabla u) \tag{2.11b}$$

$$\frac{\partial v}{\partial t} + \nabla \cdot (v\vec{u}) = -\frac{1}{\rho}\frac{\partial p}{\partial y} + \nu\nabla \cdot (\nabla v) \tag{2.11c}$$

$$\frac{\partial w}{\partial t} + \nabla \cdot (w\vec{u}) = -\frac{1}{\rho}\frac{\partial p}{\partial z} + \nu\nabla \cdot (\nabla w) \tag{2.11d}$$

Here ν is the kinematic viscosity. The velocity vector can be considered the sum of a mean velocity and a fluctuating part: $\vec{u} = \bar{\vec{u}} + \vec{u'} = (\bar{u}, \bar{v}, \bar{w}) + (u', v', w')$. The Navier-Stokes equations can now be transformed to the so-called Reynolds Averaged Navier-Stokes equations [39]:

$$\nabla \cdot \bar{\vec{u}} = 0 \tag{2.12a}$$

$$\frac{\partial \bar{u}}{\partial t} + \nabla \cdot (\bar{u}\vec{\bar{u}}) = -\frac{1}{\rho}\frac{\partial \bar{p}}{\partial x} + \nu \nabla \cdot (\nabla \bar{u}) - \nabla \cdot \left(\overline{u'\vec{u'}}\right) \tag{2.12b}$$

$$\frac{\partial \bar{v}}{\partial t} + \nabla \cdot (\bar{v}\vec{\bar{u}}) = -\frac{1}{\rho}\frac{\partial \bar{p}}{\partial y} + \nu \nabla \cdot (\nabla \bar{v}) - \nabla \cdot \left(\overline{v'\vec{u'}}\right) \tag{2.12c}$$

$$\frac{\partial \bar{w}}{\partial t} + \nabla \cdot (\bar{w}\vec{\bar{u}}) = -\frac{1}{\rho}\frac{\partial \bar{p}}{\partial z} + \nu \nabla \cdot (\nabla \bar{w}) - \nabla \cdot \left(\overline{w'\vec{u'}}\right) \tag{2.12d}$$

Note that the process of time averaging introduced a new term in Eqs. 2.12b-2.12d which was not present in equations 2.11b-2.11d. These new terms (last term on the right hand side of Eqs. 2.12b-2.12d) result from six additional stresses: the so-called Reynold stresses.

$$\bar{\bar{\tau}} = \begin{bmatrix} \tau_{xx} & \tau_{xy} & \tau_{xz} \\ \tau_{yx} & \tau_{yy} & \tau_{yz} \\ \tau_{zx} & \tau_{zy} & \tau_{zz} \end{bmatrix} = \begin{bmatrix} -\rho\overline{u'^2} & -\rho\overline{u'v'} & -\rho\overline{u'w'} \\ -\rho\overline{u'v'} & -\rho\overline{v'^2} & -\rho\overline{v'w'} \\ -\rho\overline{u'w'} & -\rho\overline{v'w'} & -\rho\overline{w'^2} \end{bmatrix} \tag{2.13}$$

The instantaneous continuity and Navier-Stokes equations (Eqs. 2.11) form a closed set of four equations with four unknowns (u,v,w,p). However by taking the time average of these equations, six new unknowns are introduced, the Reynold stress terms. It is the objective of RANS turbulence modelling to develop procedures to estimate these stress terms. In other words, in RANS modelling the mean flow is resolved and the effect of turbulence on the flow is modelled.

Various RANS models have been developed in the last decades. Three main categories can be distinguished: the linear eddy-viscosity models, the non-linear eddy-viscosity models and the Reynolds-stress transport models. In the present work only linear eddy-viscosity models will be applied. These models are shortly discussed in the next section. For more details on non-linear eddy-viscosity models (e.g. v^2-f model of Durbin [40]) and Reynolds stress transport models [41] the reader is referred to literature.

In the eddy-viscosity models the Boussinesq hypothesis [39] is used. This hypothesis states that the Reynolds stresses are related to the mean velocity gradients through the turbulent viscosity μ_t according to Eq. 2.14.

$$-\rho\overline{u_i'u_j'} = \mu_t \left(\frac{\partial \overline{u_i}}{\partial x_j} + \frac{\partial \overline{u_j}}{\partial x_i}\right) - \frac{2}{3}\rho k \delta_{ij} \tag{2.14}$$

Here the suffix notation is used to simplify the notation. The convention of the notation is that i or j = 1 corresponds with the x-direction, i or j = 2 with the y-direction and i or j = 3 with the z-direction. For example $u_2 = v$, $x_2 = y$. δ_{ij} is the Kronecker delta (= 1 if $i = j$, = 0 if $i \neq j$) and k is the turbulent kinetic energy.

$$k = \frac{1}{2}\left(\overline{u'^2} + \overline{v'^2} + \overline{w'^2}\right) \tag{2.15}$$

The last term in 2.14 is necessary to assure that the sum of the three normal Reynolds stresses equals twice the turbulent kinetic energy multiplied with density. This way an equal third is allocated to each normal stress component. However this implies that the normal stresses are isotropic which in reality is not the case. Reynolds stress transport models overcome this problem by solving directly for the Reynolds stresses but their numerical stability is poor and convergence is harder for these models.
The turbulent viscosity μ_t can be determined using the appropriate turbulence model. A number of eddy-viscosity models are developed, some models more complex than others. Each turbulence model however has its own range of flow problems where it is suited for and up till now no model is found applicable to all classes of flow problems. The level of complexity depends on the number of additional equations that are solved to determine the turbulent viscosity.
Zero-equation models (mixing length models) attempt to describe the Reynold stresses through simple algebraic equations for μ_t as function of position. **Two-equation turbulence models** like the k-ϵ and k-ω model use two transport equations to model the transport of turbulence properties, turbulent kinetic energy k and turbulence dissipation rate ϵ in the case of the k-ϵ and turbulent kinetic energy and specific dissipation rate ω in case of the k-ω model. **One-equation models** like the Spalart-Allmaras model only solve one additional transport equation [42].
A second class of turbulence models are Large Eddy Simulations (LES). These models use a filtering approach. The large scale eddies are resolved while the small scales are filtered and modelled. This technique is more accurate than RANS but requires significantly more computational resources. By definition LES is unsteady and three-dimensional resulting in the need for a fine grid resolution and small time steps.
To overcome some disadvantages of LES, especially the difficulty LES encounters in near wall regions, new modelling approaches have been developed. These approaches, so-called hybrid RANS-LES, try to combine the best of both RANS and LES. RANS is used to solve the near wall regions, while LES is used in the bulk flow. This results in less severe grid requirements and thus a reduced computational effort. However these techniques are still under development and are currently limited to academic use. More details on LES modelling and hybrid RANS-LES can be found in literature [39].
In the present work only two-equation models are used, more specifically the k-ϵ and k-ω model. For each of these models variations can be identified (standard k-ϵ, Realisable k-ϵ, RNG k-ϵ, modified k-ω, SST k-ω). The performance of these different turbulence models is thoroughly discussed in [43] for flows over bluff bodies and in [44] and [45, 46] for indoor air flows. Goethals [44] concluded, based on a literature study, that the RNG k-ϵ often gives the best results for indoor

environment simulations. The SST k-ω model also appears promising but is less widely used.

Boundary layer modelling

Different near wall treatments are possible in RANS modelling. This section will focus on the near wall treatments used in this work.
For fully developed turbulent flow a characteristic shape of the velocity profile near the wall is found. This profile is often represented by dimensionless wall units:

$$y^+ = \frac{u_\tau y}{\nu} \tag{2.16}$$

$$u^+ = \frac{u}{u_\tau} \tag{2.17}$$

Where y^+ is the dimensionless distance to the wall, y the actual distance, u^+ the dimensionless velocity in the boundary layer, ν the kinematic viscosity, u the actual velocity and u_τ the friction velocity given by:

$$u_\tau = \sqrt{\frac{\tau_w}{\rho}} \tag{2.18}$$

τ_w is the wall shear stress $[Pa]$. Figure 2.6 shows the dimensionless velocity boundary layer profile. Three layers can be distinguished. In the first layer, near to the wall, the dimensionless velocity equals the dimensionless distance to the wall. This is the laminar or viscous sublayer. In this very thin layer ($y^+ < 5$) the momentum transport occurs by diffusion. The velocity profile is represented by a linear law:

$$u^+ = y^+ \qquad (y^+ < 5) \tag{2.19}$$

Next a transition layer is found also referred to as the buffer layer ($5 < y^+ < 30$). Here the linear law gradually transforms to a logarithmic law further from the wall. Past the buffer layer, the so-called log-law layer is distinguished ($\pm 30 < y^+ < 10^2 - 10^3$).

$$u^+ = \frac{1}{\kappa} \ln y^+ + B \qquad \left(\pm 30 < y^+ < 10^2 - 10^3\right) \tag{2.20}$$

In this log-law layer transport of momentum is meanly determined by turbulence. Typical values for the constants in Eq. 2.20 are $\kappa = 0.42$ and $B = 5.5$ [38]. Further away from the wall, outside the boundary layer, the flow is no longer effected

by the viscous effects induced by the wall. In Eq. 2.20 outside boundary values for y^+ are approximately 10^2 – 10^3. These values are however Reynolds number dependent.
Since for fully developed flow a dimensionless law-of-the-wall is found, it is possible to model the near wall effect by implementing so-called wall functions instead of solving the boundary layer directly. This allows the use of a courser grid near the wall and thus reduces computational effort. However, the law-of-the-wall is only valid for fully developed flows. This strongly reduces its applicability. Air flow in a building context is complex and phenomena like vortex shedding, reattachment, jet impingement, etc. can occur. For these phenomena it is no longer possible to formulate a universally applicable law-of-the-wall.

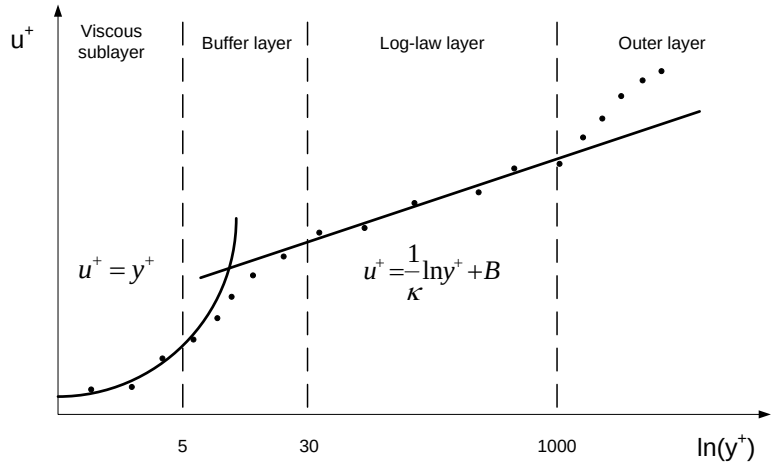

Figure 2.6: Schematic representation of the dimensionless velocity profile u^+ as a function of y^+. The law of the wall is compared with experiments (•) by for example [47]

Most two-equation turbulence models like e.g. the k-ϵ model were developed to solve turbulence in the core region of the flow. These models need an additional low Reynolds number correction to account for the near-wall region. This correction can be done by using wall functions but as stated earlier these wall function are not well suited for non-equilibrium flows. Therefore two-layer models were developed. In these two-layer models the turbulent core is solved with a two-equation turbulence model and the viscosity affected region near the wall is solved with a one-equation model. Another possibility is to use models developed for low Reynolds numbers (LRNM). In LRNM the entire boundary layer is resolved and an additional damping of the turbulence is applied for low

turbulent Reynold numbers. An example of a low Reynolds number model is the k-ω model. The SST-k-ω model is a blending of a LRNM (k-ω) for the viscosity affected near wall region and a HRNM (high Reynolds number model), the k-ϵ model, for the fully turbulent region.

2.2.2 Moisture transport in air

Together with the Navier-Stokes and continuity equations (Eq. 2.11) a species transport equation has to be solved if moisture transport in air is to be modelled. Moisture is transported in air as water vapour. This water vapour can be transported through air by convection and diffusion. This results in a mass balance for water vapour in air stating that the change of the amount of water vapour in a control volume of air is due to water vapour transported along with the air movement through the boundaries of the control volume and due to vapour diffusion through the boundaries of the control volume. Water vapour diffusion in air can be described by Fick's law of diffusion [48]. Fick stated that the diffusion mass flux of component A (in this case water vapour) into component B (air) is proportional to the gradient of the mass fraction of component A.

$$\vec{g_v} = -\rho D_{va} \nabla Y \tag{2.21}$$

Y is the mass fraction of water vapour in air $[-]$, D_{va} is the diffusion coefficient of water vapour in air $[m^2/s]$, ρ is the density of the air-vapour mixture and $\vec{g_v}$ is the water vapour diffusion flux $kg/m^2 s$. The molecular diffusion of water vapour in air D_{va} is given by Eq. 2.22 [49]

$$D_{va} = 2.31 \cdot 10^{-5} \frac{101325}{P_{op}} \left(\frac{T}{273.16} \right)^{1.81} \tag{2.22}$$

The effect of turbulence on the diffusion can be incorporated by introducing a turbulent diffusion coefficient D_t. Similarly to the introduction of a turbulent viscosity when the Navier-Stokes equations were time-averaged, a turbulent diffusion can be introduced when the vapour transport equation is time-averaged. The ratio between the turbulent viscosity and the turbulent diffusivity is given by the turbulent Schmidt number. A number of experiments showed that this Schmidt number can often be assumed constant. For this work a value of $Sc_t = 0.7$ is assumed.

$$Sc_t = 0.7 = \frac{\nu_t}{D_t} \tag{2.23}$$

Combining the turbulent diffusion coefficient and the molecular diffusion results in an effective diffusion coefficient D_{eff}. The differential form of the moisture transport equation in air is then given by:

$$\frac{\partial}{\partial t} (\rho Y) + \nabla \cdot (\rho \vec{v} Y) = -\nabla \cdot \vec{g} = \nabla \cdot (\rho D_{eff} \nabla Y) \tag{2.24}$$

2.2.3 Heat transport in air

To model the transport of heat in air, an energy transport equation is needed. This energy equation is found by writing down the energy balance for a control volume. This energy balance states that the change in total internal energy in time is due to heat transported through the boundaries of the control volume along with the flow and due to heat transported through the boundaries by diffusion. This diffusion incorporates the conduction of heat and the transport of sensible and latent heat due to water vapour diffusion. This implies that there is a coupling of the heat transport equations and the water vapour transport. In the development of the heat transport equations some assumptions and simplifications were made:

- The air is modelled as an ideal gas.
- Pressure variations are small so they do not affect thermodynamic properties.
- Potential energy changes are assumed negligible.
- Kinetic energy changes are neglected.
- Viscous heating is neglected.
- No volumetric source terms are present (e.g. chemical reactions, droplet evaporation, condensation,...).

In general the following energy conservation equation can be formulated:

$$\frac{\partial \rho E'}{\partial t} + \nabla \cdot (\rho H' \vec{v}) = -\nabla \cdot \vec{q'} \tag{2.25a}$$

with

$$E' = u + \frac{1}{2}v^2 + PE \tag{2.25b}$$

$$H' = u + \frac{p}{\rho} + \frac{1}{2}v^2 + PE \tag{2.25c}$$

where PE is the potential energy and $\frac{1}{2}v^2$ represents the kinetic energy, q' is the total heat transported by diffusion (sensible and latent) and u is the internal energy. Eq. 2.25a can be expanded to:

$$\frac{\partial \rho E'}{\partial t} + \nabla \cdot \left(\rho \left(E' + \frac{p}{\rho} \right) \vec{v} \right) = -\nabla \cdot \vec{q'} \tag{2.26a}$$

$$\frac{\partial \rho E'}{\partial t} + \nabla \cdot \rho E' \vec{v} + p \nabla \cdot \vec{v} + \vec{v} \cdot \nabla p = -\nabla \cdot \vec{q'} \tag{2.26b}$$

Combining this with the mass conservation equation, Eq. 2.27,

$$\frac{\partial \rho}{\partial t} + \nabla \cdot (\rho \vec{v}) = 0 \tag{2.27}$$

the following can be derived:

$$\cancel{E' \frac{\partial \rho}{\partial t}} + \cancel{E' \nabla \cdot \rho \vec{v}} + \rho \vec{v} \cdot \nabla E' + \rho \frac{\partial E'}{\partial t} + p \nabla \cdot \vec{v} + \vec{v} \cdot \nabla p = -\nabla \cdot \vec{q'} \tag{2.28}$$

where the first two terms cancel out. Next this can be combined with Bernouilli's equation. Bernouilli's equation can be written as follows, neglecting viscous dissipation:

$$\rho \frac{\partial \frac{1}{2} v^2}{\partial t} + \rho \vec{v} \cdot \nabla \left(\frac{1}{2} v^2 + PE \right) + \vec{v} \cdot \nabla p = 0 \tag{2.29}$$

Subtracting Eq. 2.29 from Eq. 2.28 results in:

$$\rho \frac{\partial u}{\partial t} + \rho \vec{v} \cdot \nabla u + p \nabla \cdot \vec{v} = -\nabla \cdot \vec{q'} \tag{2.30}$$

Combining this again with the continuity equation (Eq. 2.27) results in the energy conservation equation expressed for internal energy:

$$\frac{\partial \rho u}{\partial t} + \nabla \cdot (\rho u \vec{v}) + p \nabla \cdot \vec{v} = -\nabla \cdot \vec{q'} \tag{2.31}$$

This equation can be rewritten for enthalpy h since $h = u + p/\rho$.

$$\frac{\partial \rho h}{\partial t} - \frac{\partial p}{\partial t} + \nabla \cdot (\rho h \vec{v}) - \vec{v} \cdot \nabla p = -\nabla \cdot \vec{q'} \tag{2.32}$$

When assuming that pressure variations in space and time are small and that they can be neglected, Eq. 2.32 can be simplified to:

$$\frac{\partial \rho h}{\partial t} + \nabla \cdot (\rho h \vec{v}) = -\nabla \cdot \vec{q'} \tag{2.33}$$

Next, the total heat transported by diffusion can be expanded to $\vec{q'} = \vec{q} + h_a \vec{g_a} + h_v \vec{g_v}$. The conductive heat flux $\vec{q}$ is given by Fourier's law of conduction, with λ the thermal conductivity $[W/mK]$:

$$\vec{q} = -\lambda \nabla T \tag{2.34}$$

Also $h_a \vec{g_a} + h_v \vec{g_v}$ can be transformed. These terms state that heat is transported along with the diffusion of water vapour and air. The diffusion of a species A into a species B is always accompanied by the diffusion of B in the opposite direction thus explaining the two terms. The net total amount of molar fluxes due to diffusion has to be zero. However in a dilute gas mixture it is a good

approximation to assume that also the net total amount of mass fluxes is zero or in other words $\vec{g_v} = -\vec{g_a}$. For an ideal gas the enthalpy h only depends on temperature. The specific heat C_p is thus also a function of temperature alone: $C_p(T) = \frac{dh}{dT}$. For the temperature ranges encountered in buildings, the specific heat can often be assumed constant. Substituting all this in Eq. 2.33 and taking into account that $h_a - h_{a,ref} = C_a\left(T - T_{ref}\right)$ and $h_v - h_{v,ref} = C_v\left(T - T_{ref}\right) + L_{ref}$ ($h_{v,ref} = 0$ for liquid water at 0°C, L_{ref} is the latent heat of evaporation at reference temperature, C_a is the specific heat of air at constant pressure and C_v is the specific heat of water vapour at constant pressure) results in:

$$\begin{aligned}\frac{\partial}{\partial t}\left[\rho Y\left(C_v T + L\right) + \rho\left(1 - Y\right)C_a T\right] \\ + \nabla\cdot\left[\vec{v}\left(\rho Y\left(C_v T + L\right) + \rho\left(1 - Y\right)C_a T\right)\right] \\ = \nabla\cdot\left[\lambda\nabla T - \left(\left(C_v T + L\right) - C_a T\right)\vec{g}\right]\end{aligned} \quad (2.35)$$

Similar to the turbulent vapour transport equation (Eq. 2.24) where a turbulent diffusion coefficient was defined to account for the effect of turbulence on the diffusion transport, a turbulent conductivity λ_t can be defined. This turbulent conductivity is given by Eq. 2.36a.

$$Pr_t = \rho C\frac{\nu_t}{\lambda_t} \quad (2.36a)$$

$$\lambda_{eff} = \lambda + \lambda_t \quad (2.36b)$$

where Pr_t is the turbulent Prandtl number which can be assumed constant and equal to 0.85.
L represents the latent heat of water evaporation at a reference temperature of 0°C. This allows to bring L outside the derivative operators in Eq. 2.35. When applying Eq.2.24 to Eq. 2.35, the latent heat cancels out of the equation. This is as expected since no phase change (condensation/evaporation) is present in the air flow. The heat transport equation can thus be rewritten as:

$$\frac{\partial}{\partial t}\left[\rho C T\right] + \nabla\cdot\left[\vec{v}\left(\rho C T\right)\right] = \nabla\cdot\left[\lambda_{eff}\nabla T - \left(C_v - C_a\right)\vec{g}T\right] \quad (2.37)$$

with the mass weighted heat capacity given by:

$$C = YC_v + \left(1 - Y\right)C_a \quad (2.38)$$

2.3 Coupled heat and moisture transport in porous materials

2.3.1 Moisture transport in a porous material

Moisture in a building context can exist in three phases: vapour, liquid and solid (ice). In the present model ice and ice formation is neglected. The two remaining phases can both be stored and transported in a porous material. This results in a moisture balance of the following form:

$$w = w_v + w_l \tag{2.39a}$$

$$\vec{g} = \vec{g_v} + \vec{g_l} \tag{2.39b}$$

$$\frac{dw}{dt} = -\nabla \cdot \vec{g} \tag{2.39c}$$

The moisture content in the porous material $w\ [kg/m^3]$ is the sum of the vapour content w_v and the liquid content w_l. The vapour content is much smaller than the liquid content and is often neglected. The moisture flux in the material $\vec{g}$ $[kg/m^2 s]$ is the result of a vapour flux $\vec{g_v}$ and liquid flux $\vec{g_l}$. This is of course only an approximation since both transport mechanisms can strictly speaking not be divided. Finally Eq. 2.39c states that the change of the moisture content in time is due to the net inflow/outflow of moisture. Note that vapour transport due to air convection is neglected here.
The vapour diffusion flux in a porous material can be described by an adjusted Fick's diffusion law.

$$\vec{g_v} = -\rho \frac{D_{va}}{\mu} \nabla Y \tag{2.40}$$

The diffusion coefficient D_{va} in Eq. 2.21 is replaced by the ratio D_{va}/μ where μ is the ratio of the vapour diffusion of water vapour in the porous material to the vapour diffusion of water vapour in air. This ratio is also addressed as the water vapour diffusion resistance factor. The resistance factor will be larger than one since diffusion through the porous material is hindered by various factors. Firstly the tortuous structure of the material increases the path length of water molecules. Secondly the open porosity reduces the surface area through which vapour can diffuse. The diffusion is also function of the saturation degree.
For very small pores vapour diffusion can no longer be described by Fick's law. At these small scales collisions of vapour molecules and pore walls become more frequent than collisions between molecules. The vapour transport is then referred to as Knudsen diffusion or effusion. This Knudsen diffusion is also driven by vapour pressure gradients. To simplify the current model, the Knudsen diffusion is not modelled separately but its effect is assumed incorporated in the vapour

resistance factor.

In the building context the total pressure can often be assumed constant ($\approx P_{atm}$). This results in an expression of Fick's law with the partial vapour pressure p_v as driving force.

$$\vec{g_v} = -\frac{D_{va}}{\mu R_v T}\nabla p_v \tag{2.41}$$

In these equations for diffusion the thermal diffusion or Soret effect is neglected. It was stated in [50] and shown by Whitaker [51] and Janssen [52] that this effect is small compared to the concentration diffusion.

The liquid flux is described by Darcy's law:

$$\vec{g_l} = -K_l \nabla p_c \tag{2.42}$$

The driving force for the liquid transport is the gradient in capillary pressure p_c $[Pa]$. K_l is the liquid permeability $[s]$. Combining Eq. 2.39c, Eq. 2.41 and Eq. 2.42 results in the following form of the moisture balance equation:

$$\frac{dw}{dt} = -\nabla \cdot (\vec{g_v} + \vec{g_l}) = \nabla \cdot \left(\frac{D_{va}}{\mu R_v T}\nabla p_v + K_l \nabla p_c \right) \tag{2.43}$$

It is now possible to transform this equation so that only two independent state variables remain. In this work temperature (T) and capillary pressure (p_c) are chosen in analogy to the work of Grunewald [53]. The partial vapour pressure is related to the relative humidity (Eq. 2.2) and this relative humidity is in turn related to the capillary pressure (Kelvin's law Eq. 2.8). This results in the following equation for the moisture balance in a porous material:

$$\begin{aligned}\frac{\partial w}{\partial p_c}\frac{\partial p_c}{\partial t} &= \nabla \cdot (K_l \nabla p_c) \\ &+ \nabla \cdot \frac{D_{va}}{\mu R_v T}\left(\frac{\rho_v}{\rho_l}\nabla p_c + RH \frac{\partial p_{sat}}{\partial T}\nabla T - \frac{p_v \ln RH}{T}\nabla T \right)\end{aligned} \tag{2.44}$$

To solve this equation three material properties are needed: the vapour diffusion resistance factor μ, the liquid permeability K_l and the moisture capacity $\partial w/\partial p_c$. For some materials these properties are listed in App. A. For other materials these properties can be found in a wide range of catalogs (e.g. [54]). A more thorough discussion on the impact of accuracy of these parameters is given in chapter 4.

2.3.2 Heat transport in a porous material

As already stated, only transport by diffusion is assumed in the here studied porous materials. Heat is thus only transported in the porous materials due to

conduction on the one hand and diffusion of water on the other hand. Water vapour diffusing through the porous materials transports sensible as well as latent heat.
Heat transport in a (porous) material due to diffusion can be described by Fourier's law of heat conduction:

$$\vec{q} = -\lambda_{mat} \nabla T \tag{2.45}$$

The heat flux $\vec{q}$ $[W/m^2]$ is proportional to the gradient of the temperature, with λ_{mat} the conductivity of the porous material $[W/mK]$. This conductivity is strongly dependent on the moisture content of the material since the conductivity of water differs from that of the material matrix. Therefore this conductivity is expressed as a function of moisture content $\lambda_{mat}(w)$.
Water is transported through a porous material as liquid and vapour resulting in a liquid and vapour flux $\vec{g}_l$ and $\vec{g}_v$ (Eqs. 2.41 and 2.42). Along with the liquid water, sensible heat is transported ($\vec{q}_l$) while sensible and latent heat is transported along with the vapour diffusion ($\vec{q}_v$).

$$\vec{q}_l = \vec{g}_l h_l \tag{2.46a}$$

$$\vec{q}_v = \vec{g}_v h_v \tag{2.46b}$$

In section 2.2.3 it was already shown that the enthalpy of liquid water h_l and vapour h_v can be assumed proportional to the temperature when the heat capacity is close to constant. This allows to rewrite Eq. 2.46 to:

$$\vec{q}_l \approx \vec{g}_l C_l T \tag{2.47a}$$

$$\vec{q}_v \approx \vec{g}_v \left(C_v T + L\right) \tag{2.47b}$$

Similar to section 2.2.3 the potential energy and kinetic energy changes in the porous material can be neglected and no chemical reactions occur in the material. The total enthalpy of the porous material E $[J/m^3]$ is thus the sum of the energy stored in the material matrix and the energy stored in the liquid water and water vapour present in the material.

$$\begin{aligned}\frac{\partial E}{\partial t} &= \frac{\partial}{\partial t}\left(\rho_{mat} h_{mat} + w_l h_l + w_v h_v\right) = \\ &\left(\rho_{mat} C_{mat} + w_l C_l + w_v C_v\right)\frac{\partial T}{\partial t} + C_l T \frac{\partial w_l}{\partial t} + \left(C_v T + L\right)\frac{\partial w_v}{\partial t}\end{aligned} \tag{2.48}$$

Where w_v is the vapour moisture content and w_l is the liquid moisture content. ρ_{mat} is the dry porous material density $[kg/m^3]$ and C_{mat} the heat capacity of the dry material $[J/kgK]$. The energy balance equation which states that a change in

stored energy is only due to heat diffusion then becomes:

$$\frac{\partial E}{\partial t} = \left(\rho_{mat} C_{mat} + w_l C_l + w_v C_v\right) \frac{\partial T}{\partial t} + C_l T \frac{\partial w_l}{\partial t} + \left(C_v T + L\right) \frac{\partial w_v}{\partial t} = \nabla \cdot \left(\lambda_{mat} \nabla T - C_l T \vec{g_l} - \left(C_v T + L\right) \vec{g_v}\right) \quad (2.49)$$

The liquid moisture content and vapour moisture content can be linked to the total moisture by the open porosity ψ_o, taking into account that $w = w_l + w_v$ and $\psi_o = \frac{w_l}{\rho_l} + \frac{w_v}{\rho_v}$.

$$w_l = \frac{\psi_o - \frac{w}{\rho_v}}{\frac{1}{\rho_l} - \frac{1}{\rho_v}} \quad (2.50a)$$

$$w_v = \frac{\frac{w}{\rho_l} - \psi_o}{\frac{1}{\rho_l} - \frac{1}{\rho_v}} \quad (2.50b)$$

3 Numerical implementation

3.1 Introduction: using Fluent® to solve transport equations

In chapter 2 the transport equations for heat and mass in the air and porous materials were derived starting from the conservation equations. In this chapter the numerical implementation of these equations is discussed. The commercially available CFD program Fluent® [38] was used for the implementation of the HAM transport model. Fluent® is a computational fluid dynamics software package based on a finite volume discretization technique. It is a widely used package originally developed for the numerical simulation of fluid flow. Some additional modules are available to take flow through porous materials into account. However these modules are mainly concerned with the convective transport through porous materials. Also multiphase flow can be modelled in Fluent® but this requires complex and fine grids. The existing porous and multiphase models in Fluent® are thus not well suited for combined heat and moisture modelling in air and porous materials. Fluent® however allows the implementation of a new set of transport equations by means of User Defined Scalar (UDS) transport equations. This approach will be used in this work.

The choice was made to integrate the HAM model into an existing CFD model. This has some advantages. First of all only one solver is needed. Previous researchers used an external coupling approach between a stand alone HAM model (e.g. HAMFEM [43] or Delphin [55]) and CFD. This external

coupling procedure requires a constant iteration between both solvers, significantly increasing computational load and memory requirements. Secondly, by using Fluent® as a solver, a wide range of already integrated solver settings and options can be used, thus reducing the programming effort.

UDS transport equations

In the Fluent® manual [56] a detailed description is found on the possibilities and functionalities of the UDS-transport equations. Additional to the transport equations a range of preprogrammed functions are available: User Defined Function (UDF).
UDS's start from the prerequisite that the transport equation for an arbitrary transported scalar variable ϕ can be formulated as:

$$\frac{\partial \rho\phi}{\partial t} + \nabla \cdot (\rho\vec{v}\phi) = \nabla \cdot (\Gamma \nabla\phi) + S_\phi \tag{3.1}$$

In this equations four terms can be distinquished. The first term on the left hand side is the change in time of the conserved property (e.g. energy, momentum, moisture,...). The second term on the left hand side covers the convective transport of the conserved property. The first term on the right hand side is the diffusive transport. Γ is here the diffusion coefficient associated with the conserved property (e.g. thermal diffusivity α in case of energy, vapour diffusion coefficient D_{va} in case of moisture). Finally S_ϕ refers to the volumetric source and/or sink terms. The equations for heat and moisture transport in air and porous material derived in chapter 2 (Eqs. 2.24, 2.37, 2.44, 2.49) now all have to be rewritten in the appropriate form.
Eq. 3.1 can be integrated over an arbitrary control volume yielding:

$$\int_V \frac{\partial \rho\phi}{\partial t} dV + \oint \rho\phi\vec{v} \cdot d\vec{A} = \oint \Gamma \nabla\phi \cdot d\vec{A} + \int_V S_\phi dV \tag{3.2}$$

in this equation $\oint \_ \cdot d\vec{A}$ is the surface integral over the boundaries of the control volume and $\int_V \_ dV$ is the volume integral over the control volume V. Discretization of Eq. 3.2 on a given finite volume, here referred to as cell, gives:

$$\frac{(\rho\phi)^{t+\Delta t} - (\rho\phi)^{t}}{\Delta t} V + \sum_f (\rho_f \vec{v}_f \phi_f)^{t+\Delta t} \cdot \vec{A}_f = \sum_f (\Gamma \nabla\phi_f)^{t+\Delta t} \cdot \vec{A}_f + S_\phi V \tag{3.3}$$

Here a time implicit discretization scheme is applied. The advantage of the fully implicit scheme is that it is unconditionally stable with respect to time step size. The first-order temporal discretization was used for the unsteady term, using

backward differences.
In Eq. 3.3 $\vec{A}_f$ is the face area which makes up the cell boundaries. This area is represented as a vector where the direction of the vector is the face normal and the longitude of the vector is the surface area of the face $[m^2]$.

The second term on the left hand side of Eq. 3.3 gives the net outflow due to convection through the cell boundary faces. By default Fluent® stores the values of the scalar variable in the cell centres. However, to calculate the convective flow, the values of the transported variable at the cell faces ϕ_f have to be known. For the simulation performed in this work a second order upwind interpolation scheme is used for the convective term. Upwind means that to determine the value at a cell face, values at the cell centre are used upstream of the face, relative to the normal velocity. When second order discretization is used the values at the cell faces are given by:

$$\phi_f = \phi + \nabla\phi \cdot \vec{r} \tag{3.4}$$

Where $\vec{r}$ is the distance vector between the upstream cell and the centre of the face, ϕ_f is the face value, ϕ the cell centre value upstream of the face and $\nabla\phi$ the gradient of ϕ in the cell upstream of the face. For this discretization scheme the gradients in the cells have to be determined. By applying the Green-Gauss theorem the following generally counts for the gradient of a scalar:

$$\int_V \nabla\phi dV = \oint \phi_f dA_f \tag{3.5}$$

Discretizing this equation yields an expression for the determination of the gradient of a scalar:

$$\nabla\phi = \frac{1}{V}\sum_f \phi_f dA_f \tag{3.6}$$

The value of ϕ_f at the face can now be determined in various ways. The simplest way is the cell-based evaluation where the arithmetic mean of the cell centres of the neighbouring cells is taken: $\phi_f = (\phi_{c0} + \phi_{c1})/2$. Fluent® also provides an alternative to this approach being the node-based evaluation where the arithmetic mean of the node values is taken. This approach is more accurate but also computationally more expensive.
A third approach also available in Fluent® is the least-squares cell-based gradient evaluation. In this method the solution is assumed to vary linearly. For each neighbouring cell an expression of the following form can be written:

$$(\nabla\phi)_{c0} \cdot \vec{r}_i = (\phi_{ci} - \phi_{c0}) \tag{3.7}$$

Where $\vec{r}_i$ is the distance vector between cell $c0$ and neighbouring cell ci. This results in a minimization problem where $(\nabla\phi)_{c0}$ is determined so that it best

satisfies Eq. 3.7 for all neighbours i. The problem is solved in a least-squares sense. More details on these discretization methods are found in [57].

The first term on the right hand side of Eq. 3.3 gives the net inflow due to diffusion through the cell boundary faces. Again the face values have to be determined in order to calculate the diffusion fluxes. The Fluent® solver employs a second order central-difference scheme. This leads to following discrete from of the diffusion flux between cell $c0$ and $c1$:

$$\Gamma_f \nabla\phi = \Gamma_f \frac{\phi_{c0} - \phi_{c1}}{r_{01}} \tag{3.8}$$

Where r_{01} is the distance between cell centre $c0$ and cell centre $c1$. The diffusion coefficient at the face between both cells, Γ_f can be determined from the values of the diffusion coefficient in the cell centres and is based on the prerequisite that the flux is continuous from cell $c0$ to face to cell $c1$. The derivation of the face diffusion coefficient is illustrated in Figure 3.1. Since $\vec{g_{01}} = \vec{g_{0f}} = \vec{g_{f1}}$ the

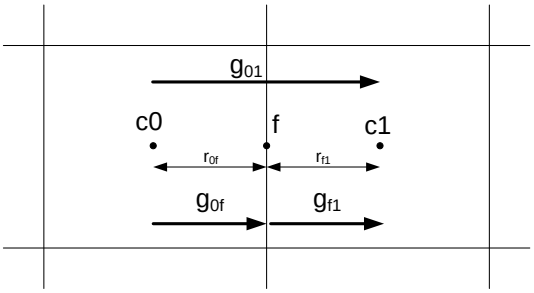

Figure 3.1: Schematic representation of the diffusion flux between two adjacent cells.

following applies for the diffusive flux:

$$\vec{g_{01}} = \frac{\frac{\Gamma_0}{r_{0f}}\frac{\Gamma_1}{r_{f1}}}{\frac{\Gamma_0}{r_{0f}} + \frac{\Gamma_1}{r_{f1}}} (\phi_0 - \phi_1) \tag{3.9}$$

In this equation r_{0f} and r_{f1} are the distances between the face and cell centres $c0$ and $c1$ respectively. This equation can be simplified if the grid is equidistant ($r_{0f} = r_{f1}$) or if the diffusion coefficients are equal. This results in the following equation for the diffusion coefficient at a face:

$$\Gamma = \frac{2\Gamma_0\Gamma_1}{\Gamma_0 + \Gamma_1} \tag{3.10}$$

Fluent® provides four macros to change the UDS transport equation. These macro's alter the coloured parts in Eq.3.3. Each colour corresponds to a macro (or

UDF, User Defined Function). These UDF's, written in a C based programming language, are dynamically loaded in the Fluent® solver. The four macros and their definition are listed below.

DEFINE_UDS_UNSTEADY : Macro to adapt the unsteady term.

DEFINE_UDS_FLUX : Macro to adapt the convective flux.

DEFINE_DIFFUSIVITY : Macro to adapt the diffusion coefficient.

DEFINE_SOURCE : Macro to adapt the source term.

By using these macros any transport equation which is of the same form as Eq. 3.3 can be implemented into Fluent®. By adding conditional expressions to the macros, different zones (e.g. air and material zone) can have different transport equations for the same transported variable.

Time scales

Diffusion of moisture in a porous material and transport phenomena in air have a significant different time scale. Phenomena such as vortex shedding or other instabilities in the air mostly have a small time scale in the order of seconds or even less. Transport in a porous material on the other hand is slow, especially moisture transport. A wet material can take days to dry out and moisture accumulation by diffusion only becomes relevant after longer periods. In hygrothermal studies, the effect of moisture is often evaluated for periods of days, weeks or even years. This wide range of time scales introduces some modelling limitations. It is not possible to model a whole week, let alone a year, with time steps corresponding with the time scales in air. This would lead to a lot of time steps and a long computational time.
However the transient hygrothermal behaviour of a system of air in contact with a porous material is dominated by the porous material. For example vapour diffusion through a porous material is much slower than in air. As a result the air response can be described as quasi steady state [58]. This implies that the time steps can be chosen to correspond with the characteristic time scales in the porous material. Since the same solver is used for both air and porous material, transport in both media are solved with the same time step. Because the time step is larger than the characteristic time scale in air, the air is modelled as steady within that time step. This does not imply that the air can not undergo transient behaviour. Changes in the boundary conditions of air, due to changes in the porous material at the air-material interface (temperature, moisture concentration) still affect the transport in air. However phenomena at a small time scale (vortex shedding, unsteady flow behaviour) are not modelled.

General solver settings in CFD

Similar to the work of Steeman [1] a double precision pressure based segregated solver is used to solve the transport equations. Double precision implies that numbers are stored with a higher amount of precision. This reduces the round off error and is therefore retained here.
To solve the momentum equations (Eq. 2.11) the pressure field and mass fluxes have to be known. However, these are not known in advance and have to be obtained as part of the solution. This is accomplished by using a pressure-velocity coupling algorithm. A pressure correction equation is solved so that both the continuity and momentum equation are satisfied. For this work the SIMPLE scheme is used. More details on pressure-velocity coupling are found in [57].
In Fluent® two pressure based solvers are available: segregated and coupled. The coupled solver solves the continuity and momentum equation in a coupled way i.e. simultaneously as a set of equations. Energy, species, turbulence and other transport equations are solved subsequently and sequentially. In the segregated solver all equations are solved subsequently. The coupled solver generally needs more computational time for each iteration but converges faster. However for this work the segregated solver is retained since *User Defined Functions* can only be implemented in the segregated solver.

3.2 Coupled CFD-HAM model for vapour transport

Steeman [1] developed a coupled CFD-HAM model capable of solving the heat and vapour transport in air and porous materials. In section 3.1 it was already highlighted how it is possible to use *User Defined Functions* to implement a transport equation in Fluent®. In this section a more detailed discussion on the implementation of the transport equations Eqs. 2.24, 2.37, 2.44 and 2.49 is held when only vapour transport is present. The assumption that moisture is only transported by vapour diffusion simplifies the model considerably and allows a direct coupling of the heat and mass transport in the air and porous material. It will be shown later on (section 3.3) that this direct coupling is no longer possible if liquid transport is also considered.

3.2.1 Heat and moisture transport in air

The heat and moisture transport equations in air were derived in section 2.2. These equations can now be reformulated in the appropriate form and discretized. As already mentioned this involves a discretization of space and time. Within each time step several iterations are needed before convergence is reached.
The discretized equations are actually solved for the unknown variable $\phi^{t+\Delta t,m+1}$,

where $t + \Delta t$ refers to the value at the next time step and $m + 1$ is the value at the next iteration within the time step. If convergence is reached, $\phi^{\Delta t+t,m}$ is approximately equal to $\phi^{t+\Delta t,m+1}$ and $\phi^{t+\Delta t,m+1} = \phi^{t+\Delta t}$. This leads to the following equations for moisture and heat transport in the air:

$$\frac{\rho^{t+\Delta t,m}Y^{t+\Delta t,m+1} - \rho^{t}Y^{t}}{\Delta t}V + \sum_f \left(\rho_f \vec{v}_f\right)^{t+\Delta t,m} Y_f^{t+\Delta t,m+1} \cdot \vec{A}_f = \sum_f \left(\rho_f D_f\right)^{t+\Delta t,m} \nabla Y^{t+\Delta t,m+1} \cdot \vec{A}_f \quad (3.11)$$

$$\frac{\left(\rho C\right)^{t+\Delta t,m} T^{t+\Delta t,m+1} - \left(\rho C\right)^{t} T^{t}}{\Delta t}V + \sum_f \left(\left(\rho_f \vec{v}_f C_f\right) + \left(C_v - C_a\right)\vec{g}_f\right)^{t+\Delta t,m} T_f^{t+\Delta t,m+1} \cdot \vec{A}_f = \sum_f \lambda_{eff}^{t+\Delta t,m} \nabla T^{t+\Delta t,m+1} \cdot \vec{A}_f \quad (3.12)$$

The colours used in Eqs. 3.11 and 3.12 refer to the macros listed in section 3.1. The discretized form of Eq. 2.24 is quite straightforward and results from implicit time stepping. The coefficients in the equation, often function of time, space, temperature and/or humidity, are evaluated at iteration m, hence the superscript m.

The discretized form of the heat transport in air (Eq. 3.12) involves a rearrangement of some terms. The sensible heat transported along with the diffusion of water vapour in air is treated as a convection term and moved to the right hand side of Eq. 3.12 although it is in fact heat transport due to (vapour) diffusion. This can mathematically be justified since this therm is the divergence of a vector ($\vec{g}$) multiplied with the temperature T and a coefficient ($C_v - C_a$).

3.2.2 Heat and moisture transport in the porous material

If only vapour transport is considered in the porous material, the liquid flux $\vec{g}_l$ is zero and Eq. 2.43 simplifies to:

$$\frac{dw}{dt} = \nabla \cdot \left(\rho \frac{D_{va}}{\mu} \nabla Y\right) \quad (3.13)$$

This transport equation can now be transformed to hold the same transported variables as in air: Y and T.

$$\frac{\partial w}{\partial RH}\frac{\partial RH}{\partial Y}\frac{\partial Y}{\partial t} + \frac{\partial w}{\partial RH}\frac{\partial RH}{\partial T}\frac{\partial T}{\partial t} = \nabla \cdot \left(\rho \frac{D_{va}}{\mu} \nabla Y\right) \quad (3.14)$$

In case of isothermal transport the time derivative term can be discretized to:

$$\frac{dw}{dt} \rightarrow \left(\frac{\partial w}{\partial RH}\frac{\partial RH}{\partial Y}\right)^{t+\Delta t,m} \frac{Y^{t+\Delta t,m+1} - Y^{t}}{\Delta t} \tag{3.15}$$

However this approach can lead to large mass conservation problems as reported in literature by several authors [59–61] because of the strong non-linearity of the moisture capacity. Therefore Janssen [62] suggested to use Celia's approach [60] to discretize the time derivative. Celia suggested to use a mixed formulation of the mass transport equation where the time derivative would be discretized as

$$\frac{\partial w}{\partial t} \rightarrow \frac{w^{t+\Delta t,m+1} - w^{t}}{\Delta t} \tag{3.16}$$

Using a truncated Taylor expansion for $w^{t+\Delta t,m+1}$, Eq. 3.16 can be estimated by:

$$\frac{\partial w}{\partial t} \rightarrow \underbrace{\left(\frac{\partial w}{\partial RH}\frac{\partial RH}{\partial Y}\right)^{t+\Delta t,m} \frac{Y^{t+\Delta t,m+1} - Y^{t+\Delta t,m}}{\Delta t}}_{A} + \underbrace{\frac{w^{t+\Delta t,m} - w^{t}}{\Delta t}}_{B} \tag{3.17}$$

Figure 3.2 illustrates the difference between the mixed approach by Janssen [62] and the direct approach as formulated in Eq. 3.15. Part A and B in Eq. 3.17 are also indicated in Figure 3.2. The figure shows that using the direct approach (Eq. 3.15) results in a significant error on the mass storage while the mixed approach is mass conservative.

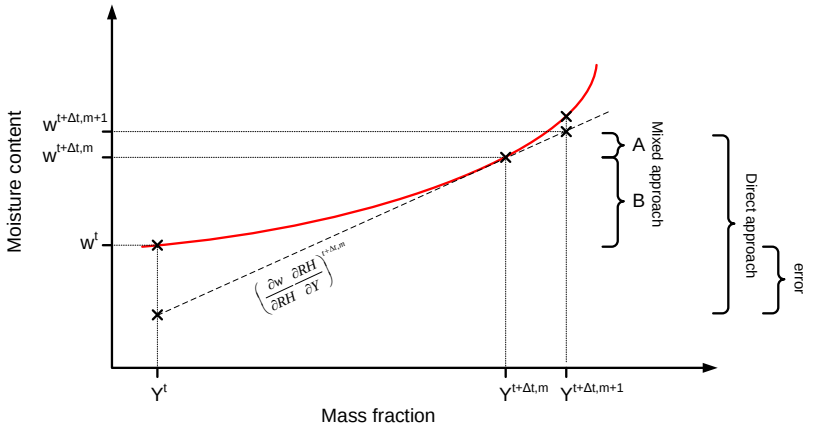

Figure 3.2: Illustration of the difference between the mixed approach and the direct approach based on Janssen [62].

The transport equation for vapour transport (Eq. 3.14) can now be discretized as:

$$\left(\frac{\partial w}{\partial RH}\frac{\partial RH}{\partial Y}\right)^{t+\Delta t,m}\frac{Y^{t+\Delta t,m+1}-Y^{t+\Delta t,m}}{\Delta t}V+\frac{w^{t+\Delta t,m}-w^{t}}{\Delta t}V = \sum_f\left(\left(\rho\frac{D_{va}}{\mu}\right)_f^{t+\Delta t,m}\nabla Y^{t+\Delta t,m+1}\cdot\vec{A}_f\right) \quad (3.18)$$

In the non-isothermal vapour tansport equation (Eq. 3.14) there were originally two time derivative terms, one for mass fraction change in time and one for temperature change in time. A Taylor series expansion of the dw/dt would result in:

$$\frac{\partial w}{\partial t} \rightarrow \left(\frac{\partial w}{\partial RH}\frac{\partial RH}{\partial Y}\right)^{t+\Delta t,m}\frac{Y^{t+\Delta t,m+1}-Y^{t+\Delta t,m}}{\Delta t} + \left(\frac{\partial w}{\partial RH}\frac{\partial RH}{\partial T}\right)^{t+\Delta t,m}\frac{T^{t+\Delta t,m+1}-T^{t+\Delta t,m}}{\Delta t} + \frac{w^{t+\Delta t,m}-w^{t}}{\Delta t} \quad (3.19)$$

However, since in this work a segregated solver is used, temperature and mass fraction have to be solved sequentially in separate equations. Eq. 3.14 can be used to solve for the mass fraction but then the temperature difference with the unknown temperature $T^{t+\Delta t,m+1}$ in Eq. 3.19 has to be cancelled out. However the main effect of temperature change on moisture storage is still captured by $w^{t+\Delta t,m}-w^{t}$.

The energy transport equation (Eq. 2.49) will also be discretized using the conservation principle applied to the moisture transport equation. Here the conserved property is the total energy $E\ [J/m^3]$. Since only vapour tranport is considered in this section, $\vec{g}_l C_l T$ can be left out in Eq. 2.49.
The time derivative of the total energy, $\partial E/\partial t$, can thus be discretized to:

$$\frac{\partial E}{\partial t} \rightarrow (\rho_{mat}C)^{t+\Delta t,m}\frac{T^{t+\Delta t,m+1}-T^{t+\Delta t,m}}{\Delta t}V + \frac{E^{t+\Delta t,m}-E^{t}}{\Delta t}V \quad (3.20)$$

where C is given by

$$C = C_{mat} + \frac{C_l w_l}{\rho_{mat}} + \frac{C_v w_v}{\rho_{mat}} \quad (3.21)$$

Steeman [1] added two extra terms to this expression to speed up convergence,

namely:

$$(C_l T)^{t+\Delta t,m} \frac{w_l^{t+\Delta t,m+1} - w_l^{t+\Delta t,m}}{\Delta t} V \tag{3.22}$$

$$(C_v T + L)^{t+\Delta t,m} \frac{w_v^{t+\Delta t,m+1} - w_v^{t+\Delta t,m}}{\Delta t} V \tag{3.23}$$

In these two extra terms the vapour and liquid moisture content $w_l^{t+\Delta t,m+1}$ and $w_v^{t+\Delta t,m+1}$ are calculated by taking the temperature at the previous iteration m but the mass fraction at the current iteration $m+1$. This is possible since the equations are solved sequentially and the moisture transport equation is solved before the energy equation.
The enthalpy transported along with the diffusion of water vapour in the porous material, $\nabla \cdot ((C_v T + L)\,\vec{g_v})$, contains two parts: a sensible heat part and a latent heat part. Similar to the transport of energy in air (Eq. 3.12) the sensible heat can again be treated as a *convective term* although it is of course diffusive transport. Since Eq. 2.39c states that $\frac{dw}{dt} = -\nabla \cdot \vec{g_v}$ when $\vec{g_l} = 0$, the latent heat accompanying the vapour diffusion, $-\nabla \cdot (L\vec{g_v})$, can be written as $L\frac{dw}{dt}$, assuming that the latent heat of water vapour L is constant.
Rearranging the terms in the appropriate order and applying the colour code as defined in section 3.1, the energy transport equation can be discretized as:

$$\begin{aligned}
&(\rho_{mat} C)^{t+\Delta t,m} \frac{T^{t+\Delta t,m+1} - T^{t+\Delta t,m}}{\Delta t} V + \frac{E^{t+\Delta t,m} - E^{t}}{\Delta t} V \\
&\quad + \sum_f (C_v \vec{g_{vf}})^{t+\Delta t,m} T_f^{t+\Delta t,m+1} \cdot \vec{A_f} \\
&\quad = \sum_f \lambda_{mat}^{t+\Delta t,m} \nabla T^{t+\Delta t,m+1} \cdot \vec{A_f} \\
&+ L \left(\left(\frac{\partial w}{\partial RH} \frac{\partial RH}{\partial Y} \right)^{t+\Delta t,m} \frac{Y^{t+\Delta t,m+1} - Y^{t+\Delta t,m}}{\Delta t} V + \frac{w^{t+\Delta t,m} - w^{t}}{\Delta t} V \right) \\
&\quad - (C_l T)^{t+\Delta t,m} \frac{w_l^{t+\Delta t,m+1} - w_l^{t+\Delta t,m}}{\Delta t} V \\
&\quad - (C_v T + L)^{t+\Delta t,m} \frac{w_v^{t+\Delta t,m+1} - w_v^{t+\Delta t,m}}{\Delta t} V
\end{aligned} \tag{3.24}$$

With E the total energy given by Eq. 3.25 and C given by Eq. 3.21.

$$E = \rho_{mat} C_{mat} T + w_l C_l T + w_v \left(C_v T + L\right) \tag{3.25}$$

Turbulence

In the model for vapour transport only, the interface between air and porous material is not recognized as a wall. If turbulence in the air is to be modelled a

LRN RANS model (k-ω) is added. Whit this model it is possible to implement the correct boundary conditions for ω at the interface since according to Menter [63] the values for ω at the wall are given by:

$$\omega = \frac{6\nu}{\beta_1 y_p^2} \tag{3.26}$$

With nu the kinematic viscosity, y_p the distance between the interface and the centre of the first cell and $\beta_1 = 0.075$.

Discussion

The model discussed here is only valid for vapour transport. The implementation of this model was first developed by Steeman [1]. The vapour transport equation (Eq. 3.14) can be expressed with mass fraction Y as the transported variable. This approach allows a direct implementation of the transport equations into an existing CFD program. Although the equations are different for the material zone and the air, the set of equations can still be solved in one iteration and there is no need to pass boundary conditions from one zone to the other. This is a great advantage compared to externally coupled CFD-HAM models (e.g. [25, 43, 64]). There is no need to iterate between different programs.
Fluent® allows this direct implementation. The transport equations are programmed as UDS-transport equations (Eq. 3.3), one for heat and one for moisture. For each transport equation four terms were determined indicated by the four colours defined in section 3.1. These terms were programmed using the corresponding UDF's. The computational grid was divided into two zones: an air zone and a porous material zone. An *IF*-condition was implemented into each UDF, forcing the transport equations for air to be solved in the air-zone and the equations for material in the porous material zone. Fluent® can thus determine where to use which equation.

In the next section it will however be shown that using mass fraction as the transported variable is only possible when liquid transport is neglected. If liquid transport is added to the model, a different modelling approach is needed.

3.3 Coupled CFD-HAM model including liquid moisture transport

In the previous section the CFD-HAM model originally developed by Steeman [1] was discussed. Steeman [1] confined his modelling to porous materials facing the indoor air. He stated that it was sufficient to describe the moisture transport in porous materials as equivalent vapour transport, since vapour transport is dominant

over liquid moisture transport in the range of relative humidities encountered in the indoor environment. By introducing this assumption, a number of moisture related damage phenomena are excluded. It is the objective of the current work to extend the model so that other moisture related (damage) phenomena can be studied where liquid moisture transport becomes important such as drying phenomena and interstitial condensation. Therefore the model of Steeman [1] has to be extended to include liquid moisture transport.
In this section the numerical implementation of this extended model is highlighted. First it is shown that a different transported variable is needed in the porous model to adequately solve the moisture transport in a porous material. The capillary pressure is therefore introduced. Next the coupling procedure between air and porous material is discussed and the advantages and limitations of the new model are indicated.

3.3.1 Mass fraction or capillary pressure?

By using mass fraction as transported variable in the moisture transport equation for both air and porous material, Steeman [1] could implement these equations in the same solver without the need for a special coupling procedure. This is of course a great benefit. It would therefore be nice if the same approach could be retained when liquid transport is added to the model. However using mass fraction as transported variable in a porous material when liquid transport is present causes some difficulties as will be discussed in this section.

Transforming Darcy's law Eq. 2.42 for liquid transport from capillary pressure p_c to mass fraction Y results in:

$$\vec{g}_l = -K_l \nabla p_c = -K_l \frac{\partial p_c}{\partial RH} \frac{\partial RH}{\partial Y} \nabla Y - K_l \frac{\partial p_c}{\partial T} \nabla T \tag{3.27a}$$

with

$$\frac{\partial p_c}{\partial RH} = \rho_l R_v \frac{T}{RH} \tag{3.27b}$$

$$\frac{\partial p_c}{\partial T} = \rho_l R_v \ln RH + \rho_l R_v \frac{T}{RH} \frac{\partial RH}{\partial T} \tag{3.27c}$$

It is thus mathematically possible to write Eq. 2.44 with mass fraction and temperature as the transported variables instead of capillary pressure and temperature. Difficulties in solving this model arise however when relative humidity near to 100% is encountered. This high relative humidity is typical when liquid moisture transport is present. Figure 3.3 illustrates what happens when the mass fraction is near to the saturation mass fraction. This figure shows a psychrometric chart with the mass fraction on the vertical axis and the temperature on the horizontal exis. The figure starts from a state below the saturation line

(situation ①). When the temperature is lowered, the mass fraction in the porous material is constant at first. The state of the porous material moves along a horizontal line from situation ① to situation ②. In situation ② the saturation mass fraction is reached. At temperature T_2 the air in the porous material can not hold more water vapour than Y_2. If the temperature would drop further to T_3, the mass fraction of water vapour in air is obliged to follow the saturation line. This implies that at saturation the mass fraction becomes temperature dependent. However for a good numerically solvable model, the transported variables should be independent.

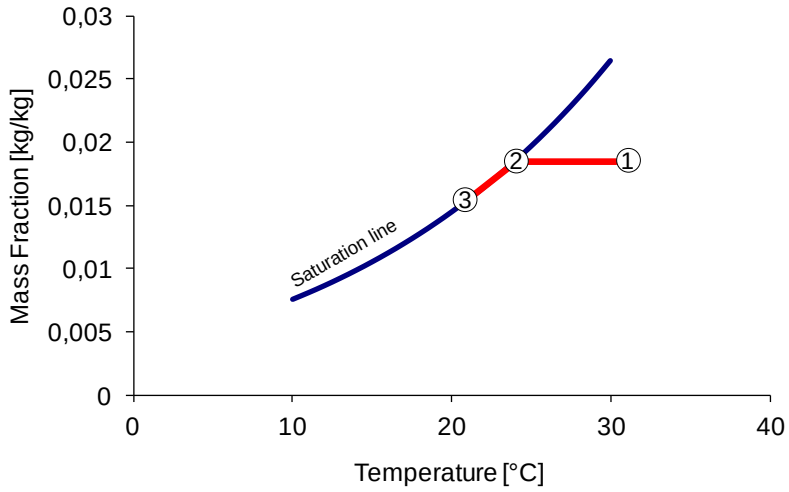

Figure 3.3: Psychrometric chart, saturation mass fraction indicated in blue

As long as the relative humidity stays well below saturation, the state of the porous material can be described by the mass fraction Y. This is the case when only vapour transport is considered and when temperature changes are small. Steeman [1] confined his work to these conditions and was thus able to use mass fraction and temperature as transported variables for moisture and energy respectively.
Using mass fraction as transported variable is also allowed for isothermal liquid transport in porous materials. However in the processes discussed and studied in this work, the assumption of isothermal conditions rarely holds. As an example the drying of a nearly saturated porous material is discussed. A more thorough discussion of drying and drying phenomena is given in chapter 5.

A wet material that is nearly saturated will have a mass fraction of water vapour close to saturation and the relative humidity in the material will be almost 100%. During a convective drying process, water evaporates from the surface into the dry air flowing over the porous material. For this energy is needed since water is transformed from the liquid state to the vapour state. The amount of energy needed for this phase change is the latent heat of evaporation. This energy is taken from the surrounding air and porous material, thus resulting in a temperature drop of the material. When no other heat sources are present the temperature of the porous material surface can drop to the wet bulb temperature. This temperature drop can be significant (e.g. air at 30 °C and 40%RH has a wet bulb temperature of ±20°C). Since the mass fraction was already near saturation, a sudden drop in the temperature would mean that the mass fraction would also have to decrease. In other words the mass fraction becomes temperature dependent. The mass fraction approach proposed by Steeman [1] is thus no longer applicable for liquid tranport phenomena such as convective drying.

From this discussion it is clear that a new approach is needed if liquid transport phenomena are to be included. Therefore the capillary pressure is proposed as the transported variable. The capillary pressure is not restricted by saturation conditions and is a better way to describe the state of a wet (nearly saturated) porous material. As shown by Eq. 2.8 the capillary pressure is 0 at saturation (RH = 100%) and goes to $-\infty$ when the material is completely dry (RH = 0%).

3.3.2 Implementation of the heat and moisture transport equation

As stated in the previous section, a formulation with a transported variable in the porous material other than the mass fraction is needed in order to solve moisture transport problems including liquid transport. Künzel [29] solved this by using the relative humidity as moisture transport potential, Janssen [65] used the matric water head. Both are related to the capillary pressure. The relative humidity is related to the capillary pressure by Kelvin's law (Eq. 2.8), the matric head ψ $[m]$ is related to the capillary pressure by Eq. 3.28 where g is the gravitational acceleration. Using capillary pressure, matric head or relative humidity is thus equivalent as long as the appropriate conversion is used. Since capillary pressure can be considered as an actual driving potential of liquid moisture transport, it will be used in this work.

$$\psi \rho_l g = p_c \tag{3.28}$$

Using capillary pressure as moisture potential is only possible in the porous material. The potential for vapour transport in the air is still the mass fraction.

This results in a model where mass fraction is used as vapour transport potential in air and capillary pressure as moisture transport potential in the porous material. Temperature can be used in both the air and the porous material as energy potential. This approach forces a reformulation of the discretized transport equations in the porous material (Eqs. 3.24 and 3.18). The transport equations for energy and moisture in the air can be retained (Eqs. 3.12 and 3.11).

In section 3.2 the discretized form of the transport equations when only vapour transport is considered, were derived. The conservative modelling principle for the time derivative term will also be applied for the discritization of Eq. 2.44. Discretizing this equation yields:

$$\begin{aligned}\left(\frac{\partial w}{\partial p_c}\right)^{t+\Delta t,m} & \frac{p_c^{t+\Delta t,m+1}-p_c^{t+\Delta t,m}}{\Delta t}V+\frac{w^{t+\Delta t,m}-w^{t}}{\Delta t}V \\ &= \sum_f \left(K_l+\frac{D_{va}}{\mu R_v T}\frac{\rho_v}{\rho_l}\right)^{t+\Delta t,m}\nabla p_c^{t+\Delta t,m+1}\cdot\vec{A}_f \\ &+\sum_f \frac{D_{va}}{\mu R_v T}\left(RH\frac{\partial p_{sat}}{\partial T}-\frac{p_v \ln RH}{T}\right)^{t+\Delta t,m}\nabla T^{t+\Delta t,m}\cdot\vec{A}_f \end{aligned} \quad (3.29)$$

Again the equation is arranged so that the time derivative term (red), the diffusive term (green) and the source terms (yellow) can be identified. Thess terms are implemented in the appropriate UDF's.

The energy transport equation Eq. 2.49 includes the sensible heat transported along with the liquid moisture transport. The resulting discretized form is similar to Eq. 3.24. However the source term added to Eq. 3.24 to incorporate the latent heat effect takes a different form since $\frac{\partial w}{\partial t} = -\nabla\cdot\vec{g}_v$ no longer holds.

$$\begin{aligned}(\rho_{mat}C)^{t+\Delta t,m} & \frac{T^{t+\Delta t,m+1}-T^{t+\Delta t,m}}{\Delta t}V+\frac{E^{t+\Delta t,m}-E^{t}}{\Delta t}V \\ &+\sum_f (C_v\vec{g_v}_f+C_l\vec{g_l}_f)^{t+\Delta t,m}T_f^{t+\Delta t,m+1}\cdot\vec{A}_f \\ =\sum_f \lambda_{mat}^{t+\Delta t,m}\nabla T^{t+\Delta t,m+1}\cdot\vec{A}_f &+\sum_f (L\vec{g_v})^{t+\Delta t,m}\cdot\vec{A}_f \\ &-(C_lT)^{t+\Delta t,m}\frac{w_l^{t+\Delta t,m+1}-w_l^{t+\Delta t,m}}{\Delta t}V \\ &-(C_vT+L)^{t+\Delta t,m}\frac{w_v^{t+\Delta t,m+1}-w_v^{t+\Delta t,m}}{\Delta t}V \end{aligned} \quad (3.30)$$

With E the total energy given by Eq. 3.25 and C given by Eq. 3.21. Similar to Eq. 3.24 the conservative modelling principle is used for the time derivative term

and the two last terms on the right hand side of Eq. 3.30 were added to improve convergence. The terms concerning the sensible heat transported along with the diffusion of water vapour and the transport of liquid water ($C_v\vec{g}_v T$ and $C_l\vec{g}_l T$) were again treated as convective terms and moved to the left hand side, although they are in reality heat transport terms due to diffusion.
The latent heat effect is incorporated by the term $\sum_f \left(L\vec{g_v}\right)^{t+\Delta t,m} \cdot \vec{A}_f$. When only vapour transport is considered, it is possible to transform this term in a computationally more favourable manner. If no liquid transport is present, all changes in moisture content are due to vapour diffusion. The effect of latent heat transport by vapour diffusion can then be directly implemented by using the calculated increase in moisture content. If liquid transport is also considered, moisture content changes are no longer only due to vapour diffusion. The calculation of the latent heat term then requires the calculation of the vapour flux through all the faces of a cell and the summation of these fluxes. This procedure is computationally more expensive, but unavoidable here.

A direct coupling of the heat and moisture transport equation in air and material in the same solver is no longer possible, since for moisture two different transport variables, namely mass fraction and capillary pressure, are used. Still a single solver can be used to solve the transport in air and porous material. However, a special procedure has to be implemented to handle the boundary conditions and pass information from the material to the air side and vice versa. This is discussed in more detail in the next section.

3.3.3 Coupling procedure and boundary conditions

Since a different transported variable is used for the moisture transport in air and porous material, a coupling procedure for the boundary conditions is needed between the air and the material zone. Four continuity conditions have to be fulfilled when the air and material zone are coupled.

- **Continuity of temperature at the boundary**: the temperature at the air side boundary T_{sa} should equal the temperature at the material side boundary T_{sm}. ($T_{sm} = T_{sa} = T_s$)
- **Continuity of the heat flux at the boundary**: Heat conduction in the porous material to the surface equals the convective heat leaving the surface.
- **Continuity of mass fraction of water vapour in the air at the boundary**: The mass fraction of water vapour at the material side of the air-material interface Y_{sm} equals the mass fraction at the air side Y_{sa}. ($Y_{sa} = Y_{sm} = Y_s$)
- **Continuity of moisture flux at the boundary**.

As already mentioned earlier a segregated solver is used. This means that each transport equation is solved separately and sequentially. The solver solution procedure is schematically presented in Figure 3.4. Before the simulation is started the necessary boundary conditions (inlet, outlet, wall conditions,...) are initialized together with the initial conditions of all the model variables. If a transient simulation is performed, the solver moves to the next time step as soon as convergence is attained within a time step. Before each iteration in a time step the DEFINE_ADJUST macro is executed. This macro is used to update some user defined properties which are function of the user defined scalars. These updated properties are necessary to solve the user defined transport equations. Examples of properties derived from the user defined scalars are relative humidity, moisture content, heat and moisture fluxes etc. An iteration within a time step starts with solving the momentum equation. Next the continuity equation in the air is solved and then the turbulence equations are solved if necessary. These equations are all standardly implemented in Fluent®.
Next the four user defined scalar equations are solved sequentially. First the vapour transport equation in the air, next the moisture transport equation in the porous material, then the energy equation in the air and finally the energy equation in the material. This results in values for mass fraction Y, capillary pressure p_c, air temperature T_a and material temperature T_m for each cell in the computational domain.
At the end of an iteration within a time step, Fluent® updates some of the air and material properties. At the end of an iteration convergence is checked. If the solution is not converged, the iterations continue till the maximum number of iterations (defined by the user) is attained or until the convergence criteria are reached.

Figure 3.5 illustrates the general coupling procedure applied in this work which fulfils the four continuity conditions for the boundary values and fluxes. First all the zones in the solver domain are initialised (the appropriate boundary profiles and initial values are implemented).
The segregated solver first solves the vapour transport in the air. To solve this vapour transport the air-material interface conditions at the air side have to be known. These values can be taken from the initial condition of the material. Here the initial state of the porous material is given by p_{c-init} and T_{m-init}. From these two values the mass fraction at the boundary of the porous material can be determined using Kelvin's law (Eq. 2.8) to transform the capillary pressure to the relative humidity at the surface. From the relative humidity and the temperature the mass fraction at the surface can be determined since the relative humidity is function of the vapour pressure (Eq. 2.2) and the vapour pressure in turn can be related to the mass fraction by Eq. 3.31.

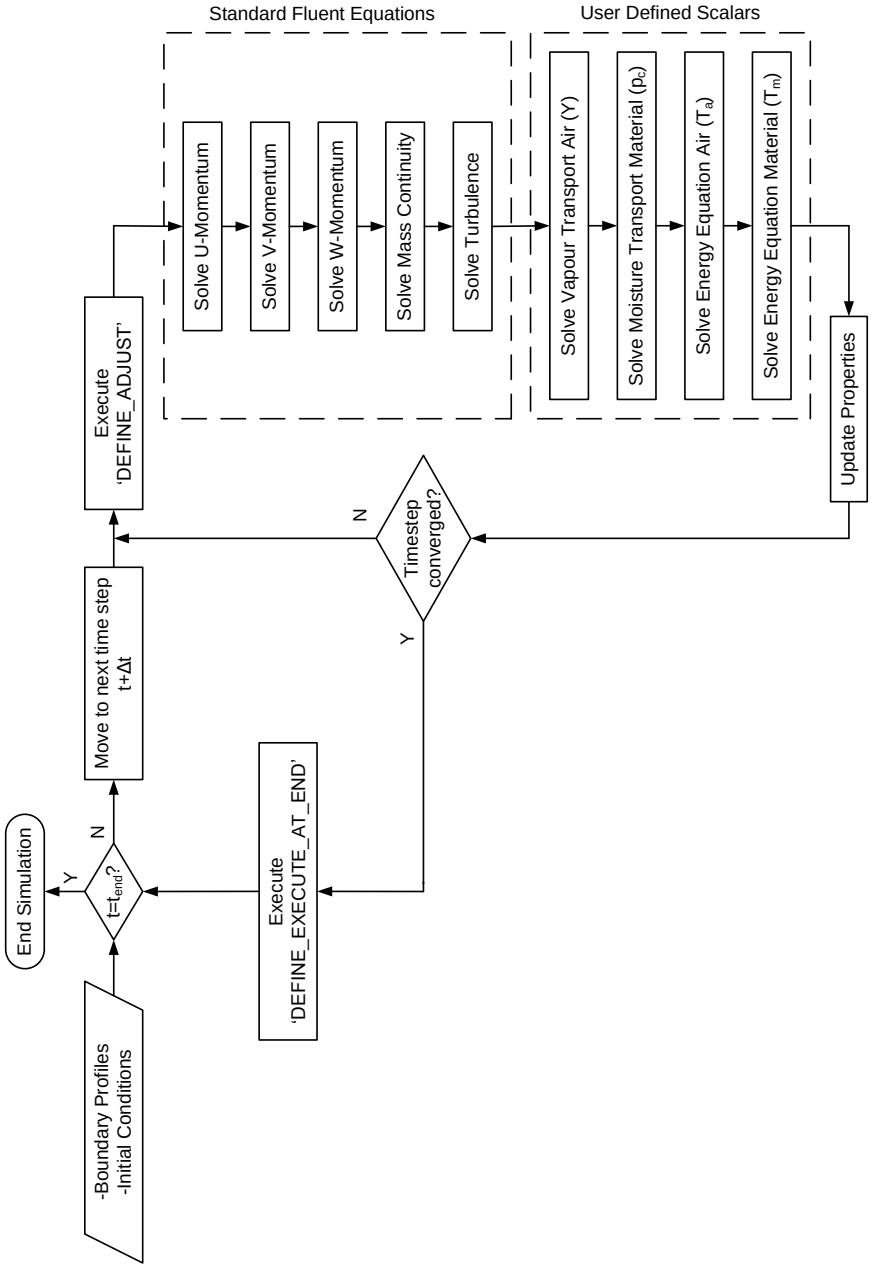

Figure 3.4: Solution procedure for segregated transient solver

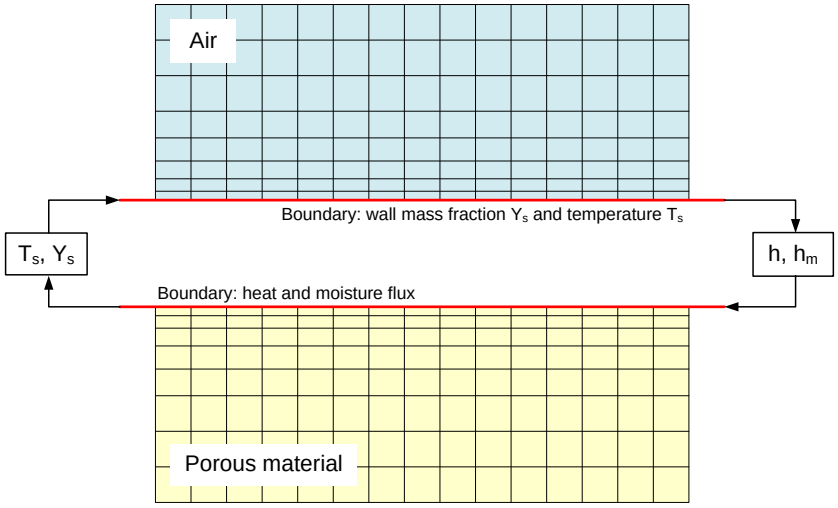

Figure 3.5: Schematic representation of the boundary conditions in the coupled CFD-HAM model

$$Y = \frac{p_v R_a}{R_v p_{atm} - R_v p_v + R_a p_v} \tag{3.31}$$

This calculated mass fraction at the material side (Y_{sm}) is then passed to the air side and used as a boundary condition for the calculation of the mass fraction in the air.

Next the moisture transport in the porous material is solved. Here the moisture flux from the porous material surface to the air is used as the boundary condition. The flux of water vapour from the porous material to the air is described by the Fickian diffusion law (Eq. 2.21). This equation can be discretized and used to determine the flux at the material surface. The discretization of Fick's law is illustrated in Figure 3.6. This figure shows a detail of a grid with two neighbouring cells, one at the air side $C0_a$ and one at the material side $C0_m$. The distance from the air-material interface to the air cell centre is given by dr_a, while the distance from the interface to the material cell centre is given by dr_m. Discretizing Eq. 2.21 results in:

$$g_v = \rho D_{va} \frac{Y_{C0_a} - Y_f}{dr_a} \tag{3.32}$$

In this equation Y_{C0_a} is the value of the mass fraction in the first air cell next to a material cell, Y_f is the mass fraction at the air-material interface.

The third UDS equation that is solved is the energy equation in the air. Similar to the vapour transport equation, the boundary values for temperature at the

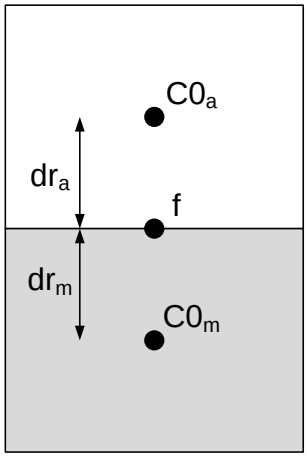

Figure 3.6: Detail of two neighbouring cells, one at the material side $C0_m$ and one at the air side $C0_a$.

air-material interface have to be known. Figure 3.5 shows how the calculated temperature at the material side is passed to the air side and used there as a boundary condition. This ensures the continuity of temperature at the interface.
Finally the energy equation in the material is solved. Here again a flux condition is used at the boundary. Discretizing Fourier's law at the material surface gives:

$$q = \lambda \frac{T_{C0_a} - T_f}{dr_a} \tag{3.33}$$

A similar coupling approach as described above was also used by Defraeye [43]. However Defraeye used two different solvers, one to solve the transport in the porous material (HAMFEM [62], a finite element based program) and one to solve the transport in the air (Fluent 6.3 [38], a finite volume based program). For the coupling between the two programs he used an explicit coupling procedure. The exchange of data between both solvers is only performed once every time step. First the CFD program is executed for one time step. Next the boundary conditions are transferred to the HAM program (heat and moisture fluxes). The HAM program is then executed for the same time step with the new boundary conditions. When this time step is calculated, boundary conditions (temperature and mass fraction) are transferred from the HAM program to the CFD program and the next time step is calculated. Defraeye reported that this explicit approach is only justified if sufficiently small time steps are used so the actual fluxes do not change significantly over the time step. His conjugate model was also limited to 2D or simple 3D problems since the HAMFEM program did not allow a high number of finite elements.

The explicit implementation proposed by Defraeye [43] is computationally expensive due to the small time steps that are required. Defraeye reported time steps of $0.1s$ or smaller. Even when an adaptive time stepping method was implemented, computational time was still considerably long.
The small time steps are needed to guarantee solver stability. An explicit coupling of air and material implies that the fluxes imposed on the material surface are fixed since they were determined from a previous iteration. However, in reality the fluxes at the surface are function of the temperature and moisture values at the surface. Since the fluxes remain constant during a time step, this could lead to an overestimation of these fluxes and cause divergence of the solution. Using an implicit solver method could overcome some of these problems. An implicit solution method has the advantage of being more stable and allows larger time steps to be used.
Therefore an adapted coupling method is proposed in this work. To improve stability the fluxes are implemented implicitly. First the implementation of the heat flux is discussed in more detail. The heat flux at the material side is determined by Eq. 3.33. To calculate this heat flux the temperature in the centre of the boundary cell and the face temperature is needed. An explicit calculation of this boundary flux would yield:

$$q^m = \frac{\lambda}{dr_a}\left(T^m_{C0_a} - T^m_f\right) \tag{3.34}$$

Here m indicates the values at the previous iteration. The next iteration is indicated by $m+1$. An implicit implementation of the heat flux would mean that not q^m but q^{m+1} is introduced in the equation system. However in the segregated solver, the material zone and accompanying equations for heat and mass are solved separately from the air zone. It is thus not possible to introduce the cell value T_{C0_a} implicitly in the equation set for the material zone.
It is nevertheless possible to reformulate the boundary heat flux using Newton's law for convective heat transfer. Here the so-called transfer coefficients are introduced. Newton's cooling law states that the convective heat transfer from a surface is proportional to the temperature difference between the surface and a reference temperature T_{ref}:

$$q = -h\left(T_f - T_{ref}\right) \tag{3.35}$$

In this equation h is the convective heat transfer coefficient $[W/m^2K]$. The reference temperature T_{ref} that is used, can differ from case to case. For example the bulk flow temperature can be used or inlet condition, but also the temperature at a certain point in the flow could be used. It is important that once the reference temperature is defined, that this definition is kept during the entire simulation.

Therefore for each simulation it should be clearly stated what was used as a reference temperature.
It is now possible to determine the transfer coefficient as follows:

$$q = -h\left(T_f - T_{ref}\right) = \frac{\lambda}{dr_a}\left(T_{c0_a} - T_f\right) \longrightarrow h = -\frac{\lambda}{dr_a}\frac{T_{c0_a} - T_f}{T_f - T_{ref}} \tag{3.36}$$

This convection coefficient varies mainly due to flow variations. As mentioned in section 3.1 for most cases the air flow can be considered quasi-steady so the convective transfer coefficient can also be considered constant during (multiple) time steps. It is thus possible to formulate an implicit scheme for the boundary flux using the transfer coefficient calculated at the previous iteration. If the air flow only changes a little in time it is sufficient to update the transfer coefficient only once in a while. The implicit formulation of the heat flux then becomes:

$$q^{m+1} = h^m\left(T_{ref} - T_f^{m+1}\right) \tag{3.37}$$

For the moisture flux an analogue formulation can be found:

$$g_v^{m+1} = h_m^m\left(Y_{ref} - Y_f^{m+1}\right) \tag{3.38}$$

With h_m the convective moisture transfer coefficient $[kg/m^2 s]$. For the reference mass fraction Y_{ref} the same remarks can be formulated as for the reference temperature T_{ref}.
This equation uses mass fraction as the driving potential. However the moisture transport equation in the porous material uses the capillary pressure. The mass fraction at the boundary Y_f is a non linear function of the capillary pressure. Eq. 3.38 can however be linearized around Y_f^m.

$$\begin{aligned}
g_v^{m+1} &= h_m\left(Y_{ref} - Y_f^{m+1}\right) \\
&= h_m Y_{ref} - h_m Y_f^{m+1} \\
&= h_m Y_{ref} - h_m\left[\frac{p_{sat}}{\rho R_v T}\exp\left(\frac{p_c}{\rho_l R_v T}\right)\right]^{m+1} \\
&\approx h_m Y_{ref} - h_m\frac{p_{sat}}{\rho R_v T}\left[\frac{1}{\rho_l R_v T}\exp\left(\frac{p_c^m}{\rho_l R_v T}\right)p_c^{m+1}\right. \\
&\left. + \exp\left(\frac{p_c^m}{\rho_l R_v T}\right) - \frac{1}{\rho_l R_v T}\exp\left(\frac{p_c^m}{\rho_l R_v T}\right)p_c^m\right]
\end{aligned} \tag{3.39}$$

In the implicit formulation of the boundary heat and moisture fluxes the unknown face values T_f and p_{cf} appear. The finite volume method implemented in Fluent® however solves for the values of the cell centres. The face values thus have to be reformulated as a function of the cell centre values. Fluent® normally uses a second order discretization to determine the face values as a function of

the neighbouring cell values (Eq. 3.4). When using UDS-equations Fluent® does not allow a straightforward implementation of this second order discretization. Implementing the implicit face boundary conditions is limited to first order. The face value is assumed equal to the adjacent cell value. This is justifiable if the grid near the boundary is fine enough.

There are different solution procedures possible depending on the nature of the problem. These different procedures can be controlled by using the 'DEFINE_EXECUTE_AT_END' macro and 'DEFINE_ADJUST' macro. The 'DEFINE_EXECUTE_AT_END' macro is executed at the end of each time step or at the end of the simulation in case of a steady simulation. The 'DEFINE_ADJUST' macro is executed at the start of each iteration. Different variation of the solution procedure can be thought out based on how often the boundary condition are updated.
In the simplest case the air flow can be considered (quasi-)steady. It is then often sufficient to determine the heat and moisture transfer coefficients once and hold these value during the rest of the transient simulation. The transfer coefficients can then for example be determined by performing a steady state simulation of the air flow, assuming constant temperature and mass fraction at the material side.
The transfer coefficients could also be updated every few time steps. This could for example be necessary if the air flow boundary conditions change significantly during the simulation. Updating the convection coefficients regularly however reduces simulation stability if the changes in the transfer coefficients are to large. Therefore extra conditions can be applied to the calculated transfer coefficients, e.g. limiting the change in transfer coefficients between two subsequent iterations to 10%.
In chapter 5 and 6 the effect of transfer coefficients and boundary conditions on the modelling outcome will be studied in more detail.

3.4 Model verification

The vapour transport model developed by Steeman [1] is already extensively and succesfully verified. In this section the verification of the newly developed model which includes liquid moisture transport will be discussed. The vapour transport model is verified and the implementation of the boundary conditions is checked for an adiabatic saturation process. Finally the liquid transport model is verified by performing an inter model comparison. A validation of the model is discussed in chapter 5.

3.4.1 Verification of vapour transport

Milly [66] presented an analytical solution to a vapour transport problem. This solution is used here for the verification of the vapour transport model. The same case was also used with success by Janssen [62], Steeman et al. [67] and Steeman et al. [21].
The considered test case of Milly (schematically shown in Figure 3.7) represents the one dimensional, coupled diffusion of heat and water vapour in a 10 cm high porous material. Initially the temperature in the material is 20°C and the relative humidity is 23.87%. A step change is imposed at the top of the material: the relative humidity changes to 27.59% while the temperature at the top is maintained at 20°C. This causes water vapour to diffuse into the porous material and leads to a varying temperature inside the material (due to latent heat release). The bottom of the material is considered to be vapour tight and adiabatic.

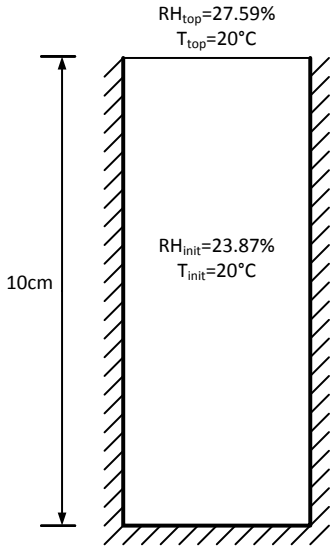

Figure 3.7: Schematic representation of the verification case proposed by Milly [66]

To obtain an analytical solution for this test case the following assumptions have to be made:

- The transfer of sensible heat by vapour diffusion and the storage of sensible heat in the liquid water and the water vapour are negligible.

- The perturbations in temperature and vapour density are so small that the relation between the moisture content and the relative humidity can be considered linear around the initial state with all other material properties considered constant.

If these assumptions are valid the analytical solution developed by Cranck [68] can be used to describe the coupled heat and water vapour diffusion. The following material properties are used: the sorption isotherm is assumed linear w = $4.615RH$ + $74.261kg/m^3$; the vapour diffusion coefficient is assumed constant D/μ = $4.37e-6m^2/s$; the volumetric heat capacity is $C\rho_{mat}$ = $2e6J/m^3K$; the material heat conductivity is λ_{mat} = $1.5W/mK$; the porosity is ψ = 0.344; the latent heat L is taken as $2.45e6J/kg$. Note that a high heat capacity is chosen to guarantee small changes in temperature and hence assure the linear nature of the transport equations.
A grid of 600 by 20 cells was used and a time step of $50s$ to reduce discretization errors.
Figure 3.8(a) and Figure 3.8(b) give the increase of the temperature and the vapour density inside the porous material, respectively, as predicted by the analytical and numerical model. Figure 3.8(b) shows that the increased water vapour density at the top of the material (x = 0.1m) results in a diffusion flux into the material until the water vapour density reaches the new level fixed at the top. Figure 3.8(a) shows how the water vapour diffusion into the material triggers a temperature increase which levels out in time under influence of the heat conduction to the surface. The excellent agreement between the analytical solution and the numerical results shows that the transport equations for water vapour in porous media have been correctly implemented and that the interaction between heat and water vapour transport is accurately represented.

3.4.2 Adiabatic saturation

Adiabatic saturation is a process in which water evaporates into air in a duct in such a way that the air is saturated with water vapour at the outlet [30]. The latent heat necessary for evaporation is extracted from the air. This results in a decrease of the air temperature along the duct. It is assumed that the water surface from which water evaporates is in equilibrium with the exit air. The temperature reached at the outlet where the air is saturated is then called the adiabatic saturation temperature. This adiabatic saturation temperature is a property of the inlet air-water vapour mixture conditions only. For the pressure and temperature range encountered in buildings this adiabatic saturation temperature is often closely approximated by the wet bulb temperature. However in this section it will be shown that assuming the adiabatic saturation temperature equal to the wet bulb temperature should be done with caution. For the adiabatic saturation temperature, the following energy

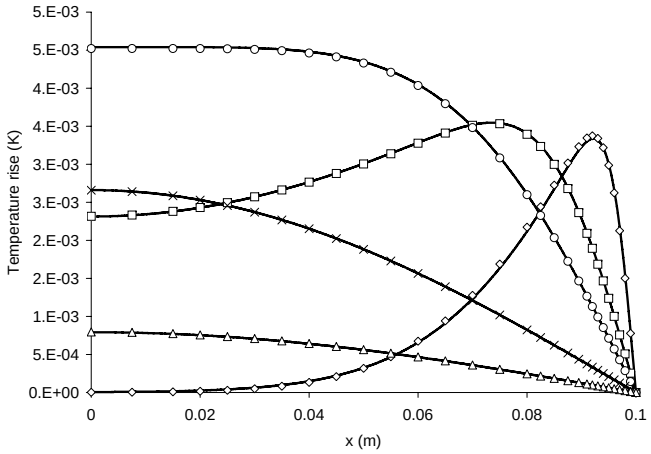

(a) Temperature increase

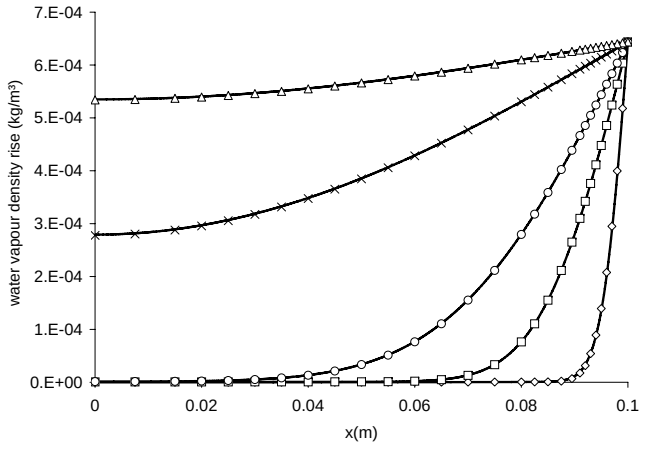

(b) Water vapour density increase

Figure 3.8: Verification for transport equations in the porous material when only vapour transport is present. Comparison at different times between the numerical model $(-)$ *and the analytical model* $(\diamond : 500s, \square : 5000s, \bigcirc : 20000s, \times : 200000s, \triangle : 500000s)$

balance can be stated [69]:

$$L\left(\omega_{sat}\left(T_s\right) - \omega_{in}\right) = C\left(T_{in} - T_s\right) \tag{3.40a}$$

$$T_s = T_{as} \tag{3.40b}$$

In these equations $T_s\ [K]$ is the surface temperature of the water surface and T_{as} $[K]$ the adiabatic saturation temperature. $\omega_{in}\ [kg_{vapour}/kg_{db}]$ is the humidity ratio at the inlet of the duct, ω_{sat} is the saturation humidity at the water surface corresponding with the water surface temperature. The humidity ratio is the ratio of the mass of water vapour to the mass of dry air (expressed in $kg_{drybasis}$ or kg_{db}). $C[J/kgK]$ is the heat capacity of the air, $L[J/kg]$ the latent heat of evaporation. The humidity ratio can be expressed as a function of the mass fraction $Y\ [kg_{vapour}/kg_{air+vapour}]$:

$$\omega = \frac{Y}{1-Y} \tag{3.41}$$

Since $Y << 1$, a humidity ratio difference can be written as a mass fraction difference.

$$\omega_{sat}\left(T_s\right) - \omega_{in} \approx Y_{sat}\left(T_s\right) - Y_{in} \tag{3.42}$$

The adiabatic saturation process is schematically depicted in Figure 3.9.

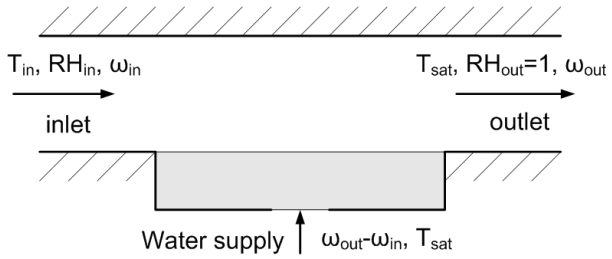

Figure 3.9: Schematic representation of the adiabatic saturation process: water evaporates until the air at the oulet is saturated with water vapour. Fresh water is supplied at saturation temperature. $T_{sat} = T_{as}$.

A process close to adiabatic saturation is convective drying. When unsaturated air flows over a wet surface, for example a saturated porous material, water will evaporate into the air. For this evaporation, latent heat is needed which results in a drop of the surface temperature. When a sample of porous material saturated with water is placed into an unsaturated air stream and all but one side of the sample are assumed impermeable and adiabatic, the temperature of the sample will consequently start to drop until the wet bulb temperature is reached. The steady-state heat balance at the wet surface is expressed by Eq. 3.43.

$$hA\left(T_{in} - T_{wb}\right) = Lh_m^Y\left(Y_{sat}\left(T_{wb}\right) - Y_{in}\right) \tag{3.43a}$$

$$T_s = T_{wb} \tag{3.43b}$$

In other words, at equilibrium, the heat flux entering the wet surface due to convection equals the heat flux leaving the surface due to evaporation. h is the convective heat transfer coefficient $[W/m^2K]$, h_m^Y the convective mass transfer coefficient on a mass fraction basis $[kg/m^2s]$, A equals the surface area $[m^2]$. At equilibrium the temperature at the surface equals the wet bulb temperature T_{wb}.

Eq. 3.43 can now be used to determine the heat transfer coefficient if the mass transfer coefficients is known or visa versa. Expression of this type are often referred to as heat and mass analogy expressions.
A similar expression for the heat and mass analogy was developed by Chilton and Colburn [70, 71] also referred to as the Chilton-Colburn analogy. Eq. 3.44 shows this analogy when the gradient of vapour density is used as driving force for vapour diffusion.

$$\frac{h}{h_m^\rho} = \rho C L e^{2/3} \tag{3.44}$$

Talukdar et al. [72] developed a similar analogy based on the evaporation of water from a tray.

$$\frac{h}{h_m^\rho} = \frac{L\Delta\rho_v}{\Delta T} \tag{3.45}$$

where ΔT and $\Delta\rho_v$ are respectively the logarithmic mean difference of the temperature and the vapour density.

$$\Delta T = \frac{(T_s - T_o) - (T_s - T_i)}{\ln\left[(T_s - T_o)\,/\,(T_s - T_i)\right]} \tag{3.46}$$

T_s is the surface temperature, T_i the inlet temperature and T_o the outlet temperature. $\Delta\rho_v$ can be defined in a similar way.
Chen et al. [73] used vapour density instead of mass fraction in Eq. 3.43 and found:

$$\frac{h}{h_m^\rho} = \frac{\left(\rho_{v,sat}\left(T_{wb}\right) - \rho_{v,in}\right) L}{T_{in} - T_{wb}} \tag{3.47}$$

In this equation $\rho_{v,sat}$ is the vapour density at saturation condition corresponding with the wet bulb temperature. T_{in} is the inlet, the bulk or the ambient temperature. When comparing Eqs. 3.45 and 3.47 it can be seen that these two equations become equivalent if the outlet conditions in Eq. 3.45 are equal to the surface conditions. This is the case for an adiabatic saturation process. The wet bulb temperature will then equal the adiabatic saturation temperature.
Chen et al. compared their analogy with the Chilton-Colburn analogy. They found a significant difference in results when applying both approaches on a drying

case. The equilibrium temperature (wet bulb temperature) when applying the Chilton-Colburn analogy was lower than when their analogy was used. The heat and mass transfer coefficient ratio, obtained based on the heat balance equation at the water surface, was different from that derived from the conventional heat and mass analogy. This can however easily be understood if Eq. 3.47 and Eq. 3.40 are investigated more closely.
Eq. 3.40 is only valid for an adiabatic saturation process. If in Eq. 3.47 the surface conditions are equal to the adiabatic saturation conditions, the following heat and mass transfer coefficient ratio can be derived:

$$\frac{h}{h_m^Y} = C \tag{3.48}$$

In other words, If the Lewis number is equal to 1, the adiabatic saturation temperature will be equal to the wet bulb temperature. If the Lewis number is different from 1, the adiabatic saturation temperature will differ from the wet bulb temperature. The discrepancy Chen et al. [73] found was the result of a wrong use of the wet bulb temperature in Eq. 3.47 where they falsely assumed that the wet bulb temperature equals the adiabatic saturation temperature. It can be stated that the expression found by Chilton-Colburn [70], Talukdar et al. [72] and Chen et al. [73] are in fact equivalent.

To illustrate all this and to verify that the boundary conditions of the drying model are correctly implemented, an attempt is made to predict the wet bulb temperature with the drying model. Convective drying of a saturated porous material was simulated. Figure 3.10 shows the details of the simulated case. The moisture content of the porous material was kept constant during the transient simulation. The air flowing over the porous material had a bulk dry bulb temperature of 23.8°C and a relative humidity of 44%. The air flowing over the sample was not simulated but instead a constant heat transfer coefficient of $22.5W/m^2K$ at the surface was taken. Air properties at 20°C gives λ_a = $0.0257W/mK$, ρ_a = $1.205kg/m^3$, C_a = $1005J/kgK$ and D_{va} = $2.625e-5m^2/s$. This results in a Lewis number equal to 0.808. Using the Chilton-Colburn analogy the mass transfer coefficient h_m^Y equals $0.0258kg/m^2s$. For a Lewis number equal to 1 the mass transfer coefficient would be equal to $0.0224kg/m^2s$. The initial temperature of the brick is 23.8°C, the initial moisture content of the brick is $97\%w_{cap}$. Material properties of the brick are listed in Appendix A. The adiabatic saturation temperature calculated according to Eq. 3.40 equals 15.91°C. If the Lewis number is lower than 1, the mass transfer coefficient is higher which will result in a lower equilibrium (wet bulb) temperature. The wet bulb temperature calculated according to Eq. 3.47 equals 15.51°C and thus 0.4°C lower than the adiabatic saturation temperature. In Figure 3.11 the simulation results are shown for the convective drying case with Le = 0.808 and Le = 1. The temperature in

the porous material drops to the wet bulb temperature and the adiabatic saturation temperature respectively. A perfect match is found between the predicted and simulated temperatures.

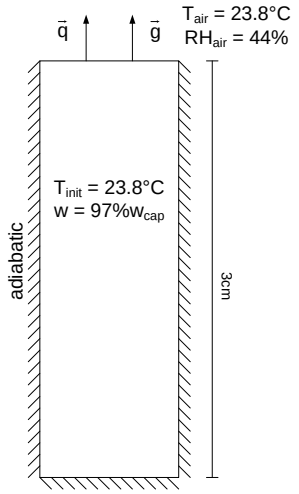

Figure 3.10: Details of 1D simulated case to illustrate adiabatic saturation.

3.4.3 Comparison with commercial HAM-model

In order to verify the model further, a comparison with validated commercially available HAM model was performed. WUFI®2D [18] was used for this comparison. This model however uses moisture diffusivity instead of permeability as input parameter for moisture transport. This makes the comparison between the coupled CFD-HAM model and WUFI® not so straight forward since these material properties have to be transformed. Carmeliet et al. [74] stated that for isothermal drying a unique relation between capillary pressure and moisture content can be assumed. Therefore it is possible to translate the permeability to the diffusivity.

$$\begin{aligned} \frac{\partial w}{\partial t} = \nabla \cdot D \nabla w = \nabla \cdot D \frac{\partial w}{\partial p_c} \nabla p_c = \nabla \cdot K \nabla p_c \\ D = \frac{K}{\frac{\partial w}{\partial p_c}} \end{aligned} \tag{3.49}$$

A problem in this transformation is the limited accuracy of the commonly used experimental techniques to determine the capillary pressure curve at low capillary pressure (high moisture contents) as also stated by Carmeliet et al. [74]. This will

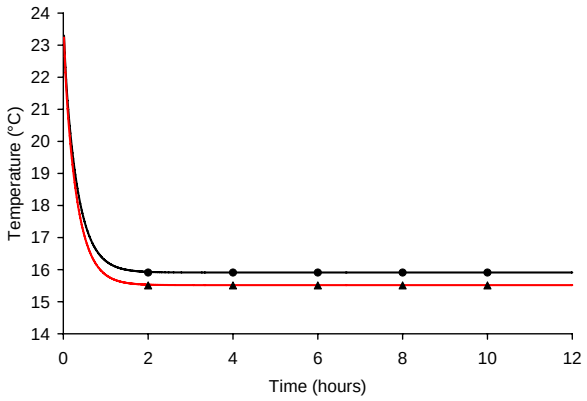

Figure 3.11: Temperature change in time in a sample of ceramic brick exposed to air at 23.8 *°C and* $44\%RH$. $h_m^Y = 0.0258kg/m^2s$ *(red line = simulation;* Δ *= analytic) corresponding with* $Le = 0.808$. $h_m^Y = 0.0224kg/m^2s$ *(black line = simulation; o = analytic) corresponding with* $Le = 1$. *The moisture content of the material is kept constant.*

lead to high uncertainty in the derivative of the sorption curve and consequently in the diffusivity near the capillary moisture content. Carmeliet et al. suggested enforcing an exponential diffusivity behaviour above a certain moisture content.

To perform an intermodel comparison, a simple 1-dimensional drying experiment is simulated. A ceramic brick sample of 30mm thick is assumed saturated and dries at the top. Figure 3.10 illustrates the boundary conditions. The sides and bottom of the brick are assumed impermeable and adiabatic. The convective heat transfer coefficient at the top is $22.5W/mK$, the convective moisture transfer coefficient is $0.0258kg/m^2s$. Material properties used for this simulation are listed in Appendix A. The temperature inside the brick sample at 10mm depth and the moisture content are monitored and compared for both simulation programs. Figure 3.12 shows the simulation results. A good agreement between both models is found.
Especially the predicted moisture content in both models agrees well. The maximum relative difference between both models for moisture is 0.7%. The difference in predicted temperature is slightly higher. Here a maximum relative difference of 3.8% was registered. These small deviations between both models are probably due to the different implementation of material properties in both models.

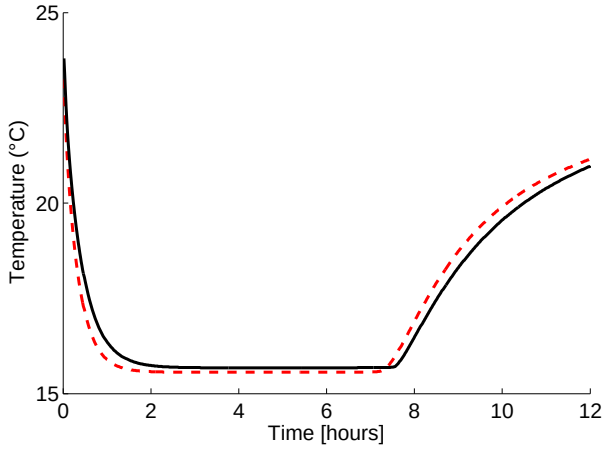

(a) Temperature at 10mm

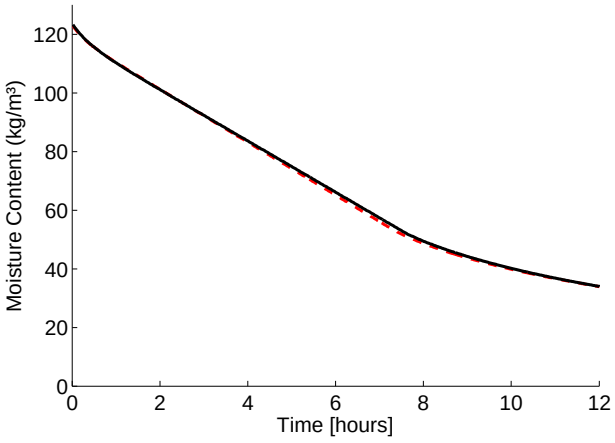

(b) Moisture content

Figure 3.12: Comparing temperature evolution in time and moisture content in ceramic brick during drying for the coupled CFD-HAM model (- -) and WUFI® with exponential liquid diffusivity (—).

4

Vapour transport modelling: experimental validation

4.1 Introduction

In the previous chapter the development of a coupled CFD-HAM model for moisture transport was elaborated. As stated there the moisture transport is dominated by two mechanisms: vapour transport by vapour diffusion and liquid water transport by capillary suction. The coupled CFD-HAM vapour transport model was developed by Steeman [1, 67] and a first verification and validation was performed during his research. The validation of the model was performed based on measurements by Talukdar et al. [75]. Although these measurements were with no doubt performed with great care, there were still some shortcomings. First of all the temperature measurements were not suited for validation purposes due to some inaccuracies during the measurements. Secondly the measurements were performed in a wind tunnel. This wind tunnel ensures a good control of the boundary conditions but the flow patterns in a wind tunnel deviate significantly from those in a room. Finally the measurements were limited to one material, gypsum board. To overcome some of these issues, it was concluded that a new setup was needed to perform suitable validation experiments.

Before the new setup is described, this chapter will first give a short overview of the state of the art in vapour transport experiments. From this overview the shortcomings of the current experimental data available in literature are identified. Based on these shortcomings, the new test setup is designed and built.

Next a validation experiment campaign is described. The measurements from this campaign were used to validate the coupled CFD-HAM model for vapour transport. Finally, to asses the impact of the uncertainties of boundary conditions and material properties, an extensive sensitivity campaign was performed.

4.2 State of the art in vapour transport experiments

Moisture experiments can be roughly classified into room-size moisture buffering experiments, building envelope performance experiments and wind tunnel experiments. In the this section an overview of literature on these types of experiments is given. An overview of existing test setups for moisture experiments is given in Table 4.1. The mean characteristics of the test facility, the type of experiments performed in the test facility and the measured variables are summarized.
From this literature overview the shortcomings and strengths of the different setups and experimental approaches are derived. These are then considered when the new setup is developed.

4.2.1 Room-size moisture buffering and humidity distribution experiments

In *room-size moisture buffering experiments* generally the response of a test room to the presence of hygrothermal materials is investigated. This type of experiments can be used for validation of numerical Building Energy Symulation (BES) tools and to investigate the impact of hygroscopic (finishing) materials on the indoor climate (damping of RH variations).
A differentiation can be made between test rooms located outdoors for which the outdoor conditions (temperature, RH) are measured, and test rooms located in a climatic chamber of which the conditions of temperature and RH can be controlled during the tests. Generally this type of tests aims to mimic the exposure to daily humidity variations, but in a controlled way.

Svennberg et al. [83] investigated the moisture buffering effect of a fully furnished room (Table 4.1). The experiments were carried out in a well-insulated and vapour tight test cell (PASSYS cell, Denmark), consisting of the actual test room and a service room. Furniture and furnishings such as carpet, curtains, a chair, ... were successively introduced into the test room and the RH in the test room was registered when a moisture cycle was imposed. The indoor temperature was kept constant during the experiment. The authors concluded that lightweight materials largely contribute to the moisture buffer capacity of a furnished room. Hedegaard et al. used the same test facility to study the moisture buffer capacity of two types of interior walls (i.e. a cellular concrete wall and a plasterboard construction) both in untreated form and covered with a finish (i.e. an

Institution and location	Geometry and dimensions	Type of experiments	Values measured	Ref.
MINIBAT				
CETHIL, INSA Lyon, France	2 identical, adjacent rooms Each 3.1m W, 3.1m D, 2.5m H Adjacent climatic room for outdoor climate -10°C 30°C& solar radiation	Mechanically ventilated room validation CFD	T air, air velocity, RH over vertical planes (robot arm) T walls surfaces	[76, 77]
CBS climate chamber				
Concordia University Montreal, Canada	Two-storey test hut in large environmental chamber 10m W, 4.4m D, 7.5m H Each room: 3.62m L, 2.44 W, 2.43m H	Full scale moisture buffer experiments	T and RH climatic chamber Hygrothermal condition of walls: moisture content, T, RH in cavity T distribution on wall surfaces T, RH supply & exhaust air T, RH, velocity in test room	[14, 78–82]
PASSYS Cell				
DTU Copenhagen, Denmark	Two identical, adjacent rooms: service + test room Each 13.8m, 2.75m H	Room size experiments Fully furnished room and interior walls	T, RH outdoor climate T, RH and air velocity in room	[83, 84]
TMT facility				
University of Saskatchewan Canada	Wind tunnel with test section Rectangular duct 20.5mm H, 298mm W	Heat and moisture transfer between air and porous materials. Convective mass transfer coefficients	inlet/outlet T and RH air flow rate T and RH in sample Moisture accumulation (gravimetry)	[72, 75, 85–89]
Test room Akita University				
Japan	Test room 4.6m surface 16.62m inside climatic chamber (38.34m)	Full scale moisture buffer experiments	Ventilation rate T and RH indoor air T wall surface Mass hygroscopic sample	[90]
Test rooms Fraunhofer Insitute				
Holzkirchen, Germany	2 identical, adjacent rooms Each 19.34m ,2.50m H	Room size experiments	T, RH outdoor climate T, RH centre room T wall surfaces Heat flow through walls Energy use electrical heating	[14, 91]

Table 4.1: Overview of former and existing experimental test setups for moisture experiments

untreated finish or a painted rendering) [84]. During the experiments, the indoor temperature was kept constant while the interior walls were exposed to cyclic humidity variations. The response of the indoor humidity and the moisture content change of a wall component specimen were measured. The results showed that finishes have a large impact on the buffer performance of underlying materials.
In the scope of the research project 'Whole Building Heat, Air and Moisture Response' of the International Energy Agency [92], the response of two identical well-insulated and vapour tight rooms was measured under a moisture production and real climatic conditions. These rooms were situated at the Fraunhofer Institute in Holzkirchen (Germany). Inside the test room, the temperature was kept at a constant level. Three cases were distinguished and compared to the reference test room: a vapour tight finishing, gypsum board applied to the walls and gypsum board applied to the walls and the ceiling [14]. The same test facility was used by Holm and Künzel [91] to investigate the moisture buffering of different wood-based finishing materials.
Yang et al. [78] have studied the moisture buffering behaviour of two types of finishing materials (i.e. uncoated gypsum and pine paneling) and of two types of furniture (i.e. a bookshelf with books and a fully furnished room). The experiments were carried out at different ventilation rates and for some cases the RH distribution in the test room was monitored during the experiments. For these tests only the lower room of a two-storey test hut built inside a climatic chamber of which the temperature and humidity were controlled, was used (CBS climate chamber at Concordia University in Montreal, Canada). Additional experiments were performed in which moisture movement through a large horizontal opening between the upper and lower room of the test hut was measured. In these tests the interior surfaces were non-hygroscopic and no furniture was added to the room [14].
Similarly Yoshino et al. [90] (test room Akita university, Japan) have used a room size experiment to look at the moisture buffering in gypsum boards. The actual test room is also located inside a climatic chamber, from which the temperature and humidity can be controlled. Different experiments were carried out with different configurations of gypsum board (e.g. on walls, ceiling, floor) and different ventilation rates (no ventilation, 1ACH and 5ACH). Each experiment consisted of 6hours of humidification followed by 12hours without humidification. During humidification water vapour was produced by evaporating moisture from two water reservoirs. The boundary conditions of the test room, ventilation rate, amount of moisture production, air temperature and humidity were measured and used to validate six numerical HAM models.

Besides climate chambers some in-situ measurements are reported in literature. Plathner and Woloszyn [93] experimentally quantified the influence of moisture buffering on the transport of airborne moisture from the kitchen to the other rooms in a fully furnished, unoccupied semi-detached two-storey test house. By comparing the water vapour increase to the concentration increase of an inert tracer gas released simultaneously, moisture buffering in porous surfaces was

found to have a large influence on the humidity distribution in the dwelling. Due to the storage capacity of the building envelope and furniture, moisture was absorbed by porous surfaces before reaching the other rooms. During the tests the outdoor climate (temperature and relative humidity) was registered, as well as the temperature and RH in the centre of each room. The latter were compared to numerical results. Similar experiments in an unoccupied three-storey house were reported by Oldengarm [94]. These experiments can be used to validate coupled multizone airflow-HAM models, however, no material properties of the furniture were available.
Simonson [95] performed a full scale investigation in a two-storey field test-house in Finland. The house had a well-insulated wooden frame construction without vapour retarder. During the experiments the conditions inside a bedroom with and without hygroscopic finishing were measured while water vapour was generated during the night to mimic the presence of two sleeping adults. Temperature and RH of the outdoor air were registered as well. The results showed that the porous building envelope decreases the peak humidity in the bedroom during the night by up to $20\%RH$ and increases the minimum indoor humidity in the winter by about $10\%RH$.

Most of the above tests are assumed to be carried out under well-mixed air conditions, which is a necessary assumption for the validation of BES models. These well-mixed conditions are generally assured by using a large enough ventilation rate or by using additional fans in the test room, e.g. in [83] and [95]. In these experiments the indoor RH and temperature are generally measured by one or only few sensors at the centre of the test rooms. However, temperature stratification and uneven moisture distribution are prevalent conditions within rooms. Moreover the distribution of RH can vary significantly along interior surfaces, which affects the moisture transfer between the indoor air and the surface material, and as a result, the moisture buffering behaviour of surface materials. Room-size experiments, in which the humidity distribution inside a room is measured and which can be used to validate CFD models are rather scarce. The experiments of Yang et al., mentioned earlier, in which the moisture distribution in one room or both test rooms were registered, enable to validate CFD tools [14, 78]. Hohota on the other hand [76], performed detailed experimental investigations on the air velocity, temperature and relative humidity field in a non-hygroscopic test room and used the results to validate a CFD model which takes into account condensation against impermeable surfaces. The experiments were carried out in the MINIBAT test facility (located in Lyon, France), which consists of two identical, adjacent test rooms. One of the rooms is adjacent to a climatic chamber which is used to mimic the outer climate while the temperature of the other wall surfaces is kept constant (Table 4.1). The same test facility was used by Teodosiu [77] to predict indoor comfort taking into account the indoor moisture distribution. The results were used to validate a CFD model. In the latter studies [76, 77] the interaction with porous surfaces was not considered.

4.2.2 Performance of building envelope systems

Several researchers used a climatic chamber to investigate the *performance of building envelope systems*. In these tests often one of the walls of the climatic chamber was interchangeable (e.g. in [79]) or the test wall is placed between two parts of the climatic chamber of which one part mimics the outer climate and another represents the inner climate (so-called hot box and cold box, e.g. in [96]). Apart from room-size experiments (see Section 4.2.1), the CBS climatic chamber at Concordia University was also used for envelope performance investigations (Table 4.1). Sadauskiene et al. [96] used the test facility to study the effect of an exterior painted thin render finish on the drying rate of exterior-insulated walls in a cold and humid climate. In these tests, the building envelope is positioned in between the hot and cold box representing dynamic indoor and outdoor conditions. Additionally, an amount of moisture could enter the construction system by means of artificial rain poured on the surface of the walls. Fazio et.al. [80] gives a detailed description of how the test-set up can be used for envelope component performance testing. The same test facility was used by Alturkistani [79] to investigate the drying capacity of different envelope configurations. In contrast to Ref. [96], here the envelope of the two-storey test house built inside the climatic chamber was tested. In the experiments, the moisture contents of the materials in the assemblies were monitored by gravimetric samples which were cut out from sheathing and stud materials. The same setup was used by Li et al. [81] for validation of a 2D HAM model. In these experiments measured and calculated moisture content profiles on sheathing are compared for different types of wall panels.
Pavlik et al. [97, 98] designed a system of climate chambers for the simulation of external and internal climatic conditions (NONSTAT). A studied envelope structure was placed in a connecting tunnel between two climate chambers. In one chamber outside conditions were simulated, in the other inside conditions were imposed. In the tested structure the moisture content, relative humidity and temperature were monitored.
Dionisi Vici et al. [99] used climate chamber experiments to look at the behaviour of wooden boards, which represented the supports of panel paintings, subjected to humidity cycles. However no detailed information about the test facility was included in the paper. Belarbi et al. [100] performed 1D and 2D experiments on lime-cement mortar and sandstone for the validation of a 2D HAM model. The experiments were carried out in a modified oven inside a climatic chamber from which the temperature and RH were controlled. Both the temperature and RH in the climatic chamber, the surface temperature and the temperature and moisture ratio distribution inside the sample were measured.

4.2.3 Wind tunnel experiments - convection coefficient experiments

The convective mass transfer coefficient is an important parameter because it is a measure of the resistance to mass transfer between flowing air and porous surfaces.

Since these mass transfer coefficients are difficult to determine experimentally, often convective heat transfer coefficients are measured and the analogy between heat and mass transfer is used to determine the convective mass transfer coefficient. Recently, wind tunnel experiments were performed in the transient moisture transfer (TMT) facility which was designed to study 1D heat and moisture transfer between a flowing air stream and a porous material and is located at the University of Saskatchewan, Canada. A good description of the test facility is given in Talukdar et al. [86]. In the experiments a small converging wind tunnel produces a steady, fully developed airflow at varying velocities, temperatures and RH, above the surface of a porous material. Two hygroscopic building material samples (i.e. cellulose insulation and spruce plywood), of which the hygrothermal properties were measured, were used. During the tests the changes in mass, relative humidity and temperature were measured at different depths inside the samples. For both material samples three different types of tests were performed: (1) a single step change in humidity (from 50%RH to 85%RH), (2) different flow rates resulting in a laminar and turbulent flow and (3) cyclical tests for which a RH of 75% imposed for two days is followed by a RH of 33% for two days [75]. Olutimayin et al. [87] applied the same test facility to study the vapour boundary layer in a bed of cellulose insulation following a step change in ambient humidity. Both an isothermal test and a non-isothermal test were performed. The experimental data are used for verification of a mathematical model. Osanyintola et al. [85, 88] used both the TMT test facility and a sealed glass jar facility to determine the moisture buffer capacity (MBC) of spruce plywood, which can be used to quantify the potential for hygroscopic materials to damp indoor humidity variations. Due to differences in boundary conditions and to a different sample size of the plywood, MBC differences up to 18% are registered. The experimental data were used to validate a numerical model.

To determine the convective mass transfer coefficients at the porous surface, experiments based on the adiabatic evaporation of water from a tray located in the lower panel of a horizontal rectangular duct were carried out e.g. by Iskra et al. [89]. In these tests both the evaporation rate from the tray of water and the vapour density difference between the air stream and the surface of water are measured. The vapour density of the air stream is determined from the measured temperature and RH of the air stream while the vapour density at the surface is based on the measured water temperature and the saturated air assumption. Talukdar et al. used the results of similar experiments for comparison with CFD simulations [72].

Bednar and Dreyer [101] reported on detailed in-situ investigations on realistic mass transfer coefficients in a test room (room area $13.4m^2$ and height $3.5m$) where different heat and moisture production and/or ventilation strategies were applied. By measuring the mass loss of a small insulated specimen ($32cm^3$), the surface temperature in the centre of the specimen and the temperature and RH of the air close to the specimen, mass transfer coefficients were determined.

4.2.4 Discussion

Above literature review reveals that a lack of experimental data exists especially for the validation of coupled CFD-HAM models. The existing facilities focus on the determination of transfer coefficients [86] or on the concentration pattern in the room [76]. Since the experiments by Talukdar et al. [86] were performed in a wind tunnel, it was not clear whether the measurements correspond well to realistic cases.
On the other hand, more data are available with respect to validation of multizone (BES) models. In these experiments the air in the room is assumed well mixed resulting in a uniform temperature and humidity. This type of experiments is not well suited for CFD model validation. The advantage of CFD extended with a heat and moisture transport model is its ability to predict temperature and humidity distributions. The impact of these temperature and moisture distributions is neglected in most experiments for multizone model validation. At this point it must be noted that in some experimental campaigns not all input data necessary for numerical tools were available, e.g. material properties [83].
From this literature review some important points of interest were considered when designing the new test facility: first the new test facility wants to generate more realistic flow patterns typically encountered in buildings instead of fully developed laminar or turbulent air flow conditions encountered in wind tunnels (e.g. Ref. [86]). Next the inlet and boundary conditions of the new facility should be well known and accurately preconditioned and controlled. The design of the setup should be flexible enough to allow multiple types of experiments ranging from validation experiments for BES-HAM models (where well-mixed air conditions are needed) to the validation of CFD-HAM model. More specifically for the validation of the coupling of CFD with HAM there is a need for data on the velocity, temperature and moisture distribution in the air and in the porous material. In the next section a climate chamber design is discussed which implements most of these issues.

4.3 Climate chamber design

The layout of the new test facility will be extensively described in the next sections. First the design of the test chamber is described. Next the air handling unit and the implemented instrumentation are discussed.

4.3.1 Test chamber

The test facility was built at the laboratory of the Department of Flow, Heat and Combustion Mechanics at Ghent University (www.floheacom.ugent.be) and consists of an outer and an inner chamber. The outer chamber is mainly used to minimize effects from the surroundings, for instance day/night temperature fluctuations. Similar to for instance the Atika test room [90], the inner chamber

is the actual test chamber. It represents a small room measuring $1.8m$ in width, $1.89m$ in depth and $1.8m$ in height (volume $6.12m^3$). The outer room measures $3.0m$ in width on $2.7m$ in depth and has a height of $2.4m$. The test facility is schematically represented in Figure 4.1, a view on the test room is shown in Figure 4.2. The wall panels (type ISOCAB [102]) of the inner and outer room consist of 6cm rigid high density polyurethane foam with a thermal conductivity of $0.0223W/mK$, sprayed in between two skins of white polyester lacquered, galvanized steel plate (thickness $0.63mm$). The panels have an overall U-value of $0.372W/m^2K$ according to the manufacturer [102]. The floor consists of multiplex panels with a phenol anti-slip surface reinforced with glass fibre. Its thermal conductivity is $0.366W/mK$. The wall opposite to the air inlet can be used as a test wall, consisting of $6cm$ mineral wool (λ = $0.04W/mK$) in a timber frame. In order to minimize the heat loss to the outer room, a small heating devise (i.e. a light bulb) was placed in the outer chamber. The light bulb turns on if the temperature in the outer room drops below the setpoint.

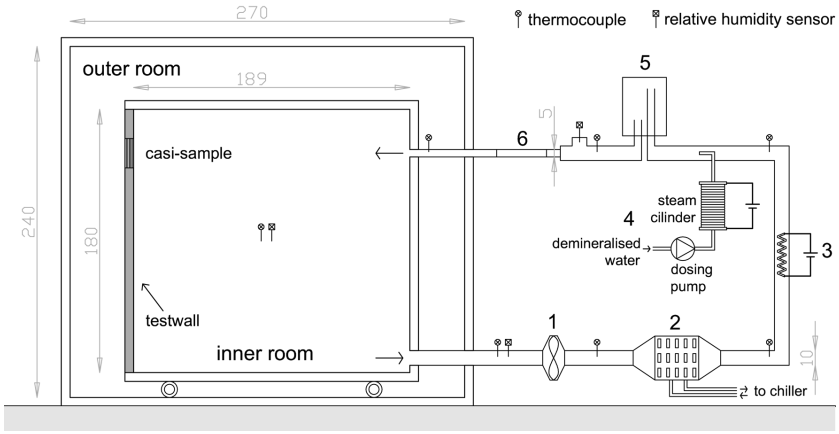

Figure 4.1: Schematic representation of the climate chamber and the air handling unit (dimensions in cm): (1) recirculation fan, (2) cooling coil, (3) resistive heater, (4) steam humidifier, (5) buffer vessel and (6) flow straightener.

4.3.2 Air handling unit

A closed air handling unit (AHU)-circuit draws air from the inner room with a recirculation fan. The ventilation air inlet and outlet are positioned in the wall opposite to the test wall at the top and bottom respectively, as indicated in Figure 4.1. Temperature, relative humidity and velocity of the entering air jet are closely controlled with a dedicated air conditioning system. The air is simultaniously cooled and dehumidified by a cooling coil (with a maximum cooling capacity of 3.5kW). When the air reaches its dew point, condensation starts and the humidity

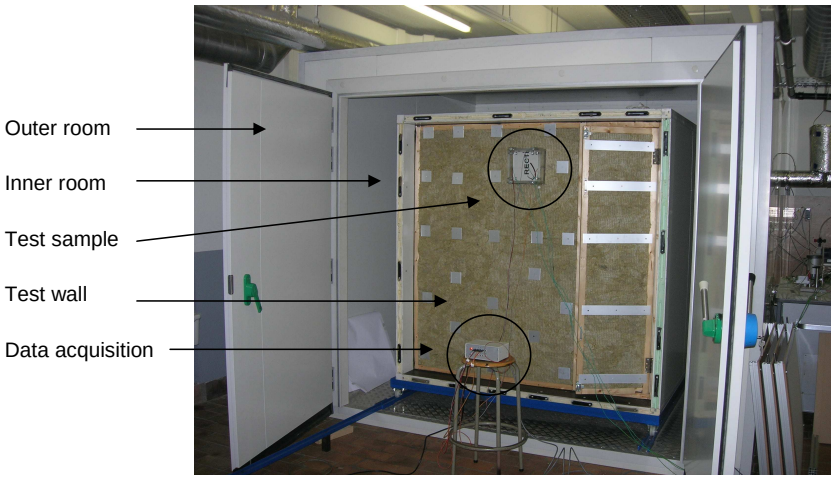

Figure 4.2: View on the outer and inner test chamber with test wall.

ratio of the air drops. The air at lowered temperature passes through a heat exchanger where a resistive heater heats up the air to the desired temperature. By heating the air, its relative humidity drops. Steam is then added to the dry air to humidify the air to the required relative humidity set point.
The steam humidifier works as follows: a dosing pump supplies a heated cylinder with demineralised water. The cylinder is kept at a high temperature (±300°C) by a resistance wire that is wrapped around the cylinder. The water that enters the cylinder immediately evaporates when it comes in contact with the hot cylinder wall. This way the time delay between the moment the liquid water enters the cylinder and the moment this water leaves the cylinder as steam is minimal. The dosing pump has a manually adjustable stroke length and the rotation speed is controllable. With a maximum of $180rpm$ (revolutions per minute) and a stroke volume of up to $0.13ml$ this results in a maximum flow rate of 1.4 litres per hour. The produced steam is then injected into the air duct. Contact of the steam with colder duct walls must be kept to a minimum to avoid condensation.
The air then passes through a buffer vessel with a volume of 25 litres. The buffer vessel is placed not far from the steam injection point in the air circuit to ensure a good mixture of the water vapour in the air. This buffer vessel levels out the relative humidity fluctuations caused by the humidification system and damps out temperature fluctuations. Finally a flow straightener ensures a fully developed flow pattern when the air enters the climate chamber.
A constant inlet air velocity is guaranteed by a fan with a constant rotation speed. The air change rate can vary between $0ACH$ and $10ACH$, corresponding to a maximum air flow rate of about $61.2m^3/h$ (mass flow rate of $68 \pm 2kg/hr$). The airtightness of both the inner room and the AHU-circuit was verified with a CO_2 tracer gas decay experiment. During the tracer gas measurements, the air change

rate was set to its maximum value (approximately $10ACH$). An infiltration rate of $0.033ACH$ was measured, which proves a satisfactory airtightness of the test room.
During operation of the test room, the temperature and the relative humidity at the air inlet of the test chamber need to be controlled closely. The applied control strategy for temperature and relative humidity is shown on Figure 4.3: a control loop for temperature and a control loop for relative humidity can be distinguished. Both temperature and relative humidity are measured at the chamber inlet (indicated in Figure 4.1). These measured values are compared with the corresponding set points. The difference between set point and measured value then serves as an input for the PID controller which steers the resistive heater for temperature control and steers the pump of the humidifier by adjusting its rotation speed for humidity control. G11, G12 and G22 on Figure 4.3 represent the transfer functions of the system.
The system is a multiple-input-multiple-output system (MIMO), which means that the two control loops cannot be entirely separated. This may render a smooth temperature and relative humidity control rather difficult. Changes in temperature change the relative humidity when the absolute humidity remains unchanged. On the other hand the hot steam added to the air flow influences the air temperature. The temperature loop has a smaller time constant then the relative humidity loop. Therefore the influence of the relative humidity on the temperature is small and can be neglected. The influence of the temperature on the relative humidity on the other hand (represented by G12) cannot be neglected due to the slow time response. This was also concluded by Huang et al. [103]. This will be further discussed in the next section (see Figure 4.4).

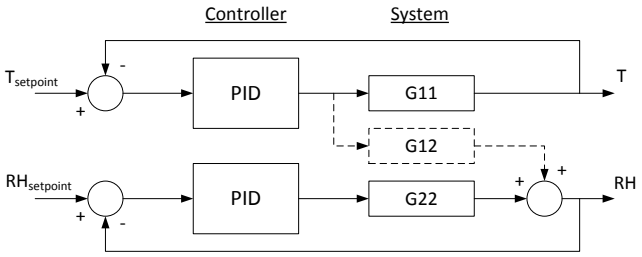

Figure 4.3: Algorithm used to control the supply air temperature and relative humidity.

4.3.3 Instrumentation

The relative humidity at the inlet of the chamber is measured by a capacitive humidity sensor TRANSMICOR T232 from GEFRAN [104]. This sensor has

an accuracy of $\pm 2\%$ between $5\%RH$ and $95\%RH$. The relative humidity in the test room and in the test sample is measured with capacitance RH sensors (type HIH-4000 humidity sensors from Honeywell [105]). Thermocouples type K are used to measure temperature in the chamber and air handling unit. All sensor signals are read by a voltage scanner and the measured values are sent to a computer where they are stored. All data are recorded every $\pm 3s$ during the experiment.

Response of the RH sensors

As mentioned in the previous section, a fast response of the sensors is essential for a smooth control of the temperature and relative humidity at the inlet of the test chamber. To evaluate the response time of the control system (and hence the performance of the controllers), two tests were conducted. Figure 4.4(b) shows the response of the relative humidity at the inlet of the chamber when the set point is altered from 50%RH to 65%RH and then back to 50%RH. During the test, the temperature of the supply air is kept constant at 25°C. Hardly any influence of the step change RH on temperature is noted in figure 4.4(b). Hence, when temperature stays constant, the response of the sensors is in the order of seconds or even less and an immediate change in relative humidity is noted. On the other hand Figure 4.4(a) shows that when the temperature changes while absolute humidity is constant, the response of the RH sensor is much slower. The response time grows tremendously when the air temperature decreases from 25°C to 20°C and then back to 25°C. A response time up to ten minutes is measured. This is in correspondence with Dooley et al. [106] who came to the same conclusions. As a result, experiments with a varying supply air temperature are difficult to perform.

Calibration of the temperature and RH sensors

To obtain good and reliable measurements in the climatic chamber, a precise calibration of the sensors used in the test chamber is indispensable. To calibrate the thermocouples a dry block calibrator was used. This method allows to calibrate thermocouples to an accuracy of ± 0.1°C.
To calibrate RH sensors, generally saturated salt solutions are used. These solutions decrease the relative humidity in the atmosphere of a closed (glass) jar to a relative humidity below 100%. The equilibrium relative humidity is known for a number of saturated salt solutions and depends on the temperature. This equilibrium relative humidity can then be used as a reference point for calibration of the RH sensors. One disadvantage of this technique is the strong dependence on temperature: small fluctuations of the temperature of the surroundings change the equilibrium relative humidity of the salts. As a result, calibration of the sensors must be performed in a controlled environment, e.g. in a climatic room. Furthermore, a relatively long time period is required before the saturated salt solution reaches an equilibrium state.
To overcome some of these drawbacks, a new calibration procedure was

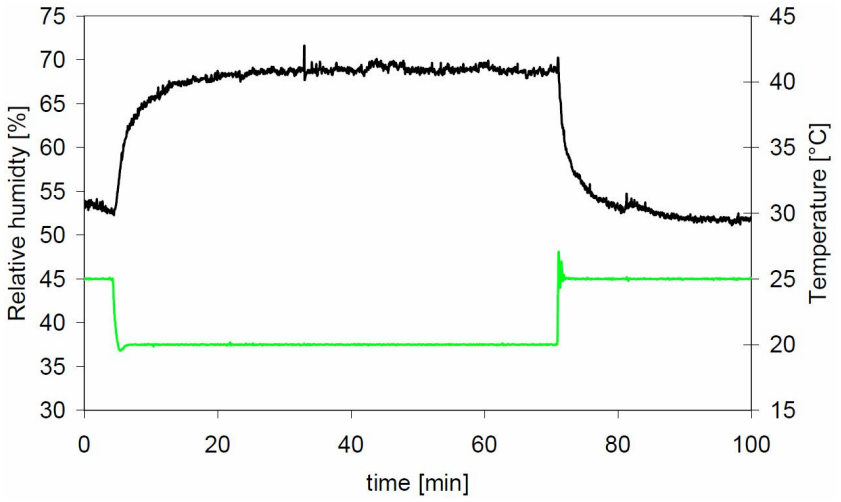

(a)

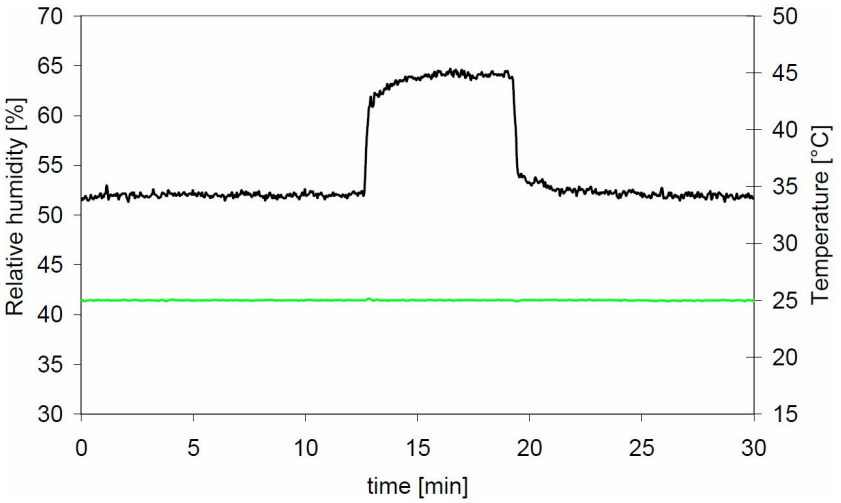

(b)

Figure 4.4: Response of the relative humidity sensor to a change of temperature, at constant absolute humidity (b) and response of the relative humidity sensor to a change of absolute humidity, at a constant temperature (a). Temperature indicated in green, relative humidity indicated in black.

developed. In this procedure saturated salt solutions are placed inside a glass box and a chilled mirror is used to determine the dew point in the box with an accuracy of ±0.2°C (Figure 4.5(a)). At the same time, the dry bulb temperature in the box is measured. The relative humidity in the box can now be determined from the measured dew point and the measured air temperature. By consequence, the salt solutions are only used to create a certain atmosphere in this procedure ($MgCl_2$(33%RH), KCO_3(43%RH), $NaBr$(59%RH), $NaCl$(75%RH)). As a result, the saturated salt solution does not necessarily need to reach equilibrium conditions and the test can be performed much quicker. Another benefit of the new test procedure is that the tests become less sensitive to the temperature of the surroundings. The new procedure allows to calibrate the RH sensors with an accuracy of ±1.4%RH.
Additionally, one of the RH sensors was calibrated in a so-called two-pressure calibrator. This method allows to very precisely calibrate RH sensors. In this method air or nitrogen with water vapour is saturated at a known temperature and pressure. The saturated high-pressure air flows from the saturator, through a pressure reducing valve, where the air is isothermally reduced to test pressure at test temperature. When equilibrium is reached, the resulting air RH can be determined by measuring the temperature and pressure in the saturator, and the test temperature and test pressure after pressure reduction. A comparison between the two-pressure method and the newly developed procedure shows good agreement between both calibration methods (Figure 4.5(b)).

4.4 Validating a coupled CFD-HAM model for vapour transport

The climate chamber described in the previous section is used to perform validation experiments for the validation of a coupled CFD-HAM model. For these experiments a test wall is built at the opposite site of the air inlet as indicated in Figure 4.1. In this test wall a test sample of calcium silicate is installed. Thermocouples and relative humidity sensors are installed in and around the sample and monitored the temperature and humidity changes. A conditioned air jet is blown on the calcium silicate sample in the test wall. During the experiment the air inlet temperature is kept constant while step changes to the relative humidity are applied.

4.4.1 Experimental setup

Test sample

In the test wall a calcium silicate sample is positioned ($20cm$ x $20cm$, thickness $10cm$). The test sample is placed directly opposite to the air inlet of the test room. Figure 4.6(a) represents a section of the test sample, Figure 4.6(b) shows a front

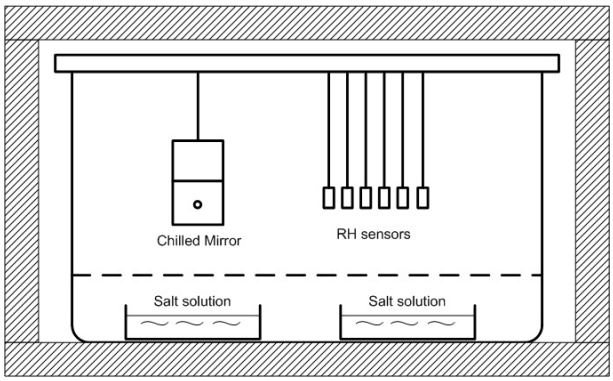

(a)

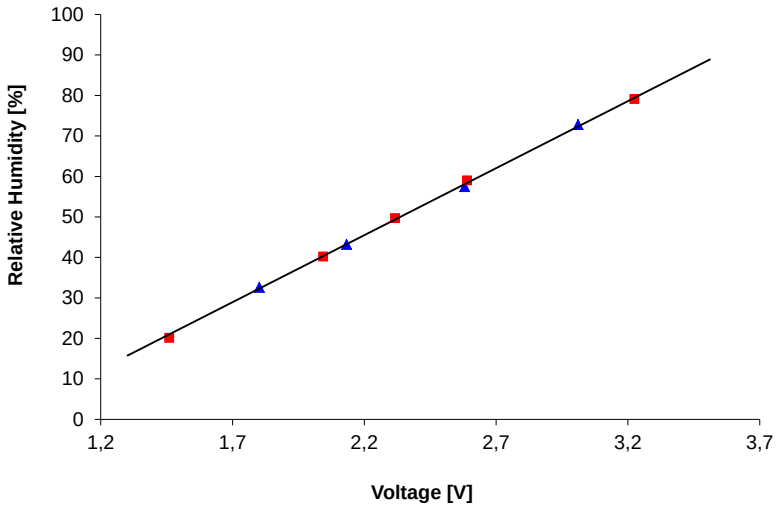

(b)

Figure 4.5: (a) Calibration setup. (b) Comparison between chilled mirror calibration (△) and two-pressure calibration (■) for a capacitive sensor.

view of the calcium silicate sample in the test wall. The sample is sliced into four layers of $10mm$, $15mm$, $25mm$ and $50mm$ thickness, respectively. Between each two material layers, in the middle, a thermocouple and a small capacitance relative humidity sensor (Honeywell HIH-4000) are placed. The positions of the thermocouples and relative humidity sensors are indicated in Figure 4.6(a). The layers are then pressed back together to ensure good contact. To examine the impact of the slicing of the sample and the insertion of the sensors, a preliminary test was performed that will be discussed in the next section. The test sample is placed in a Plexiglas box. The four sides and the back side are sealed with paraffin to avoid moisture exchange. At the sides and the back the sample is insulated with $4cm$ mineral wool to avoid heat exchange with the surroundings. These measures should ensure 1D moisture transport in the material sample.
The calcium silicate used in the tests is a highly hygroscopic material which makes it suitable for use in the validation experiments of a coupled CFD-HAM model where vapour transport is studied. The material properties of the calcium silicate were extensively measured by different laboratories during the HAMSTAD-project (Heat, Air and Moisture Standards Development) [107, 108]. Some of these properties are listed in Appendix A.
In the calcium silicate material a fine and a coarse pore system were distinguished. The measurements showed an open porosity ψ_0 ranging from 84% to 90%. The open porosity ψ_0 is defined as the ratio between the pore volume open for moisture transport and the total volume of the material sample. The material properties measured by the KU Leuven laboratory were used in the validation study. A dry vapour resistance factor of 5.42 and a dry thermal conductivity of $0.06W/mK$ were registered. The measured saturation moisture content w_{sat} was $894kg/m^3$. Note that the water vapour resistance factor is quasi independent of the RH. The minimum and maximum values of the material properties measured by the other laboratories are not presented in Appendix A but were used in a sensitivity study performed by Steeman et al. [109]. From this sensitivity analysis it was found that the measured value of 5.42 for the dry vapour resistance factor was too high and not in correspondence with measurements by other laboratories. Therefore Steeman et al. proposed a value of 3. This value was also adopted in this work.

Preliminary experiment: effect of sample cutting

Preliminary experiments were carried out to check whether sample cutting may have an effect on the temperature and relative humidity profiles which are measured on different depths in the sample. Due to cutting of the calcium silicate sample at the different positions (at $10mm$, $25mm$ and $50mm$) for the installation of the thermocouples and a relative humidity sensors, it is possible that small air layers arise between the different material parts when the sample is assembled again. Because of this, the material properties may no longer be homogeneous along the depth of the material, which can affect the overall permeability and sorption of the sample. In turn this may influence the temperature and relative humidity profiles measured inside the sample. To check the possible effect of

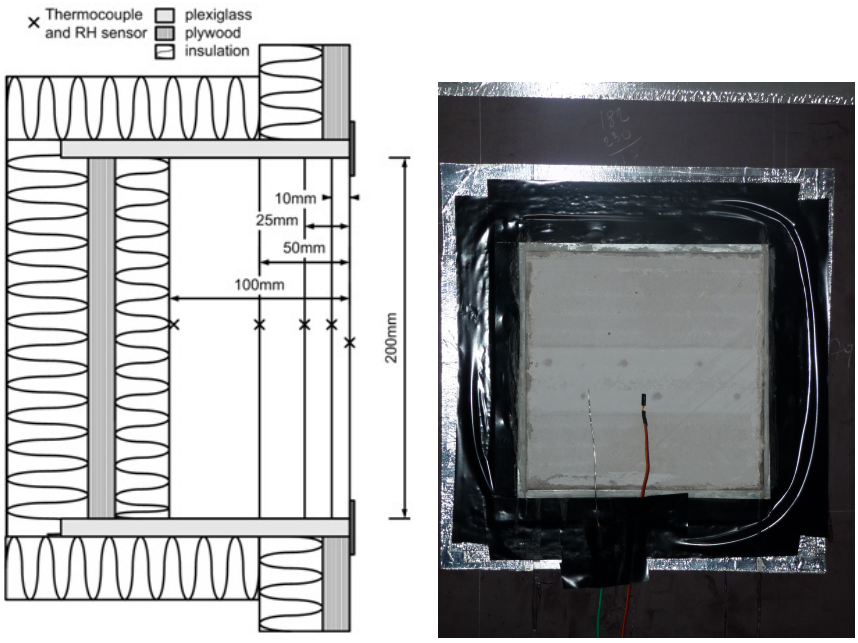

(a) (b)

Figure 4.6: Schematic representation of the calcium silicate test sample (a) and view on the test sample (b)

the cutting edges in the sample, a new sample is prepared which is only sliced at $25mm$ depth. In this material sample the influence of a possible air layer at $10mm$ depth is hence excluded. Both samples are successively installed in the test wall and with each sample an identical experiment is performed. Before each experiment the calcium silicate sample is preconditioned for four days by supplying air ($10ACH$) at 25°C and 50% relative humidity until the temperature and relative humidity differences inside the sample are smaller than the uncertainty interval of the sensors (i.e. ±0.1°C and ±1.4%RH). During the experiment the supply air temperature is kept at 25°C, while a relative humidity step is imposed from 50% to 70%: 8 hours of high relative humidity (70%) are followed by 16 hours of low relative humidity (50%). This cycle is repeated five times. Apart from the calcium silicate sample in the test wall no other porous material is present in the room.
Figure 4.7 compares the measured temperature and relative humidity profile at $25mm$ for the last three cycles. The first two cycles are not depicted here. During the first two cycles some transition and startup phenomena occur that are not relevant for the current comparison.
Note that the latent heat of evaporation has a strong effect on the temperatures inside the sample: the temperature in the sample rises if water vapour is absorbed by the sample while a temperature decrease is noted when water vapour is released from the sample. The relative humidity measured at $25mm$ in both samples is quasi identical. Also the associated temperature measured in the sample is comparable, in the third cycle a difference of about 0.2°C is noted.
The temperature and relative humidity curves at the front and the back side of the sample show that in both experiments the boundary conditions are similar (Figure 4.7d and Figure 4.7f). At the front side of the sample, the relative humidity between the two tests differs from $0.5\%RH$ up to $1.4\%RH$ when the relative humidity of the supply air is 70%. The maximum difference between the temperatures measured at the front side is 0.1°C. At the back side, the average difference in relative humidity is smaller than $0.5\%RH$ while the maximum temperature difference is about 0.2°C. Note that the thermocouple and relative humidity sensor at the front and back side of the sample do not exactly register the conditions at the sample surface but rather measure the temperature in a small air layer near the surface.
Consequently, the experiments demonstrate that the cutting edges do not have a considerable effect on the temperature and relative humidity profile measured in the sample. Furthermore the experiments have shown to be reproducible.

4.4.2 Experimental validation

Prior to the experiment the calcium silicate sample is preconditioned for four days by supplying air ($10ACH$) at 25°C and 50% relative humidity until the temperature and relative humidity differences inside the sample are below the uncertainty interval of the sensors (i.e. ±0.1°C and ±1.4%RH). During the experiment the supply air temperature is kept at 25°C, while a relative humidity

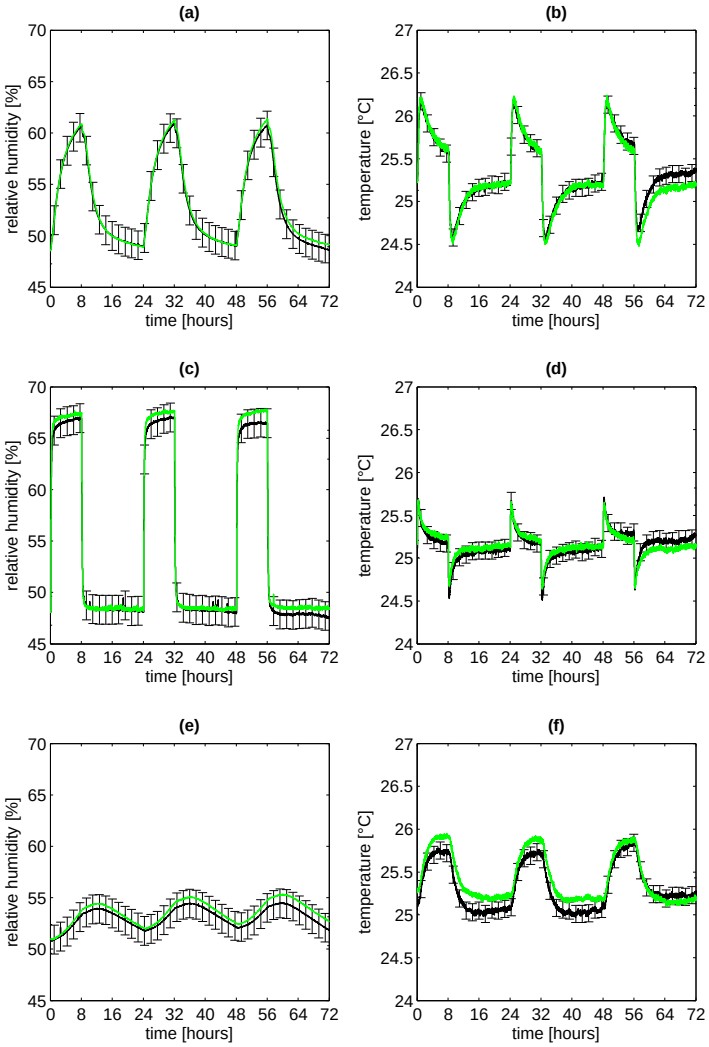

Figure 4.7: Influence of the cutting edge on the measured temperature and relative humidity in the sample: original sample (black line) and adapted sample (green line). Measurements in the sample at 25mm (a,b), measurements at the front surface of the sample (c,d) and measurements at the back of the sample (e,f)

step is imposed from 50% to 70%: 8 hours of high relative humidity (70%) are followed by 16 hours of low relative humidity (50%). This cycle is repeated five times. Apart from the calcium silicate sample in the test wall no other porous material is present in the room. A 2D hotwire anemometer is used to measure the velocity field inside the test room. The anemometer is connected to a robot arm which is controlled by a computer. The robot arm can move in two directions, allowing measurements in the vertical plane of the jet.
A commercial CFD package (Fluent® [38]) was used to simulate the climate chamber. A 3D structured rectangular grid with 138708 elements was used to discretize the chamber and calcium silicate sample. A grid independency study was performed by comparing the results of the coarse grid with a refined grid of 1109664 cells (two times finer in every direction). When comparing the calculated velocity for both grids, deviations up to 7% were found. However, the largest deviations were located away from the sample. For the the current validation only the flow near the sample is of interest, so it was concluded that using the coarser grid would result in sufficient accuracy.
For simplicity a constant inlet velocity of $10m/s$ was chosen with a turbulence intensity of 5%. The walls of the chamber are assumed adiabatic except for the back walls of the test sample. Here a constant temperature of 25.4°C is assumed. This value corresponds with the measured temperature at the back of the sample and gave the best results for the simulations.
The incompressible ideal gas law was used to calculate the density. Constant values for the dynamic viscosity, thermal conductivity and mass diffusivity were used. As the interest of the study lies in the heat and mass transfer to the wall (the calcium silicate sample), it is important that the near wall behaviour of the flow is correctly represented. A sufficiently refined grid is used near the wall ($y+ < 4$) in combination with a $k-\omega$ LRN turbulence model. This turbulence model is known to perform well close to walls. A second order upwind scheme is used for the discretization of the convective terms in the transport equations in order to reduce numerical diffusion. The SIMPLE algorithm is used for the pressure-velocity coupling. A double precision representation of real numbers is used to reduce round-off errors.

Velocity measurements and simulations in the climate chamber

The transient hygrothermal behaviour of a system consisting of air in contact with a porous material is dominated by the response of the porous material. As the characteristic time scale of heat and moisture transfer in the air is in the order of seconds while the time scale characterizing the hygrothermal response of the porous material is in the order of minutes or hours, the air response can be described as quasi steady state [58]. In other words, the transient hygrothermal behaviour of the air is caused by the varying boundary conditions at the interface with the porous material and at each time step the air can be considered in equilibrium with the new boundary conditions. This does not imply that the air

flow cannot feature unsteady phenomena (such as vortex shedding), yet these phenomena appear at a time scale much smaller than the time scale of the heat and moisture transfer we are interested in and do not need to be captured. The time step for the coupled CFD-HAM simulation can thus be chosen based on the characteristic time scale for heat and moisture transfer in the porous material.
As the transport equations in both the air and the porous material are solved in the same solver, this time step is used for both media. The airflow is hence also modelled as unsteady. However, because the time step is that large compared to the characteristic time scale in the air, the unsteady term in the heat and mass transport equations becomes negligible compared to the convective term and the equations reduces to a quasi-steady form.
For the transient simulations performed in this study a time step of 60 seconds was chosen. The effect of the time step size is evaluated by performing a simulation with a time step of 30 seconds. No appreciable effect was found.

Figure 4.8 shows the comparison between the measured velocity field in the middle of the chamber and the simulated velocity. A good agreement between both is found. However, the jet shown in Figure 4.8(b) is calculated under steady conditions. As mentioned earlier, in reality the jet will experience unsteady phenomena. Because this small time dependency of the jet has no influence on the heat and moisture transport to the porous material, the jet is solved quasi steady state. Small deviations between the measured and simulated jet can thus be attributed to the time dependency of the jet, but this does not affect the results for humidity and temperature in the test sample. Also, mass transfer between the air and the porous materials is dominated by the vapour diffusion resistance and not by the mass transfer coefficient when the velocity is high enough (forced convection). This implies that a wrong estimation of the velocity near the material or indirectly a wrong estimation of the mass transfer coefficient has little effect on the mass transfer. Note that this is only valid for cases with forced convection. For very low air velocity, where buoyancy driven flow becomes important, the vapour diffusion resistance is no longer dominant. Here the driving forces for airflow are temperature gradients and to a smaller extent humidity gradients. This means that the airflow and by consequence the transfer coefficient depend on the air temperature and relative humidity.

Temperature and humidity measurements and simulations in the sample

Figure 4.9 shows a comparison of the measured and simulated relative humidity and temperature at three depths in the calcium silicate sample. The material properties of the calcium silicate used in this study are listed in Appendix A. This comparison shows a good agreement between measurement and simulations at a depth of $10mm$. Deeper in the material (at $25mm$ and $50mm$) the deviations are more pronounced. Several explanations for these deviations can be found. First the exact location of the sensors in the material will have an effect on the measurement results. Secondly the exact boundary conditions are of great importance and finally

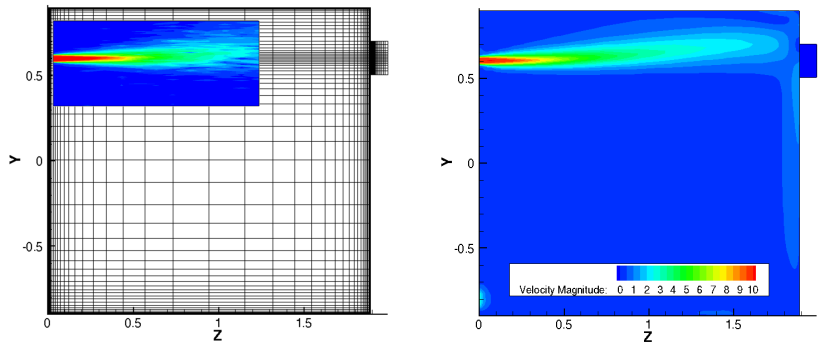

(a) (b)

Figure 4.8: Comparison of the measured velocity in the middle of the room (a) and the simulated velocity (b). Velocities are indicated in m/s.

the input data of material properties can have a severe impact on the simulation results.

Figure 4.9(c) shows the relative humidity in the sample at a depth of $25mm$. Three simulation curves are shown together with the measured data (including the error bars). In green the simulation results at exactly $25mm$ are shown. The dashed lines in red and blue show the simulation results at a slightly different position in the material. The red dashed lines are the simulated values at a depth of $23.2mm$ ($1.8mm$ less deep in the material); the blue dashed lines are the simulation results at a depth of $26.6mm$ ($1.6mm$ deeper in the material). During adsorption there is a clear underestimation of the relative humidity. However slight changes in the position of the sensor will result in a higher or lower relative humidity measured in the material. It is not unlikely that the exact location of the sensor in the material deviates from the assumed $25mm$, since the sensor has a thickness of $2mm$. Figure 4.9(c) clearly shows the effect of the sensor positioning. A sensor position at $23.3mm$ would result in a better agreement of the simulations with the measurements. Changing the position of the sensor in the order of $2mm$ has only little effect on the simulated temperature (Figure 4.9(c)).

The temperature difference between measurements and simulations during desorption at a depth of $25mm$ (and also to a lesser extent at $10mm$) can be attributed to an underestimation of the boundary conditions during desorption. It is assumed that the temperature of the incoming air is constant at $25°C$. However in reality there is an uncertainty on this value of $0.1°C$. A change in the incoming air temperature has a direct effect on the temperature in the sample. In other words, an increase of $0.1°C$ of the incoming air during desorption would result in an increase of the simulated temperature and thus a better fit with the measurements. This will be discussed in more detail in section 4.5. Deeper in the porous

material (at $50mm$) the effect of inlet air temperature is less pronounced since here the temperature at the back of the sample (which was at 25.4°C) has a greater influence.
The largest discrepancies between model and measurements are found at a depth of $50mm$. Although a good agreement for temperature is found, the relative humidity differs op to $4\%RH$. This difference can no longer be attributed to sensor positioning and boundary conditions solely. Previous studies [109] showed that besides boundary conditions also material input data can have a severe impact on the modelling outcome. Wrong estimations of this data (especially sorption isotherm and vapour resistance factor) becomes more important deeper in the material as these effects accumulate.
It is clear that measuring and modelling moisture transport in porous materials is difficult since there are so many parameters involved. It is in fact a combination of uncertainties on different factors (sensor position, boundary conditions, material properties) that results in a deviation between measurements and simulations. Bearing all this in mind, it can still be concluded that there is an overall rather good agreement for the coupled CFD-HAM model with the measurements.

4.4.3 Discussion and conclusions

The experimental validation of the coupled CFD-HAM model for vapour transport showed good agreement between the simulations and measurements. Deviations between measurements and simulations were attributed to various causes such as uncertainty in the boundary conditions and the effect of the sensor positioning. However still some questions remained. Especially the impact of the material properties on the simulation outcome remains unclear. It is shown in various studies [110–112] that there is still a large uncertainty on some measured hygrothermal material properties. This uncertainty will have its impact on the simulation accuracy. In the next section this is studied in more detail.

4.5 Sensitivity analysis of a coupled CFD-HAM model for vapour transport

4.5.1 Reference case

In order to perform a sensitivity analysis on the coupled CFD-HAM model, a proper reference case was selected. The same case was used by Steeman et al. [67] to validate the coupled CFD-HAM model. The case is based on an experimental setup discussed in detail by Talukdar et al. [86]. In this paragraph only a short description of the test facility is given.
Figure 4.10 shows a schematic representation of the reference case setup. Only the section of interest is shown. The figure represents a part of a wind tunnel. Preconditioned air enters the section on the right hand side with a fully developed air profile. This air flows over a sample of porous material. Gypsum board was

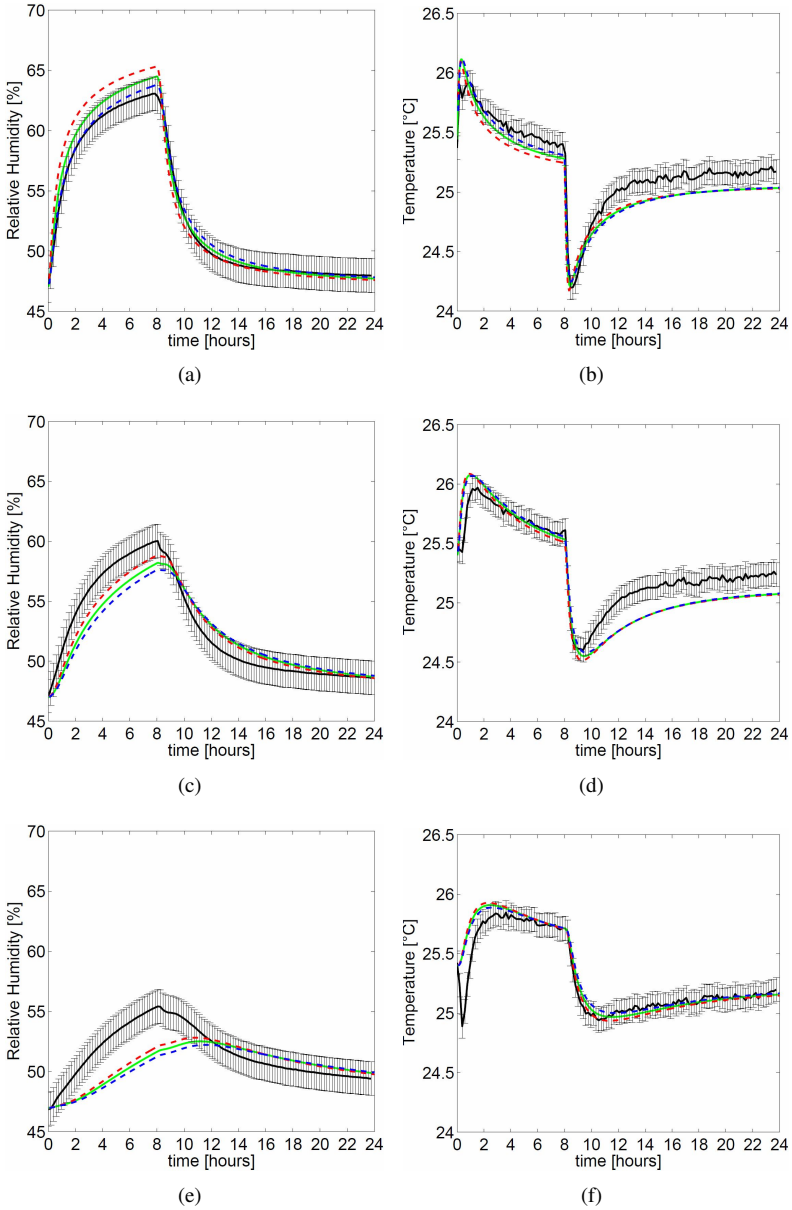

Figure 4.9: Relative humidity (a) and temperature (b) at a depth of 10mm (—), 8.3mm (- -) and 11.5mm (- -) in the calcium silicate. Black line with error bars corresponds with the measurements. Similar graphs for relative humidity (c) and temperature (d) at 25mm depth (—), 23.2mm (- -) and 26.6mm (- -). Relative humidity (e) and temperature (f) at 50mm (—), 47.7mm (- -) and 52.5mm (- -)

used for this investigation. Three gypsum boards with a thickness of $12.5mm$ were stacked on top of each other. The gypsum boards have a length of $500mm$ and a width of $298mm$. Only the top of the stack is in contact with the air duct, the other boundaries are assumed to be adiabatic. The cross section of the duct has a height of $20.5mm$ and a width of $298mm$. Air enters the duct at a constant temperature. The samples were preconditioned at a low relative humidity (30%) and constant temperature (23.3°C). Afterwards the relative humidity was changed to a higher value (RH = 71.9%, T = 23.8°C) for 24 hours and then lowered again for 24 hours (RH = 29.6%, T = 22.5°C). Thermocouples and RH sensors were placed at a depth of $12.5mm$ and $25mm$ to measure temperature and relative humidity in the hygroscopic material.
The average air velocity in the duct was $0.82m/s$ which corresponds with a Reynolds number of 2000. The air was preconditioned before it entered the test section and an upstream developing section ensured a fully developed flow pattern. For the case of Re = 2000 the airflow pattern was assumed to be laminar in accordance with [89].
A 2D structured grid was used, counting 33800 rectangular cells. The grid was dense near the air-material interface and gradually coarsened towards the bottom of the porous material and the centre of the duct. The grid dependency was investigated by using Richardson extrapolation [113]. The original grid was refined with a factor 2 and a factor 4 for both the X and Y direction and the mass flow through the interface was calculated. Using Richardson extrapolation the exact mass flow rate through the interface can be calculated out of the different mass flow rates for the different grid sizes. Because the difference between the exact value and the simulated value was less than 1% it was assumed that the solution is grid independent. In order to reduce numerical diffusion a second order upwind scheme is used for the discretization of the convective terms. The PISO algorithm is used for the pressure-velocity coupling. To reduce the round-off errors, a double precision representation of real numbers is used.

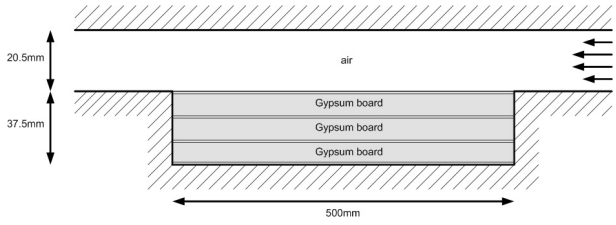

Figure 4.10: Test section of the wind tunnel setup [86] with three gypsum boards stacked on top of each other.

4.5.2 Material properties

The material properties used for the reference case were taken from IEA Annex 41 [111]. These properties are needed as input for the HAM model. Report 2 of Annex 41 comprises an elaborate round robin test for some of these porous material properties. Samples of the same gypsum board were sent to different laboratories where the material properties were determined. Figure 4.11 and 4.12 show the average sorption isotherm and vapour resistance factor calculated from the data of Annex 41 together with the upper (w+) and lower (w-) measured values. The round robin test performed in subtask 2 of this Annex revealed large discrepancies in the sorption isotherm and vapour resistance factor measured by 14 laboratories. Differences up to 20% were found. It is expected that this will have an influence on the model outcome, since the accuracy of the solution is to a great extent determined by the accuracy of the input parameters.
Table 4.2 lists five properties of gypsum board used in the sensitivity analysis. For each property an upper and lower limit is determined, which corresponds to an increase or decrease of 5% of the original value. This is indicated in the table by Min(-5%) and Max(+5%). First, simulations are performed with the reference values. The output of these simulations is referred to as the reference case. The sensitivity analysis is performed by changing one property at a time (so-called One-at-a-Time analysis). Note that for this analysis the effect of density and open porosity is not evaluated independently: it is assumed that an increase of the open porosity by 5% would result in a decrease of the density by 5% and vice versa. The properties listed in Table 4.2 are fairly easy to measure and can be often determined quite accurately [114]. Only a change of 5% in these parameters will be considered. In most cases the uncertainty found on the measured properties will be less than 5%.
To model the material properties as accurately as possible the following analytical functions are used to describe the sorption isotherm and the vapour resistance factor of gypsum board (Figure 4.11(a) and 4.12(a)). The coefficients a, b, c and n are determined by fitting the analytical functions to experimental data.

$$w_a = \frac{RH}{aRH^2 + bRH + c} \tag{4.1}$$

$$w_d = a\left(1 - \frac{\ln RH}{b}\right)^{-\frac{1}{c}} \tag{4.2}$$

$$\mu = \frac{\mu_0}{1 + aRH^n} \tag{4.3}$$

For the analysis with hysteresis at least two sorption isotherm curves are needed: w_a is the sorption curve during adsorption and w_d during desorption. The corresponding coefficients for Eqs. 4.1 to 4.3 are listed in Table 4.3. For each function a set of coefficients is given for the average curve fit, for the lower curve (-) and for the upper curve (+). No sensitivity analysis was performed on the desorption isotherm, so for this curve only one set of coefficients is given.

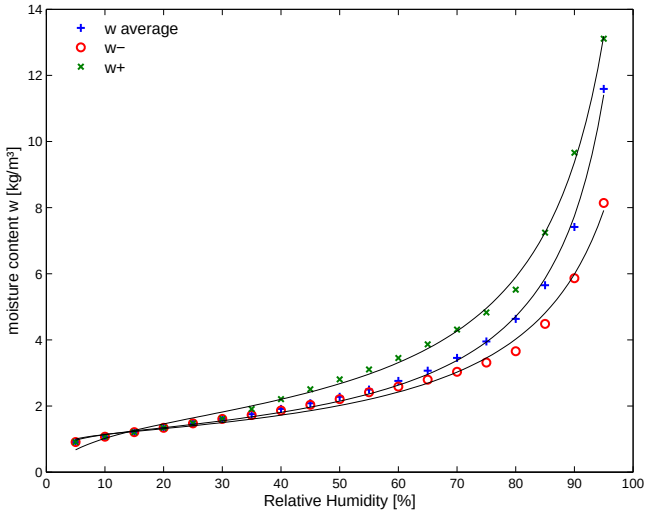

(a)

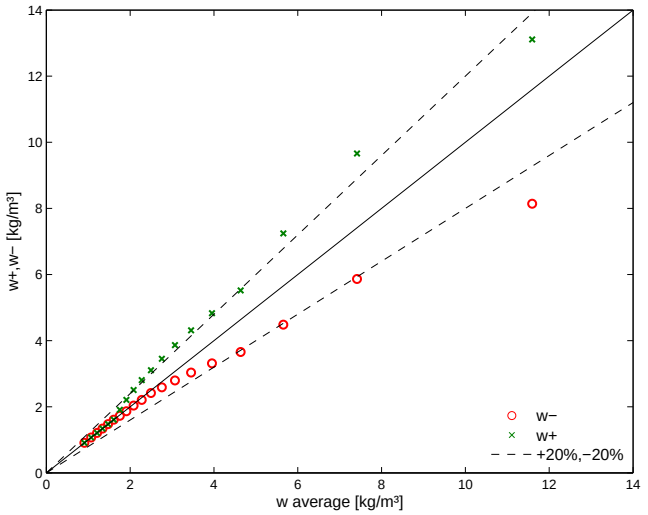

(b)

Figure 4.11: Sorption isotherms for gypsum board (data from [111]) (a) and measured differences between the curves (b). Full lines in (a) correspond with equation 4.1, ×, + and ○ correspond with measurements.

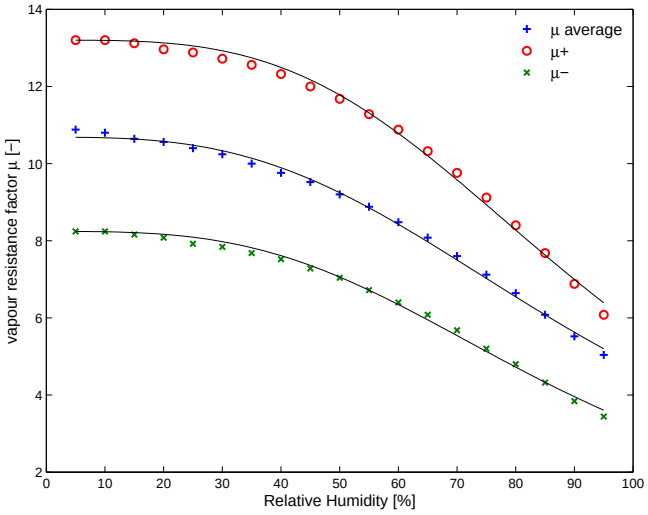

(a)

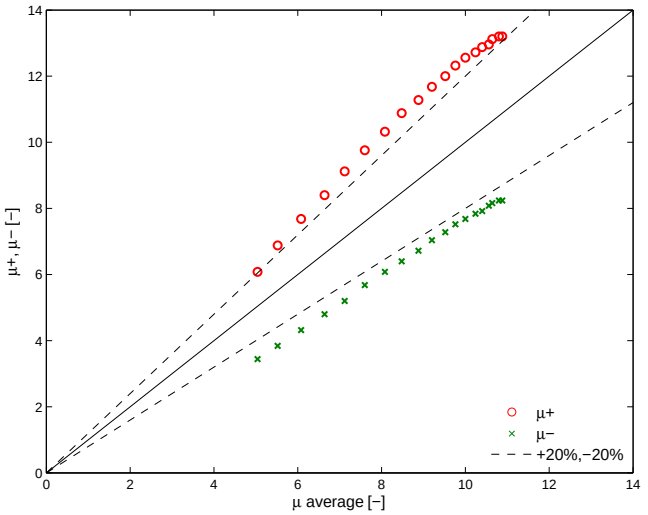

(b)

Figure 4.12: Vapour resistance factors for gypsum board (data from [111]) (a) and measured differences between the curves (b). Full lines in (a) correspond with equation 4.3, ×, + and ∘ correspond with measurements.

Material property	**unit**	**Reference value**	**Min (-5%)**	**Max (+5%)**
Thickness d	m	0.0125	-	-
Density ρ	kg/m^3	690	655.5	724.5
Open porosity ψ_0	-	0.419	0.448	0.39
Thermal conductivity λ	W/mK	0.198	0.188	0.208
Heat capacity C_{mat}	J/kgK	840	798	882

Table 4.2: Material properties gypsum board.

	+	**Average**	**-**
Absorption isotherm w_a			
a	−0.562516742	−0.81655	−0.8054748
b	0.560112656	0.85157	0.883480733
c	0.047583587	0.011176	0.007663124
Desorption isotherm w_d			
a		1.391382	
b		0.079139	
c		1.944272	
Vapour resistance factor			
μ_0	13.2	10.68205	8.24
a	1.268102	1.229557	1.512357696
n	3.392995	2.983921	3.174273855

Table 4.3: Coefficients for sorption isotherms and vapour resistance factor of gypsum board needed in equation 4.1 and 4.3.

4.5.3 Sensitivity analysis

Studies of [111] and [110] showed a large variability of measured material properties, which stresses the importance of a sensitivity analysis. The effect of changes in the material properties on the numerical results will be studied in this section. In total five material properties are studied: dry density (combined with open porosity), thermal conductivity, heat capacity, sorption isotherm and vapour permeability. The latter is represented here as a water vapour resistance factor. The material properties of air are assumed to be constant in the model and are not investigated here. Their effect on the model is assumed to be negligible compared to the variability of the porous material properties. The same counts for the latent heat of vaporization which is assumed to be constant in the model.
Temperature and relative humidity at a depth of $12.5mm$ and $25mm$ in the bed of gypsum board is simulated and a comparison between the different cases is made. In order to compare the results of the different simulations, Figure 4.13 proposes five parameters derived from a typical temperature and RH response inside gypsum board at a depth of $12.5mm$ to a step change in relative humidity (step change from 30%RH to 71.9%RH, and back to 29.6%RH). ΔRH_a indicates the magnitude of change in relative humidity after an adsorption phase. ΔRH_d is the magnitude of RH change during a desorption phase. RH_{max} gives the maximum simulated relative humidity. T_{max} stands for the maximum simulated temperature and T_{min} for the minimum temperature. A similar approach was used in Annex 41. For all simulations the boundary and inlet conditions are the same. As a result the effect of material properties can be revealed.

Table 4.4 lists the simulated values for ΔRH_a, ΔRH_d and RH_{max} at a depth of 12.5mm and 25mm. Table 4.5 does the same but for the simulated maximum temperature T_{max} and the minimum temperature T_{min}. Results for the reference case are shown in the first row of Table 4.4 and 4.5.
When the relative humidity of the supplied air is changed from 30% to 71.9%, vapour diffuses from the moist air to the drier porous material. During this adsorption phase, the relative humidity inside the material rises (as well as the moisture content). For the reference case the relative humidity reaches its highest value of 68.02% at a depth of 12.5mm and 65.64% at a depth of 25mm before the relative humidity of the supplied air is lowered again. Hygroscopic materials like gypsum board store liquid moisture at a relative humidity below 100%. At low relative humidity ($RH < 40\%$) water molecules are adsorbed/desorbed at the porous walls which is accompanied by a heat of adsorption. As mentioned before, in this model the heat of adsorption is assumed to be equal to the heat of vaporization. Hence, even though the relative humidity in the surrounding air is only 71.9%, part of the water vapour entering the gypsum board will condense in the pores. This phase change in accompanied by latent heat release which explains the shape of the temperature curve on Figure 4.13. During the adsorption phase, water vapour condenses in the hygroscopic material resulting in a temperature rise in the material. During the desorption phase water vapour evaporates from the material which requires energy. As a result the temperature inside the gypsum

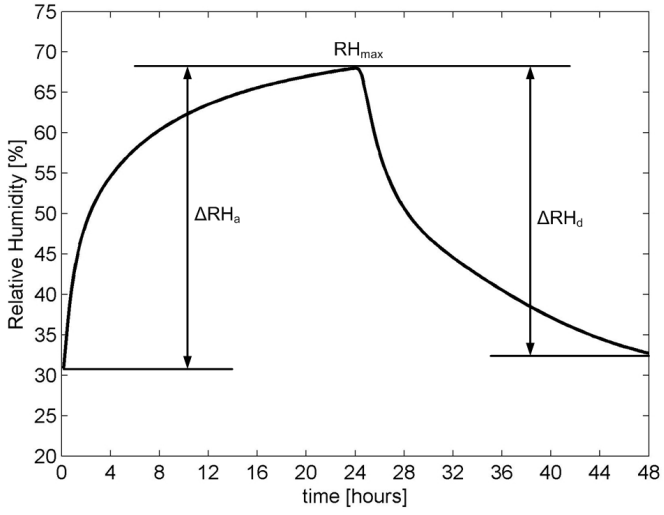

(a)

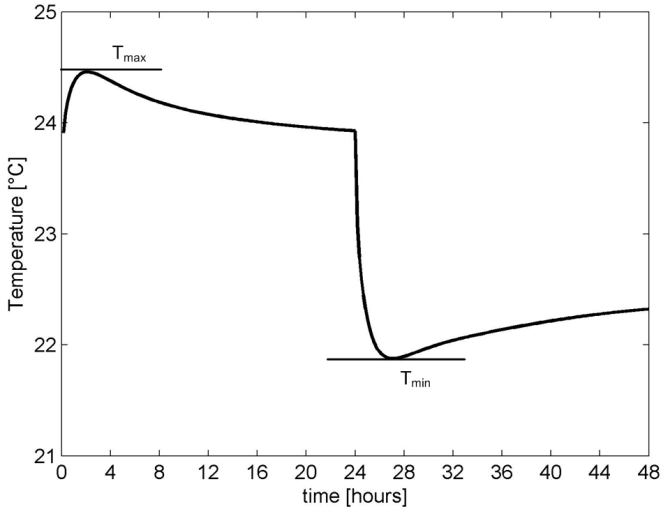

(b)

Figure 4.13: Typical response of the relative humidity (a) and temperature (b) in gypsum board at a depth of $12.5mm$ *for a step change induced in the relative humidity of the surrounding air (*$29.6 - 71.9\%RH$*)*

board drops.

Density, thermal conductivity and heat capacity variations

The reference case is compared to the cases with different material properties. These simulations clearly show that changes of 5% in dry density, thermal conductivity and heat capacity have virtually no effect on the model outcome regarding both temperature and relative humidity (see Table 4.4). The same results were also found by [87]. Olutimayin et al. measured and modelled heat and moisture transfer in cellulose insulation. He also performed a sensitivity analysis but changed the material properties by 10% instead of 5%. Still he concluded that the effect of thermal conductivity on the simulated temperature was less than 1% and could thus be neglected.

Sorption isotherm and vapour resistance factor variations

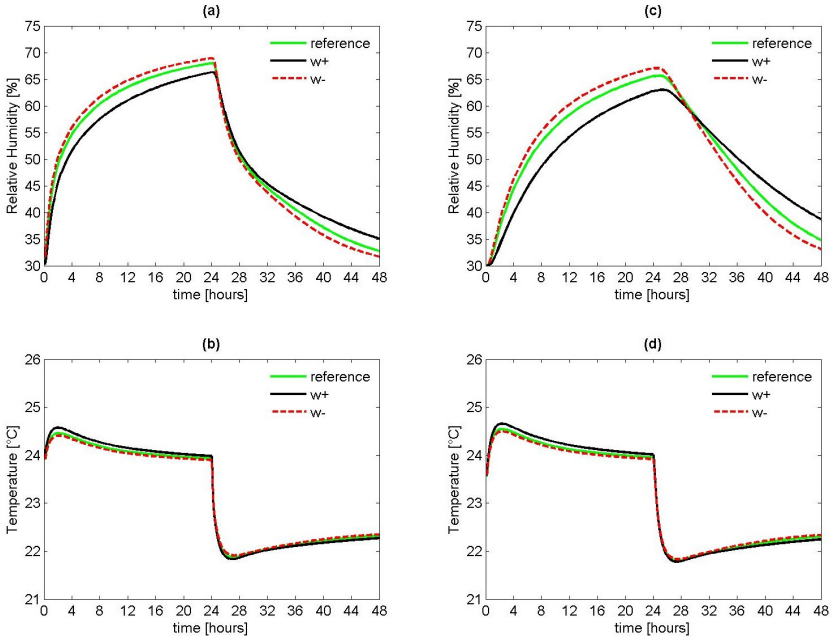

Figure 4.14: Effect of variation in sorption isotherm on the model outcome. Relative humidity at a depth of $12.5mm$ *in the gypsum board(a). Temperature at a depth of* $12.5mm$ *(b). Relative humidity at* $25mm$ *(c). Temperature at* $25mm$ *(d).*

Simulations were performed for different sorption isotherms and vapour resistance factors corresponding with the curves shown on Figure 4.11 and 4.12. The results of these simulations are shown in Figure 4.14 and 4.15.

	@12.5mm			@25mm		
	$\Delta RH_a\,[\%]$	$\Delta RH_d\,[\%]$	$RH_{max}\,[\%]$	$\Delta RH_a\,[\%]$	$\Delta RH_d\,[\%]$	$RH_{max}\,[\%]$
Reference case	38.02	35.31	68.02	35.64	30.83	65.64
Experiment	41	40.2	71.5	38.9	36.4	69.1
$\rho + 5\%$	38.02	35.32	68.02	35.64	30.84	65.64
$\rho - 5\%$	38.02	35.31	68.02	35.64	30.83	65.64
$\lambda + 5\%$	38.02	35.32	68.02	35.66	30.86	65.66
$\lambda - 5\%$	38.01	35.30	68.01	35.62	30.80	65.62
$C_{mat} + 5\%$	38.02	35.32	68.02	35.64	30.84	65.64
$C_{mat} - 5\%$	38.02	35.31	68.02	35.64	30.83	65.64
Sorption isotherm +	36.30	31.27	66.30	33.03	24.32	63.03
Sorption isotherm -	38.96	37.26	68.96	37.07	33.96	67.07
μ+	36.84	32.58	66.84	33.77	26.27	63.77
$\mu-$	39.18	37.97	69.18	37.51	35.45	67.51
$w + \mu-$	37.77	34.38	67.77	35.32	29.43	65.32
$w - \mu+$	37.88	34.74	67.88	35.35	29.76	65.35
$w + \mu+$	34.87	28.56	64.87	30.73	19.80	60.73
$w - \mu-$	39.99	39.46	69.99	38.79	37.65	68.79
RH + 2%	39.54	34.45	69.54	36.95	29.49	66.95
RH - 2%	36.38	36.09	66.38	34.21	32.09	64.21
T + 0.1°C	38.01	35.98	68.01	35.65	31.57	65.65
T - 0.1°C	37.94	35.23	67.94	35.55	30.71	65.55
Layered	40.18	39.11	70.18	39.12	37.08	69.12
Uniform	40.15	39.07	70.15	39.08	37.01	69.08
Brick	39.90	39.72	69.90	38.52	37.95	68.52
CaSi	37.22	34.99	67.22	34.53	30.58	64.53
Re = 5000	38.21	35.66	68.21	35.85	31.24	65.85

Table 4.4: Relative humidity change in the adsorption phase ΔRH_a, relative humidity change in the desorption phase ΔRH_d and the maximum relative humidity RH_{max} at a depth of $12.5mm$ and $25mm$.

	@12.5mm		@25mm	
	T_{max} [°C]	T_{min} [°C]	T_{max} [°C]	T_{min} [°C]
Reference case	24.46	21.88	24.54	21.81
Experiment	24.8	22.2	24.9	22.3
$\rho + 5\%$	24.44	21.89	24.53	21.82
$\rho - 5\%$	24.47	21.86	24.56	21.79
$\lambda + 5\%$	24.46	21.88	24.54	21.81
$\lambda - 5\%$	24.46	21.88	24.55	21.80
$C_{mat} + 5\%$	24.44	21.89	24.53	21.82
$C_{mat} - 5\%$	24.48	21.86	24.56	21.79
Sorption isotherm +	24.57	21.83	24.66	21.78
Sorption isotherm -	24.41	21.91	24.50	21.83
$\mu+$	24.37	21.97	24.44	21.92
$\mu-$	24.57	21.75	24.68	21.65
$w + \mu-$	24.70	21.69	24.81	21.61
$w - \mu+$	24.33	22.00	24.40	21.94
$w + \mu+$	24.48	21.94	24.54	21.91
$w - \mu-$	24.51	21.79	24.62	21.68
RH+2%	24.51	21.86	24.60	21.79
RH-2%	24.41	21.90	24.50	21.82
T+0.1°C	24.54	21.97	24.63	21.89
T-0.1°C	24.38	21.78	24.46	21.71
Layered	24.51	21.83	24.62	21.72
Uniform	24.52	21.81	24.63	21.71
Brick	23.86	22.36	23.86	22.36
CaSi	25.35	20.97	25.67	20.82
Re = 5000	24.34	21.97	24.43	21.90

Table 4.5: Maximum temperature T_{max} and minimum temperature T_{min} during simulation at a depth of $12.5mm$ and $25mm$.

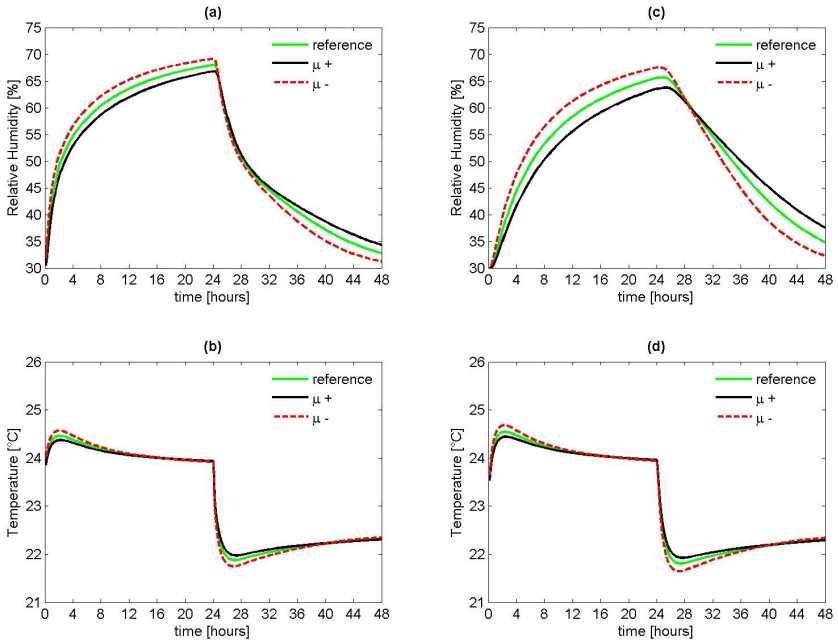

Figure 4.15: Effect of variation in vapour resistance factor on the model outcome. Relative humidity at a depth of $12.5mm$ *in the gypsum board (a). Temperature at a depth of* $12.5mm$ *(b). Relative humidity at* $25mm$ *(c). Temperature at* $25mm$ *(d).*

Figure 4.14 shows that a higher sorption isotherm (w+) results in a decrease of the maximum relative humidity by 1.72% points and a decrease of the sorption isotherm (w-) results in a relative humidity increase by 0.94% points. These values are relatively low compared to the differences between the sorption isotherms. A variation of the sorption isotherm also affects the simulated temperature. The temperature change due to latent heat effects is slightly smaller for a lower sorption isotherm and slightly larger for a higher sorption isotherm. These results correspond with what can be physically expected. A higher sorption isotherm will result in a higher moisture content and a higher specific moisture content ($\partial w/\partial RH$). This means that the same moisture content would correspond with a lower relative humidity or, more vapour would have to diffuse into the porous material to reach the same relative humidity. In other words it will take a longer time for the air in the porous material to reach a certain relative humidity. The temperature variation due to the phase change increases because more vapour condenses during adsorption and evaporates during desorption.
Talukdar et al. [86] performed a similar study for spruce plywood and applied a 10% variation for each material property. They found similar results. Increasing the sorption isotherm with 10% resulted in a reduction of the relative humidity by 6% relative to the applied step change, which was 50%RH. A reduction of the sorption isotherm increased the relative humidity by 6% relative to the step change. They found that the difference between the measured and the simulated values for relative humidity were typically smaller than the fluctuations they found when using different sorption isotherms. They concluded that the sorption isotherm they used for the modelling agreed well with reality.
Changing the vapour resistance factor by a higher or lower curve also changes the model outcome (see Figure 4.15). Similar to the higher sorption isotherm, a higher vapour resistance factor results in a lower relative humidity during the adsorption phase and a higher relative humidity during the desorption phase. The opposite counts for a lower vapour resistance factor. Again, the effect is more pronounced deeper in the material.
A higher vapour resistance factor corresponds to a lower vapour permeability. Thus it is more difficult for the water vapour to penetrate the porous material. This explains why a lower relative humidity is found during adsorption and a higher relative humidity is found during desorption. Simultaneously the temperature change due to the latent heat effect is less pronounced for a higher vapour resistance factor and the other way around for a lower vapour resistance factor.
However, in reality the sorption isotherm and vapour resistance factor do not change independently since both are function of the pore structure. To investigate the combined effect of a changed sorption isotherm and vapour permeability, four simulations were performed: high sorption with high vapour resistance (w+ μ+), high sorption with low vapour resistance (w+ $\mu-$), low sorption with high vapour resistance (w- μ+) and low sorption with low vapour resistance (w- $\mu-$). The results of these simulations are shown in Figure 4.16. Again a higher sorption isotherm (associated to a larger moisture capacity) results in a lower relative humidity during adsorption and a higher relative humidity during desorption. In

other words this will dampen the humidity variation in the material. Combining this higher sorption isotherm with a higher vapour resistance will further reduce the amplitude of the humidity change in the material. On the other hand, the combination with a lower vapour resistance will counter the effect which explains why the curve for w+ $\mu-$ does not differ much from the reference simulation.

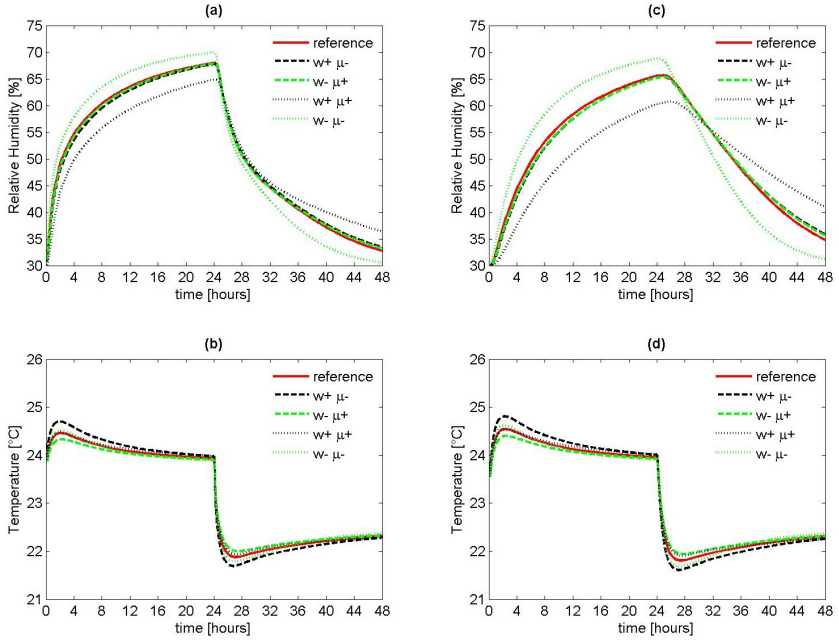

Figure 4.16: Combined effect of sorption isotherm and vapour resistance factor. Relative humidity and temperature at a depth of $12.5mm$ *in the gypsum board (a,b) and at* $25mm$ *(c,d).*

Similar effects are found for a lower sorption isotherm combined with a higher vapour resistance. A lower sorption isotherm will result in a higher relative humidity during adsorption and a lower relative humidity during desorption. A combination with a higher vapour resistance (w- $\mu+$) will reduce the effect and will result again in a relative humidity curve that does not differ a lot from the reference case. On the other hand, a combination with a lower vapour resistance (w- $\mu-$) will intensify the relative humidity increase/decrease. In other words, the relative humidity change in a material is damped by a higher moisture capacity and slowed down by a lower permeability (higher vapour resistance).
Also the temperature is influenced by a change in sorption and/or permeability. This is shown in Figure 4.16 (b) and (d). Unlike the relative humidity response, the largest effect is found for w+ $\mu-$ and w- $\mu+$. A low vapour resistance means that vapour easily diffuses into or out of the material. A combination with a high

sorption means that this vapour is easily stored by the material in the liquid phase. So more water vapour will condense/evaporate resulting in an increased latent heat effect. A high vapour resistance and a low sorption isotherm results in a reduced latent heat effect.
With respect to the latent heat effects, a high sorption isotherm and high vapour resistance (w+ μ+) counteract each other. A high sorption (and higher moisture capacity) will increase the latent heat effect, a higher vapour resistance (lower permeability) will reduce the latent heat effect.

Note that the combination of the sorption isotherms and the vapour resistance factors is arbitrary and does not necessarily correspond with a real material. To find out if similar conclusions still hold for real materials two extra simulations were performed on two other materials. The first material is calcium silicate (CaSi). This material has a higher sorption isotherm than gypsum board and also a higher permeability. The second material is ceramic brick, which has a much lower permeability and sorption isotherm than the gypsum board. The material properties for these cases were taken from [108]. To model the sorption isotherm and the vapour resistance, again the analytical functions given by Eqs. 4.2 and 4.3 are used. The corresponding coefficients are found in Table 4.6. The simulation results are shown in Table 4.4 and 4.5 and in Figure 4.17. For CaSi almost no change in relative humidity is found. A higher sorption isotherm and a higher permeability counter each other with respect to the relative humidity response of the material. However, more vapour condenses in the CaSi during adsorption resulting in a higher latent heat effect. These results correspond with the previously discussed w+ $\mu-$ case.
Ceramic brick has a much higher vapour resistance and a lower sorption isotherm than gypsum board. This results in almost no latent heat effect temperature change in the material. These results correspond with the w- μ+ case. However, due to the much lower sorption isotherm, less water condenses inside the material and the relative humidity inside the material is less damped due to the lower moisture capacity. These simulations prove that the model predicts the correct trends.

Influence of air velocity, transfer coefficients, inlet temperature and relative humidity

Simulation results shown up till now were all computed with laminar flow conditions. The average inlet velocity of $0.82m/s$ corresponds with Re = 2000. Increasing the Reynolds number to 5000, and thus increasing the average velocity, results in a turbulent flow over the gypsum sample. Increasing the Reynolds number will also increase the transfer coefficients for heat and mass. Nevertheless, when analyzing the results in Table 4.4 and 4.5 it is clear that this higher mass transfer coefficient has almost no effect on the response of the relative humidity inside the material. Mass transfer between the air and the porous materials is thus obviously dominated by the vapour diffusion resistance and not by the mass transfer coefficient. The same conclusions were also drawn in subtask 2 of Annex

	Calcium silicate	**Ceramic brick**
Density ρ (kg/m^3)	270	2005
Porosity ψ_0 (-)	0.894	0.157
Thermal conductivity λ (W/mK)	$0.06 + 5.6 \times 10^{-4} w$	$0.5 + 4.5 \times 10^{-3} w$
Heat capacity C_{mat} (J/kgK)	1000	840
Sorption isotherm		
a	894	157
b	0.000254	0.000111
c	1.38112	1.485996
Vapour resistance factor		
μ_0	5.420218	29.10871
a	0.053657	-0.00031
n	31.5258	2.075083

Table 4.6: Material properties of calcium silicate and ceramic brick adopted from [108]

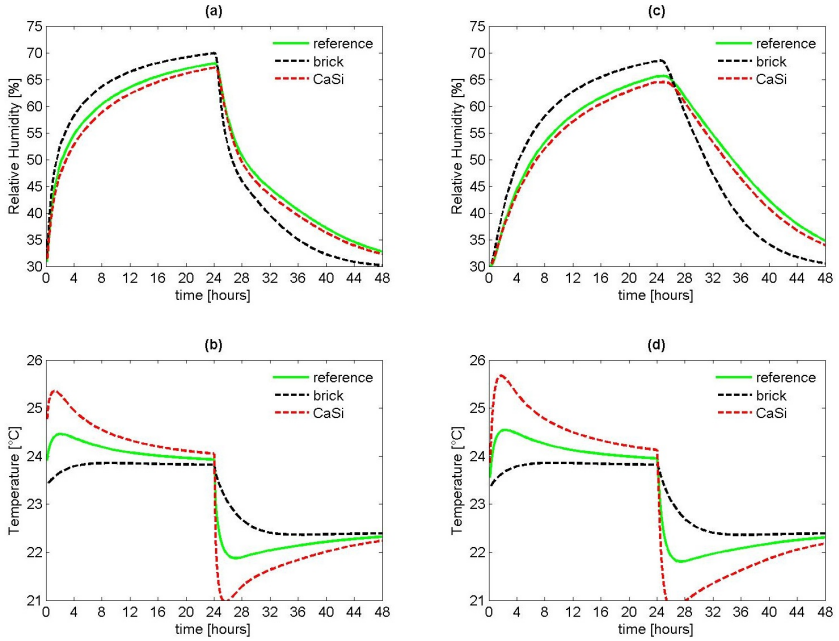

Figure 4.17: Comparison of the model results for CaSi, brick and gypsum board.

41 [111] where a change of 10% in the mass transfer coefficient had no significant effect.
Increasing the heat transfer coefficient leads to changes in the temperature response. In case of a higher heat transfer coefficient, the temperature change due to the latent heat effect is damped out due to the better heat transfer from the material to the air.
Two more boundary conditions can be considered: the inlet temperature and inlet relative humidity. These conditions were measured during the experiments and are accompanied by an uncertainty. For the temperature this uncertainty was 0.1°C, for relative humidity this uncertainty was 2%RH. An under- or overestimation of these boundary conditions will affect the model results. To evaluate the impact of an incorrect boundary condition estimation, simulations with altered inlet conditions were performed (inlet temperature ± 0.1°C, inlet relative humidity $\pm 2\%$). The results of these simulations are found in Table 4.4 and 4.5. Changing these parameters clearly has a direct impact on the model outcome. Changes to the inlet temperature only affect the temperature result inside the material and have almost no effect on the relative humidity in the material. However, changing the inlet relative humidity affects both temperature and relative humidity. A higher inlet relative humidity will result in a higher relative humidity inside the material, but also a higher latent heat effect in the material, because more water vapour will condense.

Hysteresis versus no hysteresis modelling

For most porous materials there is no unique relationship between the moisture content and the relative humidity because hysteresis occurs during the sorption/desorption process. The material will behave differently during adsorption and desorption. Therefore a hysteresis model based on the *ink bottle effect* was included in the coupled CFD-HAM model. This model was originally proposed by Mualem [115] and then later simplified by Milly [116]. A more detailed explanation of this model is found in [1].
Temperature and relative humidity measured by James et al. [112] at a depth of $12.5mm$ and $25mm$ in the gypsum board are plotted on Figure 4.18. The uncertainties on the measurements were $\pm 2\%$ for relative humidity and ± 0.1°C for temperature. No perfect match between the measured and simulated relative humidity was found, but the results were still acceptable. To obtain a better agreement between the model and the experiment, the relative humidity should be higher during the adsorption phase and lower during the desorption phase. Figure 4.18 shows that the agreement is better at a depth of $12.5mm$ than at $25mm$.
Implementing a hysteresis model improves the predicted relative humidity during the desorption phase. This is in agreement with the expectations. The hysteresis model uses a desorption isotherm during the desorption phase which has higher values for moisture content than the adsorption isotherm at the same relative humidity. As a result, implementing a hysteresis model gives similar results during desorption as the lower isotherm (w_a-) in Figure 4.11. Combining a lower

sorption isotherm with hysteresis result in an even better agreement, also during the adsorption phase as would be expected.
The agreement between the simulated and measured temperatures is rather poor. Strange fluctuations in the measured temperature are found which could be explained by the fluctuating inlet temperature. Although the test setup was designed to supply a constant inlet temperature, reality showed that this was not always the case. Inaccurate positioning of the thermocouples and RH sensors could also explain some of the deviations. Therefore it is hard to conclude whether the model has good agreement for temperature or not.

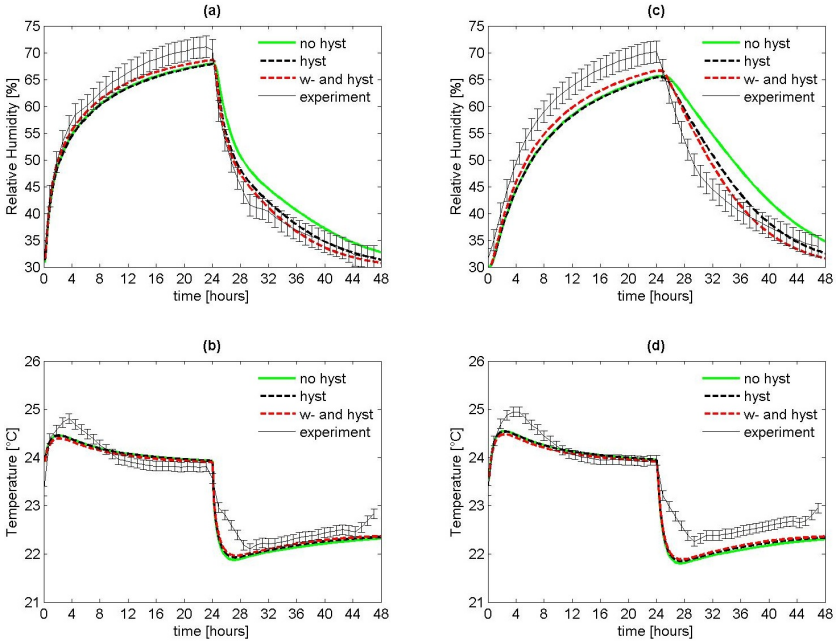

Figure 4.18: Comparing the model with hysteresis and without at a depth of $12.5mm$ *(a,b) and* $25mm$ *(c,d) for relative humidity and temperature.*

Modelling gypsum board as layered

Gypsum board is built up out of multiple layers but modelled as a uniform material which could affect the simulations. The gypsum board used in this study has a thickness of $12.5mm$ and consists out of three layers: a layer of finishing paper at both sides (thickness $0.5mm$) and a layer of gypsum in between (thickness $11.5mm$). Roels et al. [117] measured the material properties for each layer separately. The sorption isotherm and the vapour resistance factor for paper and gypsum are given by Eqs. 4.4 and 4.5. The corresponding coefficients are listed

		Sorption isotherm	
	w_{sat}	a	n
Finishing paper	155	1.35e-6	1.48
Gypsum	130	50.7e-6	1.55
Uniform	130	24.8e-6	1.52
	Vapour resistance factor		
	a	b	c
Finishing paper	0.1	4.78e-3	4.10
gypsum	0.1	4.78e-3	4.10

Table 4.7: Coefficients for the sorption isotherm and vapour resistance factor of finishing paper and gypsum [117]

in Table 4.7. No hysteresis is considered so only the adsorption isotherm is used.

$$w = w_{sat}\left(1 + \left(-a\rho_l R_v T \ln\left(RH\right)\right)^n\right)^{(1-n)/n} \tag{4.4}$$

$$\mu = \frac{1}{a + b\exp\left(cRH\right)} \tag{4.5}$$

Here ρ_l represents the liquid water density ($998.2kg/m^3$) and R_v is the specific gas constant for water vapour ($462J/kgK$).
Figure 4.19 shows the simulation results for relative humidity and temperature in the gypsum board for uniform modelling and layered modelling. These results differ from the reference case because a slightly different sorption isotherm and vapour resistance have been used: the curves used here are the ones measured by Roels et al. [117] and correspond to the lower curves in Figure 4.11 and Figure 4.12. This explains why the predicted relative humidity is higher during adsorption and lower during desorption. The difference in simulated relative humidity and temperature for the uniform and layered modelling is negligibly small. By consequence modelling the gypsum board as layered has limited impact on the model outcome.

4.5.4 Discussion en conclusions

During the research by Steeman [1] a first validation of the coupled CFD-HAM model was performed using the measurements performed by Talukdar et al. [86, 112]. An additional validation experiment was conducted and is elaborated in section 4.4. Finding a perfect match between the measurements and the simulations was difficult. However inter-model comparison conducted during IEA ANNEX 41 [111] and in [112] showed good agreement between the different models, including the here discussed coupled CFD-HAM model. All models showed similar deviations from the measurements. In the previous section an

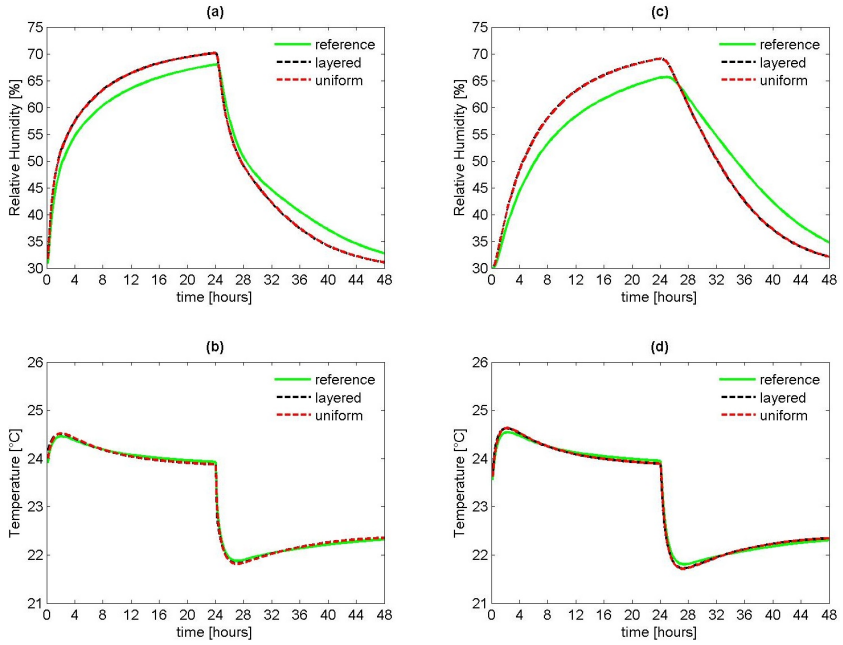

Figure 4.19: Modelling gypsum board as a uniform material or layered. Temperature and relative humidity at a depth of $12.5mm$ *(a,b) and* $25mm$ *(c,d).*

attempt was made to find an explanation for the deviations. It was postulated that the discrepancies between the model and the measurements are probably due to uncertainties in the model inputs: material properties and boundary conditions. Therefore an extensive sensitivity study was performed based on a *One-at-a-Time* analysis. In this analysis only one parameter is altered while the other parameters are fixed.

First five material properties were evaluated: density (and porosity), thermal conductivity, heat capacity, sorption isotherm and vapour permeability. The first three properties listed here (density and the thermal properties) can be measured quite accurately. The uncertainty on these properties is small, often less than 5% [114]. Changes of 5% of these parameters showed almost no effect on the model outcome.

Previous studies showed that measuring hygrothermal properties such as sorption isotherm and vapour resistance is much more difficult [110]. The material properties of the material used for the experiment of Talukdar et al. [86] were determined by 14 laboratories in total [111]. This allowed an estimation of the uncertainty on these material properties. From this analysis an average, minimum and maximum value for the sorption isotherm and vapour resistance was determined. These values are then used for the sensitivity analysis. Deviations in these hygrothermal material properties could mount up to 20%. From the analysis in section 4.5.3 it can be seen that these deviations translate to differences in predicted relative humidity of 2% points. This indicates that the discripencies found between the measurements and simulations (as shown in Figure 4.18) can be atributed to the uncertainties in the material properties.

The temperature measurements performed by Talukdar et al. [86] were not well suited for validation purposes. Temperature validation could however be realized with the new benchmark experiment described in section 4.4. A good agreement between measured and simulated temperature was found. The remaining discrepancies between the measurements and simulations from section 4.4 were attributed to uncertainties in the boundary conditions. The uncertainty on the inlet temperature was of the same magnitude as the temperature measured in the chamber (± 0.1°C) and the same counts for the relative humidity ($\pm 1.4\% RH$). A wrong estimation of the inlet temperature and humidity is directly translated to a mismatch of the simulation outcome. The inlet velocity has only little influence on the model outcome since the vapour transport in hygroscopic porous materials is dominated by the vapour diffusion in the porous material.

Finally the impact of some model simplifications was studied. When gypsum board was modelled, the material was assumed uniform, while in reality it is built up out of different layers. Also the effect of hysteresis was not implemented in the model. Figure 4.18 shows the simulation results when a hysteresis model is implemented. This figure shows that the impact of a hysteresis model is of the same order of magnitude as the impact of material property uncertainty. Figure 4.19 on the other hand showed that modelling gypsum board as layered had no effect on the model outcome.

In short the discrepancies with the measurements are at the one hand due to

uncertainty in the hygrothermal material properties and at the other hand due to uncertainty of the input boundary conditions. Bearing this in mind it can be stated that the model agrees well with measurements.

5

Validating the coupled CFD-HAM model including liquid water transport

5.1 Introduction

In chapter 3 it was shown that it is possible to formulate and implement a coupled CFD-HAM model which is able to model the heat transport in air and porous materials in conjugation with the vapour and liquid water transport.
This chapter will discuss in more detail the implementation and validation of the liquid water transport model.

To study the liquid transport in a porous material one specific type of transport problems is highlighted: convective drying of porous materials. Convective drying can be defined as the removal of water from a wet material by a drying medium, in most cases air, which flows over the material. When the vapour pressure in the air is lower than the surface vapour pressure, water will evaporate from the material surface and is transported away from the surface by the moving air.
Convective drying combines some important features of the coupled CFD-HAM model. This makes it an interesting case to validate the model with. During convective drying of a porous material liquid water and water vapour is transported in the material in strong combination with heat transport. It will be shown in this chapter that heat and mass transport cannot be solved separately when studying drying. At the same time drying rates are strongly determined by convective transport in the air. It is thus important to model not only the transport in the material accurately but also the transport in the air.

This chapter is basically composed of three parts. The first two sections give a more detailed description of drying phenomena and an overview of the state of the art in convective drying modelling. Next the coupled CFD-HAM model is validated with a well documented drying experiment from literature [43]. Finally a new drying experiment is discussed and used for model validation. This new experiment uses different boundary conditions and another material, which results in a different drying behaviour.

5.2 Short introduction to drying phenomena

Convective drying of porous materials is of importance in a wide range of application areas [35]. Some examples where convective drying is applied on an industrial scale are drying of foods, biofuels, paper, textiles, wood, coal,... In the present study the focus lies on the drying of porous building materials. Convection is the most common mode for drying in the built environment. Generally in convective drying, heat is supplied by heated air (or gas) flowing over the surface of the porous material. Other modes of drying are conductive drying where the heat needed for evaporation of the moisture from the surface is provided through conduction and radiative drying where the necessary heat is provided through e.g. microwaves or solar radiation. Microwave drying is not of importance in the building context and will not be discussed here.

Moisture in a porous material can be either bound or unbound. Removing unbound moisture can generally be done by two means: evaporation and boiling [35]. Boiling occurs when the vapour pressure at the surface and in the material equals the atmospheric pressure. This is accomplished by raising the temperature of the porous material to the boiling point of water. In evaporation, drying is carried out by convection, that is, by passing air over the material. If the partial vapour pressure of the air is lower than the vapour pressure at the surface, moisture will be transferred to the air and is carried away. In this case the saturation vapour pressure is less than the atmospheric pressure. Drying accomplished in a building environment is almost always due to evaporation. Therefore, from here on convective drying will always refer to drying by evaporation, unless mentioned otherwise.

Figure 5.1 qualitatively depicts a typical drying rate curve of a capillary active hygroscopic material. The actual time evolution of the drying rate depends on the moisture content, the material characteristics and the air conditions (temperature, vapour pressure, velocity). During the first stage of drying, the drying rate is constant, therefore it is also referred to as constant drying rate period (CRP). The surface contains free moisture. This moisture evaporates from the surface during the drying process. The drying rate is determined by the diffusion rate of water vapour into the surrounding air. In other words the drying rate is in this stage

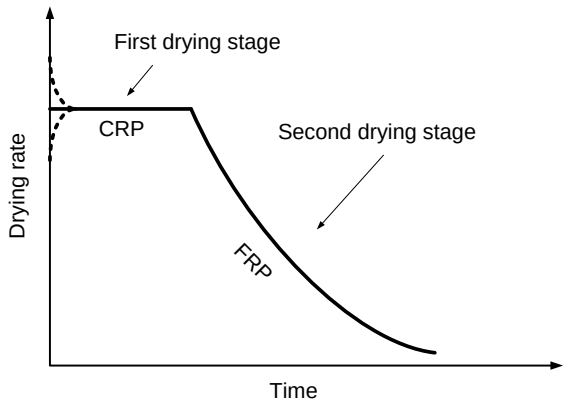

Figure 5.1: Typical surface averaged drying rate curve

determined by the exterior air conditions (temperature, humidity and velocity). During the constant drying rate period moisture is transported from the inside of the porous material to the surface by capillary forces. As long as this transport equals the evaporation rate from the surface, the drying rate will remain constant (if the boundary conditions remain constant).
If the moisture content reaches a critical level at which the moisture can no longer reach the surface at a sufficient rate, further drying will cause dry spots to appear on the surface. The wet areas will still have a high drying rate but the surface averaged drying rate will drop. This is the start of the second drying stage or the first part of the falling rate period (FRP).
The drying rate will be determined by the internal moisture transport as a result of moisture concentration gradients in the material. As the material dries out, moisture movement decreases further and consequently the drying rate drops. The drying rate continues to fall until the moisture content inside the material is in equilibrium with the surrounding air. At that point the drying rate becomes zero and drying stops.
For actual drying the transition between the different regimes may be less sharp as depicted in Figure 5.1. Also temperature will play an important role in the drying rate. The drying rate at the surface is amongst others determined by the difference in partial vapour pressure at the surface and partial vapour pressure of the surrounding air. A higher difference will result in a higher drying rate. During the first drying stage, the surface is saturated with moisture and the partial vapour pressure at the surface will be the saturation vapour pressure. This saturation vapour pressure depends on the temperature according to the Clausius-Clapeyron equation (Eq. 2.3). Higher temperatures will result in higher saturation vapour pressure and vice versa. During the first drying period (CRP) the temperature

will attain the wet bulb temperature. If however the starting temperature in the material is higher than the wet bulb temperature, the temperature will start to drop and accordingly the drying rate will also drop. When initially the temperature is lower than the wet bulb temperature, the material temperature will start to rise and so will the drying rate initially. This is indicated on Figure 5.1 by the dashed lines.

Solid materials can be classified according to their transport properties as follows [35, 36]:

Non hygroscopic capillary-porous media. For this type of materials there is a clearly recognizable pore space. These pores will be filled with liquid water if the material is saturated. The amount of physically bound water is negligible (the material is non hygroscopic). No shrinkage will occur during drying. Material examples are sand and some ceramics such as ceramic brick.

Hygroscopic-porous media. For this type of materials there is again a clearly recognizable pore space. There will be however also a large amount of physically bound liquid. This will result in a significant amount of water stored in the material even at relative humidities below 100%. This category can be further subdivided into two groups: the **hygroscopic capillary-porous media** and the **strictly hygroscopic media**. Examples of hygroscopic capillary-porous media where micropores as well as macropores are present include wood, clay textiles and cement based material. Examples of strictly hygroscopic materials where only micropores are present include silica gel and alumina. Hygroscopic materials cannot be dried to a moisture content of zero. The lowest atainable moisture content is the equilibrium moisture content corresponding with the relative humidity of the surrounding air at a given temperature.

Colloidal (non-porous) media. In these materials there is no clearly defined pore space and all liquid is physically bound. Examples are soap, glue and various food products.

Since most building materials are hygroscopic and/or capillary porous of nature, only these two classes will be of importance in this work. The latter class (colloidal) will not be discussed.

Each type of material will have a different drying progress due to its nature. For a capillary-porous material typical moisture content profiles for convective drying are shown in Figure 5.2.
The fired-clay brick used in the measurements and simulations shown in Figure 5.2, is clearly a capillary porous material. At first the moisture content in the brick seems to equally decrease over the entire brick depth. This is during the first drying stage (CRP). Liquid moisture is still easily provided to the surface and the brick uniformly dries out. When the moisture content in the brick becomes

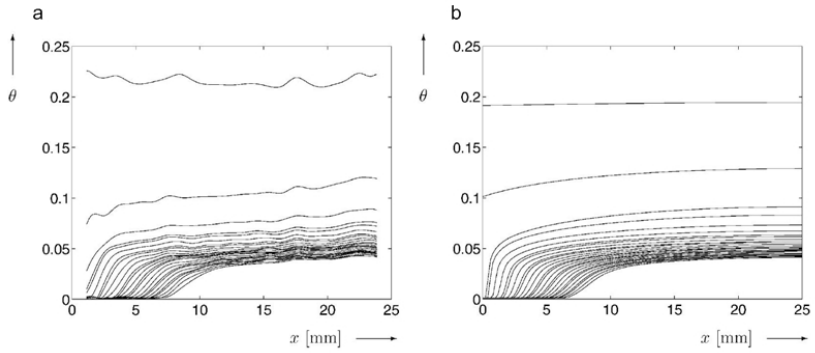

Figure 5.2: Typical moisture profiles with time for fired-clay brick. The time between subsequent profiles is 2 hours. (a) shows the measured profiles, (b) shows the simulations according to Landman et al. [118]. The x-axis represents the depth in the material [mm], the y-axis represents the moisture content [m^3/m^3].

too low and reaches a critical moisture content, the moisture at the inside of the material can no longer be provided to the surface at a sufficient amount and the surface dries out. The drying enters the second drying stage (FRP). During this stage a drying front develops inside the material and slowly moves inside the brick. The drying rate is now internally determined by the diffusion rate inside the brick.

Figure 5.3 compares the drying curves during drying of a capillary porous material (non hygroscopic)(Figure 5.3(a)) and a hygroscopic material (Figure 5.3(b)). Both materials start at a saturation moisture content W_0. At the surface ($x = 0$) the porous material is dried by a drying medium (e.g. air). As time progresses the moisture content in the material decreases. Figure 5.3 shows a strongly different drying behaviour for both material types. As already mentioned the capillary porous material will first dry out evenly. As the moisture content decreases, the moisture content near the surface will decrease faster since at lower moisture contents not enough water can be transported to the surface to compensate the water leaving the surface through evaporation. If the surface is dried out, the drying rate is dominated by the moisture transport in the material and a clear moisture front is formed which moves into the material as the drying process proceeds.
Initially the hygroscopic porous material will dry out similarly to the capillary porous material. However the moisture content will not drop below the equilibrium moisture content W_{eq}. This is the moisture content corresponding with the relative humidity of the surrounding air. If the moisture content at the surface drops below the maximum hygroscopic moisture content W_{hygr}, the drying rate will start to decrease. Near the surface, vapour diffusion becomes the dominant moisture

transport mechanism. As soon as the moisture content of the entire material is below W_{hygr}, the moisture transport and drying rate are completely governed by vapour diffusion.

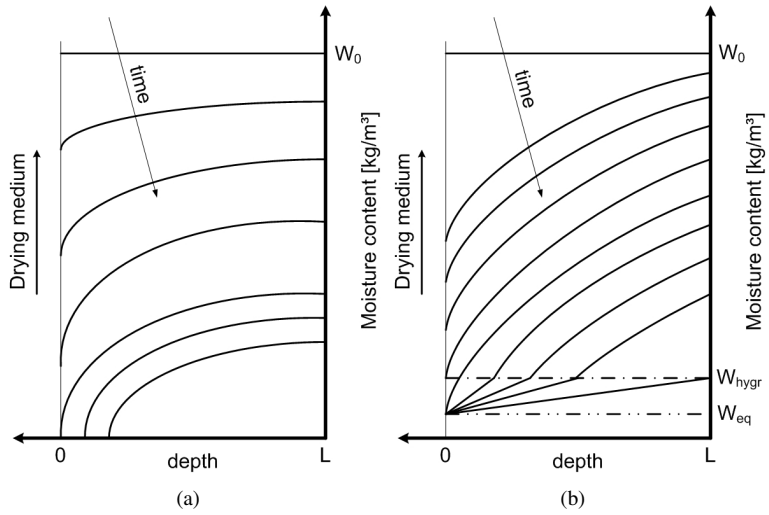

Figure 5.3: Moisture content profile evolution in time during the drying of (a) a capillary porous material and (b) a hygroscopic material. Figures based on [36].

5.3 Modelling convective drying

In the convective drying studied here, the dried medium is a porous material (hygroscopic and/or capillary active) and the drying medium is (moist) air. There is a wide range of literature available that studies the interaction of a wet porous material and the surrounding air. In the large collection of available models two groups can be distinguished: analytical models and numerical models.
Analytical models are often confined to 1D models. The applied boundary conditions are fixed temperature and humidity at the boundary (Dirichlet (first-type) boundary conditions), fixed fluxes at the boundaries (Neumann (second-type) boundary conditions) or fixed transfer coefficients (Robin (third-type) boundary conditions). The impact of the air on the drying process is incorporated in these boundary conditions. Only boundary conditions of the third type can be used to model convective drying. If more complex boundary conditions are present, like spatially and/or temporally varying boundary conditions, 1D models do no longer suffice and most often more-dimensional numerical models have to be addressed.
Numerical convective drying models can be subdivided into two main categories,

depending on how the interaction with the drying medium (often air) is modelled. The first category of models uses transfer coefficients to model the convective heat and mass transfer. A second category of models uses a conjugated approach. Momentum, heat and mass transport in the air are solved simultaneously with the heat and mass transport in the porous material, while continuity of the temperature, the mass fraction and the heat and mass fluxes at the interface are assured. In the following section a short overview is given of the state-of-the-art modelling approaches for combined heat and mass transport during convective drying in air.

5.3.1 Analytical modelling

In its simplest form drying can be described by a diffusion equation with the diffusivity considered to be constant (Eq. 5.1). It is then possible to derive an analytical solution for this type of equations [68, 119].

$$\frac{\partial w}{\partial t} = D\frac{\partial^2 w}{\partial x^2} \tag{5.1}$$

Analytical solutions can be useful to gain a better insight in drying physics and can be used to verify more complex models. For example Milly [66] developed an analytical solution to a 1D coupled heat and moisture transport problem based on the solutions provided by Cranck [68]. He used this analytical solution to verify his 1D numerical finite element model. The same verification exercise was used in chapter 3. The model described by Milly in [66] only uses boundary condition of the first kind (constant value) and second kind (constant flux).
Recently Abahri et al. [120] developed an analytical solution of the coupled 1D heat and moisture transfer problem in porous building materials with boundary conditions of the first kind. Again a constant diffusivity was assumed.

Drying problems however often have a complex nature and the simplified 1D diffusion equation with constant diffusivity does not suffice to capture all drying phenomena in detail. Therefore Landman et al. [118] developed an approximate analytical solution for a 1D drying process of brick with non-linear diffusion and a mass transfer coefficient at the surface. They compared their model with a numerical model and experimental results performed by Pel [121]. The objective of their study and modelling approach was to obtain a better insight in drying phenomena.
Landman et al. conclude that an analytical solution for non-linear diffusion problems can only be found for limited types of diffusion functions (such examples are found in [68], e.g. exponential functions). The model proposed by Landman et al. is isothermal and thereby strongly simplified. Nevertheless Landman et al. were able to give a good estimate of the drying front speed travelling into the dried material.

However most convective drying processes do not allow simplifications as stated above. In case of convective drying of building materials the diffusivity

shows strong non-linearities. Moreover, building components can be built up out of multiple materials with different properties for heat and mass giving it a strong heterogeneous character. At the same time the boundary conditions are not fixed in time and space, resulting in 2- and 3-dimensional distributions of temperature and moisture. Consequently it is no longer feasible to solve all coupled heat and mass transport problems, especially drying problems, by analytical approaches. Using numerical techniques to solve the coupled partial differential equations that describe the transport in porous materials, allows to overcome some of these issues.

5.3.2 Convective transfer coefficients as a boundary condition

To incorporate the influence of airflow properties on convective drying without modelling the convection in the air simultaneously with transport in the porous material, there is often resorted to transfer coefficients. In numerical modelling this is referred to as boundary conditions of the third kind.
A distinction can be made between models using constant (averaged) convective transfer coefficients and spatially varying transfer coefficients. These transfer coefficients can be found in literature where they are derived analytically (e.g. [122, 123]), experimentally (e.g. [124]) or from CFD simulations (e.g. [72, 89, 124]).

Constant or averaged convective transfer coefficients

Most of the currently used HAM models for building envelope simulations apply constant transfer coefficients at their boundary (e.g. [8, 29]). Hagentoft et al. [27] developed a series of one-dimensional benchmark cases for the combined heat, air and moisture transport in building components. The transfer coefficients at the surfaces were taken to be constant. A distinction was made between inside conditions and outside conditions. It was assumed that the material side facing the building interior, was mostly subjected to natural convection. The material side facing the exterior, resulted in higher convection coefficients. In ASHRAE Fundamentals [9] approximate values for these coefficients are given. The apparent transfer coefficients for heat range from

$$\begin{aligned} h_o &= 16.7 \; to \; 33.3 \, W/(m^2 K) \\ h_i &= 5 \; to \; 8.3 \, W/(m^2 K) \end{aligned} \tag{5.2}$$

Here h_o is the outside heat transfer coefficient and h_i the inside coefficient. The so-called apparent transfer coefficient is defined as the combination of the convective and radiative transfer coefficient, h_c and h_r respectively.

$$q = h(T_{en} - T_s) \tag{5.3a}$$

$$h = h_c + h_r \tag{5.3b}$$

Hagentoft et al. [27] used $h_o = 25W/m^2K$ and $h_i = 8W/m^2K$ as constant apparent heat transfer coefficients for inside and outside. These values clearly range within the suggested values by ASHRAE [9]. The mass transfer coefficients were derived from these values by using the heat and mass analogy. This resulted in $h^p_{m,o} = 2 \times 10^{-7} s/m$ and $h^p_{m,i} = 3 \times 10^{-8} s/m$ with h_m the mass transfer coefficient. The superscript p indicates that this is the transfer coefficient valid for partial vapour pressure as driving force.
T_{en} is the environmental temperature and combines the temperatures of the surfaces within the field of view of the considered envelope assembly and the air temperature. For indoor surface heat transfer this approach may be acceptable when only heat transfer is considered. However ASHRAE [9] states that this approach becomes questionable when heat transfer at the outdoor surface is considered. In this case T_{en} must include all short- and long-wave radiation contributions perpendicular to the assembly's exterior surface. For moisture transfer calculations, T_{en} is best not used. In this case it is better to calculate the heat flux contributions from short- and long-wave radiation separately.

Besides HAM models for building envelope studies, several models have been developed to study convective drying of porous materials. Berger et al. [125] were able to study drying phenomena using a 1D finite difference model with constant heat and mass transfer coefficients as boundary conditions. The influence of various internal and external physical parameters was studied. Amongst others their study showed the impact of transfer coefficients on the drying rate. This model showed that the convective transfer coefficient determined the drying rate during the constant drying rate period. During the falling rate period the drying rate is mostly determined by the internal transport properties and the impact of the convective transfer coefficients is negligible. Although these conclusions were derived with a simplified 1D model, they can be generally used.

Wang et al. [126] used transfer coefficients from literature for both the mass and the heat transfer. A 1D model for the study of convective drying of food, more specifically potatoes was developed. This model incorporated the effect of shrinkage during drying. Since vapour density was used as the driving force in Wang's model, the convective mass transfer coefficient becomes apparently dependent on the vapour density. This reveals a first disadvantage of the use of transfer coefficients. Different authors use different driving forces for mass transport, resulting in different transfer coefficients.
Steeman et al. [23] stated that it is erroneous to assume that transfer coefficients can be translated directly from one driving force to another. This significantly complicates the interchangeability of transfer coefficients found in literature. In literature different variables are used to express the amount of water vapour in the air: water vapour density $\rho_v[kg/m^3]$, water vapour partial pressure $p_v[Pa]$, mole fraction $Z[mol/mol]$ or vapour mass fraction $Y[kg/kg]$. A study by Steeman et al. [23] showed that it is best to use the mass fraction difference as driving force. Convective mass transfer coefficients related to vapour pressure as driving force

are only applicable to isobaric systems and mass transfer coefficients related to vapour density are only allowed under constant density conditions (in other words constant temperature, relative humidity and pressure).

Using a constant transfer coefficient is not always justified. Transfer coefficients can only be assumed constant over the surface of a porous material if all boundary layers are fully developed. This is often not the case even for simple geometrical conditions. The presence of developing boundary layers or complex geometries with leading edge effects, vortex shedding, reattachment and stagnation zones leads to large distributions of transfer coefficient values along the surface. To incorporate this effect a more detailed modelling approach is needed where these distributions are included.

Spatially varying transfer coefficients

Masmoudi et al. [127] presented a detailed discussion of the approximations and discrepancies underlying the classical approach with constant transfer coefficients. It was found that simplifying drying problems to 1D problems is not generally applicable. In convective drying the leading edge effect will be significant if the sample size is not clearly larger than the mass or temperature boundary leading edge zones. This implies that 2D or if necessary 3D simulations are needed for an accurate prediction of the heat and mass transfer.

The importance of the leading edge zone was also discussed by [128–130]. Kaya et al. [128] developed an implicit model based on the work of Hussain et al. [131]. The model however neglects the impact of latent heat on drying. The heat and mass transport equations are thus only coupled by the temperature and moisture dependence of the hygrothermal material properties. Nevertheless their model seemed to agree reasonably well to experimental data. Kaya et al. state that a constant transfer coefficient may not reflect reality. They introduce a spatially varying transfer coefficient. The values for these transfer coefficients are found by first analysing the flow around the dried object. The temperature field around the object is modelled using a commercial CFD package for a constant material boundary temperature. The convective heat transfer coefficient can then be calculated from this temperature field by using Eq. 5.4,

$$-\lambda \left.\frac{\partial T}{\partial n}\right|_s = h\left(T_s - T_{ref}\right) \tag{5.4}$$

where s is the coordinate at the surface and n is the normal to the surface. The mass transfer coefficient was determined through the heat and mass analogy. Strangely enough the moisture content was reported as driving force for moisture transport in the air. No values for 'moisture content' in the air where reported though. The correct driving force in air would however be the mass fraction of

water vapour in air, making the reported values for h and h_m difficult to interpret. A similar approach to that of Kaya et al. [128] was used by Chandra Mohan et al. [129] who developed a drying model with spatially varying transfer coefficients for three dimensional objects. First CFD was used to calculate the external flow and temperature field. Next, the convective heat transfer coefficient as a function of space was determined. The mass transfer coefficient was determined through the heat and mass analogy. Curve fitting equations were used to express the variable transfer coefficients and these equations were used as boundary conditions for a three-dimensional coupled heat and mass transfer finite element model. This model was then used to determine the heat and moisture distribution as a function of space and time. A parametric study revealed the impact of the air velocity and temperature on the drying rate. The study also showed the impact of the leading edge effect on drying. Transfer coefficients at the leading edge will be higher than those at the trailing edge, which results in a distributed drying rate over the surface.

Shokouhmand et al. [130] performed 3D simulations of the air flow and temperature distribution around bricks in a brick dryer. The transport coefficient distribution determined with these simulations were then used in a 2D heat and moisture transport model. Higher transfer coefficients at the edges resulted in faster drying of these edges. This leading edge effect was found to be crucial in the determination of the correct drying time.

The models developed in [128–130] combine two solvers: one for the CFD calculations and one for the HAM calculations. This has the disadvantage that information is to be transfered from one solver to the other. Ljung et al. [132] overcome this problem by implementing the HAM model into an existing commercial CFD package. With this model they were able to predict the drying behaviour of an iron ore pallet with complex 3D geometry.

The drying models discussed up till now are sometimes categorized as the classical approach of the conjugate transport problem: the flow field is assumed steady and solved separately from the material model [133]. This can be justified if the heat and mass transfers are moderate and if the fluxes through the solid-fluid interface do not disturb the velocity field. The variations in air density are ignored and air is considered to be incompressible. The heat and mass transfer coefficients are then determined by solving transport in the air only once and assuming constant boundary conditions at the material surface (constant temperature and moisture concentration). This is however only valid during the constant drying rate period.
The assumption of constant surface temperature and moisture content does not apply during the second drying rate period. When the surface of a porous material starts to dry out, large temperature and moisture distributions along the surface can occur. Masmoudi et al. [127] showed the effect of heterogeneities in the moisture content distribution at the surface (such as dry zones) on the transfer at the interface. The transfer coefficients clearly showed dependency on the surface

moisture distribution. Similar results where found by Defraeye et al. [26].

For forced convection the impact of varying air density on the flow field can be ignored. This will however not be the case for natural convection where the flow is determined by density gradients due to temperature and/or concentration gradients. So changes and variations in the boundary conditions will affect the flow field. Assuming a constant flow field is thus no longer valid for natural or mixed convection cases.

From this discussion it can thus be stated that a more complete modelling of the drying behaviour is needed to capture drying in its full complexity.

5.3.3 Conjugate modelling: a complete approach

A problem is usually referred to as conjugate when coupled mechanisms of heat and/or mass transfer within and between different phases in the same system are involved [133]. In the previous section an overview was given of some recent modelling attempts of convective drying. In these previously discussed models, the coupling between the drying medium (often air) and the dried medium is accomplished by using convective transfer coefficients at the boundary of the dried porous medium.
In this section a more complete approach is discussed for the modelling of convective drying (or heat and mass transfer between air and porous material more generally). Instead of solving the transport in the porous material separately from that in the air, both are solved simultaneously. Continuity of heat and mass at the boundary has to be assured together with continuity of the fluxes at the boundary as expressed by Eq.5.5:
at the interface, continuity of temperature and mass fraction:

$$T_m = T_a \tag{5.5a}$$

$$Y_a = Y_m(T_m, RH_m) \tag{5.5b}$$

and continuity of heat and mass fluxes:

$$\lambda_a \frac{\partial T}{\partial x}\bigg|_s = \lambda_m \frac{\partial T}{\partial x}\bigg|_s - L\rho_{v+a} D_{va} \frac{\partial Y}{\partial x}\bigg|_s \tag{5.5c}$$

$$\rho_{v+a} D_{va} \frac{\partial Y}{\partial x}\bigg|_s = K_{tot} \frac{\partial P_c}{\partial x} \tag{5.5d}$$

where K_{tot} is the combined permeability of water vapour and liquid water

An early attempt to develop a coupled model was done by Amir et al. [134]. Amir et al. developed an implicit finite difference model that simultaneously solved the set of equations for a laminar boundary layer and a porous thick

slab immersed in the boundary layer. The laminar velocity boundary layer was considered to be steady and independent of heat and moisture. This allowed them to solve the velocity boundary layer separately from the heat and moisture transport equation. The heat and moisture transport equation in the boundary layer and in the porous material were then solved simultaneously and coupled. One advantage of the complete conjugate approach, is that there is no longer a need for the use of transfer coefficients. In fact, the transfer coefficients can be determined a posteriori.
Zeghmati et al. [135] continued the work of Amir et al. by extending the model to include transient laminar natural convection. The Boussinesq approximation was assumed for the boundary layer momentum equation.
Dolinskiy et al. [136] employed a similar model to simulate the drying of a thick slab for the initial period of drying (moisture content exceeded the maximum sorption moisture content). The authors found that the analogy between heat and mass transfer, often employed to predict transfer coefficients, was not applicable. This was due to the fact that, for maintaining the analogy, not only the differential equations describing the heat and mass transfer have to be analogous, but also the boundary conditions. They found that these boundary conditions could substantially differ in time and space.

Because moisture transport in air and material is described by different potentials, conjugate drying models often use two solvers: one to solve the transport equations in the air and one to solve the transport in the porous material. When two solvers are used, a specific solution methodology is needed.
Oliveira et al. [133] describe such a solution procedure for laminar flow to study convective drying of a wood board and repeated the same procedure later to study soybean drying [137]. A finite element code was developed.
In the first step the continuity and momentum equations in the air are solved separately. This is allowed if the flow is assumed steady and if the impact of density on the flow is neglected. The velocity field obtained from this calculation is assumed invariable during the rest of the simulation. Next the boundary layer is solved using boundary conditions of the first kind (constant temperature and concentration). The results of this numerical analysis are used to determine the heat and moisture fluxes at the surface. These fluxes are used as boundary conditions of the second kind for the porous material. Transport in the porous material is then solved. The temperature and moisture distribution in the porous material provide new boundary conditions for the air side for the next time step. This procedure is repeated until the final drying time is reached.
This explicit time marching procedure was also used by Murugesan et al. [138]. They developed a 2D finite element model to study the drying behaviour of ceramic brick. It was stated that buoyancy can have a significant effect on the transport mechanism in the air and must be taken into account by allowing changes of the flow field over time.

When explicit coupling procedures are used two separate solvers can be used.

This brings along the advantage that two separately developed models can be coupled and the developer of drying models should only be concerned with the implementation of the coupling procedure. For example Gnoth et al. [25] developed a coupling procedure between a CFD model developed for cavities and a commercially available HAM model, Delphin® [19]. Defraeye et al. [26] coupled the commercial CFD package Fluent® with an in house developed HAM model HAMFEM [62].
When using an explicit coupling procedure too large time steps will cause instability. Time steps should be small so that heat and mass fluxes at the material boundary do not change during a time step. Defraeye improved convergence by using an adaptive time stepping algorithm. This ensured that the optimal time step was used during the simulations. Nevertheless a long computational time was still needed even for relatively simple cases.

In literature examples can be found where an implicit coupling is used for the heat and moisture transport equations. The unsteadiness that the explicit models are facing, is overcome and a significant reduction of computational time is noticed. De Bonis et al. [139] developed a finite element model using a commercial finite element package to study the performance of the drying process of fresh-cut vegetables. Lamnatou et al. [140, 141] developed a finite volume model to study the drying of apple slices.

Finally a hybrid approach is reported in literature. Saneinejad et al. [142] coupled a model for heat and mass transport with a commercial CFD model (Fluent®) and a radiation model to study the heat and moisture transport in a street canyon. Instead of calculating the fluxes at the air side and passing them to the material side explicitly, the transfer coefficients were calculated first at the air side. These transfer coefficients were then passed to the material side were they could be implemented as an implicit boundary condition. This significantly improved convergence and solution stability.
A similar approach is used in this work and was discussed in chapter 3. Saneinejad et al. coupled two individual solvers while the model developed in this work implemented a HAM model into a commercial CFD solver. Since only one solver is used it is easier to transfer data from the material to the air domain and vice versa.

5.3.4 Discussion

In literature a wide range of drying models are available. These models were divided in three groups with increasing accuracy. The **first group** comprised the **analytical models**. Analytical solutions are only found for simplified drying cases such as one-dimensional drying with constant diffusivity. Boundary conditions are limited to Dirichlet, Neumann or Robin boundary conditions (constant transfer coefficients).

However in drying often 2D or 3D configurations are found. For these complex configurations numerical models are needed. The **second group** of drying models are the **numerical models using convective transfer coefficients** as boundary condition. These transfer coefficients can have complex forms and vary in space and time. The simplest approach is using constant transfer coefficients. This is however only valid if the flow is fully developed which is often not the case. The literature study performed in this section revealed the importance of spatially varying transfer coefficients. Especially during the constant drying rate period the impact of the leading edge effect can be significant.
It can thus be concluded from this study that the use of transfer coefficients as a boundary condition to model convective drying, is only justifiable if the transfer coefficients are function of surface location so that they can incorporate important effects such as e.g. developing boundary layers at the leading edge. If constant boundary layers are for some reason still preferred, it is important that the impact of this simplification is estimated in advance. For some cases a constant coefficient is acceptable, but this should always be checked. Otherwise large discrepancies in temperature and moisture prediction during drying can occur.

A more accurate and detailed study of the convective drying process is possible when spatially varying transfer coefficients are used. These coefficients can be derived from analytical solutions for some simple cases or from CFD solutions when more complex geometries and flow conditions are present.
The most common approach to determine the transfer coefficients from CFD is by solving the flow with the assumption of constant boundary temperature and mass fraction. For convective drying this approach is only strictly applicable during the constant drying rate period when the surface temperature is almost constant and near to the wet bulb temperature and the surface mass fraction corresponds with the saturation mass fraction for that temperature. Nevertheless this approach is often used with reasonably good results.

The **third group** of convective drying models are the **numerical models using a fully conjugate approach**. In this approach it is no longer necessary to determine the transfer coefficients in advance. Heat and moisture transport are solved in the air as well as is the material, while continuity of temperature, mass fraction, heat flux and moisture flux is assured at the boundaries.
The explicit coupling of these boundary conditions allows the use of separate solvers for the material and air domain. The advantage of this approach is that readily available solvers can be used and the developer should only be concerned with the coupling procedure. However as stated before, the explicit coupling restricts the time step size which increases the computational time.
Implicit coupling overcomes this time step restriction. However, for a full implicit coupling of the boundary conditions only one solver can be used and the equations for heat and mass together with the boundary conditions have to be solved in a

coupled way.

A hybrid approach was suggested by Saneinejad et al. [142] combining the benefits of using separate solvers and implicit solver methods. Instead of coupling the air and material zone by passing the heat and moisture fluxes directly, the transfer coefficients are calculated from these fluxes. These transfer coefficients are then passed to the material side. The convective boundary condition at the material side can then be implemented implicitly. This significantly improves convergence. These types of models are only recently being developed and used but show to be promising. In the current work an adopted version of this approach is implemented and used in chapter 6.

The conjugate drying models discussed in this section are to the knowledge of the author the most advanced models currently available. However a study on the existing modelling methods by Defraeye [143] revealed that the high accuracy of the fully coupled conjugate models is not always needed and wanted. The high accuracy brings with it the cost of more computational time and effort.
Defraeye stated that the sensitivity to the convective boundary conditions is case dependent. So in some cases simplified models suffice. Defraeye suggested performing a sensitivity analysis with respect to the convective boundary conditions before implementing a full conjugate model.
Therefore the next section (section 5.4) will study the impact of some modelling assumptions such as constant transfer coefficients and 1D and 2D modelling versus 3D in more detail for the specific case of brick drying. Simultaneously the newly implemented heat and moisture model is validated.

5.4 Validating the coupled CFD-HAM model including moisture transport

The coupled CFD-HAM model is validated in two steps. In this section a drying experiment from literature is used (Defraeye [43]). In this experiment a sample of ceramic brick is dried by convection, by placing it in a wind tunnel. Dry air flows over the top side of the brick and the brick is dried out from one side, while the other sides are impermeable for moisture. During this validation study the impact of some model assumptions (2D vs. 3D modelling and the use of constant transfer coefficients) is assessed.
In the next section (section 5.5) a new experiment is developed and used for validation. In the new experiment the drying of Calcium Silicate is studied.

5.4.1 Experimental setup

This section gives a more detailed description of the setup used by Defraeye [43]. Defraeye constructed a small wind tunnel from transparent polymethyl methacrylate (PMMA) to perform convective drying experiments on building

materials such as ceramic brick. A schematic representation of the wind tunnel with test section is found in Figure 5.4. Air is drawn in by a fan, passes over a flow straightener (honeycomb) and flows through a convergent section before entering the test section. Because of the high width to height ratio, the flow in the tunnel can be assumed two-dimensional. A detail of the test section is found in Figure 5.5.
The open circuit wind tunnel was placed in a climate chamber where the mean temperature was set at 23.8°C (with a standard deviation of 0.2°C) and the mean relative humidity was set at 44% (with a standard deviation of 0.8%). The sample of ceramic brick was wetted and placed in the wind tunnel so that the top face of the sample becomes the bottom of the test section. The sample was wetted to a moisture content of $126 kg/m^3$ which is approximatly the capillary moisture content ($130 kg/m^3$). The sides of the sample were insulated with extruded polystyrene (XPS) and made impermeable for moisture. The velocity at the inlet of the test section and the turbulence intensity were measured with a PIV (particle image velocimetry) system.
During the drying experiment temperatures at the side of the ceramic brick were measured with thermocouples. Figure 5.4 shows the location of these thermocouples. In total 6 thermocouples were installed at a side wall. The temperature was measured at a depth of 10mm, 20mm and 30mm from the material-air interface and 10mm in the lower insulation (at 40mm from the interface). To measure the inflow effect and the effect of a developing moisture and temperature boundary layer, a thermocouple was installed upstream and downstream of the centre thermocouples, both at a depth of 10mm. The weight change of the test sample was continuously monitored by a balance.

Figure 5.5 shows a detail of the test section. The sample of ceramic brick measuring 10mm by 30mm by 90mm, is placed in a container of plexiglass (PMMA). At the bottom of the container a layer of 20mm insulation (XPS) is installed. the front and back side of the container are covered with 15mm of insulation (XPS), the side walls of the brick sample are insulated with 30mm of XPS. The test section can be assumed symmetric along the x-axis since the flow in the channel was found to be two-dimensional [144].

5.4.2 Comparison of experiment and simulations

The experiments performed by Defraeye [43] are now used to perform an extensive validation study of the coupled CFD-HAM model. This validation is conducted in three phases to gain a better understanding of the occurring phenomena during drying. In a first phase only the cross section of the ceramic brick will be modelled. This implies that 2D and 3D effects of the air flow will be neglected. The boundary conditions of the brick are assumed constant. Transfer coefficients are assumed to be constant in time and space. 3D edge effects are neglected. This does however not imply that the simulation is one-dimensional since heat flow from sides and bottom is allowed and will result in a 3D distribution of heat and mass in the brick. The consequences of the proposed simplification are discussed in section 5.4.2.1.

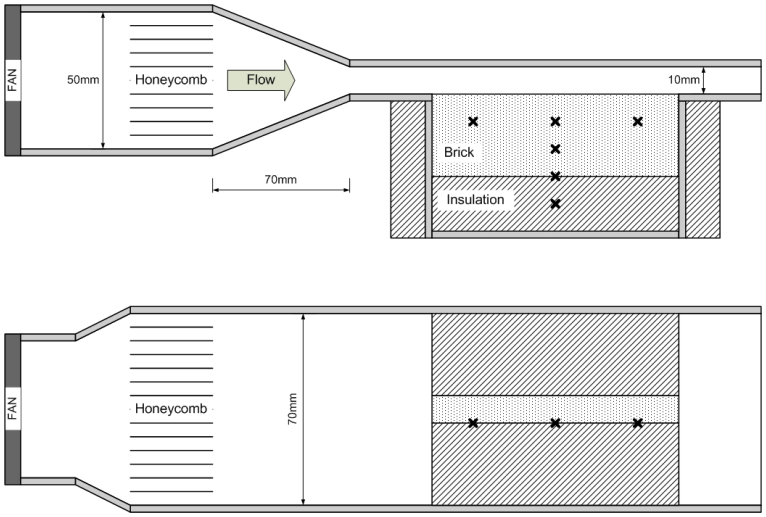

Figure 5.4: Schematic representation of wind tunnel used by Defraeye [43] to perform drying experiments. Above: side view. Under: top view

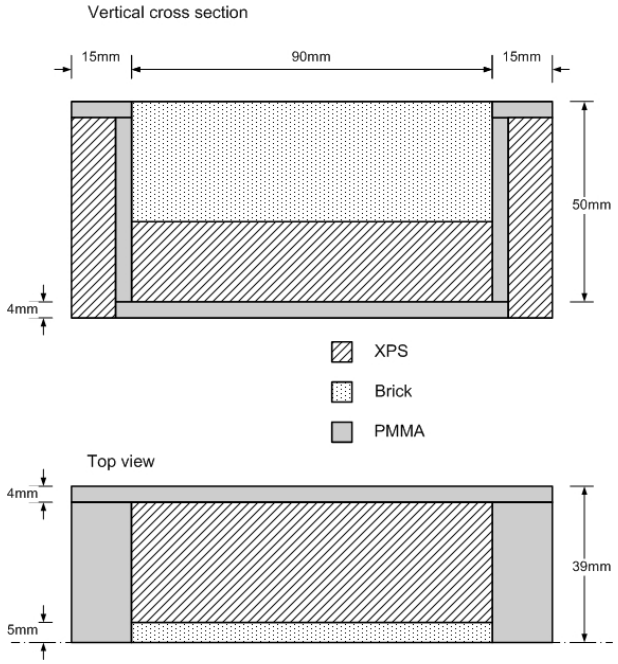

Figure 5.5: Model of test section of experimental setup by [43]

In the next section (section 5.4.2.2) a more thorough study of the effect of a developing boundary layer at the brick surface is examined. The air flow in the channel is assumed to be two-dimensional and a longitudinal section of the brick is used for simulation. This 2D simulation will however result in an underestimation of the heat gain through the (not perfect) insulation along the side walls of the brick, since 3D edge effect are again neglected.
Finally a full 3D simulation of the brick is performed including the insulation and plexiglass out of which the sample container is built up. The transfer coefficients derived in section 5.4.2.2 are used at the brick top surface assuming 2D airflow in the wind tunnel.

5.4.2.1 2D model of cross section

First the experiments of Defraeye [43] are modelled by a 2D model representing a cross section of the setup. The heat and mass transfer coefficient along the surface are assumed to be constant for this case. Figure 5.6 shows the cross section of the setup together with the electric analogy of the boundary conditions. The dimensions are the same as those of Figure 5.5. The ceramic brick is surrounded by insulation material (XPS) and air flows over the brick at the top. All sides of the brick except the top are assumed impermeable for moisture. The inlet conditions of the air are those measured by Defraeye [43]: air inlet temperature T_a = 23.8°C, air inlet relative humidity 44%. Defraeye determined the heat transfer coefficient at the top of the brick by CFD simulations performed for a 2D wind tunnel with constant surface temperature at the bottom. This resulted in a heat transfer coefficient as a function of the position in the duct. From this spatially varying transfer coefficient, an average value was determined of $22.5 W/m^2K$. From the heat and mass analogy he calculated a mass transfer coefficient of $0.0258 kg/m^2 s$.

As shown in Figure 5.6 the boundary conditions can be represented by their electric analogy. λ_{XPS} and λ_{PMMA} are the heat conductivities of the insulation material and plexiglass respectively, h_a is the heat convection coefficient at the air side, h_e is the heat convection coefficient at the remaining sides. This transfer coefficient h_e is assumed to be constant and incorporates the effect of radiation from the surrounding. h_e was estimated at $8 W/m^2K$ by Defraeye. The temperature of the surroundings, T_e was also constant and corresponded with the temperature of the climate chamber (23.8°C). Radiation at the interface brick-air was taken into account in a simplified way by assuming that the brick top face only sees the upper wall of the wind tunnel. This resulted in a view factor of 1. The temperature of the top wall of the wind tunnel, T_{roof}, was measured by Defraeye and an average value of 23.3°C was found. The radiative heat flux at the brick-air interface can be calculated according to [145] as:

$$q_{rad} = \frac{C_b}{\frac{1}{\epsilon_1} + \frac{1}{\epsilon_2} - 1} \left(T_{roof}^4 - T_s^4 \right) \tag{5.6}$$

In this equation q_{rad} $[W/m^2]$ is the radiative flux between the roof of the wind tunnel and the brick surface, ϵ_1 and ϵ_2 are the emissivities for the roof and the

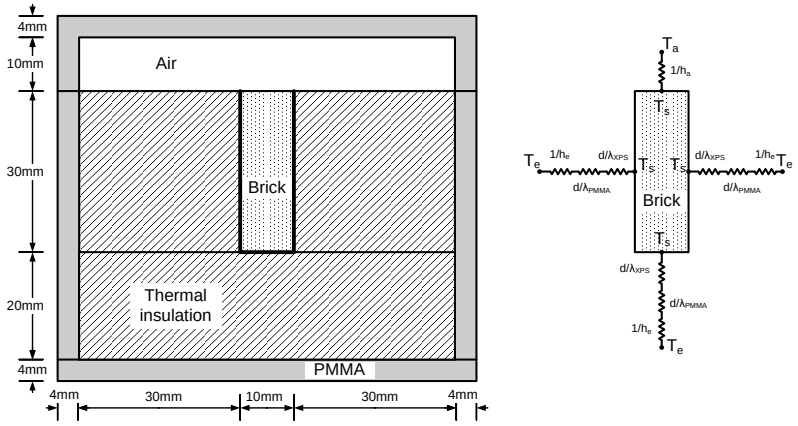

Figure 5.6: 1D model of drying experiment by [43] and electric analogue of the boundary conditions

brick surface, respectively, which are assumed to be 0.97 and 0.93. T_s is the surface temperature of the brick. C_b is the Stefan-Boltzmann constant ($5.67 \times 10^{-8} W/m^2K^4$).
From the electric analogy, the boundary conditions at the side of the brick can be written as:

$$q = \frac{1}{\frac{1}{h_e} + \frac{d_{PMMA}}{\lambda_{PMMA}} + \frac{d_{XPS}}{\lambda_{XPS}}} \left(T_e - T_s\right) \tag{5.7}$$

In this equation d_{PMMA} is the thickness of the plexiglass (4mm), d_{XPS} is the thickness of the insulation (30mm at the sides, 20mm at the bottom).
The boundary conditions at the top can be written as:

$$q = h_a(T_a - T_s) + (L + C_v T_s)h_m^Y \left(Y_a - Y_s\right) + \frac{C_b}{\frac{1}{\epsilon_1} + \frac{1}{\epsilon_2} - 1} \left(T_{roof}^4 - T_s^4\right) \tag{5.8a}$$

$$g = h_m^Y (Y_s - Y_a) \tag{5.8b}$$

The temperature in Eq. (5.8a) is expressed in °C. L is the latent heat of water at reference temperature 0°C ($2500 kJ/kg$), C_v is the heat capacity of water vapour ($1875.2 J/kgK$). The second term on the right hand side incorporates the latent heat leaving the surface due to evaporation. Y_a is the mass fraction of the air entering the wind tunnel (corresponding with inlet temperature and relative humidity). Y_s is the mass fraction at the brick-air interface. The third term on the right hand side is the contribution of radiation (Eq. (5.6)).
For these simulations a grid of 200×20 cells was used. The grid was finer near the top. A grid independency study was performed starting from a grid of 100×10

cells. The grid was then refined in both directions by a factor 2. This refinement was performed several times until no significant change in simulation outcome was found. The grid of 200×20 was found to suffice and is used for further simulations. Figure 5.7 shows a comparison of the measurements performed by Defraeye [43] with the simulations for a 2D cross section of the brick. Figure 5.7 also shows the simulation results for adiabatic boundary conditions. The temperature predicted during the CRP (constant drying rate) period is the wet bulb temperature as predicted in section 3.4.2. Allowing a heat flow through the boundary walls and incorporating radiation from the top surface will alter the equilibrium temperature to a higher temperature. The temperature at a depth of 10mm in the brick is initially $23.8°$C. Three periods during drying can be distinguished in the temperature course. First the temperature drops to the wet bulb temperature (in case of adiabatic side walls). This is the so-called decreasing drying rate period preceding the constant rate period. In this first transitional period there is an imbalance between the heat leaving the surface due to evaporation and heat supplied to the surface through convection. This causes the temperature to drop if the initial temperature is higher than the wet bulb temperature. If the temperature in the material reaches the wet bulb temperature, the heat flow from and to the surface is balanced and the temperature remains constant. This continues until dryout occurs at the surface. At that point the evaporation rate at the surface decreases and again an imbalance exists between the supplied heat and the heat leaving the surface. Less evaporation means that less latent heat is needed and the temperature at the surface will start to rise. This third drying period is called the falling rate period. Figure 5.7(a) clearly shows the three drying periods.

If the side walls are assumed to be adiabatic and radiation at the top is neglected, the equilibrium temperature during the constant drying rate period will be the wet bulb temperature as shown in section 3.4.2. Figure 5.7(a) shows the effect of radiation at the top surface on the equilibrium temperature. Radiation from the wind tunnel top wall to the brick-air interface will result in a new equilibrium temperature at that surface. This temperature is slightly higher than the wet bulb temperature. By leaving the assumption that the side walls are adiabatic and allowing a heat flow through the insulation, the temperature at equilibrium will even further increase.

Figure 5.7(a) also shows the measurements of the temperature at 10mm in the brick sample. The comparison with the simulations show a clear underestimation of the simulations. Assuming that the simulations were performed accurately, this would indicate that the current model is underestimating the heat gains to the brick due to the introduced simplifications. The main simplifications here are the 2D modelling assumptions (neglecting 3D edge effect) and the constant transfer coefficients at the surface. Further on (section 5.4.2.2 and 5.4.2.3) these effects will be studied in more detail.

As more heat gains are taken into account (radiation and heat gain through insulation), the equilibrium temperature rises and the constant drying rate period decreases. Figure 5.7(a) shows, for the simulated cases, how the constant drying rate period ends after 7 hours for the adiabatic case and after 5 hours for the

non-adiabatic case. A higher temperature will result in a higher saturation mass fraction during the constant drying rate period and thus a higher evaporation rate. The brick will dry out faster. This is depicted in Figure 5.7(b), which shows the scaled mass loss in time. This scaled mass loss is the ratio of the mass loss to the initial moisture content $(m_{w,init} - m_w)/m_{w,init}$. During the constant rate period the slope of this curve is constant and is a measure for the drying rate. The steeper slope for the non-adiabatic case indicates a higher drying rate which results in a faster decrease of the moisture content in the brick. Due to the faster decrease in moisture content, the surface will dry out sooner and this in turn results in an earlier onset of the falling rate period. During the constant drying rate period, the drying rate is constant and significantly higher than during the falling rate period. The drying rate is, as explained in section 5.2, determined by outside transport conditions (convective transport in the air). When dryout at the surface occurs, the internal transport of water in the brick becomes the dominating mechanism. A moisture front starts to developed and slowly moves into the brick. This is also depicted in Figure 5.8. This figure shows the evolution of the moisture content in the brick. Initially the moisture content in the brick was constant over the depth and the brick was almost capillary saturated (97% of saturation). During the constant drying rate period the moisture content in the brick almost equally decreases along the depth of the sample. This corresponds with the findings of Landman et al. [118]. As the drying process continuous, the brick will dry out faster near the surface, indicating that below a certain moisture content it becomes more difficult for moisture to transport through the brick. A very low moisture content at the surface (almost zero) will indicate dryout. Transport is from then on dominated by vapour diffusion from the wet moisture front in the brick to the surface. When this occurs, it becomes very difficult for moisture to transport through the surface due to the high water vapour resistance factor of ceramic brick. The simplified 2D model allows to verify if the new model predicts the correct trends during drying. More specifically the different drying periods are reproduced by the model. It is however difficult to validate the simplified model quantitatively.

5.4.2.2 2D model of longitudinal section

As stated in the previous section, a 2D model of the cross section of a porous material subjected to convective drying is not able to fully grasp al the drying phenomena. Figure 5.7(a) clearly shows the underestimation of the temperature by the 2D cross section model. As stated in section 5.4.2.1 such a model incorporates too large simplifications. One of the simplifications cited in that section was the use of constant transfer coefficients. This is only valid for a fully developed thermal and mass boundary layer. For developing boundary layers the heat and mass transfer coefficients will vary in space.
Heat and mass transfer at the leading edge of a sample subjected to convective drying will be higher since at this leading edge the boundary layers still have to develop and are still thin. This will result in a faster dryout at this leading edge

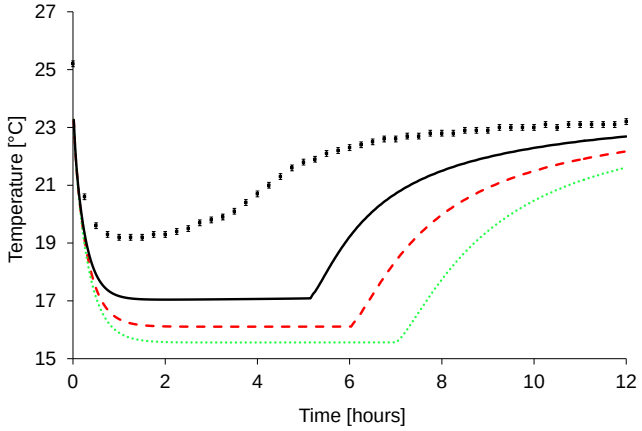

(a) Temperature at 10mm

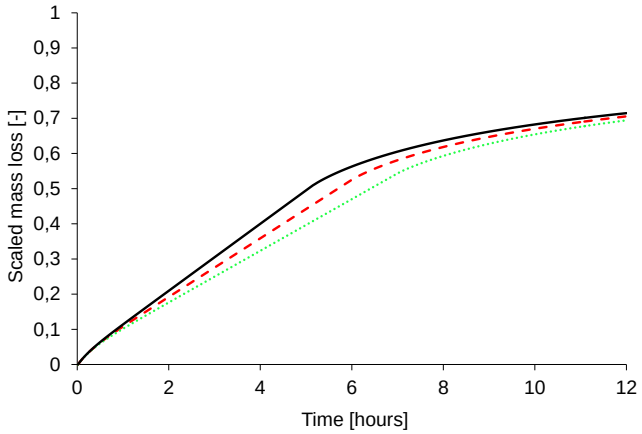

(b) Scaled mass loss

Figure 5.7: (a) Temperature at 10mm in the brick. (b) Scaled mass loss. Comparison between different boundary conditions: heat flux through insulation (—), adiabatic side and bottom (. . .), adiabatic side and bottom with radiation at top (- -). Measurements by Defraeye [43] (■)

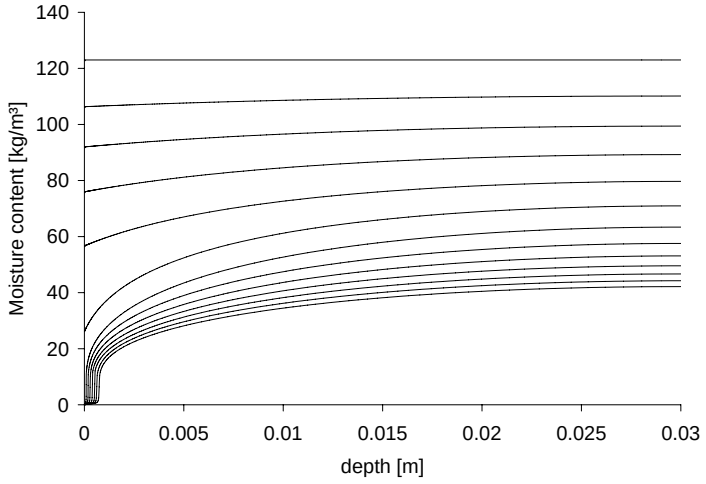

Figure 5.8: Moisture content along the depth of the ceramic brick sample every hour (total 12 hours)

and a distribution of temperature and moisture in the sample. In this section this leading edge effect is modelled and compared with simulations using constant transfer coefficients.
The convective transfer coefficients used in this section were determined separately with new CFD simulations and compared with the coefficients calculated by Defraeye [43]. A longitudinal section of the setup described in section 5.4.1 was used. The section is shown in Figure 5.9(a). Four simulations were performed:

Case 1 In the first case only heat transfer was modelled. Temperature in the brick and at the brick surface were constant. The inlet temperature was 20°C and the wall temperature T_w was 10°C.

Case 2 For the second case, the temperature was kept constant (no heat transfer allowed). Inlet mass fraction was $0.008004kg/kg$ and the wall mass fraction Y_w was $0.1kg/kg$.

Case 3 During the third simulation both heat and mass transport in the air were modelled simultaneously. The temperature and mass fraction in the brick and at the surface were kept constant. The inlet temperature was 20°C and the wall temperature T_w = 15°C. The inlet mass fraction was $0.008004kg/kg$ and the wall mass fraction $0.1kg/kg$.

Case 4 In the fourth case drying of a brick during the constant drying rate period was simulated. The brick was assumed saturated during the whole

simulation. The temperature at the brick surface decreased until an equilibrium between the heat leaving the surface due to evaporation and the heat going to the surface due to convection was reached.

The newly calculated average heat and mass transfer coefficients are listed in Table 5.1. Defraeye predicted the convective heat transfer coefficients in CFD by using a constant temperature boundary condition. He used the Chilton-Colburn analogy to calculate the convective mass transfer coefficient.
The cases listed in Table 5.1 use a slightly different velocity inlet profile. Figure 5.9(b) depicts the velocity profile as measured by Defraeye [43]. Defraeye used this profile as input for his simulations. In the new CFD simulations this profile was approximated by a fourth order polynomial also shown on Figure 5.9(b). This results in a small difference between the convection coefficients predicted by Defraeye and the coefficients predicted here. The cases using constant boundary conditions (constant temperature, constant mass fraction or both) have a very good agreement. There is also a strong agreement with the Chilton-Colburn analogy. Case 4 however slightly deviates from the other cases. During this case the temperature at the surface is not constant but varies over the length. The capillary pressure at the surface and in the brick was constant during the simulation and corresponded with a moisture content of $97\%w_{sat}$. Since the temperature varies over the length of the sample, also the saturation vapour pressure will vary at the surface and consequently also the water vapour mass fraction. The different type of boundary condition explains the deviation in convection coefficient. Also the heat and mass analogy seems less applicable although deviation is still small.

	CHTC $[W/m^2K]$	CMTC $[kg/m^2s]$	CMTC from analogy $[kg/m^2s]$
Defraeye [43]	22.4	-	0.0259
no mass, T_w = cte	23.8	-	0.0273
no heat, Y_w = cte	-	0.0272	-
T_w = cte, Y_w = cte	23.5	0.0272	0.0270
drying, saturated material	22.8	0.0286	0.0262

Table 5.1: Comparison of average convective heat transfer coefficients (CHTC) and mass transfer coefficients (CMTC)

Now that the convective transfer coefficients are determined and discussed, they can be used as boundary conditions for the CFD-HAM model. To asses the effect of the different convective transfer coefficients on the drying simulation outcome, 2D simulations were performed on the longitudinal section. Drying of a ceramic brick was simulated starting from $97\%w_{sat}$. The boundaries of the brick (except

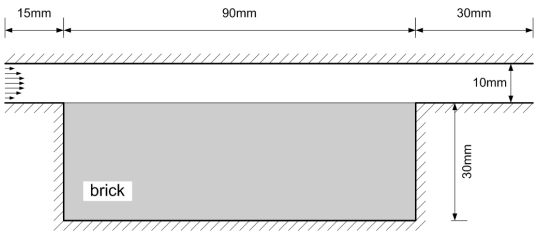

(a)

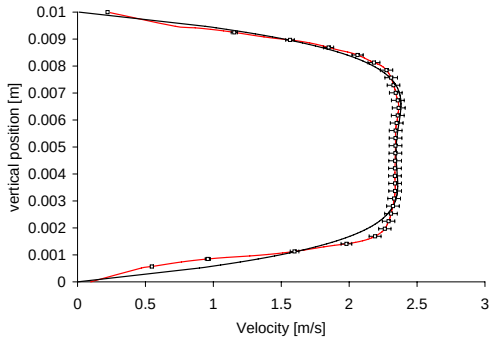

(b)

Figure 5.9: (a) Longitudinal section of the test setup used in section 5.4.2.2 for simulations. (b) Velocity profile measured by Defraeye [43] (red line) compared with the 4_{th} order polynomial approximation (black line)

the top) were assumed to be impermeable for moisture and adiabatic. A drying period of 12 hours was simulated. Table 5.2 compares for these simulation the starting time of the falling rate period and the predicted equilibrium temperature during the constant drying rate period. The onset of the falling drying rate period is defined as the time where the temperature at a depth of $10mm$ starts to rise again.

	onset FRP [minutes]	equilibrium temperature [°C]
Defraeye	213	15.47
$T_w = cte, Y_w = cte$	209	15.53
drying, mat saturated	223	15.28

Table 5.2: Comparison of the onset time of the falling rate period (FRP) and the equilibrium temperature during the constant drying rate period for different convective transfer coefficients.

Table 5.2 compares three cases: a simulation performed with the convective transfer coefficients used by Defraeye [43] (Eqs.5.10a and 5.10b), a simulation performed with the transfer coefficients found when using a constant temperature and constant mass fraction at the boundary and a simulation performed with the coefficients found when heat and mass transfer from a saturated brick is modelled. The average values of the heat and mass transfer coefficient were already listed in Table 5.1. The following observations can be made when looking at Table 5.2:

- The heat and mass transfer coefficients found by Defraeye when using constant temperature and mass fraction are lower than when a polynomial approximated velocity profile is used. Lower average heat and mass transfer coefficients result in a slightly lower equilibrium temperature and a slightly longer constant drying period. The longer constant drying period is a consequence of the lower surface temperature which results in a reduced drying rate.
- The heat transfer coefficient found for combined heat and mass transport from a saturated brick, is lower than that found for constant wall temperature. The mass transfer coefficient on the other hand is higher. This high mass transfer coefficient combined with a lower heat transfer coefficient results in a new equilibrium temperature which is lower. The lower temperature is translated in a delay of the onset of dryout.

It can thus be concluded that the drying process in the brick, resulting in a temperature and moisture distribution in the brick, is determined by the combined effect of convective heat and mass transport from the brick to the air. Small changes in the convective heat and mass transfer will have their effect on the model outcome, however these effects can be considered of less importance

compared to effects of other parameters such as 2D modelling versus 3D and the effect of non-adiabatic boundary conditions.

Figure 5.10 shows a comparison of the temperature at 10mm for a simulation of the cross section of a brick (see section 5.4.2.1) using average transfer coefficients and a simulation of the longitudinal section using spatially varying transfer coefficients. When a constant transfer coefficient is used, the graph shows an overestimation of the constant drying rate period. Dryout at the surface will occur sudden and equal over the entire surface. This results in an abrupt transition from constant drying rate period to falling rate period. If a growing boundary layer at the surface of the brick is considered, heat and mass transfer at the leading edge will be larger and dryout will start at that side. This results in parts of the surface being dried out while others are still wet. At the dry parts, convection to the surface will be higher than the latent heat leaving the surface, which results in a temperature rise at these zones. For the wet zones, the equilibrium temperature is still the wet bulb temperature. Due to the more gradual progression of the dryout at the surface, there is no longer a sudden transition between the different drying phases. The temperature in the brick will rise more gradually as is seen in Figure 5.10. From the measurements it can be seen that simulation of brick drying incorporating a developing boundary layer for heat and mass will predict the trends in drying more accurately. However when comparing Figure 5.10 with Figure 5.7 it is clear that a correct prediction of the drying phenomena in a brick is only possible if all the boundary conditions are correctly implemented. This implies that a 3D simulation is necessary with a developing boundary layer at the top and non-adiabatic boundary conditions at the sides.

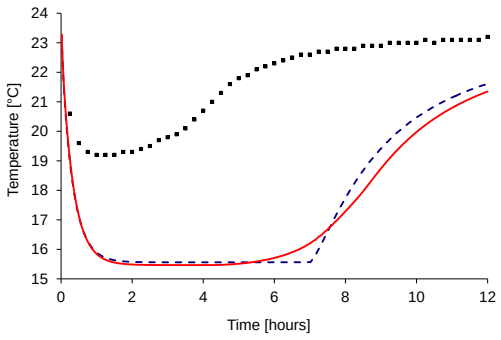

Figure 5.10: Simulation of the temperature at a depth of 10mm in ceramic brick using constant heat and mass transfer coefficients at the top (- -) and spatially varying transfer coefficients (—), comparison with measurements from [43] (■)

5.4.2.3 3D model

The previous studies showed that a more complex model is needed in order to capture the heat and mass transport in the setup more accurately. Figure 5.11 shows a 3D view of the test sample of ceramic brick embedded in the insulation and the plexiglass. The corresponding dimensions are found in Figure 5.5. The sample of ceramic brick measured $10mm$ thick by $30mm$ deep by $90mm$ long. Only half of the setup has to be modelled since a symmetry plane can be identified as also stated in section 5.4.1 and shown in Figure 5.5. This considerably reduces the computational effort.

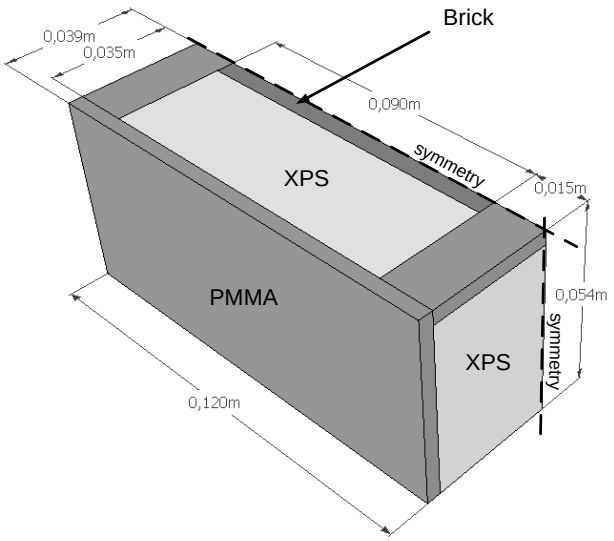

Figure 5.11: 3D representation of the test sample embedded in insulation and plexiglass as it is used for the simulations. Only half of the setup is depicted and simulated since a symmetry plane is assumed along the sample centre.

The side faces facing the climate chamber (bottom, front, back and left face) of the setup are all assumed impermeable for moisture. Heat can flow through all faces. Moisture exchange is only possible at the top face. At the side walls the heat flux is determined by Eq. 5.9.

$$q_{side} = h\left(T_e - T_s\right) \tag{5.9}$$

The heat transfer coefficient h is the same as used in section 5.4.2.1 and was estimated at $8W/m^2K$. This coefficient incorporates the effect of radiation as well.

The heat and mass transfer at the top face of the brick was assumed two-dimensional and varied along the length of the duct. The corresponding heat and mass transfer coefficient used for the current simulation were taken from Defraeye [43]. He determined these transfer coefficients by using CFD simulations of the wind tunnel assuming constant temperature at the bottom. The mass transfer coefficient was determined through the heat and mass analogy. An exponential approximation of these coefficients as a function of the position in the duct is given by Eqs. 5.10a and 5.10b.

$$h\left(x\right) = 7.7577x^{-0.2958} \tag{5.10a}$$

$$h_m^Y\left(x\right) = \rho R_v T 5.514 \times 10^{-8} x^{-0.2958} \tag{5.10b}$$

The experiments performed by Defraeye [43] are now used to validate the 3D HAM model. Temperatures measured at various depths in the sample of ceramic brick were compared with simulations. The material properties used in the simulations are listed in appendix A. Graphs of the temperature evolution in the brick are reported in Figure 5.12. Temperature at depths of 10mm, 20mm, 30mm (at the interface brick/insulation) and 40mm (10mm in the insulation) are compared with measurements. A measurement uncertainty of 0.1°C was reported by Defraeye and indicated in the figures. Figures 5.12(a)-(d) show a good agreement between the model and the experiments. The largest deviations are found near the surface. The temperature at a depth of 10mm is slightly underestimated by the model. Also the onset of the falling rate period is delayed in the simulations. Nevertheless the equilibrium temperature (the lowest temperatures in Figure 5.12) is closely approximated by the model. Deeper in the material the approximation becomes even better. At a depth of 40mm (10mm in the insulation) the agreement is almost perfect. This indicates that the applied boundary conditions closely approach reality. Two mean reasons for the deviations between the measurements and the simulations can be formulated. The first is the uncertainty in the material properties. This was also addressed by Defraeye [146] and similar studies were performed by Roels et al. [147] and in section 4.5. Secondly there is an uncertainty on the implemented boundary conditions and initial conditions. The heat transfer coefficient at the side walls was not measured but estimated and the inlet temperature was taken to be constant, though in reality the temperature varied slightly. The inlet velocity profile was measured using PIV but as stated by Defraeye [43] it is difficult to estimate the uncertainty on these measurements. Defraeye assumed an uncertainty of 2%. As discussed in section 5.4.2.2 variation in the convective heat and mass transfer coefficient at the top surface will lead to variations in the drying process. Finally the deviations between measurements and simulations can be the result of flaws in the measurement setup such as defects in the insulation or an incorrect positioning of the sensors. This is however hard to check and will not be considered here.
The good agreement between the predicted temperature at various depths and the measured temperature clearly shows that the boundary conditions are correctly implemented. The correct implementation of the combined heat and

mass transport at the surface results in a good estimation of the equilibrium temperature in the brick during the constant drying rate period. These temperature measurements also allow for the indirect validation of the moisture transport in the brick. The simulations in Figure 5.12 show a good prediction of the onset of the falling rate period. This is only possible if the moisture transport in the material is correctly modelled.

Defraeye also measured the leading edge effect by placing several thermocouples along the length of the sample at a depth of 10mm in the sample. A comparison of these measurements with the simulation outcome is made in Figure 5.13. Although there is no perfect match between simulation and experiment it is clear that the trends are well predicted. The upstream temperature reaches the same equilibrium temperature as the centre temperature both in the simulations and the measurements. However dryout occurs sooner upstream which results in a faster occurring temperature rise upstream. Downstream the temperature is higher both in the measurements and in the simulation. The onset of dryout happens later here and this delays the temperature rise.

During the experiments the weight change of the sample was also monitored. The scaled mass loss is shown in Figure 5.14. This mass loss was scaled using the initial moisture content of the brick sample (3.4g). Due to this small initial moisture content and relative high weight of the sample itself, a weight change is difficult to measure and is accompanied by large uncertainties. An uncertainty of 0.1g on the weight measurement was reported [43]. The uncertainty on the weight change is then 0.14g. This results in an uncertainty of 4% on the scaled mass loss.

During the constant drying rate period the moisture content in the brick decreases linearly. This initial drying period is clearly shown in the experimental results on Figure 5.14 where a constant slope in the mass loss curve continues for the first three hours. A similar duration was found by the simulations. Afterwards the decreasing rate period starts. The slope of the mass loss curve in Figure 5.14 is no longer constant but decreases. Comparison of the measurements and the simulations shows that the mass loss during the constant rate period is well predicted but that there is a deviation for the decreasing drying rate period. The cause of these deviations is again difficult to assess. Similar to the deviations in predicted and measured temperature, uncertainty in material properties and boundary conditions can be put forward.

5.4.3 Inter-model comparison for drying

Results from an existing finite element HAM model (HAMFEM [62]) developed at KULeuven were also compared with results of the model developed in this work. This comparison is found in Figures 5.14-5.16. The scaled mass loss in Figure 5.14 shows good agreement between both models. HAMFEM initially shows a

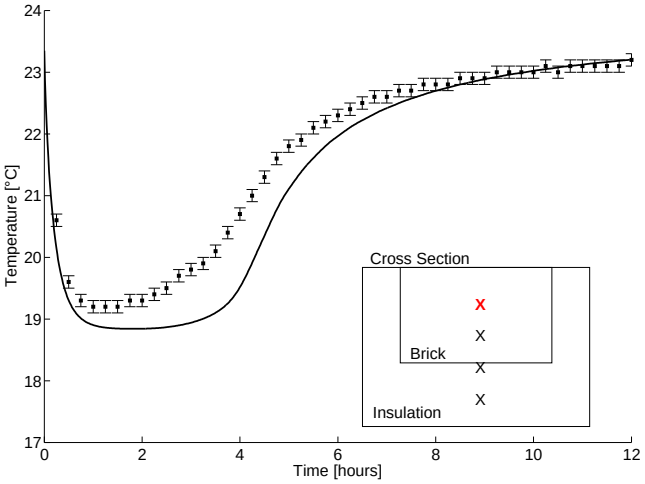

(a) Temperature at 10mm in the brick.

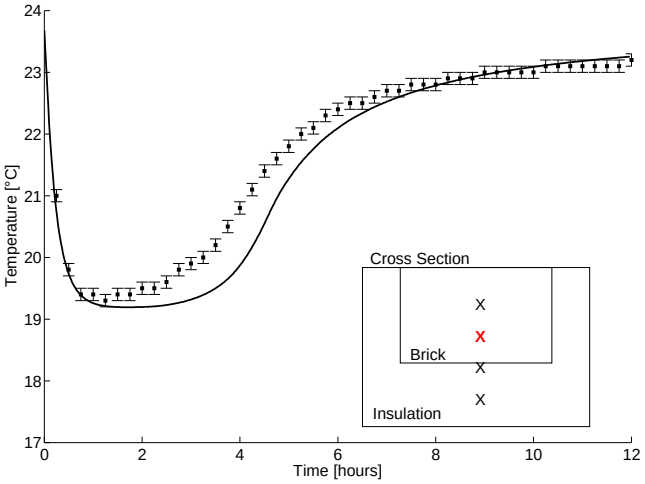

(b) Temperature at 20mm in the brick.

Figure 5.12: Simulated temperature at various depths (—), compared with the measurements of Defraeye (□) [43]. Measurement error indicated on figure. The right bottom of the graphs show a cross section of the test section and the position of the temperature measurement

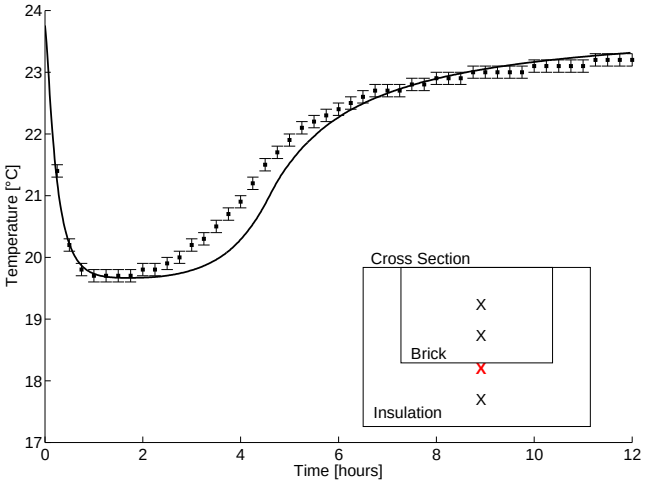

(c) Temperature at 30mm, at the bottom of the brick.

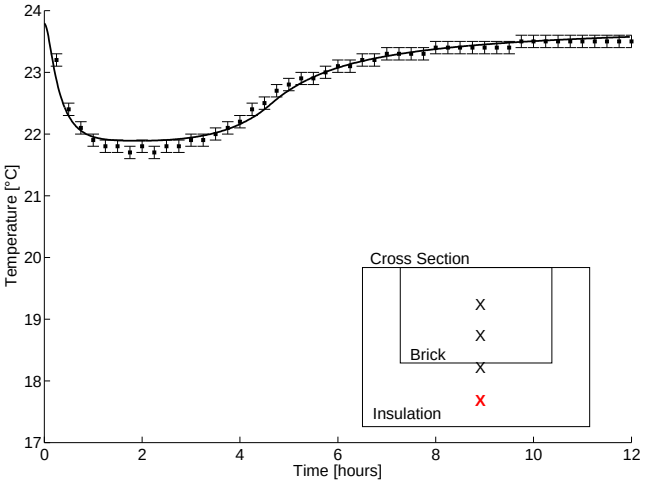

(d) Temperature at 40mm, in the insulation.

Figure 5.12: (Continued) Simulated temperature at various depths (—), compared with the measurements of Defraeye (□) [43]. Measurement error indicated on figure. The right bottom of the graphs show a cross section of the test section and the position of the temperature measurement

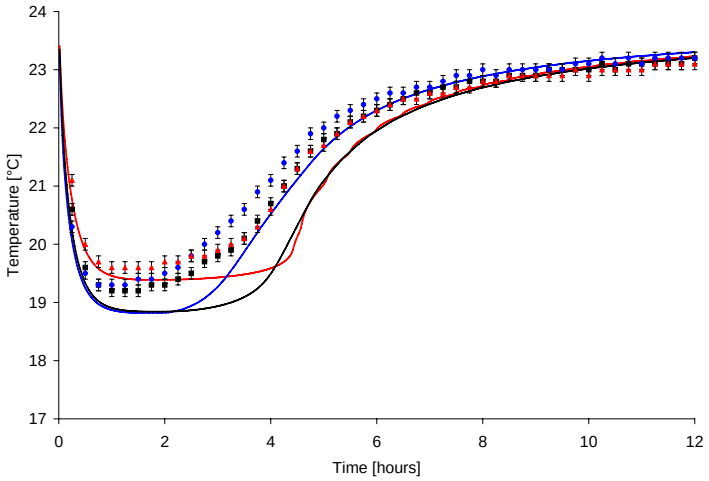

Figure 5.13: Simulated temperature at 10mm in the ceramic brick, up stream of the centre (blue), in the centre (black) and downstream (red). Comparison with measurements upstream (○), centre (□) and downstream (△)

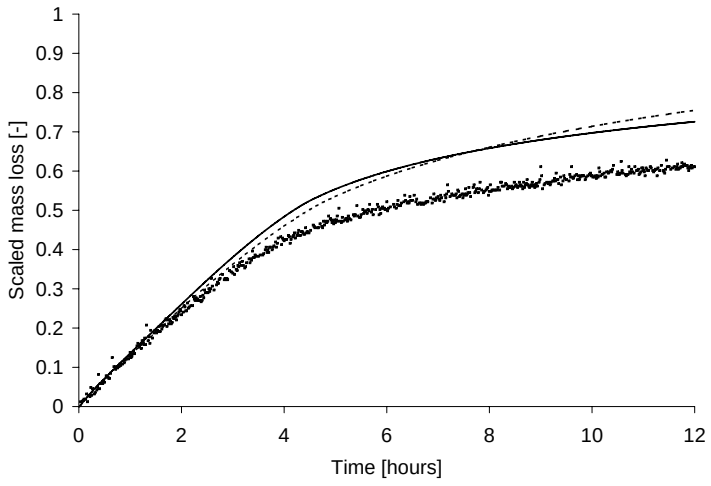

Figure 5.14: Scaled mass loss. Comparison between simulation with new CFD-HAM model (—), HAM model developed at KULeuven [43] (- -) and measurement performed by Defraeye [43] (■)

better agreement with the measurements (during the constant drying rate period) but afterwards deviations become larger.
Similar conclusion can be formulated for the predicted drying rate. Figure 5.15 shows the surface area averaged drying rate. Initially the drying rate predicted by the new HAM model is a bit higher. This corresponds with the higher temperatures found in Figure 5.16. During the decreasing rate period the drying rate of the new model falls faster which results in a slower mass loss (in correspondence with the measurements) and a faster temperature increase compared to the HAMFEM model.

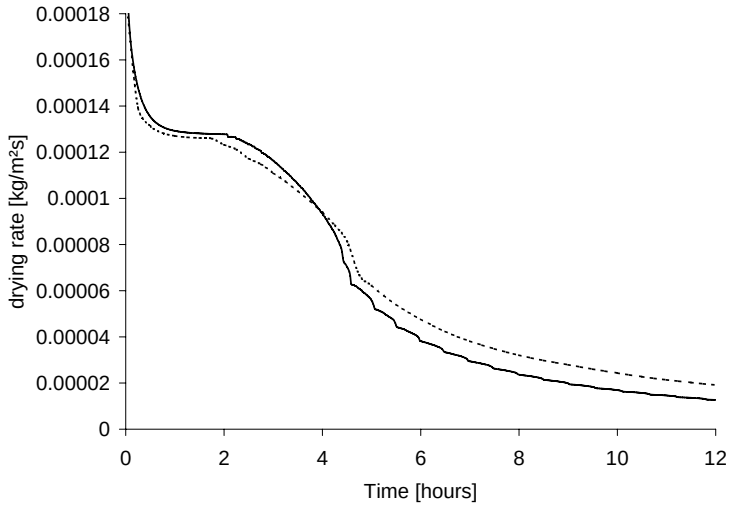

Figure 5.15: Drying rate. Comparison between simulation with new HAM model (—) and HAM model developed at KULeuven [43] (- -)

Figure 5.16 shows the inter-model comparison of the temperature evolution in time in the brick at various depths. Although the same boundary conditions are used in both models, there is a difference noticeable between both models. The deviations become larger deeper in the material. At $10mm$ and $20mm$ the temperature during the constant drying rate period agree rather good. The HAMFEM model however underestimates the temperature during the falling rate period. The reason for the deviations is difficult to asses. Different numerical techniques are used in both model (Finite Volume vs. Finite Element) and also the discretization is different. A denser grid was used in the CFD-HAM model compared to the HAMFEM model. Overall the new model is in better agreement with the measurement results when the same boundary conditions are used.

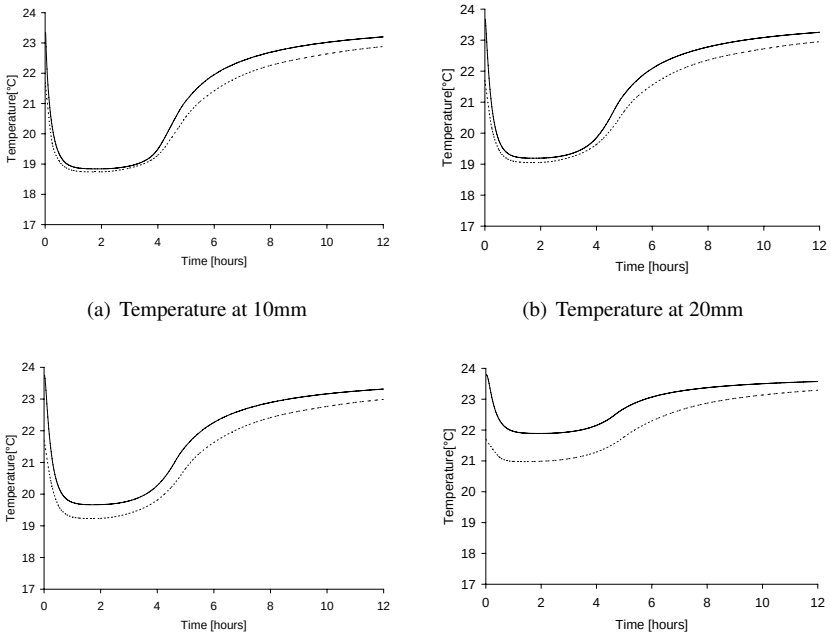

(a) Temperature at 10mm

(b) Temperature at 20mm

(c) Temperature at 30mm, at bottom of brick

(d) Temperature at 40mm, 10mm in insulation

Figure 5.16: Comparison between new HAM model (—) and HAM model developed at KULeuven [43] (- -) for temperatures at various depths in the brick

5.4.4 Moisture distribution in the brick: comparison with neutron radiography measurements

Data provided by the Swiss Federal Laboratories for Materials Science and Technology (EMPA) was used to further study the moisture transport behaviour in the ceramic brick. With neutron radiography this research group was able to measure the moisture content evolution in the ceramic brick over the depth of the sample. More details on the used measurement setup can be found in [148–150].
Figure 5.17(a) shows the comparison of the moisture content distribution in the ceramic brick over time for the simulation and measurements. This comparison shows that during the first hours the agreement is fairly good, but at later times (after 3 hours) the simulation shows a faster decrease of the moisture content compared to the measurements. This is in agreement with the mass measurement and simulation shown in Figure 5.14. This mass comparison showed a good agreement during the constant drying rate period (first 3 hours) and afterwards an overestimation of the simulated mass loss.
Some shortcomings of the neutron radiography appear in Figure 5.17(a). At the top and bottom of the sample some scattering was present. This resulted in a falsely decreasing moisture content at the bottom of the sample and a too fast decreasing moisture content at the top. For a correct comparison between the measured and the modelled moisture content only the central region in the brick, between $0.5cm$ and $2.5cm$, should be compared.

Although the temperature evolution in time is fairly well predicted by the model, there seems to be a systematic overestimation of the mass loss in the brick. This overestimation is found in both the CFD-HAM model and the HAMFEM model. This raises the suspicion that the deviation is caused by uncertainties in the material properties.
As shown in chapter 4 uncertainties on material properties can be large and the consequences correspondingly. It is however not the objective of the current chapter to asses the impact of material property uncertainty on the modelling outcome. Instead of performing a full scale sensitivity analysis only a few parameters were studied to check if the model deviation could indeed be caused by the material properties.
Studies in chapter 4 and by Defraeye [43] showed that the hygric material properties namely retention curve, permeability and vapour resistance factor are the most important. The comparison of measurements and simulations showed that the first drying period is well captured. This suggests that the permeability and the retention curve at high moisture contents agree well with reality. The large deviations occur during the second drying rate period (FRP).
Three parameters were altered to check the impact on the modelling outcome: water vapour resistance factor, retention curve and liquid permeability. It was found that increasing the vapour resistance factor from 24.79 to 32 had no significant impact on the mass loss in the brick and the moisture distribution.
Next the vapour retention curve was altered to study its effect. The retention curve

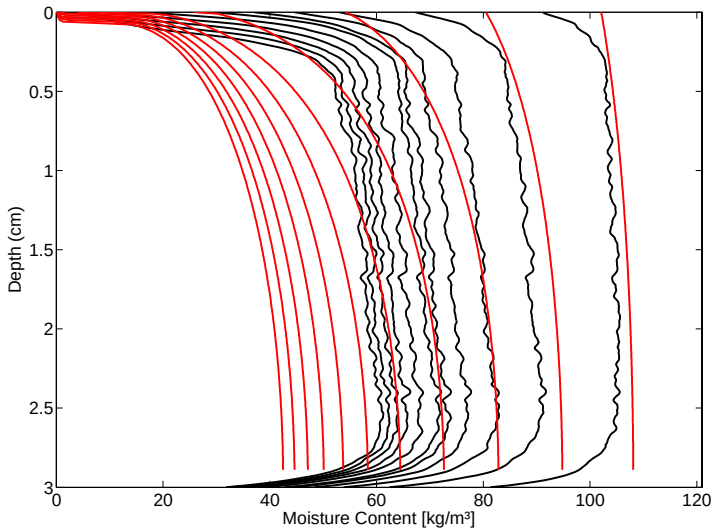

(a) Moisture distribution when using the original material properties as reported by [151].

Figure 5.17: Comparison of the measured (—) and simulated (—) moisture content distribution in the ceramic brick sample over time. Time difference between two lines is one hour.

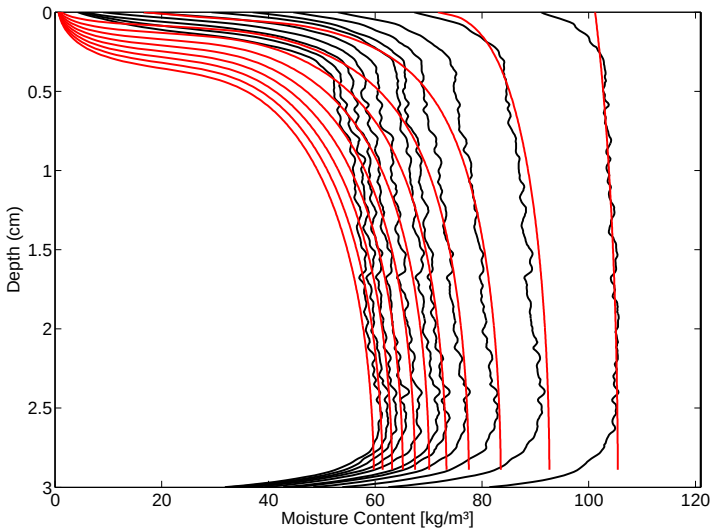

(b) Moisture distribution when using an adjusted retention curve.

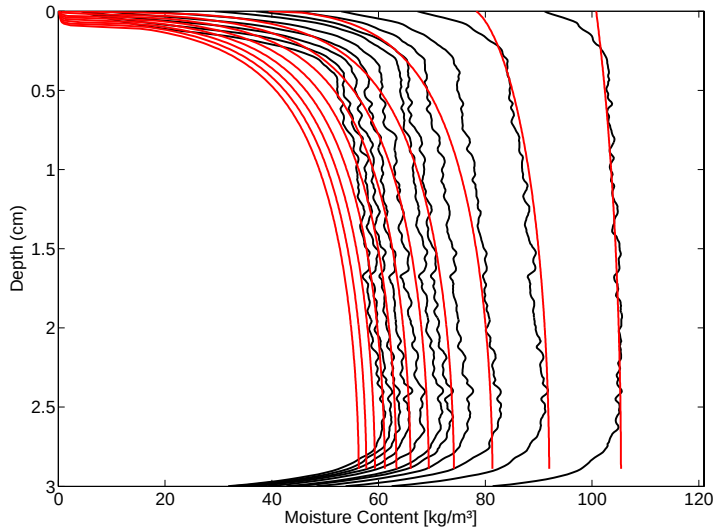

(c) Moisture distribution when using an adjusted liquid permeability.

Figure 5.17: (Continued) Comparison of the measured (—) and simulated (—) moisture content distribution in the ceramic brick sample over time. Time difference between two lines is one hour.

was adjusted in such a way that the curve only changed at high capillary pressures, so it would not affect the drying behaviour during the first drying period (CRP). Eqs. A.3 and A.4 in Appendix A give the original retention curve as found by Derluyn et al. [151] and the adjusted equation. The adjustment is highlighted in red. A graphical representation of these curves is also found in Appendix A.
Figure 5.17(b) shows the simulation results for the adjusted moisture retention curve. Comparing this with Figure 5.17(a) shows a better agreement when the retention curve is adjusted. However, the agreement only improves for the overall moisture content in the brick. The distribution of the moisture content deviates from the one measured by neutron radiography. For the altered retention curve the drying front moves too fast into the brick compared to the measurements. Adjusting the retention curve thus improves the overall moisture content prediction as shown in Figure 5.18 but does not improve the moisture content distribution. This suggests that deviations between measurements and simulations with the original material data can not solely be caused by a wrong estimated retention curve.
To study this further, the liquid permeability was also altered. The original liquid permeability curve and the altered version are listed and shown in Appendix A. By lowering the permeability, a better agreement can be found between measurements and simulations as shown in Figure 5.17(c). The agreement is better for both the moisture distribution (Figure 5.17(c)) and the overall moisture content (Figure 5.18). This comparison indicates that it is better to alter the liquid water permeability than the retention curve. Although uncertainty exists on all material parameters, in this case it is most likely that the largest deviations are caused by the uncertainty on the liquid permeability.
Figure 5.18 compares the mass loss computed with the original material data and the mass loss computed with the adjusted retention curve and liquid permeability. Both changes agree well with the mass loss measurements. But, as shown in Figure 5.17 a good prediction of the mass loss does not imply a good prediction of the moisture content distribution. It can thus be stated that both should be validated before a conclusion can be drawn on the correctness of the model and the used material properties.
Nevertheless, a good agreement for moisture does not guarantee a good agreement for temperature as is seen in Figure 5.19. Since heat and moisture transport in porous materials are strongly coupled, changes in retention curve or permeability have consequences for both temperature and moisture distribution. Where before the model underestimated the temperature, now the model seems to overestimate the temperature both for altered retention curve and permeability. Since the model with adjusted retention curve and permeability result in similar mass loss curves (Figure 5.18), the drying rates for both cases will be almost the same. The temperature in the brick is to a great extent determined by the drying rate (latent heat loss), therefore the predicted temperature curves are again similar for both cases.
The original model underpredicts the temperature whereas the adjusted models overpredict the temperature. However, the magnitude of difference between

measurements and simulations for the original case and the altered cases is similar. The models with adjusted retention curve and permeability do not result in a worse agreement of temperature, but at the same time there is also no improvement. It is thus difficult to make a sound conclusion on the impact that the adjustments have on the temperature course in the material.

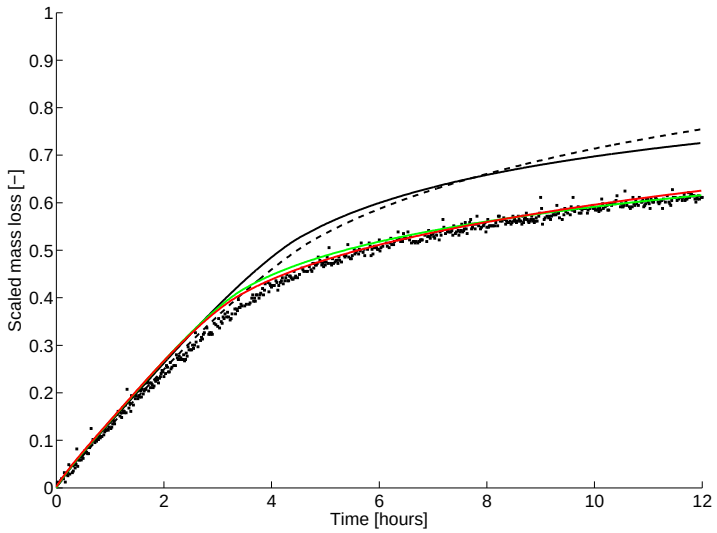

Figure 5.18: Scaled mass loss. Comparison of experiment (■) and simulation with new CFD-HAM model (—), HAM model developed at KULeuven [43] (- -) and new CFD-HAM model with adjusted retention curve (—) and adjusted liquid permeability (—)

5.4.5 Conclusion

In this section a convective drying experiment found in literature was described and used to validate the coupled CFD-HAM model including liquid water transport. Although the experiment was originally designed for 2D model validation, the current study showed that a 3D modelling approach is needed for adequate validation results. By applying an increasing model complexity the impact of a number of modelling assumptions is studied.

2D cross section model. The simplest drying model for convective drying is a 1D model where all boundaries except one are assumed impermeable and adiabatic. This modelling approach clearly underestimated the temperature

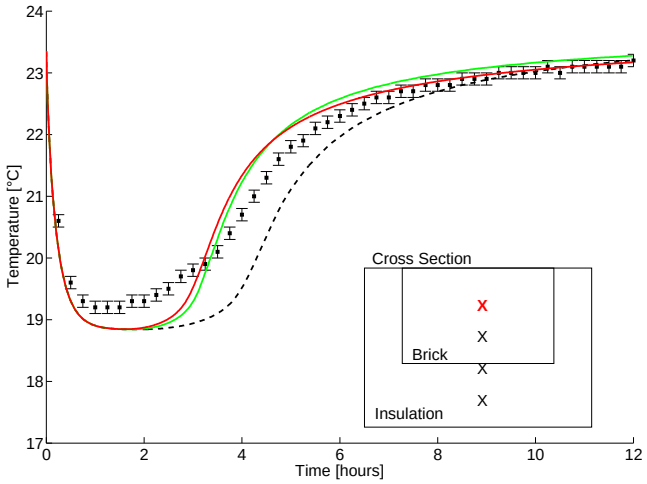

(a) Temperature at 10mm

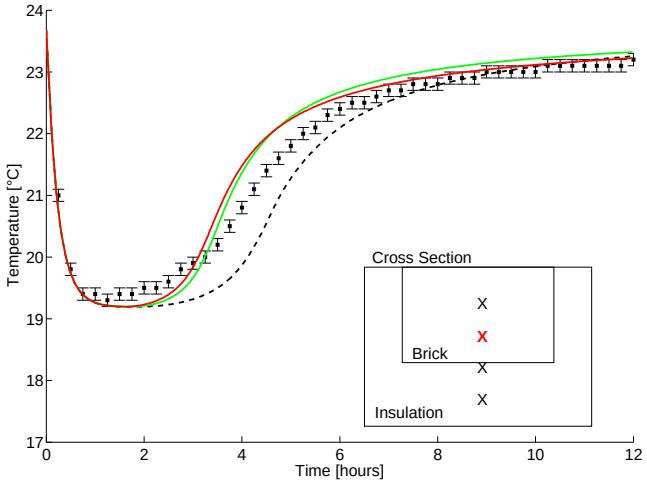

(b) Temperature at 20mm

Figure 5.19: Comparison between HAM model with original material data (- -), HAM model with adjusted retention curve (—) and HAM model with adjusted liquid permeability (—) with measurements (■) for temperatures at various depths in the brick

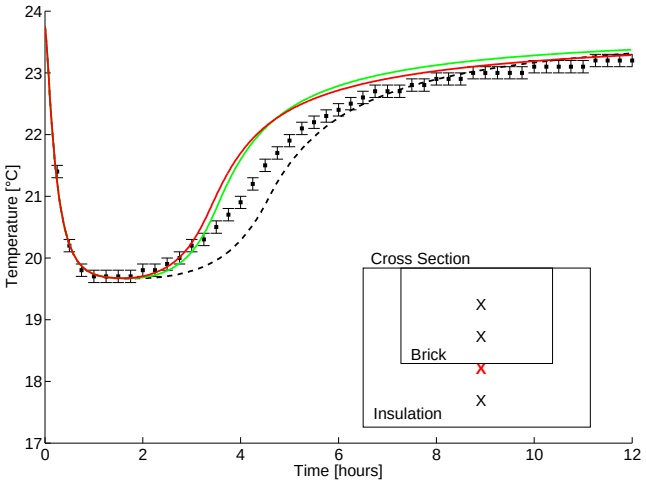

(c) Temperature at 30mm, at bottom of brick

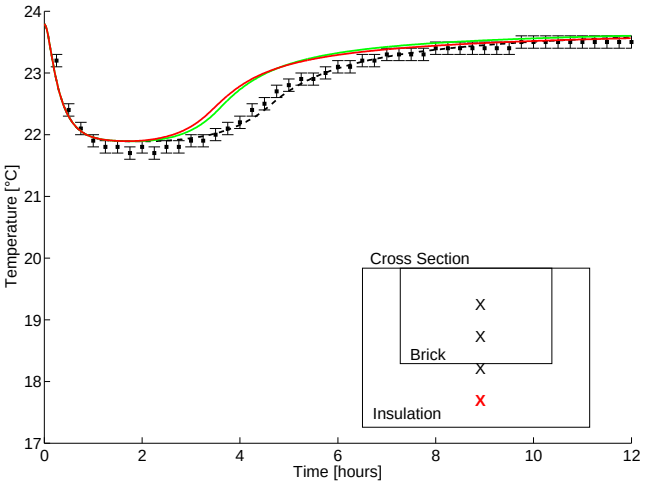

(d) Temperature at 40mm, 10mm in insulation

Figure 5.19: (Continued) Comparison between HAM model with original material data (- -), HAM model with adjusted retention curve (—) and HAM model with adjusted liquid permeability (—) with measurements (■) for temperatures at various depths in the brick

during the constant drying rate. Also the impact of the leading edge on the non-uniform heating and drying is not captured by such a model.

2D longitudinal section model. By upgrading to a 2D model with spatially varying convective transfer coefficients the modelling outcome is clearly improved. The model showed the impact of a distributed convective transfer coefficient on the temporal temperature and moisture distribution in the material. It was clear that for an accurate representation of the drying behaviour in a porous material this non-constant transfer coefficient is essential. The model however is not able to capture the temperature levels accurately. A systematic underestimation of the temperature in the material is noticed.

3D model. Finally the model was extended to a full three-dimensional representation of the test section including the insulation surrounding the brick and the plexiglass holding the sample. The temperature agreement for this configuration was much better, indicating that there is a strong three-dimensionally distributed heat gain through the insulation which can not be captured by simplified 1D or 2D models.

The simulated mass loss was also compared with the mass loss measured by Defraeye [43]. Here a significant discrepancy was found between the simulations and measurement even when a 3D model was applied. A similar discrepancy was found by Defraeye. He stated that this was probably due to inaccurate mass measurements so no real conclusions could be drawn.
To further study the moisture content in the brick, experimental data provided by the Swiss Federal Laboratory for Materials Science and Technology (EMPA) was used. This data showed the same discrepancies with the simulations as the mass measurements which suggests that this discrepancy is probably not only due to measurement error.
Further simulations with altered material properties showed that the discrepancies between simulations and experiments could be caused by inaccuracies in these properties. By adjusting the liquid water permeability of the ceramic brick it was possible to get simultaneously a good agreement for the mass loss and moisture distribution in the brick.
It is however dangerous to fit the measurements and simulations by *tuning* the material properties. For model validation these practices should be avoided since the material properties are then no longer measured independently. This independent measurement of material properties is a necessity for unbiased model validation.

It can be concluded that the drying experiment performed by Defraeye is useful for model validation but shows some shortcomings and should not be used as the only benchmark. The largest discrepancies between measurements and simulations were found for the mass loss. To conclude whether these discrepancies are due to material property inaccuracies, new property

determination measurements should be performed on the ceramic brick. This is however time consuming and not in the scope of this work.
A new experimental run with a different material could however answer some of the remaining questions and uncertainties in the model validation. Therefore a new experiment is designed based on that of Defraeye, using a different material and a larger sample size. This experimental setup is discussed in detail in the next section.

5.5 New drying experiment

5.5.1 Introduction

The previous section (section 5.4) showed a good agreement between experiments and simulations for the drying model. However as mentioned before the experiment by Defraeye [43] has some shortcomings. Therefore a new experiment was developed and conducted. This new experiment tries to tackle the two main shortcomings of the experiment by Defraeye: uncertainty in the mass measurements and a dataset limited to only one material namely brick. Therefore a different material than ceramic brick was chosen.

Calcium Silicate (CaSi) was used as porous material for the convective drying experiment. This hygroscopic and capillary active material has a much higher capillary moisture content than ceramic brick. This results in larger weight change during drying. This large mass change can be measured more accurately. The material properties of CaSi are listed in Appendix A.
Furthermore the setup by Defraeye was limited in size, more specifically the width of the sample was limited to $1cm$ since the setup was also used for neutron radiography to quantify the liquid water content in the ceramic brick during drying. For the new setup this limitation no longer applies. Thus a larger sample can be used which again results in a larger total mass change during drying.

A drawback of the new material is the longer drying time even at higher air velocities. This resulted in a time consuming experiment taking up to 12 days for one experimental run where Defraeye's experiment only took 12 hours.

5.5.2 Experimental setup

The new drying experiment resembles the experiment performed by Defraeye [43]. Defraeye monitored the drying behaviour of ceramic brick by measuring the temperature at various depths along the side surface of the brick with thermocouples (see Figure 5.4). In the new setup again thermocouples are used for the temperature monitoring only this time the thermocouples are inserted in the CaSi sample by drilling small holes. At the same time the mass change of

the test setup is measured by a precision balance (PE1200 Mettler-Toledo). After calibration the precision of the balance was estimated at $2g$. The total mass of the test setup with saturated sample is $\pm 1200g$ resulting in a relative uncertainty of 0.16%. The relative uncertainty increases to 0.25% when the sample is dry. Temperature is measured with an accuracy of 0.1°C after calibration.
To ensure well controlled boundary conditions the climate chamber discussed in section 4.4 was used. With this chamber and the accompanying air handling unit it is possible to control the supply air velocity, temperature and humidity. The inlet temperature was controlled at 30 ± 0.1°C the inlet relative humidity was $20 \pm 1.4\%$. Figure 5.20 shows the location of the test sample and the balance in the climate chamber. The velocity profile at the climate chamber inlet was measured with a hotwire anemometer. Since the inlet of the chamber can be assumed symmetrical, only half of the inlet was measured. The velocity profile is depicted in Figure 5.21.

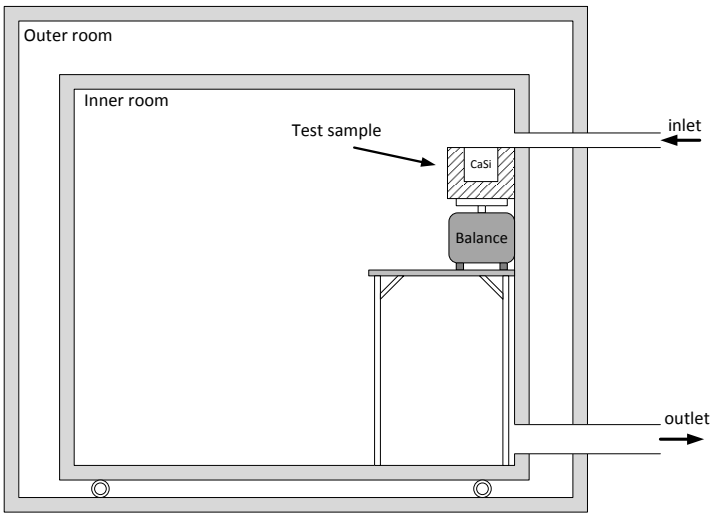

Figure 5.20: Schematic representation of the climate chamber with the test sample of CaSi placed on top of a balance. For chamber dimension see Figure 4.1, for sample dimensions see Figure 5.22

The Calcium Silicate test sample measures $10cm$ by $10cm$ by $5cm$. The same material was used as in section 4.4. The material properties of CaSi were measured extensively during the HAMSTAD project by KULeuven [108]. These properties were used as input for the CFD-HAM model.
The sides and bottom of the sample were sealed for moisture by silicone rubber. Polyurethane foam with a thickness of $5cm$ was used as insulation for the sample sides. The material properties according to the manufacturer are listed in

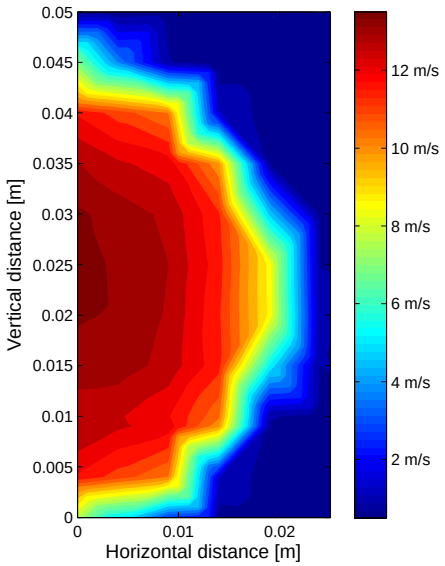

Figure 5.21: Velocity profile at the inlet of the climate chamber

Appendix A. Figure 5.22 shows the schematic representation of the test sample and the location of the different thermocouples. Six thermocouples were inserted in the CaSi sample, one row of three thermocouples were installed at $7mm$ depth in the sample, the second row of three thermocouples was placed at $17mm$. An extra thermocouple was installed at the bottom of the sample and finally the last thermocouple was inserted in the bottom insulation. Figure 5.22 shows the exact location of the thermocouples.

The sample was saturated with water and installed in the climate chamber just beneath the chamber air inlet, so the air jet flows over the sample top surface. Temperature and mass evolution over time were monitored during the drying of the sample. The drying time for the sample under these conditions (air velocity, temperature and humidity) was around 12 days. The experimental outcome will be discussed in more detail in section 5.5.5.

5.5.3 Limitations of the measurement setup

The new test setup in the climate chamber has some limitations. For a better interpretation of the experimental results, it is important to discus these issues.
The first issue is related to the long duration of the experiment. As mentioned it takes around 12 days for the saturated CaSi sample to completely dry out. During this time the conditions in the climate chamber can be affected by the outside climate conditions. Although the climate chamber is well insulated it can not be avoided that small heat gains or losses still occur through the chamber walls. To reduce these gains or losses a second chamber was built around the climate chamber. Even then small temperature fluctuations were noticed inside the chamber caused by long term fluctuation of the outside such as day-night fluctuations and weather fluctuations.
These temperature variations will introduce an extra uncertainty in the measurements on top of the sensor uncertainty after calibration. To estimate this uncertainty, the drying experiment is repeated several times.

A second drawback of the climate chamber is the round air inlet. Defraeye used a rectangular open wind tunnel setup [43]. The channel test section had a height to width ratio of 7 which is the minimum ratio for 2D channel flow according to Dean [144]. This 2D flow is easier to measure and model.
The new setup uses the round inlet of the climate chamber. This round inlet complicates the estimation of the convective boundary conditions at the top of the CaSi sample. The airflow over the CaSi surface will have a three-dimensional character and by consequence the heat and mass transfer coefficient distribution over the surface will be two-dimensional. It is possible to estimate these transfer coefficients by using CFD.

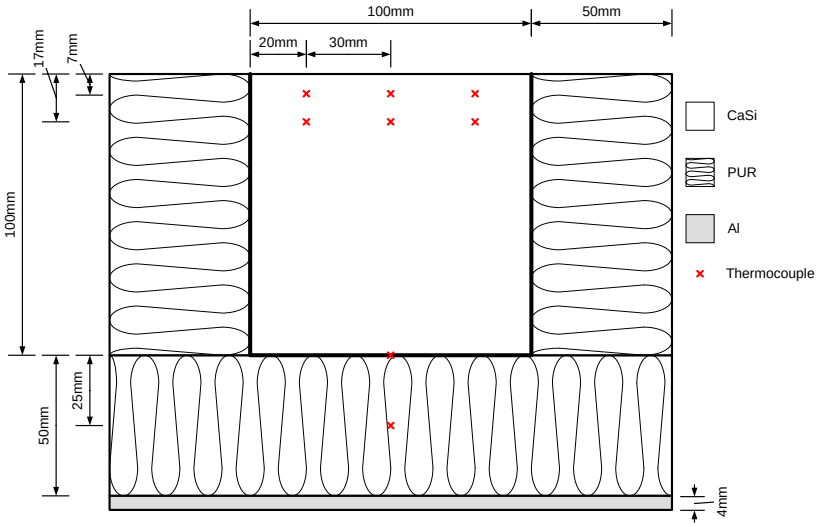

(a) Longitudinal section test sample

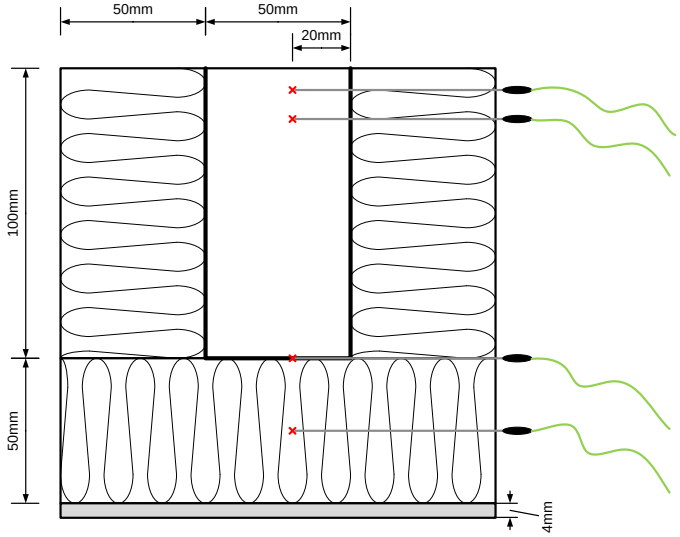

(b) Cross section test sample

Figure 5.22: Schematic representation of the longitudinal (a) and cross section (b) of the test sample for the drying experiment with CaSi. PUR = polyurethane, Al = aluminum

5.5.4 Simulation settings

In order to estimate the convective transfer coefficients at the top of the sample preliminary CFD simulations were performed. For these simulations only the part near the inlet of the chamber was simulated. The temperature and mass fraction at the surface of the sample were kept constant. The inlet temperature was 30°C, the surface temperature of the CaSi was 20°C. The inlet mass fraction was $0.005226kg/kg$ which corresponds with a relative humidity of 20%, the surface mass fraction was $0.01448kg/kg$. The measured inlet velocity profile depicted in Figure 5.21 was used as inlet conditions for the CFD simulation. The average turbulent intensity measured at the inlet was 3%.

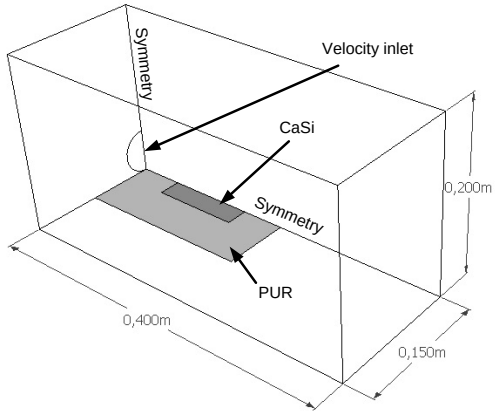

Figure 5.23: Schematic representation of part of the climate chamber used to simulate the air flow over the top of the sample. Indicated in dark gray is the CaSi top surface, in light gray the PUR surface is highlighted.

A symmetric boundary condition is assumed for the middle plane of the inlet so only half of the inlet and test section is to be simulated. Figure 5.23 shows the computational domain used for these simulations. All external boundary faces were modelled as pressure outlets except the surface where the inlet is located. This plane was modelled as a wall. The symmetry boundary face is also indicated in the figure. Only the flow, temperature and concentration field near the top surface of the CaSi have to be calculated exactly. Further from the CaSi surface the exact values for velocity, temperature and concentration are of less importance. The size of the domain can thus be limited to the area near the surface.
The SST $k-\omega$ model was used for the turbulence modelling. Since the convective transfer coefficients have to be determined, a very fine grid is needed near the surface so that the boundary layers for velocity, heat and moisture are fully

resolved. Therefore the $y+$ value should be around 1. The SIMPLE algorithm for pressure-velocity coupling was used. The convective terms where discretized with a second order upwind scheme. A double precision solver was used to reduce roundoff errors.
The grid independency was checked by comparing simulation results for a grid with 580800 cells with the results for a grid two times refined in every direction (8 times more cells). The average predicted heat and mass transfer coefficient, h and h_m, at the CaSi top surface were used for comparison. Table 5.3 shows the results. The difference between both predicted transfer coefficients was limited to 1%, so it was concluded that the courser grid sufficed for the current simulations.

	580800 cells	**4646400 cells**	**difference**
h	50.3	50.8	1%
h_m	0.0597	0.0603	1%

Table 5.3: Average heat and mass convective transfer coefficient for a course grid and a four times denser grid

Since the air flow in the calculation domain is three-dimensional, the predicted transfer coefficients also have a more complex distribution. The predicted convective heat and mass transfer coefficients are shown in Figure 5.24. The transfer coefficients will be higher near the inlet where the boundary layer starts.
A wake zone can be noticed in one corner of the CaSi surface. Here the velocity is low and by consequence the transfer coefficients are low. The wake zone where recirculation occurs, is caused by the cylindrical inlet and the cylindrical form of the jet flowing over the CaSi surface. It is clear from this simulation that the flow field near the surface is complex and detailed CFD simulations are needed to capture all effects accurately.

For the actual drying simulations of the CaSi sample a new computational domain was made, representing the test section as shown in Figure 5.22. The grid was fine near the top surface and courser towards the bottom. The PUR insulation was included in the computational domain.
In total seven surfaces need boundary conditions. These surfaces are indicated in Figure 5.25. The top surface has two parts: the CaSi surface and the PUR top surface. The PUR is assumed impermeable for moisture. A constant convective heat transfer coefficient of $25W/m^2K$is imposed for this surface.
The boundary condition for the CaSi top surface is more complicated. Here the transfer coefficients predicted by the preliminary CFD simulations (Figure 5.24) are imposed. Only half of the test sample has to be modelled due to symmetry. The symmetry boundary condition is indicated in Figure 5.25. The remaining PUR surfaces (sides and bottom) are all assumed impermeable for moisture and

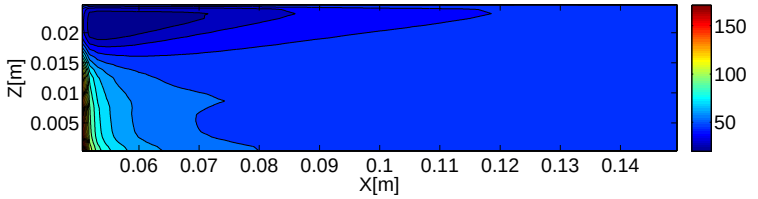

(a) CHTC

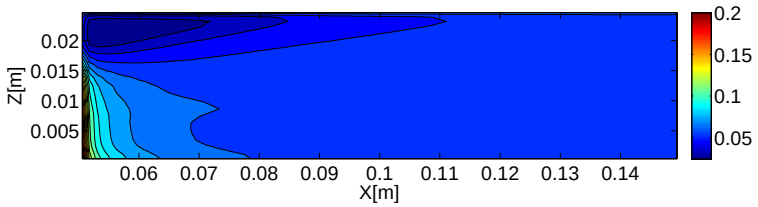

(b) CMTC

Figure 5.24: Distribution of the convective transfer coefficients at the surface of CaSi.

have again a constant heat transfer coefficient, h = $8W/m^2K$.
An additional radiation heat flux is added to the top surface to incorporate potential heat gains through radiation from the environment. The heat flux by radiation is estimated with Eq. 5.6. T_{roof} is here the roof surface temperature of the climate chamber. The temperature of the surface is assumed to be 30°C. The emissivity of CaSi is estimated at 0.9 and that of the climate chamber wall (polyester lacquered, galvanized steel plate) was estimated at 0.9.
The reference temperature was 30°C. The reference mass fraction was $0.005226kg/kg$, corresponding with a relative humidity of 20%.

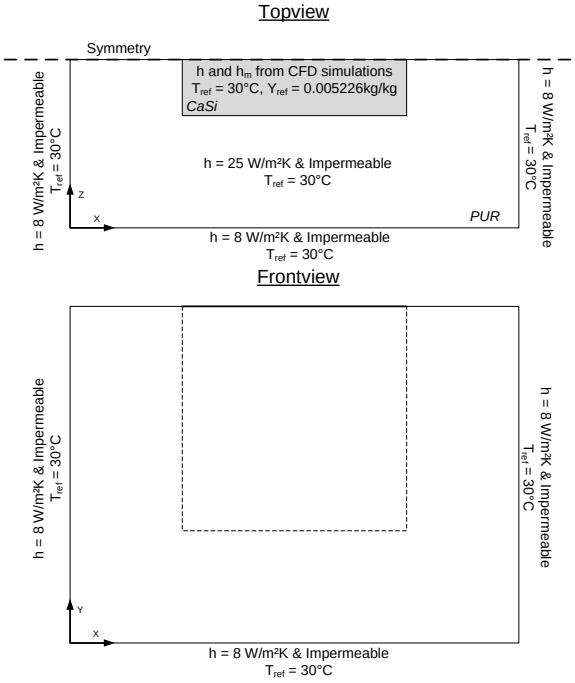

Figure 5.25: Computational model for CaSi sample: boundary conditions on exterior surfaces.

5.5.5 Drying experiment - comparison with simulations

As mentioned in section 5.5.3 the boundary conditions during the tests could vary due to the imperfect insulation of the climate chamber. These fluctuations increased the uncertainty of the measurement outcome. To asses the impact of the boundary conditions the measurements were performed several times. From these

measurements an average mass loss curve could be derived. This average curve is depicted in Figure 5.26 together with the simulation results. Errorbars are added to the graph. These bars indicate two times the standard deviation of the successive measurements. They are a measure of the uncertainty on the mass loss due to variations in the boundary conditions between different measurement campaigns. The graph shows a very good agreement between measurements and simulations. In other words the model is able to predict the drying of a sample of CaSi over a long period. These simulations were performed with the original data for the CaSi sample as listed in Appendix A. In contrast to the experiments performed by Defraeye and discussed in section 5.4, here it was not necessary to tune the material parameters to get a good fit for the mass measurements. This stresses the importance and impact of material property data. Due to the large uncertainty on material property data, especially hygric properties such as retention curves and moisture permeability it is often difficult to get a good agreement between measurements and simulations. A representative validation of a HAM model is thus only possible if sufficient cases are studied.

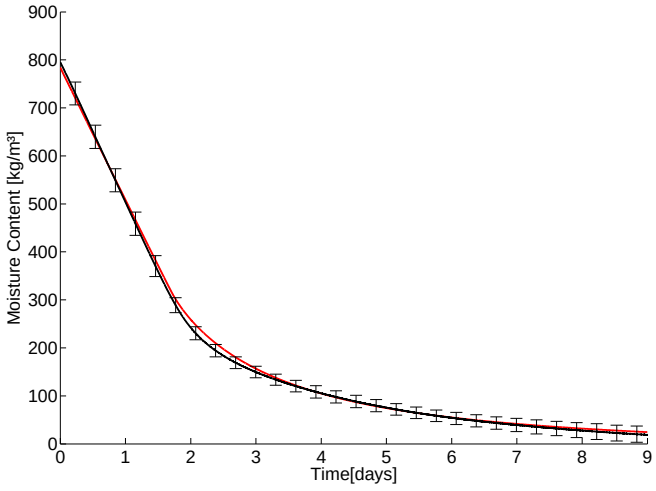

Figure 5.26: Comparison of the simulated moisture content in CaSi (—) with the average of the measured moisture content (—)

The moisture content curves in Figure 5.26 clearly show two distinct drying phases during the drying of the saturated CaSi sample. The first two days the mass of the sample decreases at constant rate. This corresponds with the constant drying rate period (CRP). After 2 days the mass change slows down and the drying rate decreases. This is the second drying period or falling rate period (FRP).
The good correspondence of the measured and simulated CRP indicates that the

heat and mass transfer coefficients at the surface are well predicted, since in the first drying phase the rate of drying is almost entirely determined by the air side boundary conditions.
Also the onset of the FRP and the mass decrease during the FRP is in good agreement with the measurements. During the falling rate period the moisture transport at the surface is dominated by vapour diffusion. Here the hygric material properties determine the drying behaviour. Since the measurements and simulations correspond well for the FRP, it can be concluded that the material properties are accurate enough.

The combination of a hygroscopic and capillary active material with a low heat conductivity, makes Calcium Silicate a porous material with very specific properties. Due to its resistance to high temperatures it is often used as fire resistant insulation. However, nowadays it is also used as hygroscopic and capillary active insulation material for building envelopes. The high moisture buffering capacity of the material enable it to dampen humidity variations and occasional interstitial condensation can be redistributed and transported out the material due to the high capillary activity [152].
Because of the special combination of material properties, the drying behaviour of CaSi will also be characteristic. The measured temperature evolution in time in the CaSi during drying is shown in Figure 5.27. Three stages can be distinguished in these curves. During the constant drying rate period the temperature in the CaSi drops near to the wet bulb temperature. Due to heat gains through the insulated sample walls and by radiation from the surroundings, the temperature during the constant drying rate period will be higher than the wet bulb temperature. Figure 5.26 and 5.27 show a constant drying rate period for the first two days.
When the surface of the CaSi starts to dry, after two days, the CaSi enters the second drying period or falling rate period. The drying rate decreases and the temperature in the CaSi rises. This temperature rise seems to occur in two phases. First the temperature rises to ± 24 °C, where a new equilibrium temperature seems to occur. After a while this temperature increases further to eventually reach the supply air temperature when the sample is completely dried.
This intermediate temperature platform can be explained by the moving moisture front in the material. As the material dries, a moisture front is formed and moves into the material. On one side of the moisture front the relative humidity is low, here the sample is dry, on the other side of the moisture front the relative humidity is high (close to 100%) and the sample is thus still wet there. It is at the moisture front that liquid water evaporates. The vapour is then transported to the surface of the sample by diffusion. For the evaporation at the moisture front, energy is needed for the phase change. This latent heat change results in a local temperature drop at the moisture front.
The intermediate temperature platform is extra pronounced due to the low heat conductivity of the CaSi when dry. The dry top layer of the CaSi acts as an insulation layer on top of the wet material, keeping the temperature in the wet part of the CaSi low.

Figure 5.28 shows the temperature distribution in the sample every 24 hours as simulated by the coupled CFD-HAM model. These simulations show how the low temperature zone moves into the material as the material dries. The local evaporation at the moisture front acts as a heat sink in the sample.
In contrast to the brick drying in section 5.4 there is no pronounced effect of the transfer coefficient distribution over the sample surface. This is also clear when looking at Figure 5.28. Here the temperature distribution in the sample is almost symmetrical and no leading edge can be distinguished. This shows that the use of spatially varying transfer coefficients is not always needed and is very case specific.
The 2-dimensional temperature distribution is mainly caused by the leaking heat flux at the sides. This results in lower temperatures in the middle of the sample and higher temperatures near the insulated boundaries.

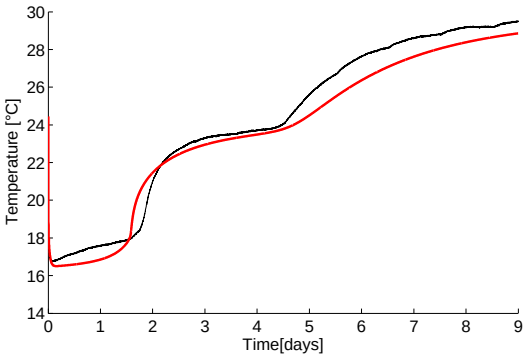

(a) Temperature at 7mm depth

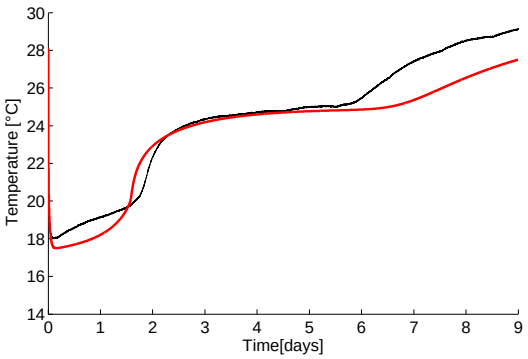

(b) Temperature at 17mm depth

Figure 5.27: Temperatures measured during the drying experiment of CaSi (—) compared to the simulations (—)

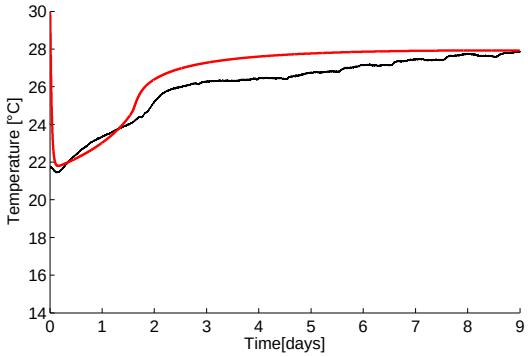

(c) Temperature at bottom of CaSi

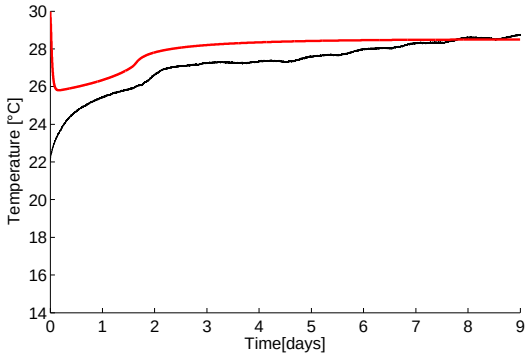

(d) Temperature in bottom insulation

Figure 5.27: (Continued) Temperatures measured during the drying experiment of CaSi (—) compared to the simulations (—)

5.5.6 Conclusions

A new test case was developed for the validation of liquid moisture transport modelling. A sample of calcium silicate was saturated with water and dried by convection. This temperature change in time at various depths was monitored together with the weight change of the sample.
These measurements showed a specific drying course of the CaSi sample. The second drying stage or falling rate period showed a jump in the temperature. This jump could be explained when the simulated temperature profiles were studied in more detail. It could be shown that during the course of drying a moisture front moves into the CaSi sample starting from the top. Above the moisture front relative humidity is below 100%, while below the moisture front relative humidity is still 100%. At this moisture front water vapour evaporates and diffuses out

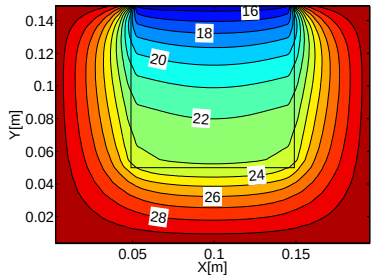

(e) Temperature distribution after 1 day

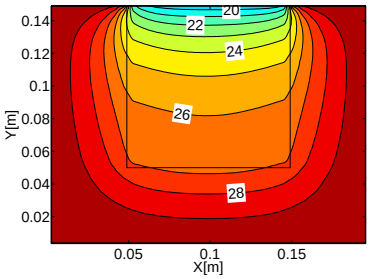

(f) Temperature distribution after 2 days

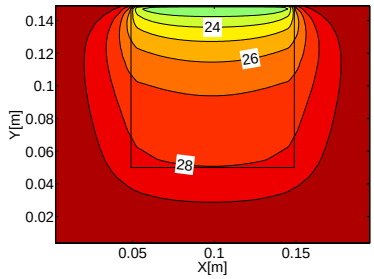

(g) Temperature distribution after 3 days

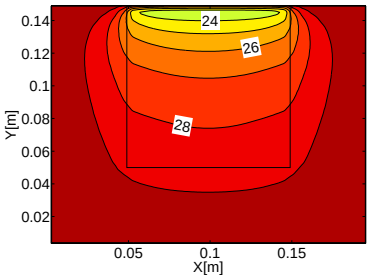

(h) Temperature distribution after 4 days

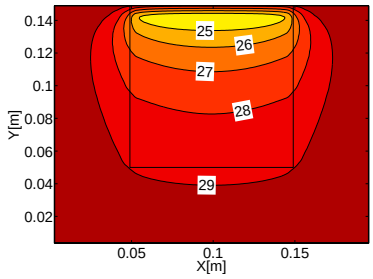

(i) Temperature distribution after 5 days

Figure 5.28: Temperature distribution in a longitudinal section of the CaSi sample

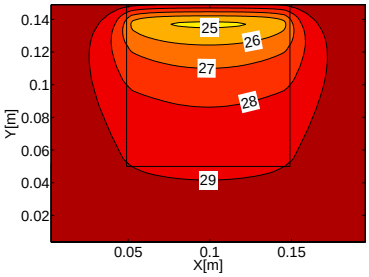

(f) Temperature distribution after 6 days

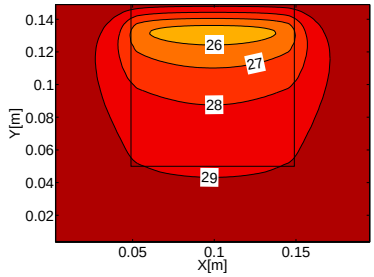

(g) Temperature distribution after 7 days

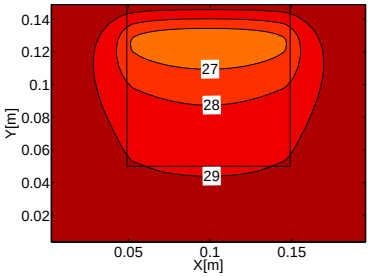

(h) Temperature distribution after 8 days

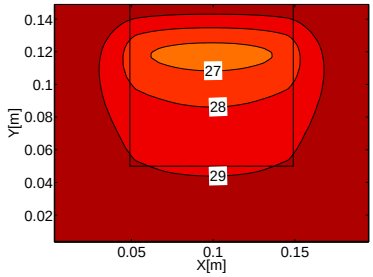

(i) Temperature distribution after 9 days

Figure 5.28: (Continued) Temperature distribution in a longitudinal section of the CaSi sample

of the CaSi sample. The moisture front acts as a heat sink resulting in a local decrease of the temperature in the sample. Once the moisture front moves past the sensor location, the temperature rises faster as observed in the measurements.

The new experimental data was used for model validation. A more complete validation of the new coupled CFD-HAM model is now possible. In combination with the validation of section 5.4 it can be stated that the new model shows good agreement with the measurements. It is able to correctly predict temperature and mass evolutions in time for two different material types.
Both validations also show the importance of a correct implementation of the boundary conditions. 3D modelling was in both cases necessary to get a good agreement. The impact of spatially varying transfer coefficients differed for both cases. In brick drying the development of a boundary layer over the top surface resulted in a clear leading edge effect. This leading edge effect was not observed in the drying of the CaSi sample. This emphasizes the conclusion of section 5.3.4 where it was stated that the importance of using spatially varying transfer coefficients is case dependent.

6

Case study: heat and moisture transport modelling in ventilated cavity walls

6.1 Introduction: modelling a ventilated cavity wall

Nowadays building envelopes are complex to assemble, sophisticated, and require considerable fine-tuning for good performance [153]. A specific class of multilayer wall systems are the cavity walls. Cavity walls are a widely used external wall type in Northwestern Europe. Their main durability problems are frost damage, rain penetration and mould development. Experience shows that they have a good moisture tolerance in cool, humid climates [154]. The outside leaf acts as a capillary barrier avoiding water from the outside to penetrate to the inside of the building. Drainage should be provided at the bottom of the wall so that water that would infiltrate the cavity can be evacuated.
Besides acting as a capillary break and preventing moisture from outside to reach the inner wall, the ventilated cavity can also help to remove moisture from the inner cavity leaf.
The findings related to the benefits of cavity walls are contradictory (Salonvaara et al. [153]). A wide range of building envelope types exists and an air cavity will not provide beneficial moisture and thermal performance for all. Furthermore, climate boundary conditions will determine to a great extent the performance of a cavity wall. A hygrothermal model could help researchers to gain a better understanding of the behaviour of cavity walls under different conditions and with varying configurations.

Modelling a cavity wall is however complicated. A cavity wall combines a lot of transport mechanisms and sources for heat and moisture, which explains the difficulty in modelling such a configuration. Figures 6.1 and 6.2 illustrate some of the main transport mechanisms for heat and moisture in cavity walls.
Figure 6.1 shows the heat fluxes, sources and sinks present in a cavity wall. For heat, three transport mechanisms can be identified: radiation, convection and conduction. At the outside, heat transport by radiation is very important. During sunny days solar radiation accounts for a large part of the heat gains of the wall. Solar radiation is referred to as shortwave radiation. Next, heat exchange by longwave radiation is possible. This is radiation emitted by the wall or received from the surroundings. The wall will also exchange radiant heat with the sky. During clear winter nights the temperature of the sky can be some 21°C lower than the environmental temperature [28]. This can result in significant longwave radiant heat losses.
In the cavity heat transfer by longwave radiation occurs when the cavity leafs have a different temperature. If convection in the cavity is low, the long wave radiation will be the most important heat transfer mechanism between the cavity leafs. Also at the indoor environment, longwave radiation from surrounding walls and objects can be of importance for the heat balance of the wall.
Air flow along the wall will result in convective heat transfer. Convection is transport by flow of a fluid, in this case air. Heat is transported from the wall surface to the air or from the air to the wall surface by the movement of air.
Transport through the (porous) solid cavity leafs is mainly by conduction. Conductive heat transport in the air is also present but will be small compared to convective transport.
Figure 6.2 illustrates the main moisture fluxes and sources in a cavity wall. Moisture sources depicted in Figure 6.2 are wind-driven rain, rising damp and outdoor and indoor vapour. This vapour is transported to the wall or in the cavity by convection and diffusion and can be absorbed in the porous wall.

The newly developed coupled CFD-HAM model is able to simultaneously solve the main transport equations governing heat and moisture transport in a cavity wall. The model is especially suited to capture the strong interaction between transport in the air cavity and transport in the porous cavity leafs. The focus of this chapter lies applying the newly developed coupled CFD-HAM model to a ventilated cavity wall and showing the abilities of the new model. Especially its ability to calculate in detail the heat and moisture distributions in the cavity wall are highlighted. It is however not the intention of this chapter to give a full performance evaluations of the studied cavity wall itself. The present model could help in such an evaluation, but would have to be complemented with other models and measurements. This is however not in the scope of this work.
Simultaneously the new model approach is compared with simplified models. In literature some of these simplified models for cavity ventilation are discussed (e.g. [155–157]). In this work it is investigated what the impact is of some of these simplifications on the heat, air and moisture transport in a cavity wall.

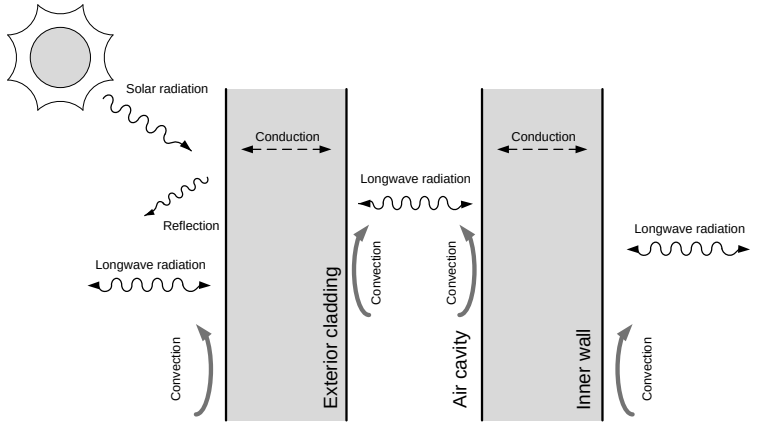

Figure 6.1: Illustration of possible heat fluxes occurring in and around a ventilated cavity wall.

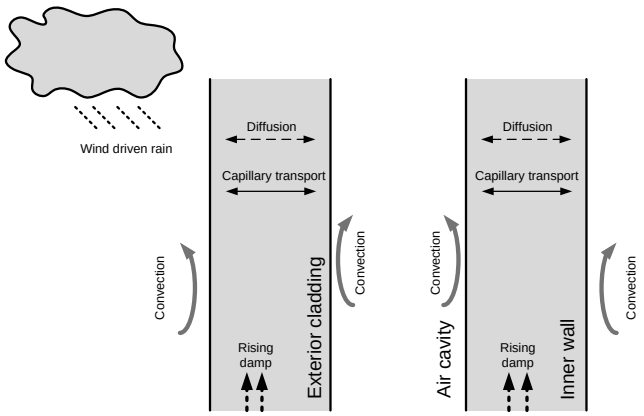

Figure 6.2: Illustration of possible moisture fluxes occurring in and around a ventilated cavity wall.

6.1.1 Cavity wall modelling in WUFI®

To model the impact of cavity ventilation on the building envelope performance, Straube and Finch [158, 159] listed some possible modelling techniques. The simplest approach according to them is *ignoring ventilation*. The cavity is modelled as still air. In WUFI-2D® [18] the thermal conductivity of the air layer is adapted to incorporate radiation, conduction and natural convection effects in a non-ventilated cavity. This results in a thermal resistance of the cavity as function of the inclination and cavity width. The vapour resistance factor of the air layer was adapted to include the effect of vapour diffusion and convection. Staube and Finch however found that this approach yields inaccurate results and state that the ventilation effect should be included in the modelling.
A second approach reported by Straube and Finch [158, 159] is *adjusting the vapour permeance* of the exterior cladding. The user adapts the vapour permeance depending on the estimated ventilation rates.
In some cases, the external cladding can be removed from the model. This is valid if the conditions in the cavity are the same as those of the outside. However the shielding effect of the external cladding for rain and solar radiation should still be included. Driving rain and solar radiation have a significant impact on the moisture transport in the cavity wall and these models tend to underestimate the moisture loading. This modelling approach can be improved by using measured cavity conditions as outside condition.

Nevertheless the aforementioned modelling techniques tend to yield inaccurate results. Therefore Karagiozis et al. [155] developed a simplified model for cavity wall ventilation and implemented it in a commercially available HAM model (WUFI®). The simplified model was able to capture the bulk performance of a cavity wall with reasonable accuracy and gave a rather good agreement with field data.
To account for ventilation, heat and moisture sources and sinks were added to the air layer. The moisture and heat added to or extracted from the cavity is modelled as a well-mixed process. The heat source/sink is determined as the amount of enthalpy entering the cavity minus the amount leaving the cavity due to ventilation. The mass source/sink is the mass entering minus the mass leaving the cavity. This can be expressed by the following equations:

$$S_h = Q_{air}\rho\left(h_{ext} - h_{cavity}\right) \tag{6.1a}$$

$$S_m = Q_{air}\left(\rho_{ext} - \rho_{cavity}\right) \tag{6.1b}$$

where S_h and S_m are the heat and mass sources/sinks respectively, Q_{air} is the volumetric air flow rate per volume of cavity $[m^3/sm^3]$, h_{ext} and ρ_{ext} are the enthalpy and air density at the cavity entrance and h_{cavity} and ρ_{cavity} are the enthalpy and density at the cavity outlet respectively.

The modelling techniques proposed by Karagiozis et al. [155] strongly simplify the actual transport mechanisms in the cavity. In reality air flow will enter the cavity through one of the cavity ventilation openings. The driving forces for the ventilation are pressure difference due to wind pressure on the building façade and pressure difference due to buoyancy. These pressure differences can fluctuate strongly in time. Also changes in outside conditions over time such as outside temperature and radiation will affect the buoyancy forces in the cavity and thus alter the flow field in the cavity.
At the same time heat and mass transfer from the cavity leafs to the cavity is determined by the flow field in the cavity. There is thus a strong coupling between the external conditions and the flow field in the cavity on the one side and between the flow field and the heat and mass transfer to the cavity on the other side. Karagiozis et al. neglect this coupling and state that assuming an averaged ventilation rate in the cavity often suffices.
Even if the ventilation rate is assumed to be constant, the flow field in the cavity would still change due to varying boundary conditions. In the simplified model implemented in WUFI®, the impact of convection as transport mechanism in the cavity is included in the adjusted thermal conductivity and vapour diffusivity. These values are however constant and their determination is based on natural convection in a closed cavity. It is clear that these parameters do not include the impact of varying boundary conditions since they do not change in time and/or space.

The assumption of constant flow conditions in the cavity is to some extent justifiable. Air velocity in the cavity is low and heat transport is mostly determined by radiation. If there is an initial difference in temperature between the cavity walls, this difference will disappear due to the radiant heat exchange between both surfaces. Since temperature differences are equalized in the cavity, the impact of buoyancy on the flow field will be less.
Simultaneously the diffusion of water vapour from and to the cavity leafs is determined by the vapour diffusion resistance of the porous materials which is often larger than that of air. This again reduces the impact of the flow conditions in the cavity on the convective transport from cavity walls to cavity and explains why the simplifications introduced by Karagiozis et al. [155] still result in reasonable agreement with measurements.

However there are some cases where the previously listed assumptions no longer apply, for example if a cavity wall is saturated with water and dried by convection. As stated in chapter 5 the moisture transport during the constant drying rate period is determined by the convective boundary conditions. In order to accurately predict the drying of a wet cavity it is thus important to capture the convective boundary conditions in the cavity with a reasonable accuracy.
Furthermore, WUFI® neglects the development of boundary layers in the cavity and the resulting distribution of convection coefficients. For example if air enters a cavity wall at the bottom, boundary layers will be thin at that point and fluxes

from porous material to cavity will be higher. For a wet wall this means that the wall will dry out faster at the bottom than at the top if air enters at the bottom.

It is not clear to what extent the simplifications proposed by Karagiozis et al. [155] hold. It is thus interesting to develop a model for heat and mass transport in a cavity, with a more detailed modelling of convection in the cavity. In the next section this model will be discussed before studying in more detail the impact of some of the simplifications used in WUFI®.

6.1.2 Cavity wall modelling using the coupled CFD-HAM model

Figure 6.3 shows an example of a cavity wall configuration. This configuration will be used for a more detailed study on heat and moisture transport. The cavity wall has an outside leaf of ceramic brick, an air cavity of $5cm$ and an inside leaf of wood fibre board (Celit® [160]), rockwool insulation and gypsum board as inside finishing. The material properties of these materials are listed in Appendix A. The wall has a hight of $2.5m$. The configuration of the wall is simplified to allow a 2D representation of the cavity. Inflow and outflow effects of the cavity vents are neglected and the cavity is modelled is a straight vertical channel (flow between parallel plates).

As outside conditions the climate in Brussels is used, based on data from Meteonorm [161]. Two cases will be studied here, a warm summer day in June and a colder day in December. Temperature and humidity on the 20^{th} of June 1995 in Brussels are used as summer condition, and the 17^{th} of December for winter conditions. The solar radiation is taken from Hens [162] and is the maximum solar radiation for a clear sky on a vertical west façade during June and December respectively. Figure 6.4(c) shows the daily variation of the solar radiation while Figures 6.4(a) and 6.4(b) shows the temperature and relative humidity for the 20^{th} of June and the 17^{th} of December respectively.

These conditions are used as exterior conditions for the ceramic brick outside leaf and as inlet conditions for the air cavity. The convective heat and mass transfer coefficients at the exterior wall surface were taken to be constant. The exterior heat transfer coefficient is $19W/m^2K$ and the mass transfer coefficient is $0.0217s/m$ (which is within the range suggested by ASHRAE [9]). As interior conditions for the cavity wall 21°C is used as constant room temperature and 50%RH as constant room relative humidity. The convective heat and mass transfer coefficients at the interior wall are $8W/m^2K$ and $0.00915s/m$ respectively.

To model the cavity wall the coupled CFD-HAM approach was used. The modelling procedure was already introduced in chapter 3 and will now be applied to the cavity wall configuration depicted in Figure 6.3.

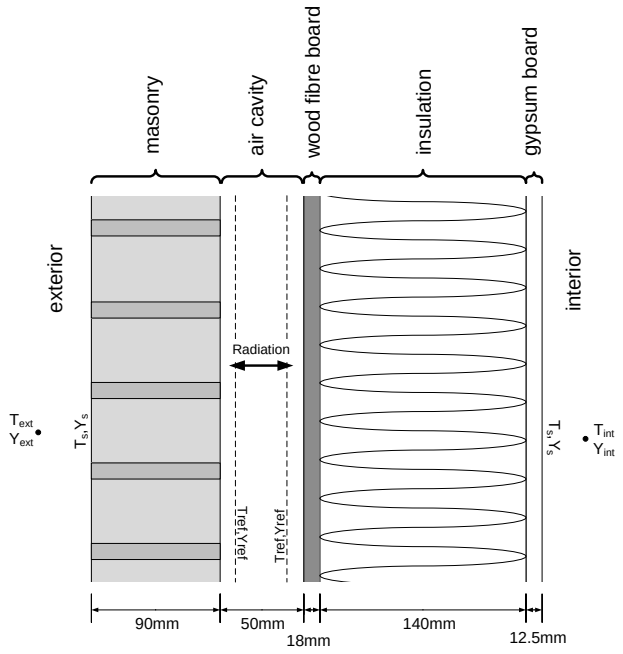

Figure 6.3: Cavity wall configuration.

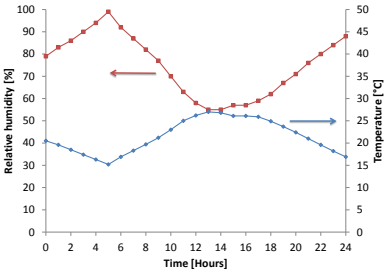

(a) Temperature-RH for a summer day

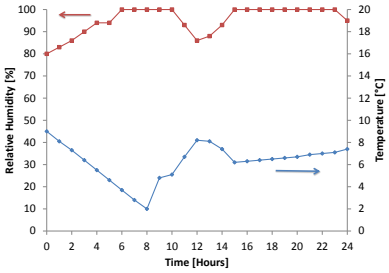

(b) Temperature-RH for a winter day

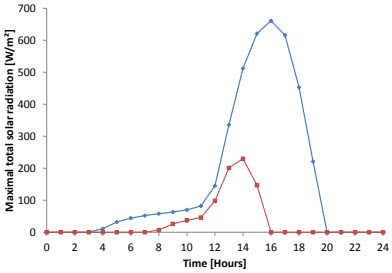

(c) Total solar radiation in June (—) and December (—) for a vertical west façade

Figure 6.4: Climate conditions for a warm summer day in June and a cold day in December in Brussels. Temperature and relative humidity from climate data in TRNSYS [161], radiation from Hens [162].

In this procedure first the airflow and heat and moisture transport in the air cavity is computed. A velocity inlet at the bottom of the cavity is used and at the top a pressure outlet is assumed. Inlet temperature and mass fraction are, as already mentioned, based on the exterior conditions depicted in Figures 6.4(a) and 6.4(b), depending on which case is solved. The boundary conditions of the side walls of the air cavity are the temperature and mass fraction of the porous material (ceramic brick and wood fibre board) surrounding the air cavity. These boundary conditions are not changed during a time step, and are only updated at the end of each time step.
At the end of each time step the heat and moisture fluxes from material to air are calculated using Eq. 3.33 for heat flux and Eq. 3.32 for the mass flux. From these fluxes a transfer coefficient can be calculated.

$$h = \frac{q}{T_{ref} - T_s} \tag{6.2}$$

$$h_m = \frac{g_v}{Y_{ref} - Y_s} \tag{6.3}$$

For flow over a vertical plate the bulk temperature and mass fraction are often used as reference (T_{ref}, Y_{ref}). However, for two parallel plates, there is no longer a clear definition of bulk flow since the boundary layers from both surfaces interfere. Therefore a different reference is used. As reference the temperature and mass fraction at a specified distance from the wall is used. This is indicated by the dashed line in Figure 6.3. So for each wall face there is a different reference, being the cell value at a fixed normal distance from the face.
The calculated transfer coefficients are then passed to the material side where they are used to calculate the heat and mass flux from the material to the air. The correct reference values for temperature and mass fraction are used to determine the fluxes, to ensure continuity of heat and mass flux at the material-air interface.
The advantage of passing on transfer coefficients and reference temperatures and mass fractions instead of fluxes is the ability to implement the boundary conditions at the material side implicitly as already mentioned in chapter 5.
When the heat and moisture transport in the porous material is calculated, the new surface values for temperature and mass fraction can be passed to the air side and the next time step is calculated.

The time step size used for the simulations with the coupled CFD-HAM model was 60 seconds. This value is based on earlier simulations with the coupled CFD-HAM model in chapter 4 and 5 and gave good results.
As explained in chapter 3 different time scales are present when heat, air and moisture transport in porous materials is modelled. Transport phenomena in the air have a much smaller time constant than phenomena in porous materials. It is thus not necessary to model all time variations in the air, since fluctuations in the air with high frequency will have no impact on the heat and moisture transport in the material. Therefore the air can be modelled as quasi-steady-state. This implies that

flow unsteadiness is neglected. The flow field can be assumed constant during the time step of 60 seconds. However, changes in the flow field by changing boundary conditions are still included.

With the aforementioned approach it is possible to include convective transport in the cavity more accurately. However convective transport is not the only transport mechanism in a cavity. Figure 6.1 showed the different heat transport mechanisms present in a cavity wall. Air velocity in a ventilated cavity wall is generally low. As a result the convective heat transport is low and no longer the main heat transport mechanism. Heat transfer due to long wave radiation starts to play a major role at these low velocities. Therefore radiation can no longer be neglected when studying coupled heat and moisture transport in cavity walls. The next section will shortly discuss the radiation model implemented in the cavity wall model.

6.2 Radiation model

When considering longwave radiation in a cavity several simplifications can be made.

- All surfaces can be assumed diffuse.
- Only grey body radiation is assumed.
- The air does not participate in the radiant heat transfer. This means that absorption, emission and scattering of the air are neglected.

These assumptions allow the use of a surface-to-surface radiation model. Emissivity equals the absorptivity ($a = \epsilon$). For a grey body the emissivity ϵ and absorptivity a are independent of the wavelength. Since the material surfaces are assumed diffuse, the reflectivity can be considered independent of the incoming direction.
For a grey-diffuse body an amount of radiation energy incident on a surface is partly absorbed (a), partly reflected (ρ_{refl}) and partly transmitted (τ). In the cavity walls studied here the surfaces can be considered opaque and the transmissivity can thus be neglected. From the conservation of energy principle the following can be stated:

$$a + \rho_{refl} + \tau = 1 \tag{6.4}$$

It is now possible to determine the net amount of energy leaving or arriving at a surface due to radiation q_{rad} $[W/m^2]$. This derivation is discussed in detail in [57] and [145]. A short explanation is found below.

The radiant energy flux J_k $[W/m^2]$ leaving a surface k (radiosity) is composed out of two contributions: the emitted energy and the reflected energy. The

reflected energy flux is dependent on the incident radiant energy flux emitted by the surroundings. This can be expressed in terms of the energy fluxes leaving all other surfaces. The energy leaving surface k is then:

$$J_k = \epsilon_k \sigma T_k^4 + \rho_{refl-k} q_{incid,k} \tag{6.5}$$

In this equation $q_{incid,k}$ is the incident radiation from the surroundings $[W/m^2]$, σ is Boltzmann's constant, ρ_{refl-k} is the reflectivity factor for surface k and ϵ_k is the emissivity factor for surface k. The amount of incident radiation on a surface from another surface is in turn a function of the surface-to-surface view factor F_{jk}. This view factor F_{jk} represents the fraction of energy leaving surface j that is incident on surface k. This view factor can be determined according to Eq. 6.6.

$$F_{jk} = \frac{1}{A_j} \int_{A_j} \int_{A_k} \frac{\cos\theta_j \cos\theta_k}{\pi s^2} dA_k dA_j \tag{6.6}$$

Here A_j and A_k are the surface areas of surfaces j and k respectively, θ_j is the angle between the normal of surface j and the line connecting the centre of surface A_j and A_k. s is the distance between the surface centres of A_j and A_k. Note that for this equation the following reciprocity relation applies:

$$A_j F_{jk} = A_k F_{kj} \tag{6.7}$$

The incident radiation from the surroundings can now be formulated as:

$$A_k q_{incid,k} = \sum_{j=1}^{N} A_j J_j F_{jk} \tag{6.8}$$

using Eq. 6.7 this results in the following expression for the radiosity:

$$J_k = \epsilon_k \sigma T_k^4 + \rho_{refl-k} \sum_{j=1}^{N} F_{kj} J_j \tag{6.9}$$

The net amount of energy leaving or arriving at the surface due to radiation is then given by:

$$q_{rad,k} = J_k - G_k = J_k - \sum_{j=1}^{N} F_{kj} J_j \tag{6.10}$$

Fluent is able to apply these equations for all radiating surfaces. In the most extreme case each surface face can be considered a radiating surface. This is however computationally very expensive. Fluent therefore suggests a clustering approach. In this approach so-called surface clusters are introduced. In a surface cluster a specified number of faces are collected. For this collection of neighbouring faces the surface averaged radiation temperature $T_{rad,avg}$ is calculated.

$$T_{rad,avg} = \left(\frac{\sum_f A_f T_f^4}{\sum_f A_f} \right)^{1/4} \tag{6.11}$$

The coupled CFD-HAM model developed and discussed in this work, uses UDS transport equations to calculate the temperature in the air and in the material. It is therefore not possible to use the standard implemented surface-to-surface model in Fluent to incorporate the radiation effect. A radiation model has to be implemented by using the appropriate UDF's.
When implementing a radiation model valid for a ventilated cavity wall, some simplifications can be introduced that significantly reduce the necessary programming effort. Since the cavity leafs are parallel and the cavity leaf dimensions are large compared to the cavity width, the radiation surfaces can be modelled as two infinite parallel plates. In this case the view factors become 1. The net radiation from a cavity leaf reduces to:

$$q_{rad} = \frac{1}{\frac{1}{\epsilon_1} + \frac{1}{\epsilon_2} - 1} \left(T^4_{rad,avg,1} - T^4_{rad,avg,2} \right) \tag{6.12}$$

Where ϵ_1 is the emissivity of the first cavity leaf and ϵ_2 is the emissivity of the second cavity leaf. $T_{rad,avg}$ is the surface averaged radiation temperature of the cavity leaf. Here the assumption is made that the surface temperature used for the radiation calculation is uniform. In reality a distribution of the surface temperature will be present due to a combination of convection, conduction, evaporation and radiation effects.

6.3 Air velocity in a cavity wall

The total pressure drop in a cavity wall can be expressed as the sum of pressure drop over the inlet Δp_{in}, the pressure drop through the cavity Δp_{cavity} and the pressure drop over the cavity outlet Δp_{out} [155].

$$\Delta p_{tot} = \Delta p_{in} + \Delta p_{cavity} + \Delta p_{out} \tag{6.13}$$

The pressure drop between two parallel plates is described by the following expression [123]:

$$\Delta p_{cavity} = f \phi 4 \frac{L}{D_h} \frac{\rho v^2}{2} \tag{6.14}$$

with f the friction factor given by Eq. 6.15 for laminar flow and ϕ a correction factor for non-circular ducts (= 1.5 for parallel plates [163]). D_h is the hydraulic diameter (which is equal to twice the cavity width for parallel plates), L is the height of the cavity, v the velocity in the cavity, ν the kinematic viscosity and ρ the air density.

$$f = \frac{16}{Re} \tag{6.15}$$

By introducing pressure coefficients, the pressure drop over the inlet and the outlet can be expressed as function of the velocity.

$$\Delta p_{in} = C_{in} \frac{\rho v^2}{2} \tag{6.16}$$

$$\Delta p_{out} = C_{out} \frac{\rho v^2}{2} \tag{6.17}$$

There are two pressures that induce movement in the cavity: the wind pressure ΔP_{wind} and the buoyancy induced pressure ΔP_{stack}. The wind pressure depends on the environmental conditions such as outside wind speed, building orientation, location and building height. The stack pressure depends on temperature and moisture concentration distributions in the cavity. The pressure drop over the whole cavity will equal the sum of the wind and stack pressure:

$$\Delta p_{tot} = \Delta p_{wind} + \Delta p_{stack} = C_{in} \frac{\rho v^2}{2} + f\phi 4 \frac{L}{D_h} \frac{\rho v^2}{2} + C_{out} \frac{\rho v^2}{2} \tag{6.18}$$

It is thus possible to determine the ventilation rate in the cavity if the driving pressure difference Δp_{tot} is known. This pressure difference is however strongly dependent on environmental conditions. Not only wind pressure fluctuates in time since wind speed and direction changes, also the buoyancy driven pressure difference changes as temperature and moisture concentrations change in the cavity over time. Straube and Finch [158] showed the effect of changing environmental temperature and radiation on the ventilation rates in a cavity. They found that the ventilation rate in a cavity is to a great extent determined by buoyancy. However it was also shown that using a fixed annual average ventilation rate can predict the field performance of a cavity with reasonable accuracy and it is not always worth the extra effort of using actual hourly ventilation rate data.

It is however not in the scope of this research to accurately predict ventilation rates in cavity walls. This study only tends to evaluate the impact of simplified cavity models such as those proposed by Karagiozis et al. [155]. If an accurate distribution of pressure is to be included in the model, extensive measurement campaigns or CFD simulations would be needed.

In literature a lot of discussion is found on the actual ventilation rate and the impact of these ventilation rates on the drying behaviour of cavity walls. Straube [164] performed a detailed study on moisture control for building envelopes. An important part of this study dealt with ventilation flow and ventilation drying of wall systems. The study showed that the ventilation rate strongly depends on the size and shape of the ventilation inlets and outlets. Cavity walls with large vent openings such as open-joint panel claddings will have ventilation rates of several hundreds of air changes per hour while brick veneer cladding with only a few open head joints experienced only several dozen air changes per hour at most.

At first only cases are considered with constant inlet velocity, since in the present study only the impact of convection modelling in the cavity is considered together with the transport of heat and moisture from the cavity leafs to the air. The estimation of the inlet velocity is based on a study by Jung [165] reported in Straube [164]. In this study a ventilation velocity of about $0.1m/s$ was found for an average wind speed of $2.6m/s$. Therefore in the present study ventilation velocities of similar magnitude are used.
It should however be noted that ventilation velocities of $0.1m/s$ or higher, although common for large ventilation vents, are rare in brick veneer cavity walls with only a few open head joints. The hereinafter reported research results are thus only valid for well ventilated cavity walls.

6.4 Drying of a cavity wall under summer and winter conditions

To evaluate the performance of a simplified cavity model, a cavity wall configuration under specific boundary conditions was simulated for a period of one day with WUFI® and compared with simulations performed with the coupled CFD-HAM model. Figure 6.3 shows the cavity wall configuration that is used. The cavity itself has a width of $5cm$. The simulations were performed under summer and winter boundary conditions. Figure 6.4 shows the respective outside temperature, relative humidity and radiation during a warm, sunny day in June and colder day in December.

In total four simulation cases are studied:

Case 1 Summer conditions are used as boundary. The outside cladding, composed out of a brick veneer wall is assumed initially saturated with water. This mimics the situation after an intensive rain shower. The purpose of this simulation is to see how the moisture content in the cavity wall evolves when a ventilated cavity is present.
Initial conditions for both simulation models (WUFI® and the coupled CFD-HAM model) are listed hereafter. The brick layer was initially assumed almost saturated with water with a relative humidity in the brick of 99.99% and a corresponding moisture content of $129.7kg/m^3$. The initial temperature of the brick was assumed to be 18°C. The cavity air layer had an initial temperature of 25°C and a relative humidity of 50%. The inlet conditions of the cavity were the same as the outside boundary conditions. The wood fibre board had an initial moisture content of $17.8kg/m^3$ which corresponds with a relative humidity of 60%. The initial temperature of the wood fibre board was 25°C. The mineral wool and gypsum board also had an initial temperature of 25°C and a relative humidity of 60%. Sky radiation during the night is neglected.

Case 2 Winter conditions are used as boundary. Again the outside cladding is assumed initially saturated with water. Sky radiation during the night is neglected.
The brick had on initial temperature of 9°C and a moisture content of $129.7kg/m^3$, corresponding with a relative humidity of 99.99%. The inlet conditions of the cavity were again the same as the outside conditions. The initial temperature and relative humidity of the cavity air was 9°C and 80% respectively. The wood fibre board had an initial moisture content of $17.8kg/m^3$, a temperature of 9°C and a relative humidity of 60%. The temperature of the insulation was initiated at 15°C and the relative humidity in the insulation was 60%. The gypsum board facing the indoor environment had an initial temperature of 20°C and a relative humidity of again 60%.

Case 3 Summer conditions are used as boundary. This case is similar to case 1, only the moisture content of the wood fibre board differs. The wood fibre board is, similar to the brick, initially assumed saturated with water. The initial moisture content of the wood fibre board is $160kg/m^3$. This situation mimics for example rain penetration to the inside leaf or water leakage resulting in a wet inside leaf.

Case 4 This case resembles case 3, only here winter conditions are used as boundary condition. The same initial conditions are used as listed in case 2. The initial moisture content of the wood fibre board is $160kg/m^3$.

For the first case three inlet air velocities were evaluated: $0.1m/s$, $0.2m/s$ and $0.3m/s$. These velocities correspond to ventilation rates of respectively $144ACH$, $288ACH$ and $432ACH$. These air change rates were used as input for the simplified WUFI® model. As indicated in section 6.3 cavity velocities of $0.1m/s$ and higher correspond to well ventilated cavities.
Constant velocities at the inlet were assumed so the air change rate in the cavity is also constant over time. Temperature and moisture gradients in the cavity however result in a redistribution of the velocity profile in the cavity due to buoyancy. This distribution changes in time since the temperature and moisture distribution in the cavity change. This results in transfer coefficients which strongly vary in time and space. The simplified model does not take these variations into account as mentioned in section 6.1.1.

Figure 6.5 shows the comparison of the coupled CFD-HAM model with the simulation result for the simplified model in WUFI® for case 1. In Figure 6.5(a) the moisture content in the brick veneer is depicted. Both models clearly show the same trends. Drying starts slow as the temperature of the surroundings and cavity is low and the relative humidity in the air is still high. At sunrise, the temperatures gradually rise and solar radiation further heats up the cavity, which increases the drying rate. This can be seen in the larger slope of the moisture content graph after 10am.
However an overestimation of the drying rate by the WUFI® model compared to

the coupled CFD-HAM model can be noticed. At an inlet velocity of $0.2m/s$, a maximum difference of 9.4% is found between the coupled CFD-HAM model and WUFI®.
When the coupled CFD-HAM model was compared with WUFI® in section 3.4.3, no remarkable difference in moisture content during drying was noticed. The same material properties were now used in this case study. This indicates that the discrepancy is caused by the way ventilation is modelled in both models.
Figure 6.5 also shows the impact of the ventilation on the drying of the cavity wall. Three different inlet velocities were compared: $0.1m/s$, $0.2m/s$ and $0.3m/s$. The coupled CFD-HAM model indicates that the effect of the ventilation rate is limited. Varying the inlet velocity from $0.1m/s$ to $0.3m/s$ showed almost no change in the drying course of the brick veneer. This seems reasonable since transfer rates to the outside are almost a magnitude higher. The drying potential of the cavity for the ceramic brick can thus be considered small. The same conclusion was found by Hens et al. [154].
The simplified WUFI® model however gives a different result. This model shows a stronger impact of the ventilation in the cavity causing the brick veneer to dry faster if higher ventilation rates are present.
Table 6.1 compares the maximum relative difference of the simulated moisture content in WUFI® and the coupled CFD-HAM model for all four cases. The relative difference is determined by dividing the absolute difference by the moisture content predicted by the CFD-HAM model. For case 1 the results for the three velocities are listed. This comparison shows that at higher velocities the deviation between both models becomes larger in the ceramic brick. The simplified WUFI® model gives a different estimation of the convection and this difference increases when velocity increases.

		Brick	**Wood fibre board**
Case 1	$0.1m/s$	7%	6%
	$0.2m/s$	9.4%	2.8%
	$0.3m/s$	12.4%	3.7%
Case 2		1.9%	8.4%
Case 3		9.1%	23.6%
Case 4		1.9%	14.5%

Table 6.1: Relative difference of predicted moisture content between WUFI® and CFD-HAM model.

The wood fibre board at the inner leaf of the cavity behaves differently from the brick. Figure 6.5(b) compares the moisture content in the wood fibre board for case 1. A fluctuation in the moisture content is noticed. First the moisture content increases, due to the high relative humidity in the air. Next the moisture

content decreases again as the cavity heats up. After $8pm$ the sun goes down and solar radiation no longer reaches the wall. Temperature drops and the moisture content in the wood fibre board increases again. Both models show these trends. However the fluctuations predicted by WUFI® are greater than those predicted by the coupled CFD-HAM model.
Comparison of the relative difference of the moisture content in the wood fibre board (listed in Table 6.1) shows no direct trend as function of the cavity velocity. However Figure 6.5(b) shows increasing fluctuations in the moisture content of the wood fibre board for increasing cavity ventilation. The CFD-HAM model shows the same trends but less pronounced. It can thus be stated that again the WUFI® model overpredicts the effect of convection and that this overprediction increases as ventilation rates increase.

Table 6.1 indicates that the difference in predicted moisture content in the wood fibre board (between 2.8% and 6%) is smaller than in the brick (between 7% and 12.4%). This is because the brick starts from saturation while the wood fibre board only contains hygroscopic moisture. When a saturated material is dried, drying will take place in the first drying stage (constant drying rate period). During the first drying stage the drying rate is determined by the convection conditions. For the wood fibre board however moisture content is much lower and moisture is transported in the wood fibre board by vapour diffusion. The moisture transfer from air to material and vice versa is in this case determined by the vapour diffusion properties of the porous material and less by the convection conditions in the air. In other words, the impact of convection is the largest for drying in the first drying stage. For hygroscopic loading the impact of simplified modelling of the convection is less.

Figure 6.6 shows the simulation results for the drying of a cavity wall under winter conditions. Case 2 is similar to case 1 as they both start from a saturated brick wall. The winter conditions applied in case 2 will result in lower temperatures in the cavity wall which in turn results in lower drying rates.
Also the relative humidity in the air is higher for these winter conditions as can be seen in Figure 6.4(b). The drying course of the brick is mainly determined by the relative humidity in the air. During a large part of the day the relative humidity is close to 100%. When the air is saturated the brick cannot dry out. The drying rate is no longer determined by the convection coefficients but by the humidity in th air. As a result there is a better agreement between WUFI® and the CFD-HAM model (only a difference of 1.9%).
For the wood fibre board the difference between both models (8.4%) is larger than in case 1. Here the wood fibre board is hygroscopically loaded. During the whole day the mass fraction in the cavity air is higher than in the wood fibre board and the moisture content of the wood fibre board monotonically rises. In case 1 periods of hygroscopic loading were altered with periods of drying. This way, the too high moisture content during loading is compensated by the too high drying rate during drying and the overall difference between both models is less for that case.

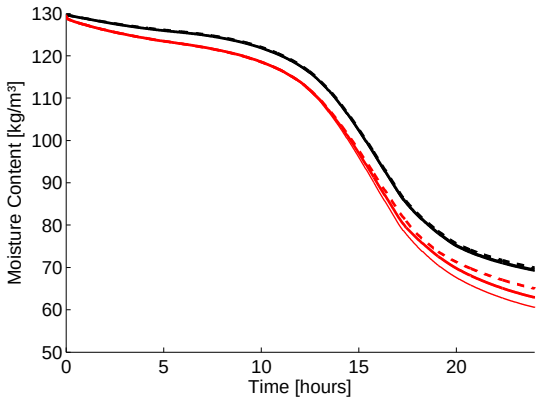

(a) Moisture content brick

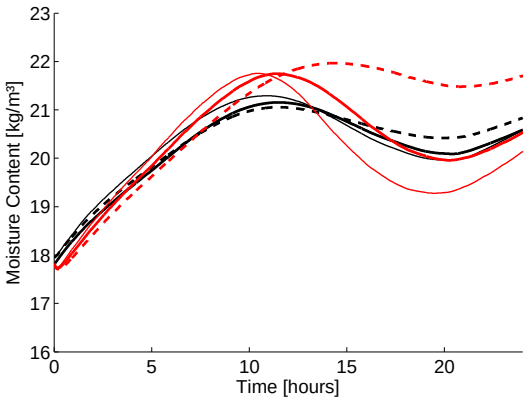

(b) Moisture content wood fibre board

Figure 6.5: Case 1: the moisture content in the brick and wood fibre board for a summer day starting from saturated brick veneer and relatively dry wood fibre board. Comparison of the coupled CFD-HAM model ($0.1m/s$- -, $0.2m/s$—, $0.3m/s$—) *and WUFI®* ($0.1m/s$- -,$0.2m/s$—,$0.3m/s$—).

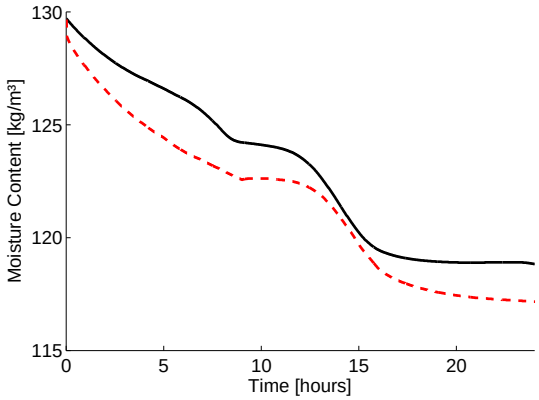

(a) Moisture content brick

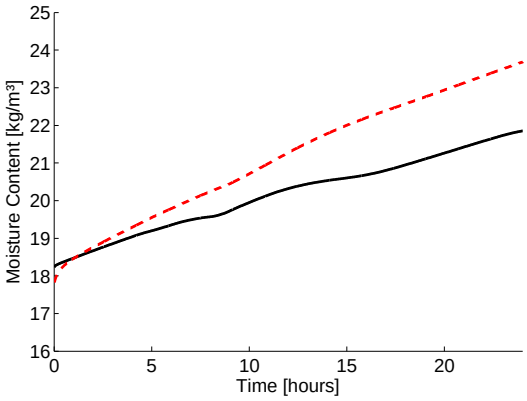

(b) Moisture content wood fibre board

Figure 6.6: Case 2: the moisture content in the brick and wood fibre board for a winter day starting from saturated brick veneer and relatively dry wood fibre board. Comparison of the coupled CFD-HAM model (—) and WUFI® (- -).

In Figure 6.5 differences of the predicted moisture content in WUFI® and CFD-HAM were larger for the saturated brick than for the unsaturated wood fibre board. However the impact of drying on the cavity side is partly masked since the brick dries out mainly to the outside, where convection is higher. This results in the WUFI model performing reasonably well for brick drying (maximum deviation between WUFI® and CFD-HAM around 12.4%).
However, the situation worsens when drying of wood fibre board is considered. These simulation results are shown in Figure 6.7. In case 3 and 4 not only the

ceramic brick was initially saturated with water but also the wood fibre board. The moisture content in the wood fibre board was compared for a simulation with WUFI® and a simulation with the CFD-HAM model. Table 6.1 shows the remarkably higher maximum difference between both simulations. The relative difference increased from 2.8% to 23.6% in summer and from 8.4% to 14.5% in winter. The WUFI model clearly predicts a faster drying at the cavity side. In the brick this difference was less pronounced since the drying of the brick took place at two sides. For the wood fibre board only drying at the cavity side is possible.

6.5 Constant inlet velocity versus constant inlet pressure

Cases 1 to 4 discussed in the previous section used a constant inlet velocity at the cavity inlet. The inlet was chosen at the bottom of the cavity. Based on literature an inlet velocity of $0.2m/s$ was used for the reference case which corresponds to quite a high air change rate of $288ACH$. Figure 6.8 shows the evolution in time of the velocity profiles half way in the cavity. The velocity profile is shown every four hours during a period of 24 hours. The shape of the profile is determined by the temperature distribution in the cavity. So called mixed convection occurs in the cavity meaning that buoyancy effect can not be neglected. The impact and importance of buoyancy on the flow field can be expressed by the Richardson number (Ri). This dimensionless number expresses the ratio of the buoyancy forces to the inertial forces. The Richardson number is defined by Eq. 6.19 where Gr (Grashof number) expresses the ratio of buoyancy forces to viscous forces. T_s is the surface temperature and T_∞ the bulk temperature, β is the thermal expension coefficient of air, D the hydraulic diameter and ν the kinematic viscosity. When the Richardson number is situated between 0.1 and 10, mixed convection occurs, $Ri > 10$ will result in mainly natural convection and $Ri < 0.1$ will be mainly forced convection.

$$Ri = \frac{Gr}{Re^2} \tag{6.19a}$$

$$Gr = \frac{g\beta\left(T_s - T_\infty\right)D^3}{\nu^2} \tag{6.19b}$$

A quick calculation reveals that for a temperature difference of 6°C, $\beta = 3.43{\cdot}10^{-3}$ $1/K$, $D = 0.1m$, $\nu = 15.11 \cdot 10^{-6} m^2/s$ and $v = 0.2m/s$, a Richardson number of around 0.5 can be found or in other words mixed convection is clearly present. This is also shown in Figure 6.8. When temperature differences between surface and bulk are high, the velocity profile clearly deviates from the parabolic profiles expected for fully developed forced laminar flow.

As discussed in section 6.1.1 Straube et al. [158] used WUFI® to model the effect of cavity ventilation. In this model the cavity flow rate can vary in time,

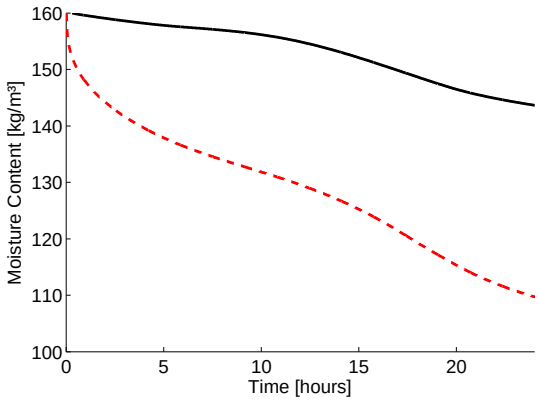

(a) Case 3: Moisture content of initially wet wood fibre board during a summer day

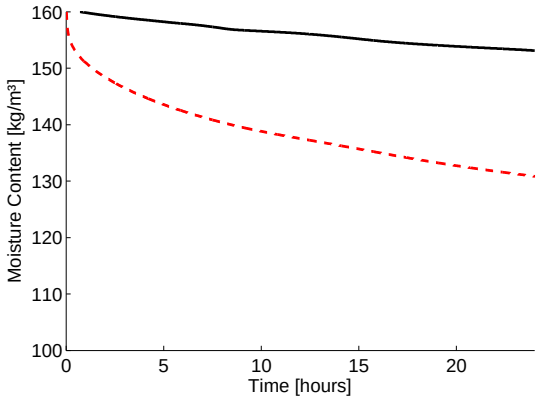

(b) Case 4: Moisture content of initially wet wood fibre board during a winter day

Figure 6.7: The drying course of a wet wood fibre board in a cavity wall under summer (case 3) and winter (case 4) conditions. Comparison between the coupled CFD-HAM model (—) and WUFI® (- -).

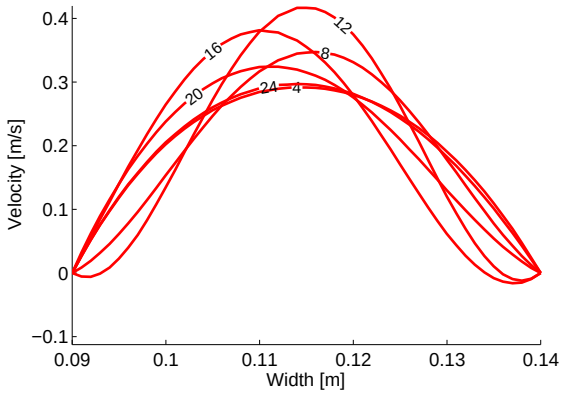

Figure 6.8: Velocity profiles halfway the cavity when a constant inlet velocity of $0.2m/s$ *is assumed. Profiles are shown for every four hours. The corresponding hours are indicated on each graph.*

however the effect of buoyancy on the spatial distribution of the velocity profile in the cavity in not included. This varying profile will result in changing transfer coefficients at the wall surfaces and thus changes in heat and mass flow from and to the walls. These effects are not included in simplified models such as those used by Straube et al. [158], where the effect of transfer coefficients is incorporated in an *effective conductivity* and *effective vapour resistance factor*. Both of these 'effective' coefficients do not change in time. In other words, the simplified models will not be able to capture heat and mass transfer in the cavity in detail when buoyancy effects become important.

In the cases discussed up till now a constant inlet velocity was assumed based on the observations of Straube et al. [158]. They found that it often suffices to use a constant air flow rate (e.g. the average air flow rate) when the impact of cavity ventilation is to be included in the modelling. However this assumption is far from reality as also discussed in section 6.3. Eq. 6.18 explains how the velocity in the cavity is a consequence of wind pressure and stack pressure. The pressure difference caused by wind results of course from the wind velocity, but also from building orientation and geometry. The pressure difference caused by the stack effect is determined by the temperature differences in the cavity which are in turn determined by climatic conditions (outside temperature and radiation). It is thus clear that velocity and air flow rate in the cavity will not be constant over time for a realistic case. Even if we assume a constant wind pressure, the flow rate in the cavity would still change due to buoyancy. A constant inlet velocity would correspond to a hypothetic case where the wind pressure would vary in such a way that it compensates the changes in stack pressure.

To study the effect of buoyancy on the flow rate in the cavity a new case is modelled. For this case a constant pressure at the bottom of the cavity is assumed. A pressure of $0.06Pa$ is chosen which corresponds with the pressure drop over the cavity when the inlet velocity would be $0.2m/s$ and no buoyancy effects would be present. The remaining boundary conditions are the same as described in case 3. In other words the cavity is simulated in summer conditions and both the brick wall and the wood fibre board are assumed initially saturated. The resulting velocity profiles in time are depicted in Figure 6.9(b). This figure shows the velocity halfway in the cavity every two hours during a period of 24 hours. Figure 6.9(a) shows the average velocity at the bottom of the cavity in function of time. These graphs clearly show the variation in time of the velocity in the cavity. Variation can even be so strong that the flow in the cavity changes direction. Positive velocities in Figure 6.9 indicate a flow from bottom to top, negative velocities indicate flow from top to bottom. This reversed flow is caused by the stack effect and can be explained when Figure 6.9 is compared with Figure 6.4. During the night outside temperatures are low and no solar radiation is present. Still the wet brick wall and wood fibre board are slowly drying, causing the air temperature in the cavity to drop even further. The cold air is denser and forces a downward flow in the cavity. As the sun comes up, outside air temperature increases and radiation heats up the wall and cavity. Buoyancy forces move the air upward in the cavity and around 9am the stack effect is strong enough to force the air upwards in the cavity. When evening falls, the temperature drops again, radiation disappears and the flow is again reversed.

The last case clearly illustrates the abilities of the newly developed coupled CFD-HAM model. When ventilated cavity walls are studied in detail it is clear that there is a strong coupling between heat and mass transport in the porous walls and the flow conditions in the cavity.
To illustrate the abilities of the model even further, temperature and moisture content distribution in the cavity wall are shown in Figure 6.10 and 6.11. Figure 6.10 shows the temperature distribution halfway in the cavity for summer conditions when both the brick and wood fibre board are initially wet. A constant pressure of $0.06Pa$ is assumed at the bottom. On the x-axis the width of the cavity wall is shown. The figure shows the five layers building up the cavity wall: the brick from 0 to $0.09m$, the air layer from $0.09m$ to $0.14m$, the wood fibre board from $0.14m$ to $0.158m$, the insulation from $0.158m$ to $0.298m$ and the gypsum board from $0.298m$ to $0.3105m$. Every two hours a curve is shown for a period of 24 hours. The figure shows how initially the temperature of the outside cavity leaf is low and slowly heats up as radiation and outside air temperature increase. When night falls, temperatures in the cavity wall again drop.
Figure 6.11 in turn shows the moisture content distribution halfway in the cavity. Both the brick wall and the wood fibre board are initially at saturation moisture content ($130kg/m^3$ and $162kg/m^3$ respectively). The figure clearly shows that the brick wall dries out faster at the outside than at the cavity side as was also concluded in section 6.4. The wood fibre board on the other hand mainly dries at

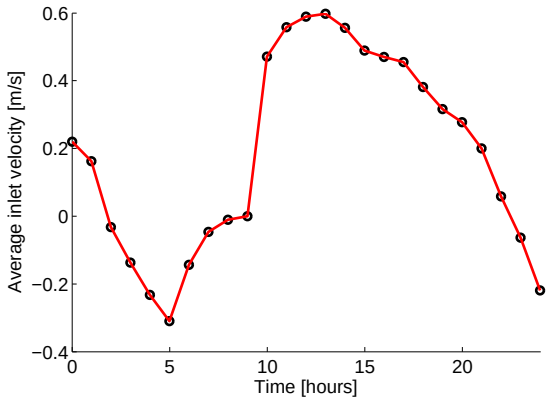

(a) Average velocity at cavity bottom

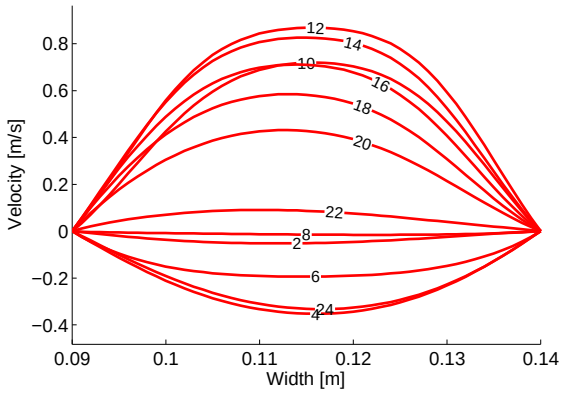

(b) Velocity profiles halfway the cavity

Figure 6.9: Figure (a) shows the average inlet velocity during 24 hours when a constant pressure of $0.06Pa$ *is assumed at the cavity bottom. Positive average velocities indicate a flow from bottom to top, negative velocities indicate a reversed flow. Figure (b) shows the velocity profiles halfway the cavity for the same constant pressure at the bottom. Profiles are shown for every two hours. The corresponding hour is indicated on each graph.*

the cavity side. In the air layer no moisture content is defined and therefore no graphs are shown for this region. The moisture content in the insulation is very low since the insulation is assumed non-hygroscopic and non-capillary. Also the moisture content in the gypsum board, used as inside finishing material, is low and corresponds with a relative humidity of around 50% inside the gypsum board.

The impact of the cavity ventilation on the brick wall drying is little. This can be seen in Figure 6.12(a). This figure compares the evolution in time of the moisture content in the brick wall for case 3 and the last case where a constant pressure at the inlet is used instead of a constant inlet velocity. Although the velocity in both cases differs a lot as noticed when comparing Figures 6.8 and 6.9(b), there is almost no difference noticed in the evolution of the brick moisture content. Indicating that a correct modelling of the convection in the cavity is not important when studying the drying behaviour of the outside leaf.
This does not count for the inside leaf. Figure 6.12(b) clearly shows a deviation in drying behaviour for the wood fibre board when comparing both cases. The wood fibre board initially dries faster for case 3 since in the first few hours velocities in the cavity are higher for case 3. However after about ten hours the velocity in the cavity is higher for the case with constant pressure at the inlet. This clearly results in a faster drying rate of the wood fibre board. The current example illustrates the importance of a correct model for the coupled solution of heat and mass transport in a cavity wall.

6.6 Discussion and conclusions

The analysis in this chapter showed some of the capacities of the newly developed coupled CFD-HAM model. The model allows a more detailed study of the complex heat and moisture transfer mechanisms in ventilated cavity walls. In a ventilated cavity an adequate simulation of radiation is very important since this has a large impact on the temperature in the cavity which in turn affects drying rates. Also transport by convection is important. In the past convection in the cavity was often modelled in a simplified way (e.g. Straube et al. [158]). This study showed that these simplifications are not always justified.
To study the impact of the simplified convection modelling in a cavity a comparison was made between WUFI® which uses a simple convection model and the newly developed coupled CFD-HAM model which models convection uncompromised.
The comparison showed that the simplified model overpredicted the drying and moistening rates of the cavity wall. Differences in predicted moisture content up to 23.6% were registered. Winter conditions resulted in less severe differences when drying of saturated walls was modelled, because for these cases the high relative humidity in the air limits the drying rates. The largest discrepancies were found for simulations in summer conditions at the inside leaf when this leaf was initially saturated.

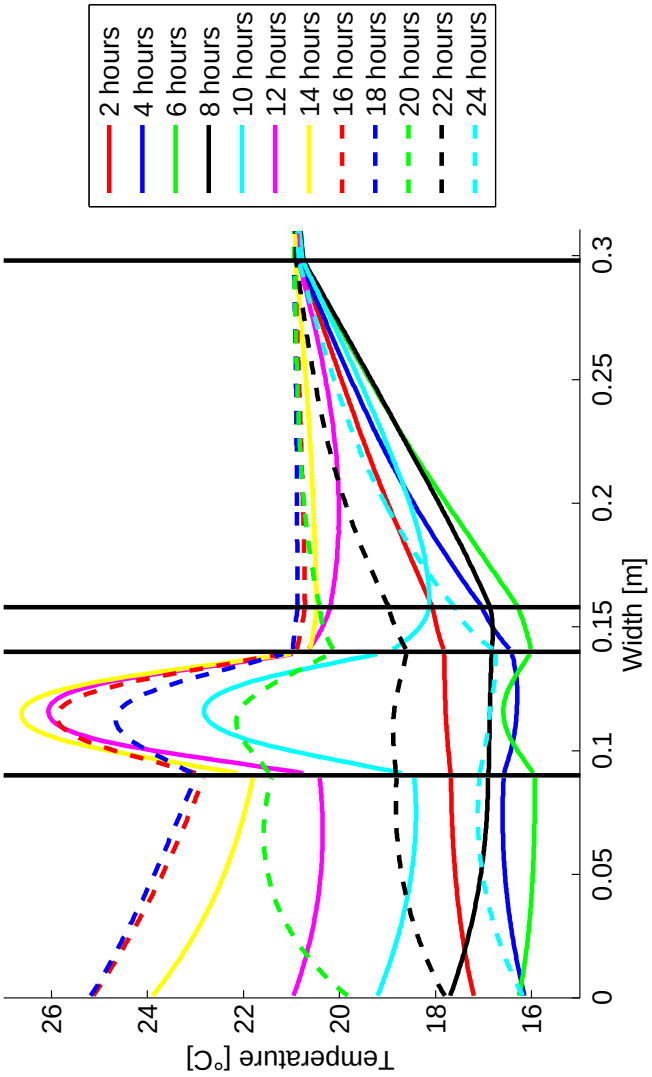

Figure 6.10: Temperature profiles halfway the cavity for a constant pressure of $0.06Pa$ *at the bottom. Temperature profiles every two hours are shown on the graph.*

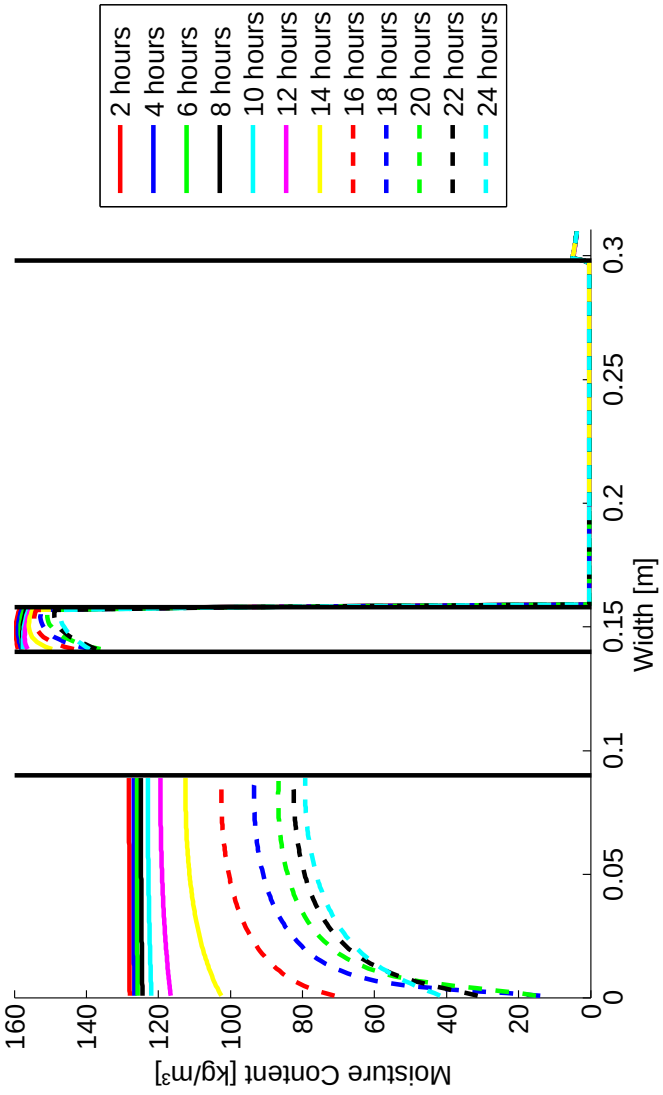

Figure 6.11: Moisture content profiles halfway the cavity for a constant pressure of $0.06Pa$ *at the bottom. Moisture content profiles every two hours are shown on the graph.*

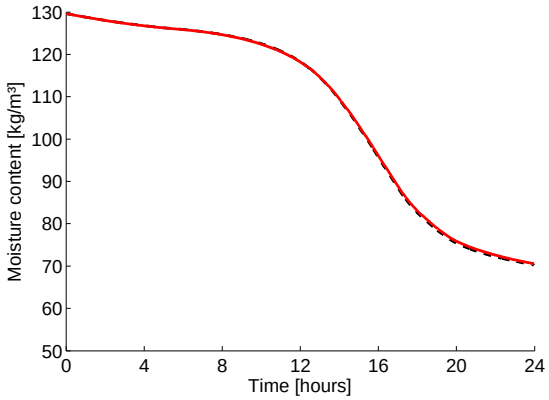

(a) Moisture content brick

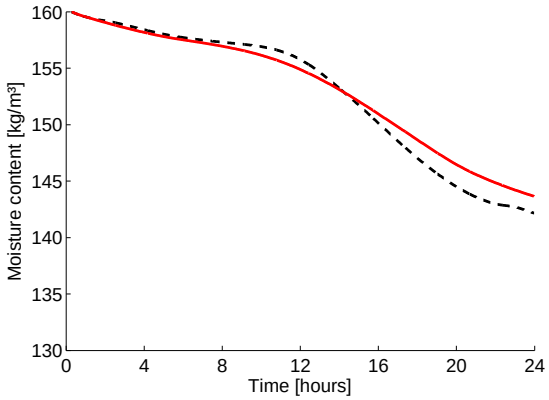

(b) Moisture content wood fibre board

Figure 6.12: Comparison of the moisture content in brick (a) and wood fibre board (b) for summer conditions, a constant inlet velocity of $0.2m/s$ *(—) and a constant pressure of* $0.06Pa$ *at the bottom (- -).*

Both models showed that the drying of the outer leaf is mainly determined by the outside conditions and dries out mainly to the outside and not to the cavity. The cavity ventilation in this case is of less importance. For the inside leaf this cavity ventilation is of major importance for drying. The study showed that the largest discrepancies between both models were found for this inner cavity leaf.
It is still the objective of both models to predict the moisture behaviour of a cavity wall as accurate as possible, so that it can be used to help practitioners and designers make the right decisions. However this study revealed that the simplified model cannot be used to evaluate the drying potential of a ventilated cavity. The simplified model systematically overestimates the ventilation effect. This has severe consequences when the model is used for cavity wall evaluation. Overpredicting drying rates results in hazardous situations going unnoticed. The simulation would in such a case indicate lower moisture contents than in reality and consequently lower risk for mould growth, wood rot or other structural damage.
A correct evaluation of ventilated cavity walls is only possible if convection is modelled in detail. The newly developed coupled CFD-HAM model allows such evaluation.
The model allows the implementation of more realistic boundary conditions such as inlet pressure instead of inlet velocity. When a fixed pressure is assumed at the bottom of the cavity, the effect of buoyancy on the flow rate in the cavity can be studied. Section 6.5 shows how both flow rate and direction are determined by the temperature in the cavity. Phenomena such as reversed flow and changing velocity profiles can only be studied in detail with advanced models such as the here newly developed coupled CFD-HAM model.

7 Conclusions and perspectives

7.1 General conclusions

In the building context a wide variety of moisture problems exists. A good moisture management from the design stage can prevent most of these problems. Therefore there is a strong need for accurate and reliable simulation tools to help the designers and engineers to make the right decisions. Nowadays several heat, air and moisture models exist which are able to predict the heat and moisture transport in porous (building) materials. However these models involve some simplifications that could have a significant impact on the model outcome. Firstly these models are often limited to one or two dimensions. Secondly the interaction between airflow and porous material is modelled in a simplified manner by using convective transfer coefficients.
In this work the impact of these simplifications on the modelling of coupled heat and moisture transport in the air and porous materials was studied. To examine this a new model was developed that included heat and moisture transport in the air as well as in the porous material. In the porous material vapour as well as liquid moisture transport is modelled.
To simplify the model implementation, the commercial available CFD solver Fluent® was used. Fluent allows the implementation of additional transport equations apart from the already present models. The heat and moisture transport equations in the air and in porous material were implemented into the CFD solver. This implementation was performed in two phases. First vapour transport in air and porous material was implemented and studied. Next the model was extended to also include liquid moisture transport in the material.

The vapour transport model was based on the work of Steeman [1]. In this approach mass fraction was used as transport variable for moisture in the air and in porous materials. Since the same transport variable was used for air and material, it was possible to solve both domains in one iterative run without the need for a coupling procedure or convective transfer coefficients at the air-material interface. However a thorough validation of this model was lacking.
A literature review revealed that there is a lack of experimental data for the validation of coupled CFD-HAM models. Three classes of experimental data were distinguished: wind tunnel experiments, climate chamber experiments and full scale measurements. All of them had certain constraints. Wind tunnel experiments have well controlled boundary conditions but the flow patterns differ a lot from those encountered in reality. Climate chamber experiments result in more realistic flow patterns, but available data in literature is scarce. Finally full scale experiments are closest to reality, but boundary conditions are difficult to control.
In this work a new experiment was designed and built, keeping in mind some important aspects. A climate chamber was designed with a well controlled incoming airflow. The air flow pattern in the room was measured and inlet temperature and humidity were controlled and monitored. Temperature and relative humidity of a porous material with one face adjacent to the room and the others sealed, were measured. These data allowed the validation of the coupled CFD-HAM model.
The experimental validation of the coupled CFD-HAM model for vapour transport with the newly acquired data showed good agreement between the simulations and measurements. However no perfect match was found. These deviations between measurements and simulations could be attributed to various causes such as uncertainty in the boundary conditions and the effect of the sensor positioning. However still some questions remained. Especially the impact of the material properties on the simulation outcome remained unclear. There is a large uncertainty on the provided hygrothermal material properties and this uncertainty will have its impact on the simulation accuracy.
To asses the impact of this material data uncertainty on the simulation outcome, a *One-at-a-Time* sensitivity analysis was performed. In this analysis only one parameter is altered while the rest is fixed. In total five material parameters were analysed. Density, thermal conductivity and heat capacity have a small uncertainty range ($< 5\%$) and changes of 5% showed no impact on the model outcome.
The hygrothermal properties (sorption isotherm and vapour resistance factor) showed larger uncertainties. Uncertainties up to 20% were reported. The sensitivity analysis showed that these uncertainties result in relative humidity differences of 2% points.
Also the uncertainty on boundary conditions was analysed. The uncertainty on inlet temperature (± 0.1°C) and inlet relative humidity ($\pm 1.4\%$) had a direct influence on the model outcome. Changes in inlet velocity had little effect. The combination of material data uncertainty and uncertainty in the boundary conditions explains the deviations between experiment and simulations. With this

in mind it can be stated that the model agrees well with the measurements.
If the model is to be extended to also include liquid transport, the mass fraction can no longer be used as the transport variable. Therefore a new variable is chosen: capillary pressure. Since two variables are now used, one for vapour transport in air and one for moisture transport (vapour and liquid) in the material, a coupling procedure is needed to link both.
A literature review revealed different possible linking methods. The review focused on convective drying models. During convective drying, vapour as well as liquid moisture is transported through a porous material and there is a strong coupling with the heat and moisture transport in the air. Three classes of drying models were distinguished. The first class was categorized as analytical models. These models solve the governing differential equations directly without the use of numerical techniques. This is however only possible when very simple boundary conditions (constant values, constant fluxes) are used. For convective drying these simplified boundaries do not suffice.
By applying the boundary layer theory, the convective transport in the air near the porous material can be modelled by using transfer coefficients. This resulted in a second class of drying models. By applying numerical techniques it is possible to implement more complex boundary conditions such as spatially varying transfer coefficients. Especially during the constant drying rate period these varying transfer coefficients have a significant impact.
The third class of convective drying models are the numerical models using a fully coupled or conjugate approach. In this approach it is no longer necessary to determine the transfer coefficients in advance. Heat and moisture transport is solved in the air as well as in the material, while continuity of temperature, mass fraction, heat flux and moisture flux is assured at the boundaries.
If the two domains, air and material, are explicitly coupled for example by first calculating the fluxes at the air side and passing these fluxes to the material side, numerical convergence may become difficult. The two domains should be coupled implicitly to improve solver stability. A *hybrid* solution technique is passing transfer coefficients instead of fluxes. At the air side the fluxes are calculated and with the correct reference for temperature or mass fraction the corresponding transfer coefficients are determined. These transfer coefficients are then passed to the material side and implemented as an implicit boundary condition. This results in a stable solution procedure with guaranteed continuity at the boundaries. This method gives promising results.
The liquid transport model was validated using data both from literature and from newly conducted experiments. The data from literature was used to investigate the impact of model simplifications on the model outcome. From these results it was concluded that 1D and 2D modelling of drying does not suffice, even for an experiment which was originally designed for 2D drying. A 3D model with spatially varying transfer coefficients was needed for a reasonable agreement with the measurements.
Again, as was the case for the vapour transport validation, no perfect match between measurements and simulations was found. Additional neutron

radiography measurements showed that the model poorly predicted the moisture distribution in the porous material. This could however be attributed to wrong estimated material properties. A modified liquid permeability resulted in a very good agreement.
To further evaluate the impact of material properties on the drying process, a new experiment was conducted with a different material. Calcium silicate, which is a capillary active, hygroscopic and insulating material, was used. This resulted in a very specific drying behaviour, which was well predicted by the drying model. It can thus be concluded that the coupled CFD-HAM model is able to accurately simulate heat, vapour and liquid moisture transport in porous materials.
Finally a case study was performed where the impact of accurate modelling of convection was evaluated. In this study heat and moisture transport in a ventilated cavity wall was investigated. The ventilated air layer between the two cavity leafs resulted in a strong coupling of transport in air and neighbouring porous walls. For an accurate simulation of the cavity wall, the coupled CFD-HAM model extended with a radiation model, is needed. Buoyancy can be very important in cavity walls. The new model is able to predict the impact of buoyancy on the air flow rate and heat and moisture transport in the cavity.
The results of the coupled model were also compared with those of a simplified cavity wall model. The comparison revealed that a correct evaluation of ventilated cavity walls is only possible if convection is modelled in detail.

7.2 Perspectives and future work

The coupled CFD-HAM model developed in this work is a valuable tool for the assessment of moisture management in the building envelope. This detailed simulation tool can help designers and engineers to make the right decisions and avoid moisture related damage. However at this point the user-friendliness of the model is limited. Simulations are time-consuming and require skilled users. To make the model more broadly accepted, a different model implementation is needed.
After the thorough study in this work, it is the author's opinion that the strategy used in this work, namely implementing all equations in an existing CFD solver is probably not the most suited. A better approach would be to use separately developed models for transport in air (CFD models) and material (HAM models) and to link these with a coupling procedure. This way a stable user-friendly and validated HAM model is combined with a stable, user-friendly CFD model, thus using the benefits of both models. A suitable coupling procedure was already suggested in this work based on the work of Saneinejad et al. [142]. By determining the transfer coefficients at the air side and coupling this back to the material a more stable implicit coupling procedure is possible.
There is no real restriction on the choice of reference temperature or mass fraction in the definition of the transfer coefficients. When studying flow over a flat plate

or in a tube the bulk values for temperature or mass fraction are clearly defined. For more complex geometries, e.g. flow between parallel plates with different boundary conditions, a suitable definition for the reference temperature and mass fraction is more difficult. In this work the values at a certain distance from the wall (e.g. $10mm$) where taken as reference values. In this case the definition of transfer coefficient tends to be lost. Maybe it is better to refer to a linearization of the fluxes and the corresponding linear coefficient instead of transfer coefficient.

The present work clearly indicated the importance of correct material property data. Large deviations between measurements and simulations can occur due to inaccuracies in material data. There is still a lot of improvement possible in measurement techniques and standardization especially concerning hygrothermal properties such as sorption isotherm, retention curve, vapour resistance factor and permeability.

The presented model is not limited to building applications. Especially drying models can be valuable to study material drying in industrial applications. The model can be used to optimize dryer design.
An other research field were the new model could be valuable is that of organic material drying (e.g. food drying, wood drying,...). However when organic materials are dried, they tend to shrink. This shrinkage deforms the material significantly and has an impact on the drying itself. The present model does not include the effects of shrinkage.

Finally, the new model is limited to the modelling of conjugate heat and mass transport in air and porous materials. If possible structural damage from these occurring phenomena is to be assessed (e.g. occurrence of cracks, buckling, surface spalling), the model should be extended with a mechanical model.

A Material properties

This appendix gives an overview of the used material properties and constants in the simulations.

A.1 Air properties

Table A.1 lists the material properties of moist air as they were used in the CFD simulations. Moist air is a mixture of water vapour and dry air. The properties were taken at 20°C. The density of air is calculated with the ideal gas law.

$$\rho = \frac{P_{op}}{\mathcal{R}T \sum_i \frac{Y_i}{M_i}} \tag{A.1}$$

Property	**Unit**	**dry air**	**water vapour**
Specific heat capacity c_p	J/kgK	1006.43	1875.2
Conductivity λ	W/mK	0.0257	–
Specific gas constant R	J/kgK	286.9	462
Molar mass M	kg/mol	0.02898	0.01799

Table A.1: Material properties of moist air (water vapour and dry air)

Some universal constants and other parameters used for the CFD simulations are listed in Table A.2.

Property	**Unit**	**Value**
Ideal gas constant $\mathcal{R}$	$kJ/kmolK$	8.314
Turbulent Schmidt number Sc_t	–	0.7
Turbulent Prandtl number Pr_t	–	0.85
Density liquid water ρ_l	kg/m^3	998.2
Heat capacity liquid water C_l	J/kgK	4192.1
Atmospheric pressure p_{atm}	Pa	101325
Latent heat of evaporation L	J/kg	$2.5 \cdot 10^6$
Dynamic viscosity μ	kg/ms	$1.7894 \cdot 10^{-5}$

Table A.2: Other constants and parameters used in the CFD simulations

A.2 Porous materials

The material transport properties of ceramic brick have been experimentally determined by Derluyn et al. [151].
The transport properties of calcium silicate were measured during the HAMSTAD project [107, 108]. The material properties of the wood fiber board Celit® produced by Isoproc [160] were taken from Desta et al. [166].

Property	**Ceramic Brick**	**Calcium Silicate**	**Wood fibre board**
ρ $[kg/m^3]$	2087	270	270
c_p $[J/kgK]$	840	1000	1550
λ $[W/mK]$	$1 + 0.0047w$	$0.06 + 5.6 \times 10^{-4}w$	0.048
μ_{dry} [−]	24.79	3	6
w_{cap} $[kg/m^3]$	130	894	162
ψ_0 [−]	0.13	0.894	0.83

Table A.3: Hygrothermal material properties

A.2.1 Moisture transport properties ceramic brick

Vapour diffusion coefficient $\delta_v\ [s]$

$$\delta_v = \frac{2.61 \times 10^{-5}}{\mu_{dry} R_v T} \frac{1 - (w/w_{cap})}{0.503\,(1 - (w/w_{cap}))^2 + 0.497} \tag{A.2}$$

Moisture retention curve

$$w\,(p_c) = w_{cap}[0.846\left(1 + \left(1.394 \times 10^{-5} p_c\right)^4\right)^{-0.75} + 0.154\left(1 + \left(0.9011 \times 10^{-5} p_c\right)^{1.69}\right)^{-0.408}] \tag{A.3}$$

This formula was adjusted to the following in section 5.4.4:

$$w\,(p_c) = w_{cap}[0.5\left(1 + \left(1.394 \times 10^{-5} p_c\right)^4\right)^{-0.75} + 0.5\left(1 + \left(0.9011 \times 10^{-5} p_c\right)^{1.69}\right)^{-0.408}] \tag{A.4}$$

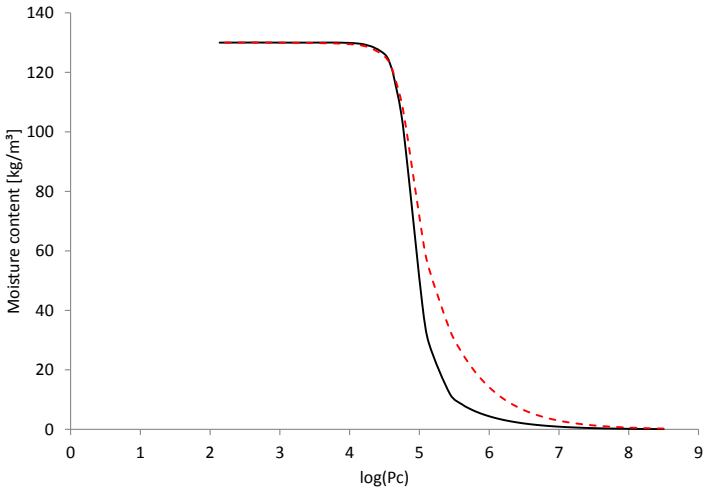

Figure A.1: Retention curve of brick. Original curve by Derluyn et al. [151] (—) and adjusted curve (- -)

Liquid permeability

$$K_l = K_s \left[\sum_{i=1}^{3} w_i \left(1 + (-a_i p_c)^{n_i}\right)^{-m_i} \right]^{\tau} \times \left(\frac{\sum_{i=1}^{3} a_i w_i \left(1 - \left[\frac{(-a_i p_c)^{n_i}}{1+(-a_i p_c)^{n_i}} \right]^{m_i} \right)}{\sum_{i=1}^{3} a_i w_i} \right)^2 \quad \text{(A.5)}$$

i	1	2	3
a_i	$1.35e-5$	$4e-6$	$5e-7$
n_i	6	2	0.7
m_i	0.8333	2	0.4
w_i	0.36	0.25	0.39
w_i adjusted	0.5	0.25	0.25
K_s	$1.15e-9$		
τ	4.003		

Table A.4: Parameters needed for Eq. A.5

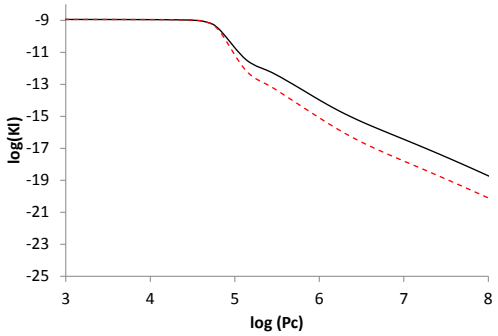

Figure A.2: Liquid permeability of ceramic brick. Original curve by Derluyn et al. [151] (—) and adjusted curve (- -)

A.2.2 Moisture transport properties calcium silicate

Water vapour resistance factor

$$\mu = \left[0.33 + 2.49 \times 10^{-6} \exp\left(6.84RH\right)\right]^{-1} \tag{A.6}$$

Sorption isotherm

$$w = w_{cap}\left[1 + \left(a\rho_{liq}R_vT\ln\left(RH\right)\right)^n\right]^{(1-n)/n} \tag{A.7}$$

with

$$a = -2.936 \times 10^{-5}$$
$$n = 1.7266$$

Liquid permeability

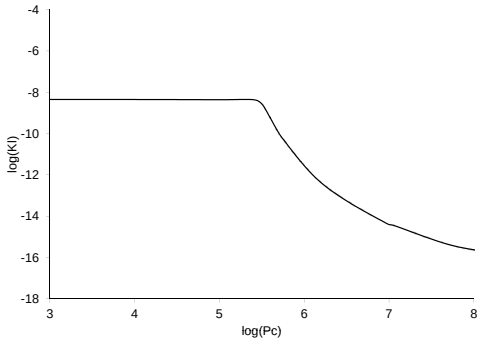

Figure A.3: Liquid permeability of calcium silicate

A.2.3 Moisture transport properties gypsum board

The material properties of gypsum board used in chapter 4 and chapter 6 were taken from Annex 41 [111].

Property	Unit	Gypsum board
ρ	kg/m^3	690
c_p	J/kgK	840
λ	W/mK	0.198
μ_{dry}	–	10.68
w_{cap}	kg/m^3	295
ψ_0	–	0.419

Table A.5: Hygrothermal material properties

Water vapour resistance factor

$$\mu = \frac{\mu_0}{1 + aRH^n} \tag{A.8}$$

with

$$\begin{aligned} \mu_0 &= 10.68205 \\ a &= 1.229557 \\ n &= 2.983921 \end{aligned}$$

Sorption isotherm

The following equation was proposed by Steeman [1] based on the measurement data provided by Roels [111].

$$w_a = \frac{RH}{aRH^2 + bRH + c} \tag{A.9}$$

with

$$\begin{aligned} a &= -0.81655 \\ b &= 0.85157 \\ c &= 0.011176 \end{aligned}$$

A.2.4 Moisture transport properties wood fibre board (Celit®)

Liquid permeability

$$K_l = D_w \frac{w}{p_c} \tag{A.10a}$$

$$D_w = 3.8 \left(\frac{a}{w_{sat}} \right)^2 1000^{\frac{w}{w_{sat}} - 1} \tag{A.10b}$$

with

$$a = 0.0052$$
$$w_{sat} = 162$$

Retention curve

$$w = \left[1 + \left(\frac{mp_c}{R_v T \rho_{liq}}\right)^n\right]^{\frac{1-n}{n}} \tag{A.11}$$

with

$$m = -900$$
$$n = 1.36$$

A.3 Non-hygroscopic materials

The material properties of XPS (extruded polystyreen) and PMMA (polymethyl methacrylate) are taken from Defraeye [43].
Properties of PUR (polyurethane) correspond with those provided by the manufacturer [167] and found in [54].
Properties of mineral wool (MW) where provided by the manufacturer [168].

Property	Unit	PMMA	XPS	PUR	MW
ρ	kg/m^3	1180	65	30	60
c_p	J/kgK	1500	1450	1470	840
λ	W/mK	0.18	0.034	0.023	0.036

Table A.6: Material properties of XPS, PMMA and PUR

B
Publications

Publications as first author in peer reviewed international journals

M. Van Belleghem, H.-J. Steeman, M. Steeman, A. Janssens, M. De Paepe. *Sensitivity analysis of CFD coupled non-isothermal heat and moisture modelling*. Building and Environment, 45(11):2485-2496, 2010.

M. Van Belleghem, M. Steeman, A. Willockx, A. Janssens, M. De Paepe. *Benchmark experiments for moisture transfer modelling in air and porous materials*. Building and Environment, 46(4):884-898, 2011.

M. Van Belleghem, G. Verhaeghe, C. T'Joen, H. Heusseune, P. De Jaeger, M. De Paepe. *Heat Transfer through Vertically Downward Blowing Single-Jet Air Curtains for Cold Rooms*. Heat Transfer Engineering, 33(14):1196-1206, 2012.

Publications as co-author in peer reviewed international journals

H.-J. Steeman, C. T'Joen, M. Van Belleghem, A. Janssens, M. De Paepe. *Evaluation of the different definitions of the convective mass transfer coefficient for water evaporation into air*. International Journal of Heat and Mass Transfer, 52(15-16):3757-3766, 2009.

H.-J. Steeman, M. Van Belleghem, A. Janssens, M. De Paepe. *Coupled simulation of heat and moisture transport in air and porous materials for the assessment of moisture related damage*. Building and Environment, 44(10):2176-2184, 2009.

M. Steeman, A. Janssens, H.-J. Steeman, M. Van Belleghem, M. De Paepe. *On coupling 1D non-isothermal heat and mass transfer in porous materials with a multizone building energy simulation model*. Building and Environment, 45(4):865-877, 2010.

M. Steeman, M. Van Belleghem, M. De Paepe, A. Janssens. *Experimental validation and sensitivity analysis of a coupled BES-HAM model*. Building and Environment, 45(10):2202-2217, 2010.

M. De Paepe, C. T'Joen, H. Huisseune, M. Van Belleghem, V. Kessen. *Comparison of different testing methods for gas fired domestic boiler efficiency determination*. Heat Transfer Engineering, 50(1):275-281, 2013.

B.Ameel, C. T'Joen, K. De Kerpel, P. De Jaeger, H. Heusseune, M. Van Belleghem, M. De Paepe. *Thermodynamic analysis of energy storage with a liquid air Rankine cycle*. Applied Thermal Engineering, 52(1):130-140, 2013.

Publications in proceedings of international conferences

M. Van Belleghem, H.-J. Steeman, M. De Paepe, M. Steeman, A. Janssens. *Design of a test chamber for investigation of moisture transport in air flows and porous materials*. Proceedings of the 8^{th} Symposium on Building Physics in the Nordic Countries - NSB2008, Copenhagen, Denmark, 2008.

M. Van Belleghem, H.-J. Steeman, A. Janssens, M. De Paepe. *Local heat and moisture transfer between indoor air and building materials: a benchmark experiment*. Proceedings of the Building Physics Symposium. Leuven, Belgium, 2008.

M. Van Belleghem, H.-J. Steeman, M. De Paepe, A. Janssens. *Heat and moisture transfer between air and porous materials : a test setup for benchmark experiments*. 4^{th} International Building Physics Conference (IBPC4). Istanbul, Tukey, 2009.

M. Van Belleghem, I. Verhaert, A. Janssens, M. De Paepe M. *Full scale validation and sensitivity analysis of a CFD-HAM model*. 10^{th} REHVA World Congress - CLIMA2010, Antalya, Turkey, 2010.

M. Van Belleghem, A. Willockx, M. De Paepe, M. Steeman, A. Janssens. *Coupled CFD-HAM model sensitivity for material properties and boundary conditions*. 1^{st} Central European symposium on Building Physics, Krakow, Poland, 2010.

M. Van Belleghem, M. Steeman, A. Janssens, M. De Paepe. *Validation of a coupled CFD-HAM model with a climate chamber experiment on a small wall sample*. Proceedings of the 9^{th} Nordic symposium on building physics - NSB2011, Tampere University of Technology, Finland, 2011.

M. Van Belleghem, L. De Backer, A. Janssens, M. De Paepe. *Development of a coupled CFD-HAM model including liquid moisture transport to study moisture transport in building materials*. 5^{th} International Building Physics Conference (IBPC5), Kyoto, Japan, 2012.

M. Van Belleghem, L. De Backer, A. Janssens, M. De Paepe. *Conjugate modelling of convective drying phenomena in porous building materials*. 6^{th} European Thermal Sciences Conference (Eurotherm 2012), Journal of Physics: Conference Series 395 (2012) 012142, Poitiers, France, 2012.

References

[1] H.-J. Steeman. *Modelling Local Hygrothermal Interaction between Airflow and Porous Materials for Building Applications*. Ph.d., Ghent University, 2008.

[2] B. Blocken and J. Carmeliet. *A review of wind-driven rain research in building science*. Journal of Wind Engineering and Industrial Aerodynamics, 92(13):1079–1130, 2004.

[3] G. Tsongas. *Case Studies of moisture Problems in Residences*. In Manual 18 - Manual in Moisture Control in Buildings. ASTM manual series, Philadelphia, 1994.

[4] J. Toftum, A. S. Jorgensen, and P. O. Fanger. *Upper limits of air humidity for preventing warm respiratory discomfort*. Energy and Buildings, 28(1):15–23, 1998.

[5] J. Toftum, A. S. Jorgensen, and P. O. Fanger. *Upper limits for indoor air humidity to avoid uncomfortably humid skin*. Energy and Buildings, 28(1):1–13, 1998.

[6] E. Vereecken and S. Roels. *Review of mould prediction models and their influence on mould risk evaluation*. Building and Environment, 51(0):296–310, 2012.

[7] N. Thaulow and S. Sahu. *Mechanism of concrete deterioration due to salt crystallization*. Materials Characterization, 53(24):123–127, 2004.

[8] A. Nicolai. *Modeling and numerical simulation of salt transport and phase transitions in unsaturated porous building materials*. Phd, Syracuse Universtity, 2008.

[9] *ASHRAE Handbook - Fundamentals*. In Chapter 25 - Heat, Air and Moisture Control in Building Assemblies - Fundamentals. ASHRAE, Atlanta, 2009.

[10] Marshall's Chartered Surveyors. *Picture of rising damp and salt efflorescence*. http://www.marshallsgroup.com/risingdamp.aspx.

[11] All4architect. *Picture of frost damage*. http://www.all4architect.com/articles/item/72-frost-damaged-bricks.html.

[12] Safeguard. *Picture of damage caused by rain penetration*. http://safeguardstore.co.uk/damp-walls/.

[13] Pacific IAQ. *Picture of mould growth inside a cavity wall*. http://pacificiaq.com/hidden-mold.

[14] M. Woloszyn and C. Rode. *IEA ANNEX41 Whole Building Heat, Air and Moisture Response - Subtask1: Modelling Principles and Common Exercises*. Technical report, 2008.

[15] US Department of Energy. *EnergyPlus Energy Simulation Software*. http://apps1.eere.energy.gov/buildings/energyplus/.

[16] University of Strathclyde. *ESP-r, Building Energy Simulation Software*. http://www.esru.strath.ac.uk/Programs/ESP-r.htm.

[17] LLC Thermal Energy System Specialists. *TRNSYS, Transient System Simulation Tool*. http://www.trnsys.com/.

[18] D. Zirkelbach, Th. Schmidt, H. M. Künzel, M. Kehrer, and Ch. Bludau. *WUFI 2D*, 2007.

[19] Bauklimatik Dresden. *Delphin*. http://bauklimatik-dresden.de/delphin/index.php. Simulation program for the calculation of coupled heat, moisture, air, pollutant, and salt transport.

[20] J. Langmans, A. Nicolai, R. Klein, and S. Roels. *A quasi-steady state implementation of air convection in a transient heat and moisture building component model*. Building and Environment, 58:208–218, 2012.

[21] M. Steeman, A. Janssens, H.-J. Steeman, M. Van Belleghem, and M. De Paepe. *On coupling 1D non-isothermal heat and mass transfer in porous materials with a multizone building energy simulation model*. Building and Environment, 45(4):865–877, 2010.

[22] M. Mirsadeghi. *Co-simulation of building energy simulation and computational fluid dynamics for whole-building heat, air and moisture engineering*. Phd, TU Eindhoven, 2011.

[23] H.-J. Steeman, C. T'Joen, M. Van Belleghem, A. Janssens, and M. De Paepe. *Evaluation of the different definitions of the convective mass transfer coefficient for water evaporation into air*. International Journal of Heat and Mass Transfer, 52(15-16):3757–3766, 2009.

[24] L. H. Mortensen, M. Woloszyn, C. Rode, and R. Peuhkuri. *Investigation of microclimate by CFD modeling of moisture interactions between air and constructions*. Journal of Building Physics, 30(4):279–315, 2007.

[25] S. Gnoth, F. Hansel, P. Hupl, and H. Fechner. *Aero-hygrothermisches Verhalten von Umfassungskonstruktionen mit Hohlrumen*. Bauphysik, 30(6):380–388, 2008.

[26] T. Defraeye, B. Blocken, and J. Carmeliet. *Analysis of convective heat and mass transfer coefficients for convective drying of a porous flat plate by conjugate modelling*. International Journal of Heat and Mass Transfer, 55(1-3):112–124, 2012.

[27] C.-E. Hagentoft, A. S. Kalagasidis, B. Adl-Zarrabi, S. Roels, J. Carmeliet, H. Hens, J. Grunewald, M. Funk, R. Becker, D. Shamir, O. Adan, H. Brocken, K. Kumaran, and R. Djebbar. *Assessment Method of Numerical Prediction Models for Combined Heat, Air and Moisture Transfer in Building Components: Benchmarks for One-dimensional Cases*. Journal of Thermal Envelope and Building Science, 27(4):327–352, 2004.

[28] H. Hens. *Building Physics - Heat, Air and Moisture: Fundamentals and Engineering Methods with Examples and Exercises*. Ernst & Sohn, Berlin, 2007.

[29] H. M. Künzel. *Simultanious Heat and Moisture Transport in Building Components - One- and two-dimentional calculation using simple parameters*. Ph.d., Fraunhofer Institute of Building Physics, 1995.

[30] M. J. Moran and H. N. Shapiro. *Fundamentals of Engineering Thermodynamics*. John Wiley & Sons, Inc., New York, 6^th edition edition, 2010.

[31] F. Descamps. *Continuum and discrete modelling of isothermal water and air flow in porous media*. Ph.d., KULeuven, 1996.

[32] J. Carmeliet, F. Descamps, and G. Houvenaghel. *A multiscale network model for simulating moisture transfer properties of porous media*. Transport in Porous Media, 35(1):67–88, 1999.

[33] S. Whitaker. *Simultaneous heat, mass and momentum transfer in porous media: A theory of drying*, volume 13 of *Advances in Heat Transfer*. Academic Press, New York, 1977.

[34] J. R. Philip and D. A. de Vries. *Moisture movement in porous materials under temperature gradients*. Transactions of the American Geophysical Union, 38:222–232, 1957.

[35] A. S. Mujumdar. *Handbook of Industrial Drying*. CRC Press, 3^{th} edition, 2007.

[36] O. Krischer. *Die wissenschaftlischen Grundlagen der Trochnungstechnik*. Springer-Verlag, Berlin / Göttingen / Heidelberg, 2^{nd} edition, 1963.

[37] D. N. Sorensen and P. V. Nielsen. *Quality control of computational fluid dynamics in indoor environments*. Indoor Air, 13(1):2–17, 2003.

[38] *Ansys Fluent 12.0*, 2009.

[39] H. K. Versteeg and W. Malalasekara. *An introduction to computational fluid dynamics: the finite volume method*. Pearson Education Limited, Essex, UK, 2^{th} edition, 2007.

[40] P. A. Durbin. *Separated Flow Computations With The K-Epsilon-Upsilon(2) Model*. AIAA Journal, 33(4):659–664, 1995.

[41] B. E. Launder, G. J. Reece, and W. Rodi. *Progress in Development of a Reynolds-Stress Turbulence Closure*. Journal of Fluid Mechanics, 68(APR15):537–566, 1975.

[42] P. R. Spalart and S. R. Allmaras. *A One-Equation Turbulence Model For Aerodynamic Flows*. Recherche Aerospatiale, (1):5–21, 1994.

[43] T. Defraeye. *Convective Heat and Mass Transfer at Exterior Building Surfaces*. Ph.d. thesis, KULeuven, 2011.

[44] K. Goethals. *Convective Heat Transfer Modelling in Offices with Night Ventilation*. Ph.d., Ghent University, 2012.

[45] Z. Q. Zhai, W. Zhang, Z. Zhang, and Q. Y. Chen. *Evaluation of various turbulence models in predicting airflow and turbulence in enclosed environments by CFD: part 1 - Summary of prevalent turbulence models*. Hvac&R Research, 13(6):853–870, 2007.

[46] Z. Zhang, Z. Q. Zhai, W. Zhang, and Q. Y. Chen. *Evaluation of various turbulence models in predicting airflow and turbulence in enclosed environments by CFD: Part 2-comparison with experimental data from literature*. Hvac&R Research, 13(6):871–886, 2007.

[47] A. K. M. F. Hussain and W. C. Reynolds. *Measurements in fully developed turbulent channel flow*. Transactions of the ASME. Series I, Journal of Fluids Engineering, 97(4):568–580, 1975.

[48] J. R. Welty, C. E. Wicks, R. E. Wilson, and G. Rorrer. *Fundamentals of Momentum, Heat and Mass Transport*. John Wiley & Sons, Inc., New York, 4th edition, 2001.

[49] R. Schirmer. *Die Diffusionszahl von Wasserdampf-Luftgemischen und die Verdampfungsgeschwindigkeit*. VDI Beiheft Verfahrestechnik, 6:170–172, 1938.

[50] K. M. Waananen, J. B. Litchfield, and M. R. Okos. *Classification of Drying Models for Porous Solids*. Drying Technology, 11(1):1–40, 1993.

[51] S. Whitaker. *The role of irreversible thermodynamics and the Onsager relations in the analysis of drying phenomena*. In sixth International Drying Symposium IDS'88, Versailles, 1988.

[52] H. Janssen. *Thermal diffusion of water vapour in porous materials: Fact or fiction?* International Journal of Heat and Mass Transfer, 54(7-8):1548–1562, 2011.

[53] J. Grunewald. *Diffusiver und konvektiver Stoff- und Energietransport in kapillarporösen Baustoffen*. Ph.d., Technischen Universität Dresden, 1997.

[54] A. Janssens. *IEA ANNEX 24 - HAMTIE - Cataloque of material properties*. Technical report, International Energy Agency, 1994.

[55] P. Steskens. *Modelling of the Hygrothermal Interaction between the Indoor Environment and the Building Envelope*. Ph.d., Technical University Denmark, DTU, 2009.

[56] Ansys. *Ansys Fuent 12.0 - UDF Manual*. 2009.

[57] Ansys. *Ansys Fluent 12.0 - Theory guide*. 2009.

[58] Z. Q. Zhai, Q. Y. Chen, P. Haves, and J. H. Klems. *On approaches to couple energy simulation and computational fluid dynamics programs*. Building and Environment, 37(8-9):857–864, 2002.

[59] P. C. D. Milly. *A Mass-Conservative Procedure for Time-Stepping in Models of Unsaturated Flow*. Advances in Water Resources, 8(1):32–36, 1985.

[60] M. A. Celia, E. T. Bouloutas, and R. L. Zarba. *A General Mass-Conservative Numerical-Solution for the Unsaturated Flow Equation*. Water Resources Research, 26(7):1483–1496, 1990.

[61] K. Rathfelder and L. M. Abriola. *Mass Conservative Numerical-Solutions of the Head-Based Richards Equation*. Water Resources Research, 30(9):2579–2586, 1994.

[62] H. Janssen, B. Blocken, and J. Carmeliet. *Conservative modelling of the moisture and heat transfer in building components under atmospheric excitation*. International Journal of Heat and Mass Transfer, 50(5-6):1128–1140, 2007.

[63] F. R. Menter. *Improved two-equation k-omega turbulence models for aerodynamic flows*. technical memorandum 103975, NASA, 1992.

[64] A. Neale, D. Derome, B. Blocken, and J. Carmeliet. *Coupled simulation of vapour flow between air and a porous material*. In Thermal Performance of Exterior Envelopes of Whole Buildings X, Atlantha, 2007. ASHRAE.

[65] H. Janssen. *The Influence of soil moisture transfer on building heat loss via the ground*. Ph.d., KULeuven, 2002.

[66] P. C. D. Milly. *Moisture and heat transport in hysteretic, inhomogeneous porous media: a matrix head-based formulation and a numerical model*. Water Resources Research—Water Resources Research, 18(3):489–98, 1982.

[67] H.-J. Steeman, M. Van Belleghem, A. Janssens, and M. De Paepe. *Coupled simulation of heat and moisture transport in air and porous materials for the assessment of moisture related damage*. Building and Environment, 44(10):2176–2184, 2009.

[68] J. Crank. *The Mathematics of Diffusion*. Oxford University Press, Oxford, 1975.

[69] R. H. Perry and D. W. Green. *Perry's Chemical Engineers Handbook*, chapter 12. McGraw-Hill, 2008.

[70] T. H. Chilton and A. P. Colburn. *Mass Transfer (Absorption) Coefficients Prediction from Data on Heat Transfer and Fluid Friction*. Industrial and Engineering Chemistry, 26:1183–1187, 1934.

[71] J. S. Lewis. *Heat transfer predictions from mass transfer measurements around a single cylinder in cross flow*. International Journal of Heat and Mass Transfer, 14:325–329, 1971.

[72] P. Talukdar, C. R. Iskra, and C. J. Simonson. *Combined heat and mass transfer for laminar flow of moist air in a 3D rectangular duct: CFD simulation and validation with experimental data*. International Journal of Heat and Mass Transfer, 51(11-12):3091–3102, 2008.

[73] X. D. Chen, S. X. Q. Lin, and G. Chen. *On the ratio of heat to mass transfer coefficient for water evaporation and its impact upon drying modeling*. International Journal of Heat and Mass Transfer, 45(21):4369–4372, 2002.

[74] J. Carmeliet and S. Roels. *Determination of the Isothermal Moisture Transport Properties of Porous Building Materials*. Journal of Thermal Envelope and Building Science, 24(3):183–210, 2001.

[75] P. Talukdar, O. F. Osanyintola, S. O. Olutimayin, and C. J. Simonson. *An experimental data set for benchmarking 1-D, transient heat and moisture transfer models of hygroscopic building materials. Part II: Experimental, numerical and analytical data*. International Journal of Heat and Mass Transfer, 50(25-26):4915–4926, 2007.

[76] R. Hohota. *Modelisation de l'humidit dans un code CFD (basses vitesses en grande cavit) comparaison avec l'experimental*. Ph.d., LInstitut national des sciences appliques de Lyon, 2003.

[77] C. Teodosiu, R. Hohota, G. Rusaouen, and M. Woloszyn. *Numerical prediction of indoor air humidity and its effect on indoor environment*. Building and Environment, 38(5):655–664, 2003.

[78] X. Yang, S. Vera, J. Rao, H. Ge, and P. Fazio. *Full-scale experimental investigation of moisture buffering effect and indoor moisture distribution*. In Building X, Florida, 2007.

[79] A. Alturkistani, P. Fazio, J. Rao, and Q. Mao. *A new test method to determine the relative drying capacity of building envelope panels of various configurations*. Building and Environment, 43(12):2203–2215, 2008.

[80] P. Fazio, A. K. Athienitis, C. Marsh, and J. Rao. *Environmental Chamber for Investigation of Building Envelope Performance*. Journal of Architectural Engineering, 3(2):97–102, 1997.

[81] Q. Li, J. Rao, and P. Fazio. *Development of HAM tool for building envelope analysis*. Building and Environment, 44(5):1065–1073, 2009.

[82] Y. Li, P. Fazio, and J. Rao. *Numerical investigation of the influence of room factors on HAM transport in a full-scale experimental room*. Building and Environment, 50:114–124, 2012.

[83] K. Svennberg, L. Hedegaard, and C. Rode. *Moisture Buffer Performance of a Fully Furnished Room*. In 9th International Conference on Performance of the Exterior Envelopes of Whole Buildings, Clearwater Beach, FL, USA, 2004. American Society of Heating, Refrigeration and Air-Conditioning Engineers, Inc. (www.ashrae.org).

[84] L. Hedegaard, C. Rode, and R. Peuhkuri. *Full scale tests of moisture buffer capacity of wall materials*. In 7th Nordic Building Physics Symposium, Reykjavic, Iceland, 2005.

[85] O. F. Osanyintola and C. J. Simonson. *Moisture buffering capacity of hygroscopic building materials: Experimental facilities and energy impact*. Energy and Buildings, 38(10):1270–1282, 2006.

[86] P. Talukdar, S. O. Olutmayin, O. F. Osanyintola, and C. J. Simonson. *An experimental data set for benchmarking 1-D, transient heat and moisture transfer models of hygroscopic building materials. Part I: Experimental facility and material property data*. International Journal of Heat and Mass Transfer, 50(23-24):4527–4539, 2007.

[87] S. O. Olutimayin and C. J. Simonson. *Measuring and modeling vapor boundary layer growth during transient diffusion heat and moisture transfer in cellulose insulation*. International Journal of Heat and Mass Transfer, 48(16):3319–3330, 2005.

[88] O. F. Osanyintola, P. Talukdar, and C. J. Simonson. *Effect of initial conditions, boundary conditions and thickness on the moisture buffering capacity of spruce plywood*. Energy and Buildings, 38(10):1283–1292, 2006.

[89] C.R. Iskra and C. J. Simonson. *Convective mass transfer coefficient for a hydrodynamically developed airflow in a short rectangular duct*. International Journal of Heat and Mass Transfer, 50(11-12):2376–2393, 2007.

[90] H. Yoshino, T. Mitamura, and K. Hasegawa. *Moisture buffering and effect of ventilation rate and volume rate of hygrothermal materials in a single room under steady state exterior conditions*. Building and Environment, 44(7):1418–1425, 2009.

[91] A. Holm and H. M. Künzel. *Experimental investigation of hygric buffering capacity of wood based interior paneling*. In 3th international Building Physics Conference - Research in building Physics and Building Engineering, Concordia University Montreal, 2006.

[92] *Energy Conservation in Buildings and Community Systems (ECBCS). Annex 41 Whole Building Heat, Air and Moisture Response (MOIST-ENG).* www.ecbcs.org/annexes/annex41.htm.

[93] P. Plathner and M. Woloszyn. *Interzonal air and moisture transport in a test house: experiment and modelling*. Building and Environment, 37(2):189–199, 2002.

[94] J. Oldengarm and W. F. De Gids. *Field experiments on airborne moisture transport*. Air Infiltration Review, 12(2):8–11, 1991.

[95] C. J. Simonson. *Moisture, thermal and ventilation performance of Tapanila ecological house - VTT Research notes 2069*. Technical report, Technical Research Centre of Finland, 2000.

[96] J. Sadauskiene, V. Stankevicius, R. Bliudzius, and A. Gailius. *The impact of the exterior painted thin-layer render's water vapour and liquid water permeability on the moisture state of the wall insulating system*. Construction and Building Materials, 23(8):2788–2794, 2009.

[97] Z. Pavlik, J. Pavlik, M. Jirickova, and R. Cerny. *System for Testing the Hygrothermal Performance of Multi-Layered Building Envelopes*. Journal of Building Physics, 25(3):239–249, 2002.

[98] Z. Pavlik and R. Cerny. *Hygrothermal performance study of an innovative interior thermal insulation system*. Applied Thermal Engineering, 29(10):1941–1946, 2009.

[99] P. Dionisi Vici, P. Mazzanti, and L. Uzielli. *Mechanical response ofwooden boards subjected tohumidity step variations: climatic chamber measurements andfitted mathematical models*. Journal of Cultural Heritage, 7(1):37–48, 2006.

[100] R. Belarbi, M. Qin, A. At-Mokhtar, and L. O. Nilsson. *Experimental and theoretical investigation of non-isothermal transfer in hygroscopic building materials*. Building and Environment, 43(12):2154–2162, 2008.

[101] T. Bednar and J. Dreyer. *Determination of moisture surface transfer coefficients under transient conditions*. In 2nd international conference on building physics - Research in Building Physics, Antwerp, Belgium, 2003.

[102] *ISOCAB*. http://www.isocab.be.

[103] B. J. Huang, Y. C. Liao, and T. C. Kuo. *Study of a new environmental chamber design*. Applied Thermal Engineering, 27(11-12):1967–1977, 2007.

[104] *GEFRAN*. http://www.gefran.se/main/datablad_PDF/Fuktgivare/T232-BT_ing.pdf.

[105] *Honeywell*. http://sensing.honeywell.com/index.php?ci_id=49922.

[106] J. B. Dooley and D. L. O'Neal. *The transient response of capacitive thin-film polymer humidity sensors*. Hvac&R Research, 14(5):663–682, 2008.

[107] O. Adan, H. Brocken, J. Carmeliet, H. Hens, S. Roels, and C.-E. Hagentoft. *Determination of Liquid Water Transfer Properties of Porous Building Materials and Development of Numerical Assessment Methods: Introduction to the EC HAMSTAD Project*. Journal of Thermal Envelope and Building Science, 27(4):253–260, 2004.

[108] S. Roels, J. Carmeliet, and H. Hens. *HAMSTAD WP1 - Moisture transport properties and material characterisation - Final report*. Technical report, KULeuven, 2003.

[109] M. Steeman, M. Van Belleghem, M. De Paepe, and A. Janssens. *Experimental validation and sensitivity analysis of a coupled BES-HAM model*. Building and Environment, 45(10):2202–2217, 2010.

[110] S. Roels, J. Carmeliet, H. Hens, O. Adan, H. Brocken, R. Cerny, Z. Pavlik, C. Hall, K. Kumaran, L. Pel, and R. Plagge. *Interlaboratory Comparison of Hygric Properties of Porous Building Materials*. Journal of Thermal Envelope and Building Science, 27(4):307–325, 2004.

[111] S. Roels. *IEA ANNEX41 Whole Building Heat, Air and Moisture Response - Subtask 2: Experimental Analysis of Moisture Buffering*. Technical report, 2008.

[112] C. James, C. J. Simonson, P. Talukdar, and S. Roels. *Numerical and experimental data set for benchmarking hygroscopic buffering models*. International Journal of Heat and Mass Transfer, 53(19-20):3638–3654, 2010.

[113] P. J. Roache. *Quantification of uncertainty in computational fluid dynamics*. Annual Review of Fluid Mechanics, 29:123–160, 1997.

[114] J. A. Clarke and P. P. Yaneske. *A rational approach to the harmonisation of the thermal properties of building materials*. Building and Environment, 44(10):2046–2055, 2009.

[115] Y. Mualem. *Conceptual Model of Hysteresis*. Water Resources Research, 10(3):514–520, 1974.

[116] P. C. D. Milly. *The coupled transport of water and heat in a vertical soil column under atmospheric excitation*. Ph.d., Massachusetts Institute of Technology, 1980.

[117] S. Roels, H. Janssen, J. Carmeliet, J. Diepens, and M. de Wit. *Hygric buffering capacities of uncoated and coated gypsum board*. In Third International Building Physics Conference - Research in Building Physics and Building Engineering, Montreal, Canada, 2006.

[118] K. A. Landman, L. Pel, and E. F. Kaasschieter. *Analytic modelling of drying of porous materials*. Mathematical Engineering in Industry, 8(2):89–122, 2001.

[119] E. Barati and J. A. Esfahani. *Mathematical modeling of convective drying: Lumped temperature and spatially distributed moisture in slab*. Energy, 36(4):2294–2301, 2011.

[120] K. Abahri, R. Belarbi, and A. Trabelsi. *Contribution to analytical and numerical study of combined heat and moisture transfers in porous building materials*. Building and Environment, 46(7):1354–1360, 2011.

[121] L. Pel. *Moisture transport in porous building materials*. Phd dissertation, Technische Universiteit Eindhoven, 1995.

[122] W. M. Kays and M. E. Crawford. *Convective heat and mass transfer*. McGraw-Hill, 3^{rd} edition, 1993.

[123] W. M. Rohsenow, J. P. Hartnett, and Y. I. Cho. *Handbook of Heat Transfer*. McGraw-Hill Companies, Inc., New York, 3^{rd} edition, 1998.

[124] A. Kondjoyan. *A review on surface heat and mass transfer coefficients during air chilling and storage of food products*. International Journal of Refrigeration, 29(6):863–875, 2006.

[125] D. Berger and D. C. T. Pei. *Drying of hygroscopic capillary porous solids - a theoretical approach*. International Journal of Heat and Mass Transfer, 16:293–302, 1973.

[126] N. Wang and J. G. Brennan. *A mathematical model of simultaneous heat and moisture transfer during drying of potato*. Journal of Food Engineering, 24(1):47–60, 1995.

[127] W. Masmoudi and M. Prat. *Heat and Mass-Transfer between a Porous-Medium and a Parallel External Flow - Application to Drying of Capillary Porous Materials*. International Journal of Heat and Mass Transfer, 34(8):1975–1989, 1991.

[128] A. Kaya, O. AydIn, and I. Dincer. *Numerical modeling of heat and mass transfer during forced convection drying of rectangular moist objects*. International Journal of Heat and Mass Transfer, 49(17-18):3094–3103, 2006.

[129] V. P. C. Mohan and P. Talukdar. *Three dimensional numerical modeling of simultaneous heat and moisture transfer in a moist object subjected to convective drying*. International Journal of Heat and Mass Transfer, 53(21-22):4638–4650, 2010.

[130] H. Shokouhmand, V. Abdollahi, S. Hosseini, and K. Vahidkhah. *Performance Optimization of a Brick Dryer Using Porous Simulation Approach*. Drying Technology, 29(3):360–370, 2011.

[131] M. M. Hussain and I. Dincer. *Two-dimensional heat and moisture transfer analysis of a cylindrical moist object subjected to drying: A finite-difference approach*. International Journal of Heat and Mass Transfer, 46(21):4033–4039, 2003.

[132] A.-L. Ljung, T. S. Lundstrom, B. D. Marjavaara, and K. Tano. *Convective drying of an individual iron ore pellet - Analysis with CFD*. International Journal of Heat and Mass Transfer, 54(17-18):3882–3890, 2011.

[133] L. S. Oliveira and K. Haghighi. *Conjugate heat and mass transfer in convective drying of porous media*. Numerical Heat Transfer, Part A: Applications, 34(2):105–117, 1998.

[134] H. Amir, G. Le Palec, and M. Daguenet. *Séchage superficiel d'un matériau poreux humide par convection forcée d'air chaud: couplage entre les équations de transfert dans le matériau et celles de la couche limite*. International Journal of Heat and Mass Transfer, 30(6):1149–1158, 1987.

[135] B. Zeghmati, M. Daguenet, and G. Le Palec. *Study of transient laminar free convection over an inclined wet flat plate*. International Journal of Heat and Mass Transfer, 34(4/5):899–909, 1991.

[136] A. A. Dolinskiy, A. S. H. Dorfman, and B. V. Davydenko. *Conjugate heat and mass transfer in continuous processes of convective drying*. International Journal of Heat and Mass Transfer, 34(11):2883–2889, 1991.

[137] L. S. Oliveira and K. Haghighi. *Conjugate Heat and Mass Transport in Convective Drying of Multiparticle Systems Part II: Soybean Drying*. Drying Technology, 16(3-5):463–483, 1998.

[138] K. Murugesan, H. N. Suresh, K. N. Seetharamu, P. A. A. Narayana, and T. Sundararajan. *A theoretical model of brick drying as a conjugate problem*. International Journal of Heat and Mass Transfer, 44(21):4075–4086, 2001.

[139] M. V. De Bonis and G. Ruocco. *A generalized conjugate model for forced convection drying based on an evaporative kinetics*. Journal of Food Engineering, 89(2):232–240, 2008.

[140] C. Lamnatou, E. Papanicolaou, V. Belessiotis, and N. Kyriakis. *Finite-volume modelling of heat and mass transfer during convective drying of porous bodies - Non-conjugate and conjugate formulations involving the aerodynamic effects*. Renewable Energy, 35(7):1391–1402, 2010.

[141] C. Lamnatou, E. Papanicolaou, V. Belessiotis, and N. Kyriakis. *Numerical study of the interaction among a pair of blunt plates subject to convective drying - A conjugate approach*. International Journal of Thermal Sciences, 49(12):2467–2482, 2010.

[142] S. Saneinejad, P. Moonen, T. Defraeye, D. Derome, and J. Carmeliet. *Coupled CFD, radiation and porous media transport model for evaluating evaporative cooling in an urban environment*. Journal of Wind Engineering and Industrial Aerodynamics, 104(0):455–463, 2012.

[143] T. Defraeye, B. Blocken, D. Derome, B. Nicolai, and J. Carmeliet. *Convective heat and mass transfer modelling at air-porous material interfaces: Overview of existing methods and relevance*. Chemical Engineering Science, 74:49–58, 2012.

[144] R. B. Dean. *Reynolds Number Dependence of Skin Friction and Other Bulk Flow Variables in Two-Dimensional Rectangular Duct Flow*. Journal of Fluids Engineering, 100(2):215–223, 1978.

[145] R. Siegel and J. R. Howell. *Thermal Radiation Heat Transfer*. Hemisphere Publishing Corporation, Washington, 3^{th} edition, 1992.

[146] T. Defraeye, B. Blocken, and J. Carmeliet. *Influence of uncertainty in heat-moisture transport properties on convective drying of porous materials by numerical modelling*. Chemical Engineering Research and Design, 2012. article in press DOI: 10.1016/j.cherd.2012.06.011.

[147] S. Roels, P. Talukdar, C. James, and C. J. Simonson. *Reliability of material data measurements for hygroscopic buffering*. International Journal of Heat and Mass Transfer, 53(23-24):5355–5363, 2010.

[148] H. Derluyn, M. Griffa, D. Mannes, I. Jerjen, J. Dewanckele, P. Vontobel, A. Sheppard, M. N. Boone, D. Derome, E. H. Lehmann, and J. Carmeliet. *Probing salt crystallization damage mechanisms in porous limestone with neutron radiography and X-ray tomography*. In 5th International Building Physics Conference (IBPC2012), Kyoto, Japan, 2012.

[149] M. Sedighi-Gilani, M. Griffa, D. Mannes, E. Lehmann, J. Carmeliet, and D. Derome. *Visualization and quantification of liquid water transport in softwood by means of neutron radiography*. International Journal of Heat and Mass Transfer, 55(2122):6211–6221, 2012.

[150] E. H. Lehmann, G. Frei, G. Khne, and P. Boillat. *The micro-setup for neutron imaging: A major step forward to improve the spatial resolution*. Nuclear Instruments and Methods in Physics Research Section A: Accelerators, Spectrometers, Detectors and Associated Equipment, 576(23):389–396, 2007.

[151] H. Derluyn, H. Janssen, P. Moonen, and J. Carmeliet. *Moisture transfer across the interface between brick and mortar joint*. In Proceedings of the 8th Symposium on Building Physics in the Nordic Countries, Copenhagen, Denmark, 2008.

[152] *Calsitherm*. http://www.calsitherm.de/en/products.htm.

[153] M. Salonvaara, A. N. Karagiozis, M. Pazera, and W. Miller. *Air Cavities Behind Claddings - What Have We Learned?* In Thermal Performance of the Exerior Envelopes of Whole Buildings X, Florida, US, 2007.

[154] H. Hens, A. Janssens, W. Depraetere, J. Carmeliet, and J. Lecompte. *Brick cavity walls: A performance analysis based on measurements and Simulations*. Journal of Building Physics, 31(2):95–124, 2007.

[155] A. N. Karagiozis and H. M. Künzel. *The effect of air cavity convection on the wetting and drying behavior of wood-frame walls using a multi-physics approach*. Journal od ASTM International, 6(10), 2009.

[156] H. Ge and Y. Ye. *Investigation of Ventilation Drying of Rainscreen Walls in the Coastal Climate of British Columbia*. In Thermal Performance of the Exerior Envelopes of Whole Buildings X, Florida, US, 2007.

[157] C. Sanjuan, M. Jose Suarez, E. Blanco, and M. del Rosario Heras. *Development and experimental validation of a simulation model for open joint ventilated facades*. Energy and Buildings, 43(12):3446–3456, 2011.

[158] J. Straube and G. Finch. *Ventilation Wall Claddings: Review, Field Performance and Hygrothermal Modeling*. Technical report, Building Science Corporation, 2009.

[159] G. Finch and J. Straube. *Ventilated Wall Claddings: Review, Field Performance and Hygrothermal Modeling*. In Thermal Performance of the Exterior Envelopes of Whole Buildings X, Florida, US, 2007.

[160] *ISOPROC*. http://www.isoproc.be.

[161] Meteotest. *Meteonorm: global meteorological database*. http://www.meteonorm.com.

[162] H. Hens. *Bouwfysica 1: Warmte en Massatransport (in Dutch)*. ACCO, Leuven, 1997.

[163] Verein Deutscher Ingenieure. *VDI-Wärmeatlas: Berechnungsblätter für den Wärmeübergang*. VDI Verlag, Dusseldorf, 7th edition, 1994.

[164] J. Straube. *Moisture Control and Enclosure Wall Systems*. Phd, University of Waterloo, 1998.

[165] E. Jung. *Long-Term Performance of Facing Masonry Exposed to the Weather and the Effect of Cavity Insulation. Results of Tests Carried out in Laboratory and on Buildings*. Baustoffindustrie, 28(6):185, 1985.

[166] T. Z. Desta, J. Langmans, and S. Roels. *Experimental data set for validation of heat, air and moisture transport models of building envelopes*. Building and Environment, 46(5):1038–1046, 2011.

[167] *RECTICEL*. http://www.recticelinsulation.be.

[168] *Rockwool*. http://www.rockwool.be.